Geological Fieldwork 2021

A Summary of Field Activities and Current Research

BRITISH COLUMBIA
Ministry of
Energy, Mines and
Low Carbon Innovation

Paper 2022-01

BRITISH COLUMBIA

Ministry of
Energy, Mines and
Low Carbon Innovation

Geological Fieldwork 2021

A Summary of Field Activities and Current Research

Ministry of Energy, Mines and Low Carbon Innovation
British Columbia Geological Survey

Paper 2022-01

Ministry of Energy, Mines and Low Carbon Innovation
Mines, Competitiveness, and Authorizations Division
British Columbia Geological Survey

Recommended citation format for individual papers:

Schiarizza, P., Orchard, M.J., and Friedman, R.M., 2022. Conodonts and detrital zircons from Triassic and Jurassic rocks above the Salmon River unconformity, Thompson Plateau, south-central British Columbia. In: Geological Fieldwork 2021, British Columbia Ministry of Energy, Mines and Low Carbon Innovation, British Columbia Geological Survey Paper 2022-01, pp. 17-30.

Front Cover:
Rounded hills in background underlain by quartz monzonite to quartz diorite of the Coast Plutonic Complex at the southwest end of the Tsimstol Mountain massif, western Kitsault River area. Grassy area in foreground with scattered outcrops of upper Hazelton Group siltstones and feldspathic wackes. Intrusive contact at base of cliff outcrop at central right, near edge of snowpack. View to the southwest. See Hunter, R.C., Sebert, C.F.B., Friedman, R., and Wall, C., 2022. Revised stratigraphy and geochronology of the Hazelton Group, host rocks for volcanogenic mineralization in the Kitsault River area, northwest British Columbia, this volume. **Photo by Rebecca Hunter.**

Back Cover:
Light-toned bedded andesitic to dacitic tuffs, lahars, and lacustrine volcaniclastic deposits, upper member of the Tranquille Formation (Eocene, Kamloops Group) cut by dark-toned, near-vertical east-trending mafic dike. View to the northeast from within Kamloops city limits. See Van Wagoner, N., and Ootes, L., 2022. Geology and geochemistry of the Kamloops Group (Eocene) in its type area, Kamloops, British Columbia, this volume. **Photo by Nancy Van Wagoner.**

This publication is available, free of charge, from the British Columbia Geological Survey website:
https://www2.gov.bc.ca/gov/content/industry/mineral-exploration-mining/british-columbia-geological-survey/publications

British Columbia Cataloguing in Publication Data

Main entry under title:

Geological Fieldwork: - 1974 -

Annual.

Issuing body varies

Vols. for 1978-1996 issued in series: Paper / British Columbia. Ministry of Energy, Mines and Petroleum Resources; vols. for 1997 - 1998, Paper / British Columbia. Ministry of Employment and Investment; vols. for 1999-2004, Paper / British Columbia. Ministry of Energy and Mines; vols. for 2005-2009, Paper / British Columbia. Ministry of Energy, Mines and Petroleum Resources; vols. for 2010, Paper / British Columbia. Ministry of Forests, Mines and Lands; vols. for 2011, Paper / British Columbia. Ministry of Energy and Mines; vols. for 2012- , Paper / British Columbia. Ministry of Energy, Mines and Natural Gas; vols. for 2014- , Paper / British Columbia. Ministry of Energy and Mines; vols. for 2018- , Paper / British Columbia. Ministry of Energy, Mines and Petroleum Resources; vols. for 2021- , Paper / British Columbia. Ministry of Energy, Mines and Low Carbon Innovation.

Includes Bibliographical references.

ISSN 0381-243X=Geological Fieldwork

1. Geology - British Columbia - Periodicals. 2. Mines and mineral resources - British Columbia - Periodicals. 3. Geology - Fieldwork - Periodicals. 4. Geology, Economic - British Columbia - Periodicals. 5. British Columbia. Geological Survey Branch - Periodicals. I. British Columbia. Geological Division. II. British Columbia. Geological Survey Branch. III. British Columbia. Geological Survey Branch. IV. British Columbia. Dept. of Mines and Petroleum Resources. V. British Columbia. Ministry of Energy, Mines and Petroleum Resources. VI. British Columbia. Ministry of Employment and Investment. VII. British Columbia Ministry of Energy and Mines. VIII. Series: Paper (British Columbia. Ministry of Energy, Mines and Petroleum Resources). IX. Series: Paper (British Columbia. Ministry of Employment and Investment). X. Series: Paper (British Columbia Ministry of Energy and Mines). XI. Series: Paper (British Columbia Ministry of Energy, Mines and Petroleum Resources). XII. Series: Paper (British Columbia Ministry of Forests, Mines and Lands). XIII. Series: Paper (British Columbia Ministry of Energy and Mines). XIV. Series: Paper (British Columbia Ministry of Energy, Mines and Natural Gas). XV. Series: Paper (British Columbia Ministry of Energy and Mines). XVI. Series: Paper (British Columbia Ministry of Energy, Mines and Petroleum Resources). XVII. Series: Paper (British Columbia Ministry of Energy, Mines and Low Carbon Innovation).

QE187.46 622.1'09711 C76-083084-3 (Rev.)

Victoria
British Columbia
Canada

January 2022

Preface

Geological Fieldwork 2021

Geological Fieldwork 2021 is the forty-seventh edition of the annual volume that presents peer-reviewed papers detailing the results of British Columbia Geological Survey (BCGS) geoscience activities. In addition to this volume, the Survey publishes other reports, maps, and databases, and contributes to peer-reviewed journals and partner publications. BCGS also publishes an annual companion volume, the Provincial Overview of Exploration and Mining in British Columbia.

I would like to acknowledge that BCGS geoscientists work and live on the traditional lands of many First Nations. As the Survey continues to assess the geological history of the province, we look forward to enhancing relationships and exchanging knowledge with Indigenous communities.

The first paper in the volume, by Wildgust et al., provides an overview of Survey activities in 2021. Using conodont and U-Pb detrital zircon data, Schiarizza et al. document how the stratigraphic break above the Chapperon Group southeast of Kamloops includes not just a sub-Triassic unconformity but an extensive sub-Jurassic unconformity, exemplifying relationships elsewhere in Quesnel terrane. The paper by Ootes et al. combines detrital zircon U-Pb, Lu-Hf isotope, and trace element data from the Lay Range assemblage to evaluate the nature of basement to the Quesnel arc terrane. Ootes et al. conclude that, in its north-central segment, Quesnellia basement bears little relationship to ancient North America or Yukon Tanana-terrane and that the arc was built on an oceanic basement of juvenile volcanic rocks formed near a continental landmass. Building on previous work, Van Wagoner and Ootes examine the geology and geochemistry of the Kamloops Group (Eocene) in its type area. Hunter et al. continued a multi-year project in the Kitsault River area, south of Stewart, presenting a detailed facies analysis of the local Hazelton Group volcano-sedimentary depositional system, providing new U-Pb zircon geochronologic data, and concluding that volcanogenic massive sulphide and related epithermal mineralization may be slightly older than in the main Eskay rift corridor and be more regionally distributed. Based on mapping, geochemistry, and U-Pb zircon geochronology, Stanley and Nelson recognize Stuhini Group rocks in the past-producing Scottie gold mine area near Stewart and a Hazelton Group stratigraphy that is comparable to elsewhere in the highly prospective 'Golden Triangle' of northwestern British Columbia. Working in the south-central part of the province, Spence et al. combine field mapping and remotely piloted aircraft-derived imagery to better understand the emplacement history of the Tulameen ultramafic-mafic Alaskan-type intrusion (Late Triassic). In the final paper of the volume, Rukhlov et al., continue to test measurement of gaseous elemental mercury as an exploration tool with new surveys at the Lara-Coronation polymetallic volcanogenic massive sulphide occurrence on southern Vancouver Island. They confirm that direct and continuous measurements in near-surface air using a portable device can map sediment-covered mineralization in real time and that gaseous elemental mercury sampling is a simple and effective technique for mineral exploration in overburden-covered areas.

Like all British Columbians, the geoscience community was not spared the effects of wildfires, drought, record-setting heat waves, floods (and resulting transportation infrastructure collapse), and the ongoing Covid-19 pandemic. Nonetheless, responding to public health orders through successive Covid-19 waves, BCGS staff remained productive and continued to deliver mapping and thematic studies. A summer decline in provincial case counts enabled an abbreviated field season during which field geologists adapted quickly to changing circumstances on the ground. In addition to papers in this volume, highlights include testing drone-borne geophysical devices to aid mapping and exploration and re-analyzing archive samples to enhance the provincial lithogeochemical database. The Survey continues to prioritize rendering data from assessment reports into accessible digital products while enhancing its digital infrastructure to better deliver data in consumable formats. The transformed data are also essential for modernizing provincial-scale mineral potential assessments currently being piloted. The main aim of this modernization is to identify areas of high prospectivity for key mineral systems across the province and to guide government, stakeholders, and Indigenous communities in land-use planning and joint decision making. The Survey is also directing efforts toward critical minerals, the commodities that are essential for transitioning to a low-carbon future.

Adrian S. Hickin
Chief Geologist and Executive Director
British Columbia Geological Survey

Table of Contents

British Columbia Geological Survey annual program review 2021-2022

Neil Wildgust[1, a], Yao Cui[1], Gordon Clarke[2], and Adrian S. Hickin[1]

[1] British Columbia Geological Survey, Ministry of Energy, Mines and Low Carbon Innovation, Victoria, BC, V8W 9N3
[2] British Columbia Geological Survey, Ministry of Energy, Mines and Low Carbon Innovation, Vancouver, BC, V6Z 2G3
[a] corresponding author: Neil.Wildgust@gov.bc.ca

Recommended citation: Wildgust, N., Cui, Y., Clarke, G., and Hickin, A.S., 2022. British Columbia Geological Survey annual program review 2021-2022. In: Geological Fieldwork 2021, Ministry of Energy, Mines and Low Carbon Innovation, British Columbia Geological Survey Paper 2022-01, pp. 1-15.

Executive Summary

This paper provides an overview of current British Columbia Geological Survey (BCGS) applied geoscience activities and highlights key findings from 2021 projects. Headquartered in Victoria, the Survey is part of the Mines, Competitiveness and Authorizations Division in the British Columbia Ministry of Energy, Mines and Low Carbon Innovation. The Survey generates geoscience knowledge and data to inform land use and resource management decisions, and to support the growth of British Columbia as a competitive jurisdiction for mineral exploration.

The Cordilleran Geoscience Section of the Survey conducts field and office research, including bedrock and surficial geology mapping programs, regional geochemical surveys, and targeted mineral deposit studies. The past year saw further progress of multi-year mapping and applied research across the province, boosted by the return of fieldwork from July through to late September as pandemic-related restrictions eased. Highlights included mapping in the Kitsault area in the northwest and the Kaslo Lake-Lardeau area in the south, and the deployment of remotely piloted aircraft systems (RPAS) to gather geophysical data in the central part of the province. Critical minerals, an emerging topic of importance in the context of material requirements for low-carbon technologies, provided the focus for a three-day online workshop hosted by the Survey in collaboration with the Geological Survey of Canada, the United States Geological Survey, and Geoscience Australia. The workshop attracted more than 700 participants from the geoscience community across the world and demonstrated the importance of minerals system research in evaluating critical mineral resources.

Responsible for maintaining and developing provincial geoscience databases, the Resource Information Section disseminates data online through MapPlace. Information managed by the team includes traditional geological maps together with thematic studies and reports, geochemical, geophysical, and geological databases, plus information such as MINFILE, COALFILE, Mineral Assessment Reports (ARIS), and Property File. These databases also support development of next-generation mineral potential assessments using machine learning, which is now a major focus for the Survey to support land use and resource planning initiatives.

The Mineral Development Office (MDO) provides investment intelligence to government and global business, publishing the annual Provincial Overview of Exploration and Mining in British Columbia volume, and includes three Regional Geologists who track minerals activity across the province.

1. Introduction

This paper provides an overview of current British Columbia Geological Survey (BCGS) applied geoscience activities and highlights key findings from 2021 projects. Headquartered in Victoria, the Survey is part of the Mines, Competitiveness and Authorizations Division in the British Columbia Ministry of Energy, Mines and Low Carbon Innovation. As the steward of geoscience and mineral resource information in the province, the Survey has an important role in stimulating activity, attracting investment, informing decisions through technical information, and providing continuous research based on more than a century of corporate memory.

The province is endowed with significant natural resources including metallurgical coal, base and precious metals, and industrial minerals. These deposits are intimately tied to the tectonic evolution of the Canadian Cordillera, which continued from protracted supercontinent breakup starting about 1600 million years ago to accretionary processes that operate today as Pacific Ocean crust slides beneath Vancouver Island. In the northeast part of the province, the Western Canadian Sedimentary basin hosts significant petroleum hydrocarbon resources.

The Survey is the primary repository for provincial geoscience knowledge. Maps, reports, and databases are freely available online to inform First Nations and stakeholder groups including local communities, the minerals industry, public safety agencies, environmental scientists, research organizations, and government agencies. Active Survey research programs (Fig. 1) continue to define the geological evolution and natural resources of the province, generating knowledge and data to support land use and resource management decisions that balance economic, environmental, and community interests. A particular focus is providing public geoscience to support the growth of British Columbia as a competitive jurisdiction for mineral exploration. Not only does this include supporting industry, but also providing mineral resource information that is essential for informed land use decisions by government and, increasingly, from communities. Linked to the provision

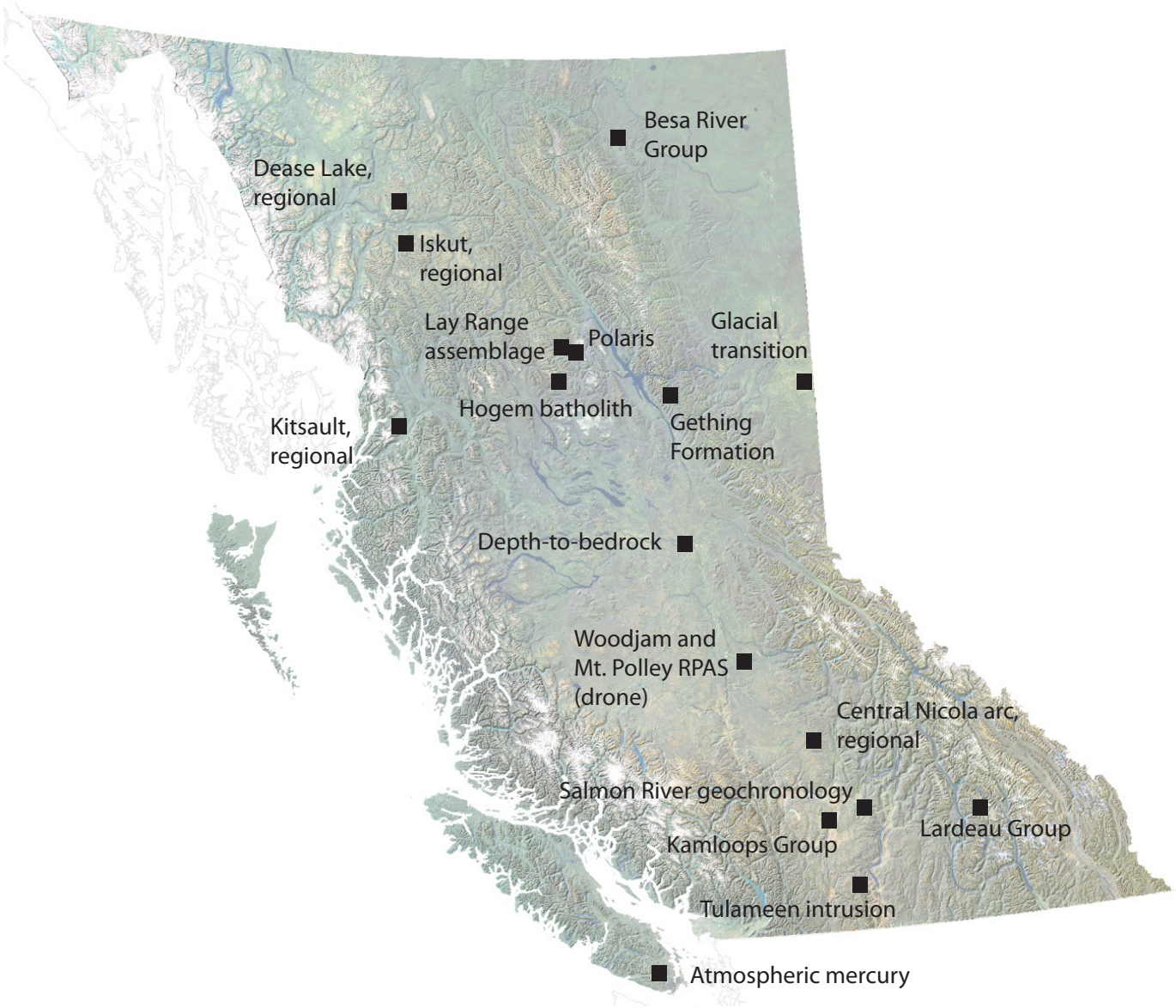

Fig. 1. British Columbia Geological Survey projects in 2021.

of geoscience information, the transformation of historic geoscience information to digital formats and databases requires coordinated effort as an ongoing, multi-year initiative.

The Survey is staffed by 35 employees, although several positions are vacant and are currently in the process of being filled. The BCGS consists of three sections: 1) Cordilleran Geoscience; 2) Resource Information and 3) the Mineral Development Office (based in a Vancouver satellite office and with Regional Geologists across the province). The Cordilleran Geoscience Section generates new knowledge through field- and desk-based research activities including bedrock and surficial geology mapping programs, regional geochemical surveys, and targeted mineral deposit studies. Section team members manage in-house laboratory facilities, curate the provincial sample archive, and build capacity through contract employment and training of geoscience assistants, typically undergraduate and graduate students. The Resource Information Section is responsible for maintaining and developing provincial geoscience databases and disseminating data online through MapPlace, the BCGS geospatial web service. The Resource Information Section is also responsible for collecting, evaluating, approving, and archiving mineral and coal exploration assessment reports submitted by industry to maintain titles in good standing. The Mineral Development Office (MDO) provides investment intelligence to government and global business, publishing the annual Provincial Overview of Exploration and Mining in British Columbia volume (e.g., Clarke et al., 2022), and includes three Regional Geologists who track minerals activity across the province (two positions are currently vacant).

The Survey welcomed Nate Corcoran as Regional Geologist for the Northeast and North Central regions in 2021. However, the Survey endured a challenging year with several retirements and resignations. Larry Jones retired as Director of the Resource Information team in August, with Yao Cui covering this position on an acting basis for the remainder of the year. In addition, the Cordilleran Section lost Graham Nixon and Janet Riddell to retirement. Larry, Graham, and Janet will be much missed by their colleagues and we wish them happy retirements after decades of service, although Graham remains connected with Emeritus status. The year also saw Deanna Miller, Sarah Meredith-Jones, and Sean Tombe leave the Survey for fresh opportunities. Jenny Boulet left for maternity leave in September and was temporarily replaced by Lisa Giesbrecht. The Survey anticipates a busy year for recruitment in 2022 as various competitions are launched to fill these vacancies.

The global Covid-19 pandemic again affected Survey operations in 2021; staff continued to work from home for much of the year. The gradual relaxation of public health restrictions in the spring and early summer allowed relatively late planning and execution of some field programs between mid July and late September. External laboratory services continued to be affected in many cases, leading to delays in analytical testing and processing of results. Despite these challenges, Survey staff maintained a full workload and publication output (Fig. 2).

2. Partnerships

The Survey adopts a collaborative approach to extend the scope and content of public geoscience while minimizing the risk of duplicative work. The Geological Survey of Canada (GSC) is an established partner; 2021 saw multiple discussions between BCGS and the GSC Geoscience for Energy and Minerals (GEM)-GeoNorth program, to align research interests and ensure coordinated engagement with First Nations in northern British Columbia. Active collaboration under GEM-GeoNorth during 2021 has focussed on provision of BCGS archive samples and expertise to support assessing the distribution of metallic mineral systems in the northern part of the province. In addition, BCGS has agreed to collaborate on a developing project that aims to examine low-temperature thermochronology to support exploration for hydrothermal ore systems at regional and deposit scales.

In collaboration with GSC, the United States Geological Survey, Geoscience Australia, and the Geological Association of Canada (Pacific section), BCGS organized and convened an online international workshop, 'Critical minerals: From discovery to supply chain' (Fig. 3). This three-day workshop, which attracted more than 700 participants drawn from a global audience, emphasized the important of mineral systems geoscience in developing low-carbon technologies to reduce greenhouse gas emissions and mitigate climate change. Each of the six sessions consisted of pre-recorded presentations followed by live Q&A slots that generated significant engagement with the audience, underlining the increased profile of critical minerals as a major geoscience topic.

The Survey signed an agreement with Newcrest Mining Limited in 2021 to facilitate extensive lithogeochemical analyses of 1000 igneous rock samples collected in northwestern BC and stored in the BCGS archive facility. Under the terms of the agreement, analyses will be undertaken using both total (fusion) and '4-acid' digestion coupled with ICP-ES and ICP-MS techniques. The resulting dataset will be published by BCGS in 2022. This project underscores the value added to geoscience in the province by the archive facility and may provide a blueprint for future collaborative research and public-private partnerships using archived samples.

3. Cordilleran Geoscience Section

Section geologists collect fundamental geoscience data through single- and multi-year field-based programs complemented by laboratory and office studies, including regional-scale mapping, mineral deposit studies, and development of new mineral exploration methods. Expertise encompasses tectonics, structural geology, stratigraphy, petrology, metallogeny, coal deposits, Quaternary and surficial geology, critical minerals, and geochemistry.

Engagement with First Nations communities is a priority for the Survey. As summer field projects are planned, liaising with First Nations is started at the earliest opportunity. During 2021, the evolving circumstances of the pandemic and wildfires across large swathes of British Columbia added extra impetus for contacting communities. As an example, planned fieldwork using a remotely piloted aircraft system (RPAS) in the Highland Valley area was suspended due to local concerns about wildfires. The project instead focussed on areas near Woodjam and Mount Polley (see section 3.2.), where discussions with the local First Nations Stewardship Forum highlighted shared interests. BCGS is committed to sharing geoscience information with all British Columbians and is expanding efforts to bring geological and mineral science to communities.

The following sections highlight ongoing and recently completed research activities aided by the partial resumption of fieldwork across the province.

3.1. Mapping, regional synthesis and compilation

Mapping is a core element of Survey and Cordilleran Section programs. The Survey delivers two key products: traditional published maps in the form of PDF files with accompanying research papers; and updates to the provincial digital geology database, which ultimately feeds into MapPlace as BC Digital Geology (Fig. 4). The digital geology database is an instrumental component of modern mineral potential assessment methods being developed by the Survey to inform land-use planning policies in the provincial government (see section 3.2.).

The past year also saw detailed planning for a multi-year project to integrate surficial geological maps from across the province into the digital geological database; work will begin in 2022 with the an inventory of published maps and data sources.

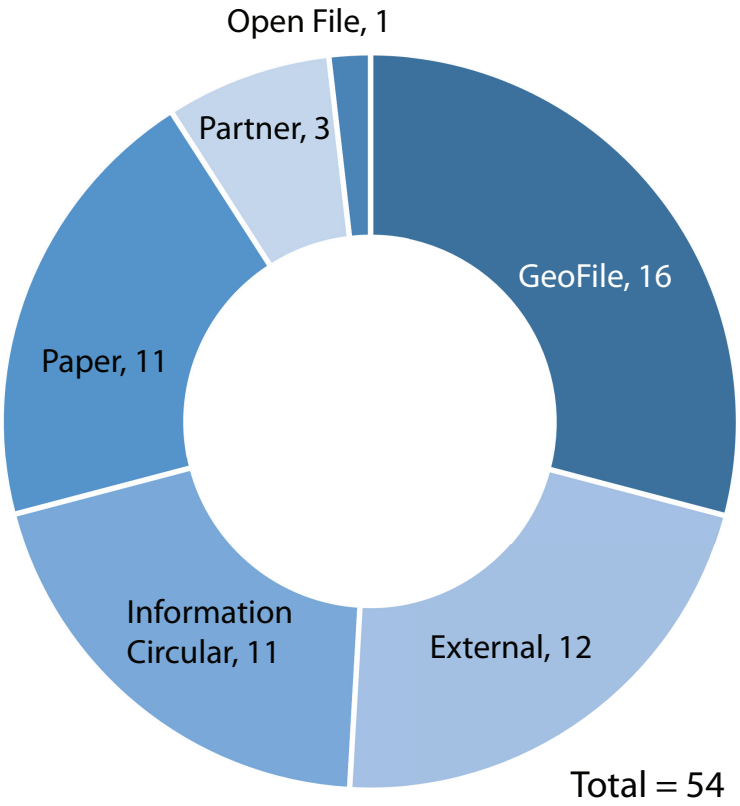

Papers*: This series is reserved for reviews and final thematic or regional works. Geological Fieldwork, our annual review of field activities and current research, is released as the first Paper of each year.

Geoscience Maps: This series is the BCGS vehicle for publishing final maps.

Open Files: These maps and reports present the interim results of ongoing research, particularly mapping projects.

GeoFiles: These publications enable rapid release of extensive data tables from ongoing geochemical, geochronologic, and geophysical work. As such, they serve the same function as data repositories provided by many journals, providing immediate access to raw data from specific projects.

Information Circulars: These publications provide accessible geoscience information to a broad audience in government, industry, and the general public. Included in the Information Circular series are the annual Provincial Overview of Mining and Exploration, **Exploration and Mining in British Columbia, and the Coal Industry Overview.

Contributions to partner publications: This category includes reports, maps, and other products published by another agency such as the Geological Survey of Canada or Geoscience BC, but have received contributions from British Columbia Geological Survey staff.

External publications: These are contributions to the peer reviewed literature and published in a recognized national or international scientific journal.

*The count refers to the total number of articles authored by BCGS personnel in a volume.

**Although five articles are included in Exploration and Mining in British Columbia, it is counted as a single volume.

Fig. 2. Types and numbers of publications produced by the British Columbia Geological Survey in 2021.

3.1.1. Northwest British Columbia

Northwest British Columbia hosts significant base- and precious-metal mineral deposits, notably in an area between Iskut and Stewart colloquially referred to as the 'Golden Triangle'. An ongoing multi-year Survey program will continue to expand regional bedrock mapping coverage to support mineral exploration; understanding the stratigraphic, magmatic, structural, metallogenic, and tectonic framework of this region continues to advance.

In support of Survey mapping programs in northwestern British Columbia, Nelson et al. (2021) provided raw U-Pb zircon datasets for 18 samples collected from between Dease

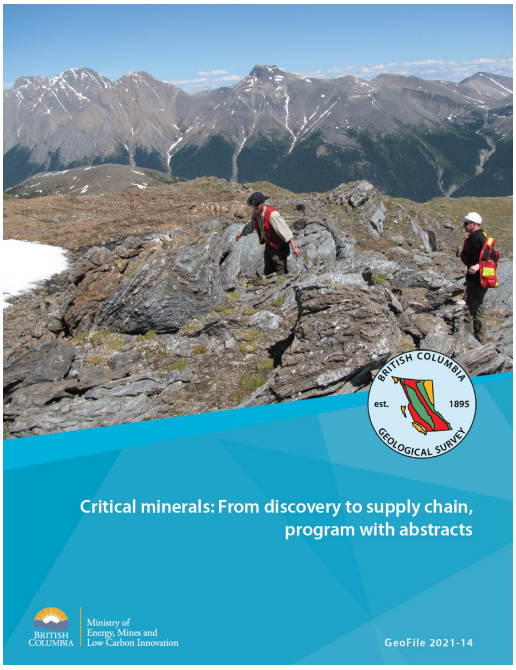

Fig. 3. Critical minerals virtual workshop held in November 2021. See British Columbia Geological Survey (2021).

Lake and Kitsault to constrain the age of intrusive and stratified protoliths, age and affinity of sedimentary sources, and timing of fault-related shearing.

Hunter et al. (2022) continued a multi-year project in the Kitsault River area, south of Stewart, presenting a detailed facies analysis of the local Hazelton Group volcano-sedimentary depositional system, providing new U-Pb zircon geochronologic data, and evaluating the implications for mineralizing systems. At the southern end of the Golden Triangle, the area hosts numerous Ag-rich volcanogenic massive sulphide (VMS) and epithermal deposits similar to those of the Eskay rift ca. 150 km to the northwest. Resolving the age and affinity of late Early to Middle Jurassic volcano-sedimentary Hazelton Group host rocks (Fig. 5) is key to understanding the metallogeny of the Kitsault area. A new U-Pb detrital zircon maximum depositional age (ca. 188 Ma) from upper Hazelton Group epiclastic rocks at the Sault Zn-Pb-Ag-Sr showing suggests that the VMS mineralization in the Kitsault River area may be slightly older than the ca. 174 Ma Au-rich VMS systems of the Eskay rift and indicates that significant precious metal-bearing VMS and/or epithermal systems formed well outside the main Eskay rift corridor in mainly volcaniclastic rocks.

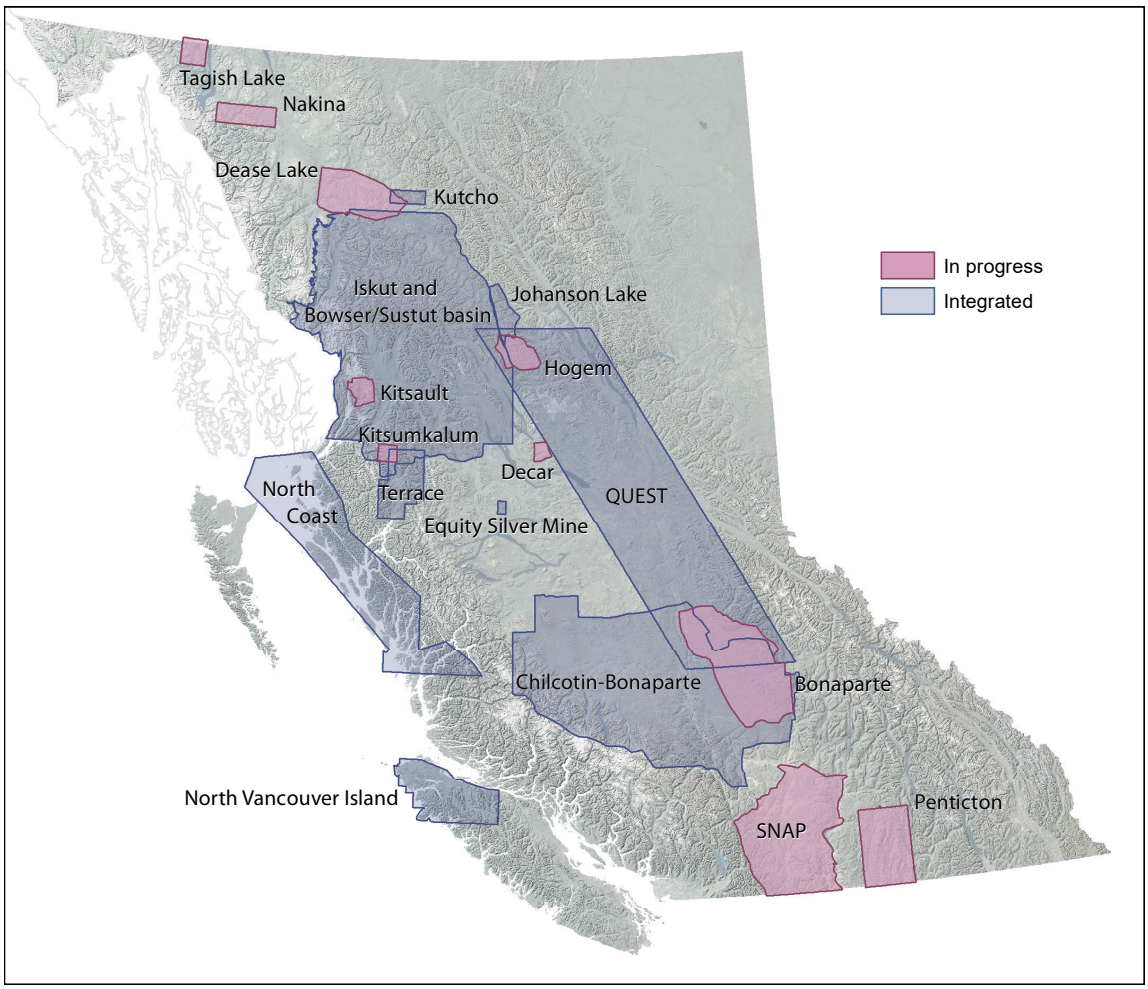

Fig. 4. BC Digital Geology, integrated and in progress.

Fig. 5. Interbedded fine and course tuff from facies 6 of the upper Hazleton Group, Kitsault area. U-Pb detrital zircon analysis yielded a maximum depositional age of ca. 168 Ma. See Hunter et al. (2022).

Fig. 6. Cliff-forming mafic volcanic rocks of the Horn Mountain Formation (upper Hazelton Group, Lower-Middle Jurassic) overlying recessive orange-weathering sedimentary rocks of the Spatsizi Formation (Lower Jurassic, upper Hazleton Group); Cake Hill pluton (Late Triassic) in foreground. Southeast of Dease Lake.

Fig. 7. Stuhini Group, lower fine-grained sedimentary-tuff unit. Interbedded argillite, plagioclase-rich, sandstone (with south-vergent fold), and limestone. See Stanley and Nelson (2022).

In the Dease Lake area, ongoing activities are geared towards publication of a 1:100,000-scale Geoscience Map, a final update to the BC Digital Geology database, and a GeoFile with geochronological and lithogeochemical data. The Geoscience Map, scheduled for publication in early 2022, will show the bedrock geology of 5000 km^2 between the community of Dease Lake and the Stikine River, based on BCGS mapping carried out between 2011 and 2018. Rocks in the area are mainly in the Stikine terrane, a Paleozoic to Mesozoic island arc that was deformed in the latest Triassic to Early Jurassic before accreting to Ancestral North America in the Middle Jurassic. The area experienced repeated calc-alkalic to alkalic, arc magmatism from the Middle Triassic through the Late Jurassic. This includes Tsaybahe group volcanism (Middle Triassic), Stuhini Group volcanism (Late Triassic), and Stikine suite plutonism (Late Triassic). This magmatism was followed by latest Triassic deformation and a latest Triassic to Early Jurassic depositional and magmatic hiatus that corresponds to a significant collisional event between the Intermontane terranes. Subsequent upper Hazelton Group volcanism (Fig. 6; late Early to Middle Jurassic), Three Sisters suite plutonism (Middle Jurassic), and Snowdrift Creek suite plutonism (late Middle to Late Jurassic) formed during and after accretion of Stikinia and other Intermontane terranes to Ancestral North America. As a result of this protracted magmatic history, the area is prospective for intrusion-related magmatic-hydrothermal mineral deposits, as illustrated by the Gnat Pass porphyry copper deposit and numerous other porphyry, epithermal, and skarn prospects. Also in the Dease Lake area, Bouzari et al. (2021) examined porphyry-related advanced argillic-alteration in the Horn Mountain Formation (Hazelton Group).

Based on mapping, geochemistry, and U-Pb zircon geochronology, Stanley and Nelson (2022) recognized hitherto unappreciated Stuhini Group rocks (Fig. 7) in the past-producing Scottie gold mine area in the southern part of the Golden Triangle, and a Hazelton Group stratigraphy that is comparable to that in the McTagg anticlinorium. The Stuhini Group volcanic rocks are highly potassic and of shoshonitic affinity, and zircons from a crystal tuff near the base of an upper volcanic unit yielded a crystallization age of ca. 214 Ma, providing new evidence of shoshonitic volcanism at the transition from main-stage Stuhini arc- back-arc activity into post-collision (Galore suite) magmatism. Zircons from a siltstone unit at the base of the Hazelton Group yielded a maximum detrital age of ca. 201 Ma, consistent with results from elsewhere in the Golden Triangle. Stanley and Nelson (2022) consider that the diverse metallogeny of the Golden Triangle resulted from collision-driven processes during Stuhini and Hazelton arc and back-arc development, drawing analogies to modern-day New Britain arc and Bismarck plate reorganization.

Colpron and Nelson (2021) published an updated review that summarized the physiography, neotectonics, crustal structure, geology, natural resources, and evolution of the

northern Cordillera, and George et al. (2021) used U-Pb zircon geochronology tied to Lu-Hf isotope analysis to consider the Triassic-Jurassic magmatic and accretionary history of Stikinia and evaluate the nature and origin of basement to Stikinia.

3.1.2. Central, southern, and northeastern British Columbia

Bedrock mapping updates for the provincial database and MapPlace are ongoing for several areas of central and southern British Columbia (Fig. 4): southwest Quesnellia; Bonaparte Lake to Quesnel River; Hogem; and Decar. An update based on mapping outside of Survey programs in the Penticton area of southern British Columbia is also in preparation.

In August, a bedrock mapping project was initiated in the Lardeau area west of Kaslo Lake (Fig. 1). Rocks historically mapped as Lardeau Group (Fig. 8) are thought to have been deposited on or near the North American continental slope. In the Lardeau area, the basal unit is the Index Formation, a commonly fine-grained carbonaceous clastic package, generally considered to be Early Cambrian and overlain by mafic volcanic rocks of the Jowett Formation. In the study area, the Index Formation includes massive sulphide mineralization (Ledgend prospect) that may extend for many km, providing a regional exploration target for nickel, cobalt, and copper, all essential elements for low-carbon technologies.

Using conodont and U-Pb detrital zircon data, Schiarizza et al. (2022) document how the stratigraphic break above the Chapperon Group 50 km southeast of Kamloops includes not just a sub-Triassic unconformity but an extensive sub-Jurassic unconformity. In the Salmon River valley, an unconformity separates schists of the Chapperon Group (pre-Permian) from less deformed limestones and siliciclastic rocks previously considered entirely Triassic. Rocks above the unconformity were previously mapped as a single Triassic unit (the Salmon River succession), and the Salmon River locale was considered to be a prime example of the Permo-Triassic unconformity recognized at numerous localities throughout south-central British Columbia. Samples collected from basal limestones (Fig. 9) yielded conodonts that confirm a Late Triassic age for rocks immediately above the unconformity. However, U-Pb detrital zircon analysis of two sandstone samples indicate that the Salmon River succession is not a single Triassic unit. Detrital zircons from near the base of the siliciclastic rocks yielded a maximum depositional age of ca. 183 Ma, and a sample collected 4.5 km to the west yielded a maximum depositional age of 190 Ma. These data show that most of the Salmon River succession is Jurassic, and that a more extensive sub-Jurassic unconformity merges with the sub-Triassic unconformity. The Salmon River succession, as now defined, is tentatively correlated with the Hall Formation (Early Jurassic, Toarcian) of the Rossland Group.

Work on a multi-year mapping project in the northern part of Hogem batholith to better understand the origin and timing of batholith emplacement and base- and precious-metal mineralization continued with further $^{40}Ar/^{39}Ar$ work, a fluid inclusion study, and a detrital zircon study evaluating the nature

Fig. 8. Moderately dipping metamorphic rocks of the Lardeau Group (Paleozoic). The lower green-grey chlorite schist of the Jowett Formation is overlain by strongly deformed sandstone and lesser carbonate of the Badshot Formation. The contact is under the geologist's knee. The photograph was taken north of Kootenay Lake, view is to the northwest.

Fig. 9. 'Limestone unit' with Triassic conodonts from above the sub-Triassic unconformity with the Chapperon Group (Paleozoic), Salmon River valley. Pebbly limestone with tabular intraformational micritic limestone clasts and granules and pebbles of chert, quartz, and quartz tectonite. See Schiarizza et al. (2022).

of the basement to Stikinia. Ootes et al. (2022) present detrital zircon U-Pb, Lu-Hf isotope, and trace element data from the Lay Range assemblage, the lowest exposed lithostratigraphic unit of north-central Quesnellia. Fossil and field evidence indicates deposition of the lower sedimentary division (Fig. 10) during the Late Mississippian to Middle Pennsylvanian and of the upper mafic tuff division during the Middle Pennsylvanian to early Permian. A quartz sandstone and a polymictic pebble conglomerate from the lower part of the lower sedimentary division yielded detrital zircon U-Pb ages between 360 and 290 Ma (Carboniferous to early Permian), with a range of older detrital zircons from ca. 3600 to 890 Ma (Archean and Proterozoic). A small population of zircons ranges from 450 to

Fig. 10. Lay Range assemblage, lower sedimentary division. At bottom of photo, sharp-based Bouma-like fining upward sequences of graded siltstones to dark grey argillites. See Ootes et al. (2022).

390 Ma (Ordovician to Devonian). The Carboniferous detrital zircons have mostly juvenile εHf(t), indicating that the parental magmas did not interact with older crust. The combined εHf(t) and trace element compositions of detrital zircons are consistent with formation in a juvenile arc during the Carboniferous. Comparison of Lay Range detrital zircon U-Pb, Hf, and trace element systematics indicate a similar timing of arc magmatism with eastern Stikinia and Wrangellia, but little relationship to ancient North America or Yukon-Tanana terrane. The older detrital zircons (Archean through Paleozoic) were sourced from a fringing landmass, possibly a continental oceanic plateau, that had little to no role in the petrogenesis of the Carboniferous magmas. The spread of ages in the Lay Range assemblage zircon distributions likely records multiple cycles of deposition, uplift, erosion, transport, and sedimentation. One possibility is that the fringing landmass was calved during rifting of the western edge of North American crust covered by Neoproterozoic through Cambrian passive margin deposits.

Field mapping of northern Hogem batholith and adjacent intrusive, volcanic, and sedimentary rocks of the Stikine and Cache Creek terranes was completed in 2019. Publication of bedrock and surficial maps is anticipated in the first half of 2022 and will be accompanied by an update to BC Digital Geology.

Van Wagoner and Ootes (2022) and Van Wagoner et al. (2021) report on the geology and geochemistry of the Kamloops Group, which forms part of a discontinuous northwest-trending belt of Eocene volcanic and sedimentary rocks that extends from central Idaho to eastern Alaska. In the Kamloops Group type area, these rocks constitute the Tranquille Formation (Fig. 11) and the overlying Dewdrop Flats Formation, each of which are divided into a number of members. Field, petrographic, and whole rock major, trace, and rare earth element data indicate that many members have comparable compositions and volcanic facies whereas others differ with geographic location, possibly reflecting various feeder vents. The volcanic rocks range from basaltic andesite to dacite; minor rhyolite occurs west of the type area in the Mount Savona Formation. The most common rock type is andesite and, although some andesites have high-Mg and adakite-like geochemical features (high Sr/Y, La/Yb), petrographic and geochemical evidence support that some of these rocks were derived from garnet-free mantle melts that mingled with garnet-free lower-crust. The geochemical features are consistent with amphibole, pyroxene, and plagioclase control resulting from mantle melts mixing with lower crust. The Kamloops study forms part of a larger project to establish the evolution of Eocene volcanism, help identify volcanic centres that may control the location of epithermal gold deposits, and estimate the contributions of volatile gases (e.g., CO_2, SO_2) to the early Eocene atmosphere.

To help steer future exploration efforts, the BCGS published a depth-to-bedrock study (Arnold, 2021) in the drift-covered area of the central Interior Plateau between the Mount Polley and Mount Milligan porphyry deposits. This project used published data including drill hole, bedrock, and surficial geology maps. Lett and Paulen (2021) published a compilation of soil and till geochemical data for two mineral properties in south-central British Columbia, the Ace, a massive sulphide and quartz vein showing, and Getty South a porphyry copper prospect.

Working in northeastern British Columbia, Ferri et al. (2021) provided a stratigraphic overview of the Liard basin and its eastern neighbour, the Horn River basin, focussing on organic-rich Upper Devonian shales of the Patry and Exshaw formations (Besa River Group) in the subsurface of Liard basin, and highlighting features that make the interval an exceptional shale gas play. Presenting whole rock, trace and rare earth element geochemistry, mineralogical, Rock-Eval, and U-Pb zircon data, Ferri et al. (2021) concluded that organic-rich Patry shales reflect establishment of anoxic bottom waters that spread across much of the Western Canada Sedimentary Basin as transgression peaked during deposition of the Exshaw Formation. Integrating aeolian landform analysis with optical dating and macrofossil radiocarbon dating, Hickin et al. (2021) examined the paraglacial to non-glacial transition following the Late Wisconsinian separation of the Cordilleran and Laurentide ice sheets in northeastern British Columbia.

Fig. 11. Hoodoos carved into andesitic to dacitic tuffs, lahars, and lacustrine volcaniclastic deposits, upper member of the Tranquille Formation (Eocene, Kamloops Group). View to the northwest; outcrop within Kamloops city limits. See Van Wagoner and Ootes (2022).

3.2. Targeted deposit studies and exploration methods

Regional mapping programs are complemented by more specific or thematic studies, typically selected to develop public geoscience knowledge and datasets in key topics that support minerals exploration or government land-use policy. Survey geoscientists test new technologies that can support future regional mapping and mineral exploration activities.

3.2.1. Deposit studies

Spence et al. (2022) describe work on the Late Triassic Tulameen intrusion, an 18 by 6 km ultramafic-mafic body in the Quesnel terrane of southern British Columbia hosted by metavolcanic and metasedimentary rocks of the Nicola Group (Upper Triassic). The intrusion is zoned with a dunite core passing outwards through olivine clinopyroxenite and clinopyroxenite to hornblende clinopyroxenite and hornblendite at the margin. Fieldwork conducted by the University of British Columbia during the summer of 2021 incorporated bedrock mapping and sampling with the assistance of remotely piloted aircraft systems (RPAS) to examine relationships between the ultramafic rock types during a period of low water in the Tulameen River. Zones of intermingled ultramafic cumulates (Fig. 12) are typical of the section and are interpreted to be the result of magma recharge and remobilization of crystal-rich magma mushes across a range of physical and rheological conditions.

Milidragovic et al. (2021) examined the chalcophile element geochemistry at the Polaris Alaskan-type mafic-ultramafic complex and concluded that two styles of PGE mineralization reflect the evolution of strongly oxidized hydrous ultramafic parental magma(s) in the absence of wall rock assimilation.

Riddell et al. (2021) reported on the analysis of ten Gething Formation coal samples from the Willow Creek mine in the Peace River coalfield of northeastern British Columbia, using the TESCAN Integrated Mineral Analyzer system to identify and quantify the mineralogy of non-carbonaceous material. Quartz, kaolinite, feldspars and siderite are most abundant; micas, other carbonate minerals, crandallite group minerals, apatite, illite and smectite, and sulphide minerals were found in trace to small amounts in most samples. Iron is most commonly hosted in carbonate minerals. Calcium occurs mainly in feldspars, phosphate minerals, and micas. Magnesium is held mainly in siderite. The ash chemistry of Willow Creek mine samples is generally similar to that of Gething Formation samples regionally, except that on average the Willow Creek mine samples contain about 50% less iron, and about 80% more phosphate.

Fig. 12. Tulameen Alaskan-type ultramafic-mafic intrusion (Upper Triassic), network of small dunite dikes with cuspate-lobate and flame-like margins projecting from a dunite enclave. See Spence et al. (2022).

Critical minerals are an important focus for the Survey, given the increasing demand for materials needed for low-carbon technologies and the accelerated pace of global investigations. L. Simandl et al. (2021) provided an overview of the implications for exploration and mining from growing demands for battery, magnet, and photovoltaic technologies. G. Simandl et al. (2021) examined the Rock Canyon Creek carbonate-hosted REE-F-Ba deposit, which has tectonic, stratigraphic, and structural similarities with Mississippi Valley-type and sparry magnesite deposits in the southeastern Rocky Mountains. In 2022, the Survey will examine critical minerals systems and develop a provincial inventory based on the federal government list (Natural Resources Canada, 2021).

3.2.2. Exploration methods

The Survey is testing remotely piloted aircraft systems (RPAS) to acquire geological data. Following up on RPAS-generated photogrammetric digital elevation models (DEMs) to support surficial geology mapping (Elia and Ferbey, 2020), work in 2021 investigated the utility of RPAS-born magnetometry and gamma-ray spectrometry devices to detect porphyry-related dispersal trains in subglacial tills.

Regional-scale till geochemistry and mineralogy surveys in British Columbia can have a low sample density (e.g., 1 sample/10 km^2) compared to other geochemical prospecting methods. Traditional magnetic and radiometric surveys can provide insight into subglacial till compositions between sample locations, but are commonly costly, time-consuming, or have a poor spatial resolution. Remotely piloted aircraft systems offer the potential to collect fast, affordable, and high-resolution data for drift prospecting studies.

The tests, the detailed results of which will be presented elsewhere, included flights totalling 155 line-km over subglacial tills in seven forestry cutblocks near the Mount Polley mine (alkalic porphyry Au-Cu) and the Woodjam developed prospect (calc-alkaline to alkalic porphyry Cu-Au). Existing geology, geochemistry, mineralogy, and geophysical datasets provide geologic control and a way of validating newly acquired RPAS-borne data. Infill till sampling supplemented these data. The RPAS flew gridded autopilot surveys at 5, 7.5, or 10 m above ground level (AGL) at 2 m/s along flight lines spaced 7.5 or 10 m apart. A GEM Systems DRONEmag potassium magnetometer was slung 2.5 m below a DJI Matrice 600 Pro (Fig. 13a) and using a 10 Hz sampling rate collected total field measurements every 20 cm on the ground. Radiation Solutions Incorporated provided a repackaged version of their

Fig. 13. a) A GEM Systems DRONEmag potassium magnetometer tethered 2.5 m below a DJI Matrice 600 Pro flying a gridded autopilot survey 7.5 m above ground level. **b)** A Radiation Solutions Incorporated RS-350 Backpack gamma-ray spectrometer, incorporating a 3"x3" NaI (Tl) crystal, retrofitted to a DJI Matrice 600 Pro. **c)** The hardware used to complete the geophysical, lidar, and photogrammetric surveys: 1. DJI Phantom 4 RTK batteries, 2. air-band handheld VHF radios, 3. magnetometer mount for DJI Matrice 600, 4. tools, VFR navigation charts, and manuals, 5. GreenValley International LiAir V70 lidar and base station, 6. laptop running GreenValley International LIDAR360 and LiAcquire software, 7. Radiation Solutions Incorporated gamma-ray spectrometer, 8. GEM Systems DRONEmag magnetometer, 9. laptop running SPH Engineering UgCS flight planning software, 10. DJI Phantom 4 RTK and base station, 11. DJI Matrice 600 Pro, 12. GSM19-G walking (base station) magnetometer, 13. DJI Matrice 600 Pro batteries, 14. RTK base station tripod, and 15. lidar base station tripod.

RS-350 backpack gamma-ray spectrometer that was mounted directly to a DJI Matrice 600 (Fig. 13b). This instrument uses a 3"x3" NaI (Tl) crystal with a 1 Hz sampling rate to collect total count data every 2 m. An SPH Engineering radar altimeter, coordinated with UgCS flight planning software, instructed the RPAS in real time to follow terrain at a constant height AGL, ensuring measured data variation was unrelated to changes in distance between the geophysical sensors and the ground. Acquired geophysical data were corrected and gridded using conventional methods for traditional airborne magnetic and radiometric surveys.

Lidar and air photo surveys were flown for the same areas at 4 m/s and 80 m AGL, using a GreenValley International Liair V70 lidar (mounted to a DJI Matrice 600 Pro) and a DJI Phantom 4 RTK. High-resolution bare Earth DEMs were produced from these data, as were orthomosaics (Fig. 14). These models and RPAS-derived digital air photo stereo pairs will supplement large-scale surficial geology mapping and be used to interpret ice-flow and till-transport histories. For example, glacially streamlined features, which indicate northwest ice flow through the Woodjam area during the Late Wisconsinan, are readily identified in RPAS lidar bare Earth models (Fig. 14a). These features cannot be mapped with confidence using RPAS photogrammetric DEMs or orthomosaics (Figs. 14b, c), and are not visible in pre-cutblock, 1:40,000-scale hardcopy air photos (Ferbey et al., 2016) in which trees obscure the subtle changes in topography that define these landforms.

The project demonstrates that commercially available hardware and software can be integrated to fly low-altitude, terrain-following RPAS geophysical surveys (Fig. 14c). The magnetic and radiometric data collected are high quality and fill a scale gap between traditional airborne and ground surveys. Furthermore, RPAS-acquired lidar data are invaluable for mapping surficial geology in forested terrain. Work

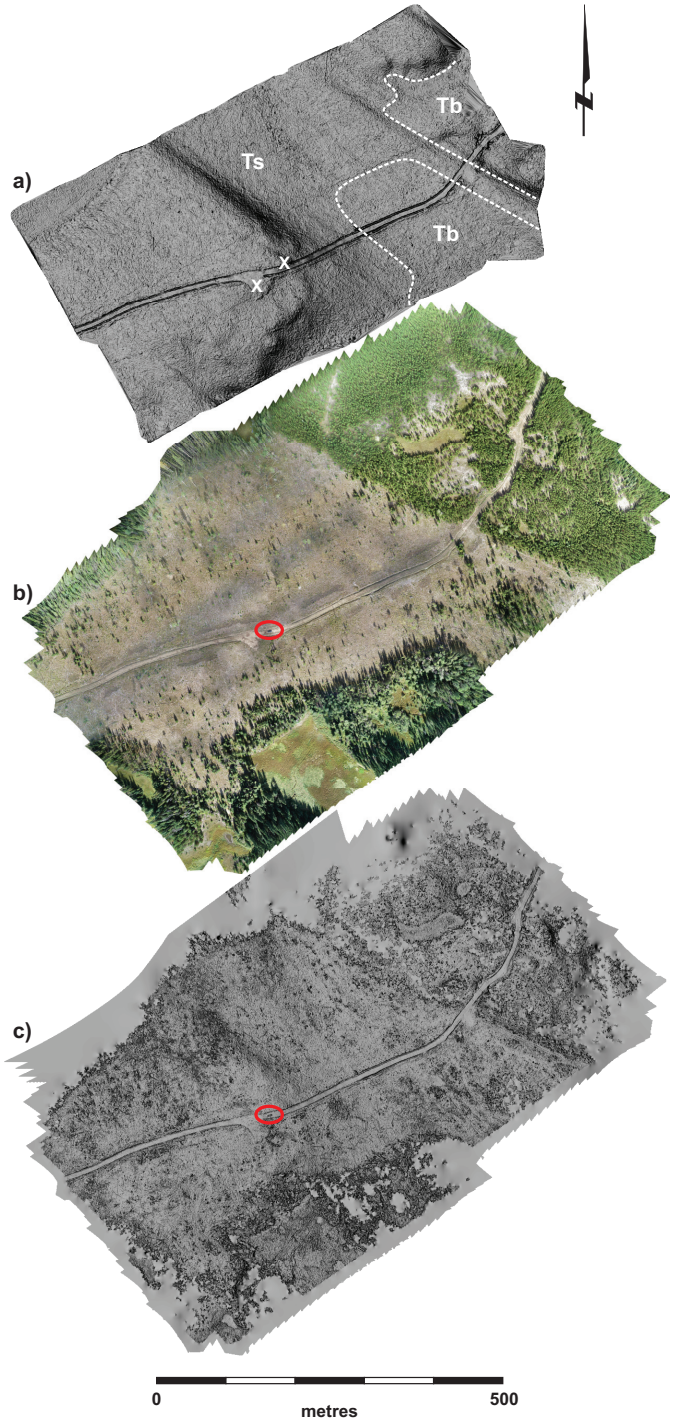

Fig. 14. a) Bare Earth digital elevation model (DEM) of a forestry cutblock west of Woodjam developed prospect, processed from lidar data acquired by LiAir V70 mounted to DJI Matrice 600 Pro. Glacially streamlined landforms (or streamlined till; Ts) indicate northwest ice flow during the Late Wisconsinan and can be differentiated from areas of thicker till (till blanket; Tb). Chilcotin Group (Miocene to Pleistocene) olivine-phyric basalt outcrops observed in the field marked with 'X'. The streamlined features are unmappable in the **b)** orthomosaic or **c)** photogrammetric DEM generated from RPAS-acquired air photos for the same area. Truck is circled in red.

planned for 2022 will continue to focus on differentiating the radiometric and magnetic signals of subglacial tills derived from potassium- and magnetite-rich porphyry systems relative to those derived from country rocks, and will investigate the ability of the method to identify subglacial tills sourced from other critical mineral hosts such as magmatic Ni±Cu±Co±PGE systems.

Based on fieldwork in the summer of 2021, Rukhlov et al. (2021, 2022) report new data from the Lara-Coronation polymetallic occurrence, southern Vancouver Island, confirming that direct and continuous analysis of gaseous elemental mercury (GEM) concentrations in near-surface air using a portable RA-915M Zeeman Hg analyzer can map sediment-covered mineralization in real time. Detailed surveys across steeply dipping, massive sulphide zones in volcanic rocks of the McLaughlin Ridge Formation (Sicker Group; Middle to Late Devonian) confirm GEM haloes in near-surface air above the mineralization. Measured GEM concentrations range from 0.61 to 251 $ng \cdot m^{-3}$ in this study, with the strongest halo (206x background Hg) above exposed mineralization. Weak haloes (1.7x background Hg) mark sediment-covered mineralized zones. Simultaneously measured meteorological and in situ soil parameters appear to have no effect on measured GEM concentrations. Real-time grid sampling of near-surface air reveals a pattern of northwest-trending GEM haloes reflecting bedrock structure, including a 224 by 30 m halo above the polymetallic VMS Coronation zone, covered by up to 22 m of overburden. This study confirms that the real-time GEM sampling of near-surface air can instantly delineate mineralized zones that are buried beneath overburden 10s of m thick. Real-time GEM sampling is a simple and effective technique for mineral exploration in overburden-covered areas.

4. Resource Information Section

The Survey collects, compiles, and disseminates provincial public geoscience information that supports effective mineral exploration, sound land use management, and responsible governance. This public geoscience includes traditional geological maps, reports, and thematic studies, province-wide digital coverage (BC Digital Geology), and databases including mineral assessment reports (ARIS), mineral inventory (MINFILE), coal information (COALFILE), geochemical and geophysical surveys, and documents donated to the British Columbia Geological Survey since the late 1880s by government, universities, industry, and individuals (Property File). The Survey operates numerous information systems to update these databases and deliver them through MapPlace, the BCGS geospatial web service, and other web portals.

Although the Survey has a long history of digitally compiling and managing geoscience, many of the information systems require modernization. As part of digital transformation efforts (Fig. 15), we are modernizing our core information systems to increase efficiency in operating and updating our geoscience

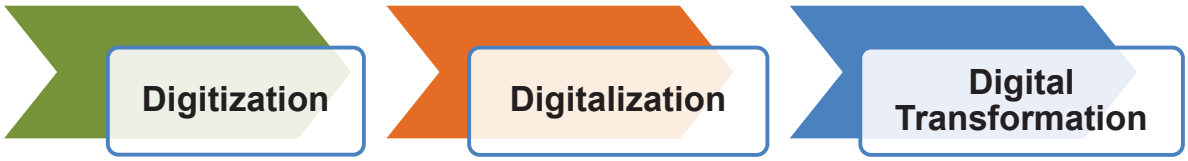

	Input	Output	Outcomes
Data	Geological mapping, field data, lab analyses, ARIS, MINFILE	Digital geology (*f_meta*) Mineral resources (*f_meta*) Mineral systems (*f_meta*)	**Framework geoscience** **Interoperable data sharing** **HTML5 compliant web services**
Process	Digitizing Updating Compiling	Automated integration Knowledge engineering	Automated transformations Mineral potential modelling
Spatial Data Infrastructure (SDI)	Geoscience Operational Database Environment (GODE)	Geoscience Application Database Environment (GADE)	MapPlace 3, OpenLayers OGC web services, OneGeology
Skills and knowledge needed	Bedrock and surficial geological mapping, geochemistry, geophysics, mineral deposits, GIS, database systems	Cordilleran geology Mineral systems Data-driven interpretation Spatial databases Data modelling	Open standards-based web services Digital cartography Geostatistics, data science

Fig. 15. Digital transformation of BCGS data.

databases, applications, and geospatial web services. This modernization will enable interoperable data sharing and applications such as mineral potential modelling.

4.1. Geoscience Spatial Data Infrastructure

Recent advancements in data science demand interoperable data sharing of framework geoscience. The Survey is identifying opportunities and prioritizing solutions to improve our digital capabilities. We are conducting a review of all geoscience databases and applications to define a system architecture and ways to implement a geoscience Spatial Data Infrastructure (SDI). The SDI will be built by following the 'FAIR' principles: Findable, Accessible, Interoperable, and Reusable. Our short-term goal is to modernize a few core information systems with a coherent operational database environment and upgraded web applications.

4.2. MapPlace

MapPlace is the BCGS geospatial web service to discover, visualize, search, and generate summary reports and maps from province-wide geoscience databases. Easy access to, and analysis of, geoscience maps and data are fundamental to inform decisions on mineral exploration, mining, environmental protection, and land use management. MapPlace provides a platform to facilitate the discovery, display, search, and analysis of geoscience information in the context of all other relevant data such as mineral titles, assessment reports, land ownership, public infrastructure, aquifers, and topographic base maps. Some of the advanced applications and user interfaces are specifically designed to enable research and analytics for mineral exploration and prospecting.

4.3. ARIS assessment reports and database

Results of mineral exploration are submitted by industry as assessment reports to the government in compliance with the Mineral Tenure Act. After a one-year confidentiality period, the assessment reports become freely available to public. The Survey manages these reports in the Assessment Report Indexing System (ARIS) database with metadata to search the locations, mineral occurrences, commodities, claims, work types, and expenditures as documented in the reports. ARIS contains more than 38,500 reports dating from 1947. The assessment reports are available online as PDF documents through the ARIS website. A version of the ARIS database for the metadata is available to download in Microsoft Access, with locations in Microsoft Excel and ESRI shapefile format. Data in formats that can be readily used, such as spreadsheets, rather than scanned .PDF files, from 620 assessment reports are available through the ARIS search application. Following work in the Interior Plateau (Norris and Fortin, 2019), the Survey continues to digitally extract assessment report-sourced surface sediment geochemical data (ARSSG), extending into northwestern British Columbia. The database currently contains more than 6.6 million determinations from more than 163,000 samples from 550 assessment reports. The data are incorporated into MapPlace and are also available on the ARSSG website, which includes sample details, geochemical results, and locations. Another project is underway to extract digital data from drillhole logs and geophysical surveys sourced from assessment reports.

4.3.1. ARIS digital data submission

Traditionally, assessment reports from mineral exploration

have been submitted in hardcopy or as files such as scanned .PDF, which render data within the files difficult to extract and use. The BCGS has set up a digital data submission portal to encourage inclusion of digital files such as spreadsheets, databases, GIS maps, and grids. Explorationists will benefit because digital data can be easily retrieved, integrated, and recast for specific needs. Digital submission will also enable the Survey to better maintain province-wide databases and create derivative products that use past results to guide future exploration. Both assessment reports and digital data can be uploaded through the ARIS data submission page.

4.4. Other databases

MINFILE is a database for mineral, coal, and industrial mineral occurrences that includes information for more than 15,500 records. In the last year, more than 400 new occurrences and 2100 updates were added to the database. COALFILE includes a collection of 1040 coal assessment reports, dating from 1900. Associated data include 16,100 boreholes, 550 bulk samples, 5400 maps, 3650 trenches, and 484 coal ash chemistry analyses. Property File is a collection of more than 85,000 archived reports, maps, photos, and technical notes documenting mineral exploration activities in British Columbia from the late 1800s. The provincial geochemical databases hold field and geochemical data from multi-media surveys by the Geological Survey of Canada, the BCGS, and Geoscience BC. The databases are updated regularly and contain results from: 1) the Regional Geochemical Survey program (RGS) including analyses from more than 66,000 stream-sediment, lake sediment, moss, and water samples (Han and Rukhlov, 2020a); 2) 10,500 till surveys (Bustard et al., 2017, 2019); and 3) 11,000 lithogeochemical samples (Han and Rukhlov, 2020b). A surficial geology index map for the province (Arnold and Ferbey, 2019) is regularly updated as is an ice-flow indicator database for British Columbia and Yukon (Arnold and Ferbey, 2020).

4.5. British Columbia Digital Geology

The BCGS offers province-wide digital coverage of bedrock geology including details from field mapping, with a typical regional compilation at a scale of 1:50,000. A geospatial frame data (GFD) model is used to simplify the compilation and integration of new mapping into the BC Digital Geology database (Fig. 16, Cui, 2021). Bedrock geology is standardized with consistent stratigraphic coding, ages, and rock types to enable computations, and is available for download in GeoPackage and ESRI shapefile formats. Customized bedrock geological maps and legends can be explored, and data downloaded as KML by spatial and non-spatial queries via MapPlace. The BCGS has transformed the digital geology to the GeoSciML Lite schema and mapped the contents using the vocabularies adopted by the IUGS Commission for the Management and Application of Geoscience Information (CGI). The GeoSciML Lite-compliant digital geology is accessible via the OneGeology portal and open standard-based

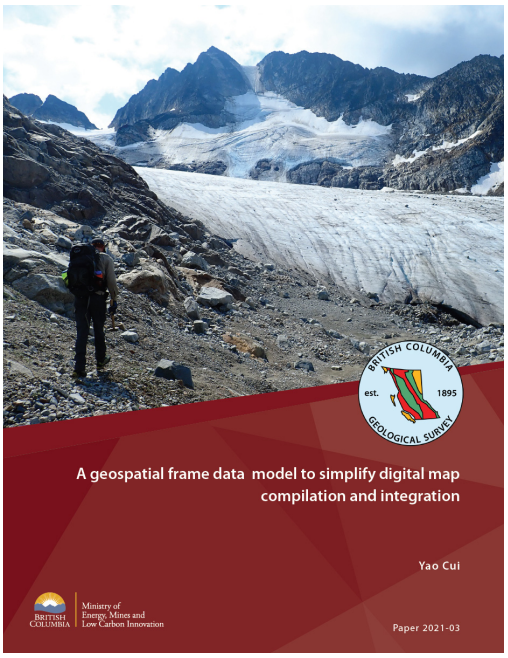

Fig. 16. The geospatial frame data (GFD) model and integration processes can be applied to any discipline that has polygons and lines to compile and produce digital map. See Cui (2021).

interface such as WMS and WFS, to enable interoperable data sharing and analytics.

4.6. Mineral potential modelling

The British Columbia Geological Survey has initiated a multi-year mineral potential mapping project. The principal aim of the project is to identify areas of high prospectivity for key mineral systems across the province to assist government with land-use planning and deliver pre-competitive geoscience data to the mineral exploration industry. The initial phase of the project included a pilot study that focussed on method development in a test area. Three mineral systems were chosen for the pilot study: porphyry copper-gold; volcanic massive sulphide (VMS) copper-lead-zinc; and magmatic nickel. A weights-of-evidence method was adopted, which produced data-driven mineral potential maps for each selected mineral system. This method allowed for a comprehensive review of outputs at every stage of the modelling process to ensure that the maps were geologically sensible and statistically valid. Based on the success of the pilot study, modelling will continue into new areas and include more mineral systems in the coming years.

5. Mineral Development Office

The Mineral Development Office (MDO) is the Vancouver base of the British Columbia Geological Survey, linking the more than 800 exploration and mining companies headquartered in Vancouver to provincial mineral and coal information. The MDO distributes Survey data and provides technical information and expertise about mineral opportunities to the domestic and

international investment community. The MDO monitors the activities of the mining and exploration sectors and produces the Provincial Overview of Exploration and Mining in British Columbia, an annual volume that summarizes activities in the different regions of the province (see e.g., Clarke et al., 2022).

The British Columbia Regional Geologists (Table 1) represent the provincial government on geological matters at a regional level and capture information on industry activity in their jurisdictions. Within their communities, they provide information on exploration trends, possible investment opportunities, land use processes, First Nation capacity building, and public outreach. In 2020, the Regional Geologists were repatriated to the BCGS as part of the MDO.

Acknowledgment

We thank George Owsiacki of Total Earth Science Services (Victoria) for the desktop publishing of this volume.

Table 1. British Columbia Regional Geologists.

Regional Geologist	Office	Region
Vacant	Smithers	Northwest
Nate Corcoran	Prince George	Northeast and North Central
Vacant	Kamloops	South Central
Fiona Katay	Cranbrook	Southeast
Bruce Northcote	Vancouver	Southwest

References cited

Arnold, H., 2021. Depth to bedrock dataset for the Interior Plateau. Ministry of Energy, Mines and Low Carbon Innovation, British Columbia Geological Survey GeoFile 2021-13, 6 p.

Arnold, H., and Ferbey, T., 2019. British Columbia surficial geology map index, British Columbia Ministry of Energy, Mines and Petroleum Resources, British Columbia Geological Survey Open File 2019-03, Data version 2020-01.

Arnold, H., and Ferbey, T., 2020. Ice-flow indicator database, British Columbia and Yukon. British Columbia Ministry of Energy, Mines and Petroleum Resources, British Columbia Geological Survey Open File 2020-03, 1 p.

Bouzari, F., Lee, R.G., Hart, C.J.R., and van Straaten, B.I., 2021. Mineralogical and geochemical vectors within advanced argillic-altered rocks of north-central British Columbia (NTS 094E/02, 15, 104I/05). In: Geoscience BC Summary of Activities 2020: Minerals, Geoscience BC, Report 2021-01, pp. 91-104.

British Columbia Geological Survey, 2021. Critical minerals: From discovery to supply chain, program with abstracts. British Columbia Ministry of Energy, Mines and Low Carbon Innovation, British Columbia Geological Survey GeoFile 2021-14, 74 p.

Bustard, A.L., Han, T., and Ferbey, T., 2017. Compiled till geochemical data for British Columbia. British Columbia Ministry of Energy, Mines and Petroleum Resources, British Columbia Geological Survey GeoFile 2017-09, 7 p.

Bustard, A.L., Ferbey, T., and Arnold, H., 2019. Regional- to property-scale till geochemical and mineralogical surveys in British Columbia for base and precious metals. British Columbia Ministry of Energy, Mines and Petroleum Resources, British Columbia Geological Survey Open File 2019-04 version 2020-01.

Clarke, G., Northcote, B., Katay, F., and Tombe, S.P., 2022. Exploration and Mining in British Columbia, 2021: A summary. In: Provincial Overview of Exploration and Mining in British Columbia, 2021. British Columbia Ministry of Energy, Mines and Low Carbon Innovation, British Columbia Geological Survey, Information Circular 2022-01, in press.

Colpron, M., and Nelson, J.L., 2021. Northern Cordillera: Canada and Alaska. In: Elias, S., and Alderton, D., (Eds.), Encyclopedia of Geology, Second Edition. Academic Press, pp. 93-106.

Cui, Y., 2021. A geospatial frame data model to simplify digital map compilation and integration. British Columbia Ministry of Energy, Mines and Low Carbon Innovation, British Columbia Geological Survey Paper 2021-03, 20 p.

Elia, E.A., and Ferbey, T., 2020. Generating photogrammetric DEMs in the field from remotely piloted aircraft systems. In: Geological Fieldwork 2019, British Columbia Ministry of Energy, Mines and Petroleum Resources, British Columbia Geological Survey Paper 2020-01, pp. 189-200.

Ferbey, T., Levson, V.M., and Plouffe, A., 2016. Surficial geology, Moffat Creek area, British Columbia, parts of NTS 93-A/3, NTS 93-A/4, NTS 93-A/5, NTS 93-A/6. Geological Survey of Canada, Canadian Geoscience Map 252 (preliminary), British Columbia Ministry of Energy, Mines, and Petroleum Resources, British Columbia Geological Survey Geoscience Map 2016-1, scale 1:50,000.

Ferri, F., McMechan, M., Richards, M.B., and Friedman, R., 2021. Organic-rich Upper Devonian shales of the Patry and Exshaw formations (Besa River Group) in the subsurface of Liard basin. British Columbia Ministry of Energy, Mines and Low Carbon Innovation, British Columbia Geological Survey Paper 2021-02, 42 p.

George, S.W.M., Nelson, J.L., Alberts, D., Greig, C.J., and Gehrels, G.E., 2021. Triassic-Jurassic accretionary history and tectonic origin of Stikinia from U-Pb geochronology and Lu-Hf isotope analysis, British Columbia. Tectonics, 40. <https://doi.org/10.1029/2020TC006505>

Han, T., and Rukhlov, A.S., 2020a. Update of the provincial Regional Geochemical Survey (RGS) database at the British Columbia Geological Survey. British Columbia Ministry of Energy, Mines and Petroleum Resources, British Columbia Geological Survey GeoFile 2020-08, 3 p.

Han, T., and Rukhlov, A.S., 2020b. Update of rock geochemical database at the British Columbia Geological Survey. British Columbia Ministry of Energy, Mines and Petroleum Resources, British Columbia Geological Survey GeoFile 2020-02, 4 p.

Hickin, A.S., Lian, O.B., Telka, A., Levson, V.M., and Marten Geertsema, M., 2021. Geomorphic and ecological age constraints for paraglacial to non-glacial transition in northeastern British

Columbia, Canada. Quaternary Science Reviews, 268, 107002. <https://doi.org/10.1016/j.quascirev.2021.107002>

Hunter, R.C., Sebert, C.F.B., Friedman, R., and Wall, C., 2022. Revised stratigraphy and geochronology of the Hazelton Group, host rocks for volcanogenic mineralization in the Kitsault River area, northwest British Columbia. In: Geological Fieldwork 2021, British Columbia Ministry of Energy, Mines and Low Carbon Innovation, British Columbia Geological Survey Paper 2022-01, pp. 63-81.

Lett, R.E., and Paulen, R.C., 2021. A compilation of soil and till geochemical data from surveys at the Ace and Getty South mineral properties, British Columbia. British Columbia Ministry of Energy, Mines and Low Carbon Innovation, GeoFile 2021-11, 9 p.

Milidragovic, D., Nixon, G.T., Scoates, J.S., Nott, J.A., and Spence, D.W., 2021. Redox controlled chalcophile element geochemistry of the Polaris Alaskan-type ultramafic complex, British Columbia, Canada. The Canadian Mineralogist, 59, 1627-1660. <https://doi.org/10.3749/canmin.2100006>

Natural Resources Canada, 2021. Critical minerals. <https://www.nrcan.gc.ca/our-natural-resources/minerals-mining/critical-minerals/23414>

Nelson, J.L., Friedman, R., and van Straaten, B., 2021. LA-ICP-MS and TIMS U-Pb data files from the Iskut project (Dease Lake to Kitsault). British Columbia Ministry of Energy, Mines and Low Carbon Innovation, British Columbia Geological Survey GeoFile 2021-10, 13 p.

Norris, J., and Fortin, G., 2019. Assessment report-sourced surface sediment geochemical database: Development and initial data release from the Interior Plateau. British Columbia Ministry of Energy, Mines and Petroleum Resources, British Columbia Geological Survey GeoFile 2019-04, 10 p.

Ootes, L., Ferri, F., Milidragovic, D., and Wall, C., 2022. The age and provenance of the Lay Range assemblage provides an indirect record of basement to north-central Quesnellia, British Columbia. In: Geological Fieldwork 2021, British Columbia Ministry of Energy, Mines and Low Carbon Innovation, British Columbia Geological Survey Paper 2022-01, pp. 31-44.

Riddell, J., Soriano, J., and Lane, G., 2021. Mineral content of some Gething Formation coals. British Columbia Ministry of Energy, Mines and Low Carbon Innovation, GeoFile 2021-12, 10 p.

Rukhlov, A.S., Mashyanov, N.R., Pitirimov, P.V., Hickin, A.S., Golovetskyy, M., and Coats, B., 2021. Supplementary data for gaseous elemental mercury (GEM) response from sediment-covered, volcanogenic massive sulphide mineralization on southern Vancouver Island. British Columbia Ministry of Energy, Mines and Low Carbon Innovation, British Columbia Geological Survey GeoFile 2021-15, 1 p.

Rukhlov, A.S., Mashyanov, N.R., Pitirimov, P.V., Hickin, A.S., Golovetskyy, M., and Coats, B., 2022. Gaseous elemental mercury (GEM) response from sediment-covered, volcanogenic massive sulphide mineralization on southern Vancouver Island. In: Geological Fieldwork 2021, British Columbia Ministry of Energy, Mines and Low Carbon Innovation, British Columbia Geological Survey Paper 2022-01, pp. 123-135.

Schiarizza, P., Orchard, M.J., and Friedman, R.M., 2022. Conodonts and detrital zircons from Triassic and Jurassic rocks above the Salmon River unconformity, Thompson Plateau, south-central British Columbia. In: Geological Fieldwork 2021, British Columbia Ministry of Energy, Mines and Low Carbon Innovation, British Columbia Geological Survey Paper 2022-01, pp. 17-30.

Simandl, G.J., Paradis, S., Savard, J., Miller, D., D'Souza, R., Araoka, D., Akam, C., Hoshino, M., and Kon, Y., 2021. Mineral control on the geochemistry of the Rock Canyon Creek REE-F-Ba deposit, British Columbia, Canada. Geochemistry: Exploration, Environment, Analysis. <https://doi.org/10.1144/geochem2020-010>

Simandl, L., Simandl, G.J., and Paradis, S., 2021. Specialty, critical, battery, magnet and photovoltaic materials: Market facts, projections and implications for exploration and development. Geoscience Canada, 48, 73-91.

Spence, D.W., Crawford, H., Scoates, J.S., Nott, J.A., Nixon, G.T., and Milidragovic, D., 2022. Mapping ultramafic cumulates at the Tulameen ultramafic-mafic Alaskan-type intrusion, south-central British Columbia, aided by remotely piloted aircraft system photogrammetry. In: Geological Fieldwork 2021, British Columbia Ministry of Energy, Mines and Low Carbon Innovation, British Columbia Geological Survey Paper 2022-01, pp. 103-122.

Stanley, B., and Nelson, J., 2022. Revised stratigraphy of the Stuhini and Hazelton groups and LA-ICP-MS zircon geochronology of the Scottie gold mine area, northwestern British Columbia. In: Geological Fieldwork 2021, British Columbia Ministry of Energy, Mines and Low Carbon Innovation, British Columbia Geological Survey Paper 2022-01, pp. 83-102.

Van Wagoner, N., and Ootes, L., 2022. Geology and geochemistry of the Kamloops Group (Eocene) in its type area, Kamloops, British Columbia. In: Geological Fieldwork 2021, British Columbia Ministry of Energy, Mines and Low Carbon Innovation, British Columbia Geological Survey Paper 2022-01, pp. 45-62.

Van Wagoner, N., Ootes, L., and Sutcliffe, B., 2021. Geochemical data from the Kamloops Group. British Columbia Ministry of Energy, Mines and Low Carbon Innovation, British Columbia Geological Survey GeoFile 2021-16, 2 p.

Conodonts and detrital zircons from Triassic and Jurassic rocks above the Salmon River unconformity, Thompson Plateau, south-central British Columbia

Paul Schiarizza[1, a], Michael J. Orchard[2], and Richard M. Friedman[3]

[1] British Columbia Geological Survey, Ministry of Energy, Mines and Low Carbon Innovation, 300-865 Hornby Street, Vancouver, BC, V6Z 2G3
[2] Emeritus, Geological Survey of Canada, 101-605 Robson Street, Vancouver, BC, V6B 5J3
[3] Retired, formerly at Pacific Centre for Isotopic and Geochemical Research, Department of Earth, Ocean and Atmospheric Sciences, The University of British Columbia, Vancouver, BC, V6T 1Z4
[a] corresponding author: Paul.Schiarizza@gov.bc.ca

Recommended citation: Schiarizza, P., Orchard, M.J., and Friedman, R.M., 2022. Conodonts and detrital zircons from Triassic and Jurassic rocks above the Salmon River unconformity, Thompson Plateau, south-central British Columbia. In: Geological Fieldwork 2021, British Columbia Ministry of Energy, Mines and Low Carbon Innovation, British Columbia Geological Survey Paper 2022-01, pp. 17-30.

Abstract

In the Salmon River valley, 50 km SE of Kamloops, an unconformity separates schists of the Chapperon Group from less deformed limestones and siliciclastic rocks. The unconformity was first documented in the 1950s, limestones above the unconformity were dated as Late Triassic in the 1970s, and the Salmon River locale was considered to be a prime example of a Permo-Triassic unconformity recognized at numerous localities throughout south-central British Columbia. The area was mapped in 2016, and the rocks above the unconformity, extending several km west from their base in the Salmon River valley, were mapped as a single Triassic unit (the Salmon River succession) of predominantly siliciclastic rocks with some limestones at the base. Samples collected from the limestones during this mapping yielded conodonts that confirm a Late Triassic age for rocks immediately above the unconformity with the Chapperon Group. However, LA-ICP-MS U-Pb detrital zircon analysis of two sandstone samples indicate that the Salmon River succession is not a single Triassic unit. Detrital zircons from a sample near the base of the siliciclastic rocks yielded a maximum depositional age of ca. 183 Ma, and a sample collected 4.5 km to the west also yielded Early Jurassic zircons. These data show that most of the Salmon River succession is Jurassic, and that a more extensive sub-Jurassic unconformity merges with the sub-Triassic unconformity. The Salmon River succession is tentatively correlated with the Hall Formation (Early Jurassic, Toarcian) of the Rossland Group. The geological relationships documented along the Salmon River exemplify relationships in a large part of southeastern Quesnel terrane, where Paleozoic rocks are unconformably overlain by Middle to Late Triassic sedimentary rocks, and also by Early Jurassic volcanic and sedimentary rocks of the Rossland Group.

Keywords: Salmon River succession, conodonts, detrital zircons, U-Pb, LA-ICP-MS, Quesnel terrane, Triassic unconformity, Jurassic unconformity

1. Introduction

Jones (1959) identified an unconformity along a segment of the Salmon River, 50 km SE of Kamloops (Figs. 1, 2) that separated undated schists of the Chapperon Group from an overlying package of less-deformed limestones and siliciclastic sedimentary rocks that he assigned to the Cache Creek Group (Carboniferous-Permian). The rocks above the unconformity were later assigned a Triassic age, following the extraction of Late Triassic conodonts from limestone a few 10s of m above the unconformity (Campbell and Okulitch, 1973; Okulitch and Cameron, 1976), and the Salmon River locality was cited as one example of a Permo-Triassic unconformity that could be recognized at numerous localities throughout south-central British Columbia (Read and Okulitch, 1977).

The unconformity was revisited by Schiarizza (2017) during mapping focussed on the Nicola Group to the west (Fig. 2). This mapping included rocks above the unconformity in a single Triassic unit. This unit, referred to as the Salmon River

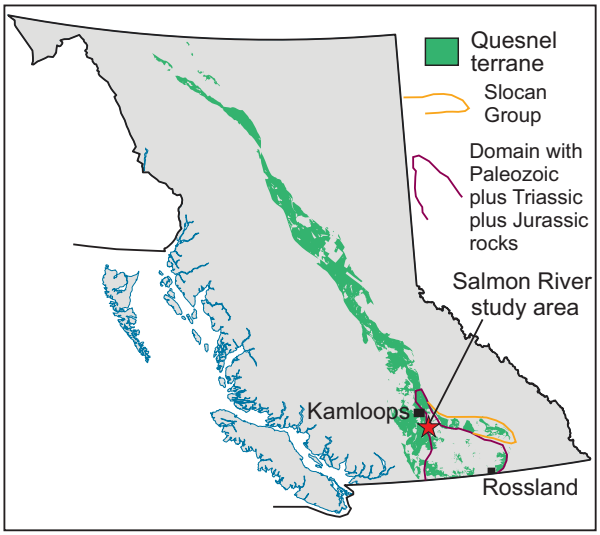

Fig. 1. Location of the Salmon River study area and distribution of Quesnel terrane in British Columbia.

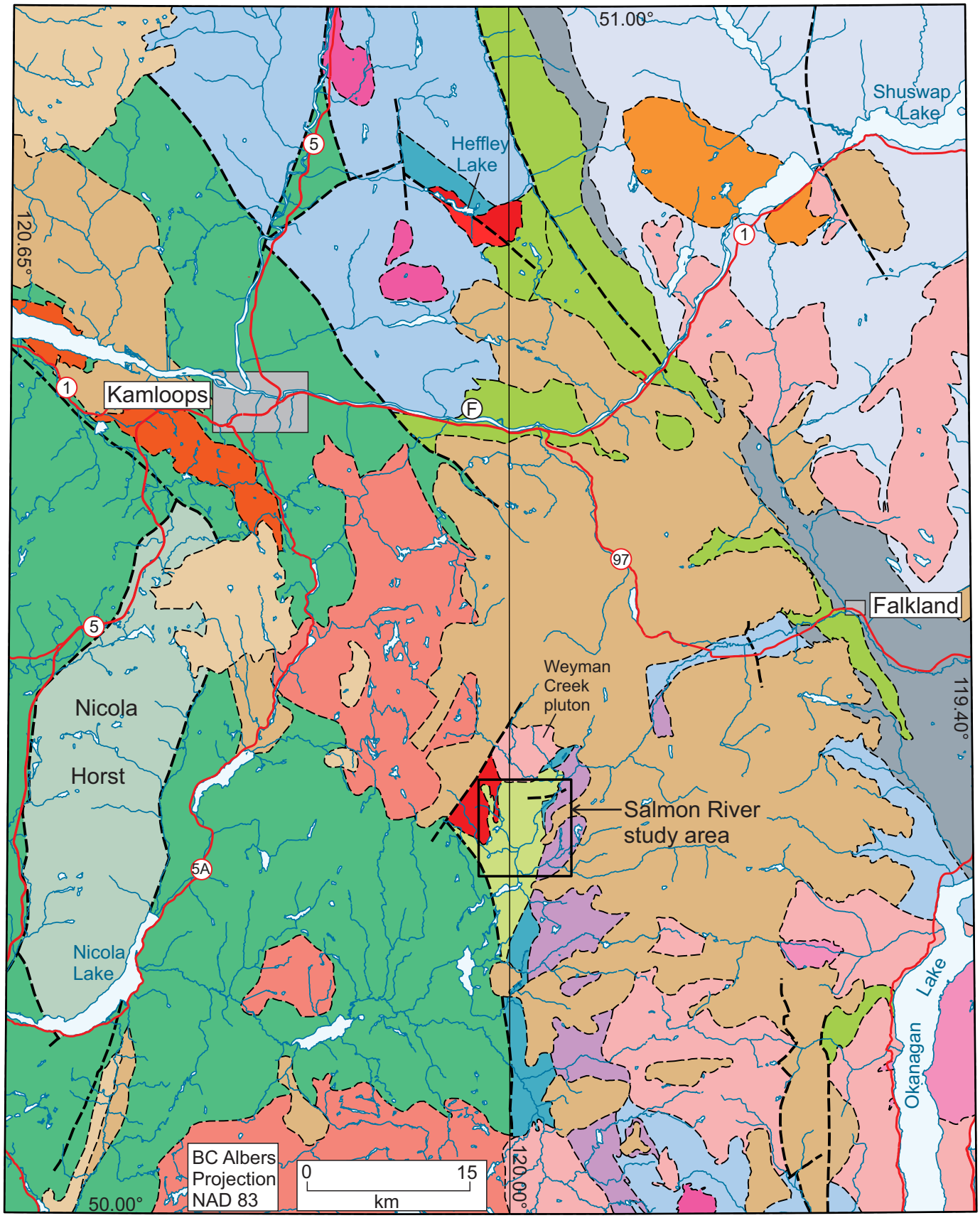

Fig. 2. Simplified geology of the eastern Ashcroft (92I) and western Vernon (82L) map areas, showing location of the Salmon River study area. Geology mainly after Monger and McMillan (1989) and Thompson et al. (2006).

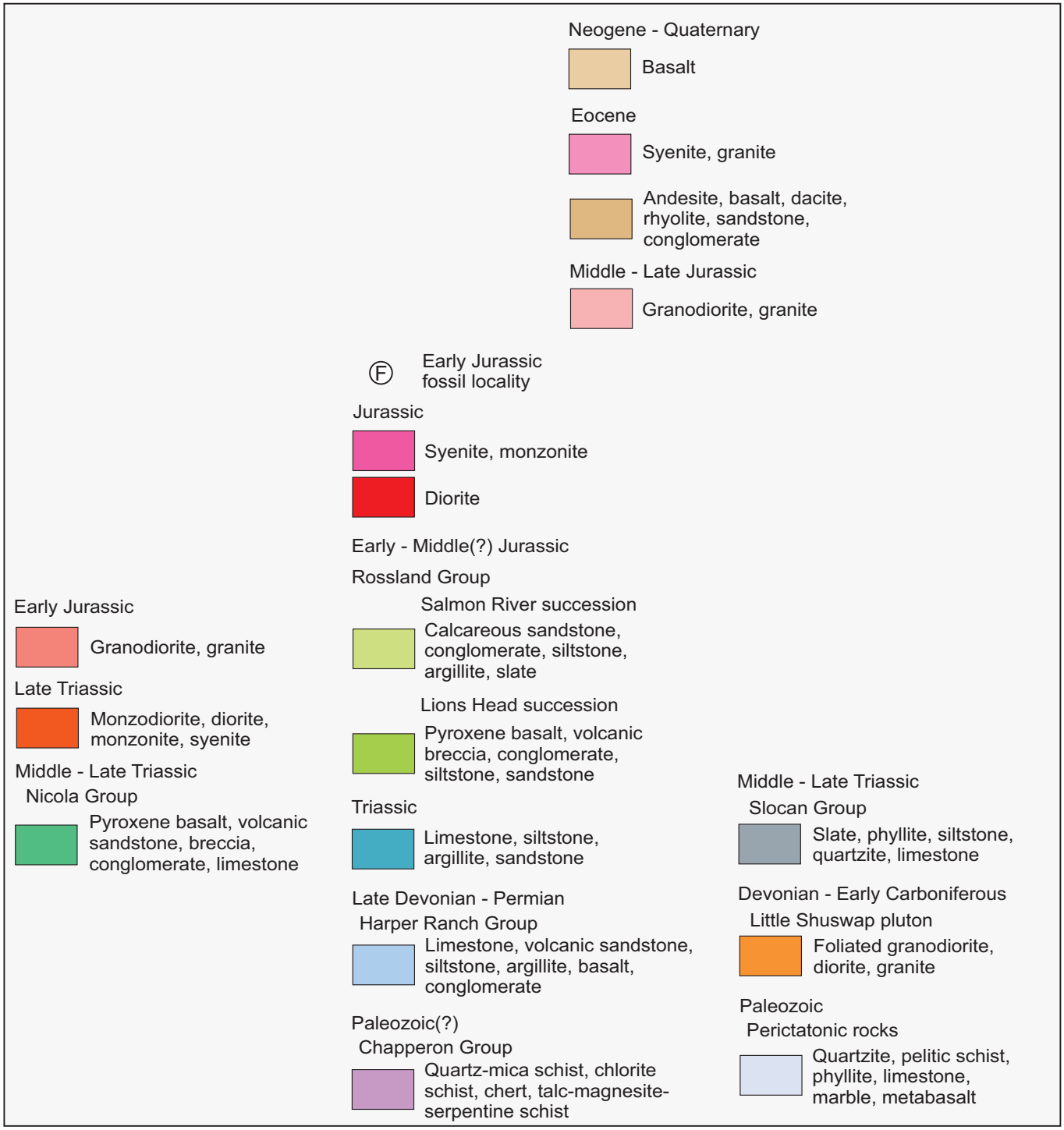

Fig. 2. Continued. Legend.

succession, was inferred to extend several km west from the Salmon River where it was juxtaposed with the Nicola Group across a very poorly constrained contact. Herein we present new conodont data from samples collected as part of this mapping that confirm a Late Triassic age for limestones immediately above the unconformity with subjacent Chapperon Group rocks. We also present new U-Pb zircon detrital ages from overlying siliciclastic rocks using Laser Ablation Inductively Coupled Plasma Mass Spectrometry (LA-ICP-MS). The detrital zircon data show that the Salmon River succession is not a single Late Triassic unit as considered by Schiarizza (2017), but that most of the unit is Jurassic, implying that a more extensive sub-Jurassic unconformity merges with the sub-Triassic unconformity.

2. Setting

The Salmon River study area is on the Thompson Plateau (Holland, 1976), about 50 km southeast of Kamloops, in the traditional territories of the Nlaka'pamux, Syilx, and Secwepemc First Nations (Fig. 1). It is in a belt of Paleozoic rocks, locally overlain by Mesozoic rocks and partially covered by Eocene volcanic rocks, that forms the eastern part of Quesnel terrane at this latitude (Fig. 2). This belt is flanked to the west by the Triassic-Jurassic arc complex, which is the most characteristic element of Quesnel terrane, here represented by volcanic and sedimentary rocks of the Nicola Group (Middle to Late Triassic) and associated suites of Late Triassic and Early Jurassic alkaline and calc-alkaline intrusions (Monger and McMillan, 1989). East of the Paleozoic Quesnel belt are mainly Devonian to Carboniferous assemblages of pericratonic metasedimentary, metavolcanic, and metaplutonic rocks, overlain by Late Triassic slates, siltstones, quartzites, and limestones of the Slocan Group (Thompson et al., 2006).

The Paleozoic rocks of Quesnel terrane in this region are assigned to the Harper Ranch Group and the Chapperon Group (Fig. 2). The Harper Ranch Group is predominant and, in its type area, east-northeast of Kamloops, includes Late Devonian and Mississippian arc-derived volcaniclastic rocks, and Late Mississippian and early Permian limestones (Beatty et al., 2006). Rocks assigned to the group farther south, west and northwest of Okanagan Lake are mainly early Permian, and include limestones, siltstones, argillites, slates, sandstones, and mafic volcanic rocks (Okulitch, 1979; Nixon and Carbno, 2001; Thompson et al., 2006). The Chapperon Group, first named and described by Jones (1959), forms a series of inliers that extend almost 50 km in the southwestern part of the Paleozoic Quesnel belt (Fig. 2). It includes biotite-quartz schists and phyllites, chert, quartzites, chlorite schists derived from mafic volcanic rocks, limestones, and serpentine-talc-magnesite schists derived from an ultramafic protolith (Jones, 1959; Thompson et al., 2006; Schiarizza, 2017). These rocks are undated, but the group is considered pre-Permian because, at the south end of the belt, it is overlain by Permian conglomerate that is included in the Harper Ranch Group (Read and Okulitch, 1977; Thompson et al., 2006).

Mesozoic rocks that overlie the Paleozoic rocks of Quesnel terrane are mainly Early Jurassic, but Triassic rocks, mainly limestones and siltstones, occur locally (Fig. 2). The predominant Early Jurassic unit is a succession of pyroxene basalts and breccias, intercalated with conglomerates, siltstones, and sandstones, that is best exposed east and northeast of Kamloops. These rocks had previously been included in the Nicola Group (Triassic), but are now assigned to the Lions Head succession of the Rossland Group (Jurassic) following Beatty et al. (2006), who discovered Early Jurassic (Sinemurian) fossils near the base of the succession, about 20 km east of Kamloops (Fig. 2). Jurassic sedimentary rocks of the Salmon River succession are spatially separate, lithologically distinct, and younger than the Lions Head succession, but may also be part of the Rossland Group.

3. Mesozoic rocks above the Salmon River unconformity

Jones (1959) assigned the rocks above the unconformity to the Cache Creek Group (Carboniferous-Permian). Preto (1964) confirmed the unconformable relationship between the Chapperon Group and overlying rocks recognized by Jones (1959), and suggested that the younger rocks might be either Cache Creek Group or Nicola Group. Campbell and Okulitch (1973) and Okulitch and Cameron (1976) reported Late Triassic conodonts from rocks above the unconformity, and subsequent workers inferred that this Late Triassic age applied both to the basal part of the succession and to siliciclastic rocks extending several km to the west. Okulitch (1979) assigned rocks above the unconformity to the Nicola Group, Daughtry and Thompson (2004a) included them in the Slocan Group, and Schiarizza (2017) referred to them as the Salmon River succession.

Conodont and detrital zircon age data presented below show that the Salmon River succession of Schiarizza (2017) comprises two separate units: a Triassic limestone unit of small aerial extent, and a Jurassic unit of mainly sandstones and siltstones that includes most of the Salmon River succession of Schiarizza (2017), as well as some rocks farther east that had been included in the Nicola Group. The Triassic rocks are referred to herein as the 'limestone unit'. The term 'Salmon River succession' is retained, but redefined to include only the Jurassic siliciclastic rocks.

3.1. Limestone unit (Triassic)

The limestone unit is exposed along the Salmon River as a local lens intervening between Chapperon Group rocks to the east and Jurassic conglomerates at the base of the Salmon River succession to the west (Fig. 3). The predominant rock types are medium to dark grey platy to flaggy micritic limestone, pebbly limestone, and thin- to medium-bedded, locally cross-stratified calcarenite (Figs. 4, 5). The pebbly limestones contain tabular intraformational limestone clasts and granules and small pebbles of chert, quartz, and quartz tectonite in a weakly to moderately foliated micritic limestone matrix. The calcarenites contain minor chert, quartz, and quartz-rich lithic grains in addition to predominantly carbonate grains. The unit also includes calcareous shales, typically as thin beds intercalated with calcarenite and, at one locality, a thin layer of green-grey faintly laminated chert.

3.2. Salmon River succession (Jurassic)

The Salmon River succession, as redefined herein, comprises Jurassic siliciclastic rocks that unconformably overlie both the Chapperon Group and the locally intervening limestone unit. The succession extends 5 to 7 km westward from its base near the Salmon River, where it is juxtaposed with the Nicola Group across an unexposed and poorly constrained contact. Detrital zircons provide Early Jurassic maximum depositional ages at two localities, one very near the base of the succession and one near the western limit of its exposure (see below).

The predominant rock types are sandstone and siltstone. Conglomerates locally form the base of the succession, and

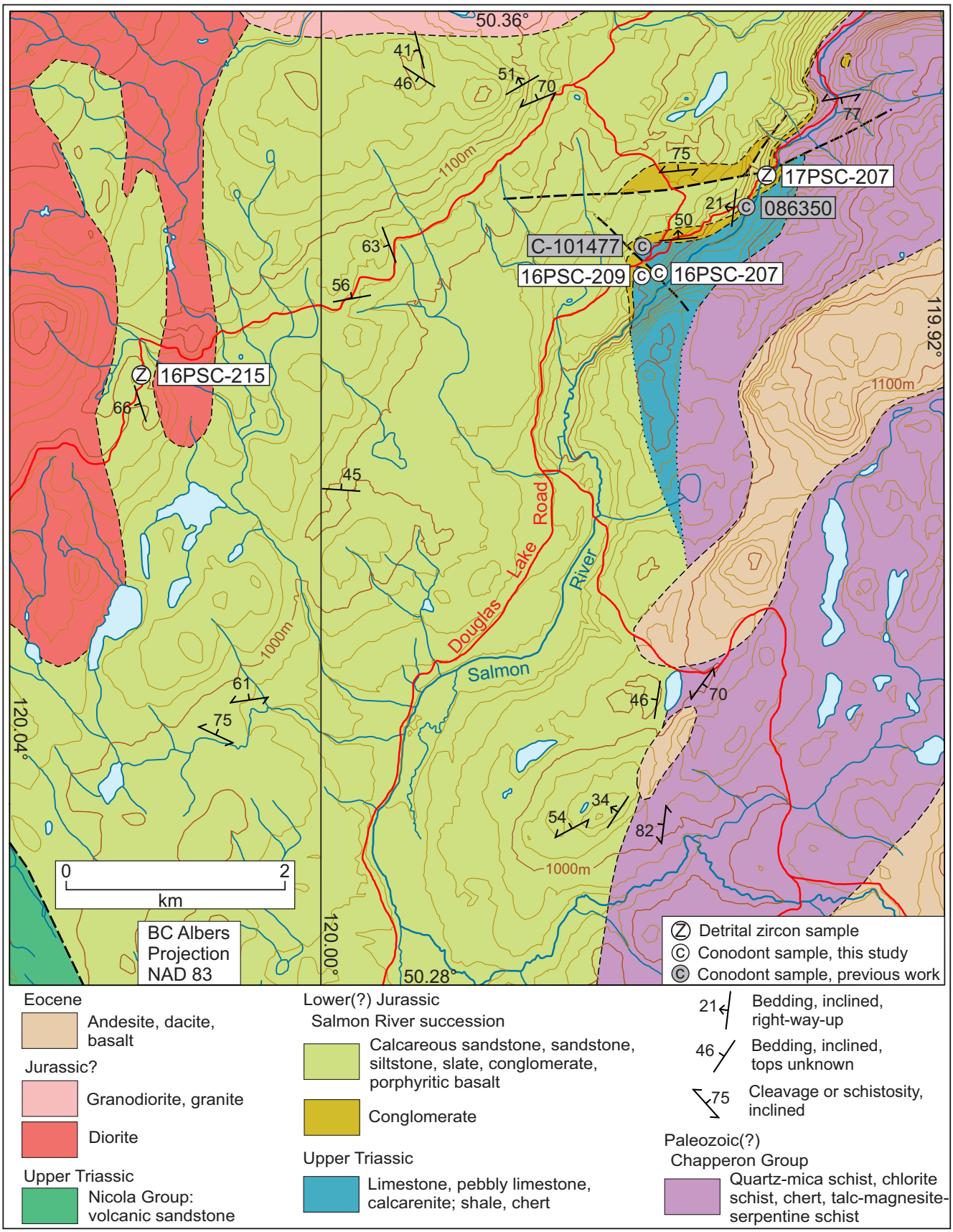

Fig. 3. Geology of the Salmon River study area showing locations of conodont and detrital zircon sample sites. Geology after Preto (1964), Read and Okulitch (1977), Daughtry and Thompson (2004a), and Schiarizza (2017).

Fig. 4. Limestone unit, pebbly limestone at conodont sample site 16PSC-207. Sample was collected from a narrow limestone lens such as in lower right of photo.

Fig. 5. Limestone unit, micritic limestone with 20 cm cross-stratified calcarenite bed, at conodont sample site 16PSC-209. Sample was collected from limestone beneath calcarenite bed.

occur elsewhere as medium to thick beds intercalated with finer grained rocks. A unit of plagioclase-hornblende-pyroxene-phyric basalt, possibly a sill, was identified at one location in the lower part of the unit, but volcanic rocks are otherwise absent. The conglomerate ranges from a few m to several 10s of m thick and rests above the Triassic limestone unit or the Chapperon Group. It is poorly stratified and polymictic, containing angular to subrounded clasts (mainly <1-5 cm, but locally to ~20 cm) in a fine-grained carbonate-cemented sandstone matrix. The clasts include chert, limestone, fine-grained quartzite, quartz phyllite, green volcanic or volcaniclastic rock, dark grey siliceous argillite, and vein quartz. Many of the clasts resemble rocks in the underlying Chapperon Group, from which they were probably derived; limestone clasts were likely derived, at least in part, from the subjacent limestone unit, as indicated by Triassic conodonts extracted from the clasts (see below).

Above the basal conglomerate, and directly above the Chapperon Group in the south, where the basal conglomerates are missing, is a section, several 100 m thick, of mainly brown-weathered carbonate-cemented sandstone. In this section, intervals of thin-bedded, fine- to medium-grained sandstone are punctuated by medium to thick beds of medium-to coarse-grained sandstone, and less common pebble conglomerate (Fig. 6). The thin sandstone beds locally display convolute lamination, cross stratification, graded bedding, and load casts, and are typically intercalated with thin beds or laminae of dark grey siltstone. The medium to thick sandstone beds locally display normal grading, and may have laminated tops. The sandstones and pebble conglomerates contain detrital grains of feldspar, fine-grained lithic fragments, chert, and quartz.

Outcrop in the western two-thirds of the Salmon River belt is sparse, and the succession is represented by scattered exposures of mainly dark grey siltstone, brown-weathered carbonate-cemented sandstone with quartz, feldspar and chert grains, and grey to green sandstone with mainly feldspar and volcanic-lithic grains (Fig. 7).

4. Conodont biochronology

Here we present fauna and age assignments, as determined by M.J. Orchard, for conodonts extracted from two samples collected from the limestone unit in 2016. We also present revised reports on two previous collections: one (GSC curation number 086350) that first documented Triassic rocks in the area; and the other (GSC curation number C-101477) from limestone cobbles within the basal conglomerate of the Salmon River succession. All collections are small and fragmentary, and some conodont elements are deformed. The Colour Alteration Index (CAI) is 5, implying post-depositional temperatures of 300°+ C. Though poorly preserved, the conodont elements show no corrosion that might imply reworking.

Fig. 6. Lower part of Salmon River succession, interbedded calcite-cemented sandstone, small-pebble conglomerate, and calcareous siltstone; detrital zircon sample site 17PSC-207.

Fig. 7. Parallel-stratified sandstone, Salmon River succession; detrital zircon sample site 16PSC-215.

4.1. Sample 16PSC-207 (GSC curation number V-012668), limestone unit

Sample 16PSC-207 was collected 130 m northwest of the Salmon River (289618E, 5580456N, UTM Zone 11, NAD83), about 1600 m southwest of the east-northeast trending fault that marks the north termination of the limestone unit (Fig. 3). It is from an exposure of pebbly limestone with a few narrow fine-grained limestone lenses (Fig. 4), which is at the top of a set of limestone and calcarenite outcrops that extends part way down to the river. The sample was collected from a fine-grained limestone lens about 4 cm wide and 30 cm long. It yielded two incomplete specimens of *Quadralella*, which ranges within the Carnian stage. Preserved features support assignment to *Quadralella* cf. *Q. angulata* (Mazza, Cau, and Rigo), but incomplete preservation precludes certainty as to substage. The age is Late Triassic, late? Carnian.

4.2. Sample 16PSC-209 (GSC curation number V-012669), limestone unit

Sample 16PSC-209 was collected from an isolated outcrop (289459E, 5580437N, UTM Zone 11, NAD83) 160 m west-southwest from sample site 16PSC-207 (Fig. 3). The exposure consists of dark grey fine-grained limestone intercalated with calcarenite beds 1-20 cm thick (Fig. 5). The calcarenite beds are locally boudinaged or folded about west-plunging folds with north-dipping axial surfaces that are parallel to a weak cleavage within the limestones. The sample came from a fine-grained, weakly-cleaved limestone unit, and yielded a conodont collection consisting of: *Ancyrogondolella* cf. *tozeri* (Orchard) (1 specimen); *A*. sp. indet. (5 specimens); *Mockina* cf. *postera* (Kozur & Mostler) (1 specimen); *Norigondolella* sp. indet. (1 specimen); S2 ramiform elements (2 specimens). The age is Late Triassic, early middle Norian.

4.3. GSC curation number 086350, limestone unit

Triassic conodonts from the Salmon River area were first described by Okulitch and Cameron (1976). They reported a small collection that included *Epigondolella primitia* Mosher, and *Metapolygnathus polygnathiformis* (Budurov and Stefanov), for which they suggested a late Carnian age. The sample (GSC curation number 086350) was collected from an exposure of limestone and limy conglomerate along or near the Douglas Lake road, plotted on Fig. 3 from the location shown by Daughtry and Thompson (2004a). Re-examination of the fauna from this location provides the following revision: *Primatella*? sp. indet. (1 specimen); *Quadralella* cf. *deflecta* (1 specimen); *Q*. sp. indet. (2 specimens). The age is Late Triassic, late Carnian, as originally proposed by Okulitch and Cameron (1976).

4.4. GSC curation number C-101477, limestone clasts in basal Salmon River succession conglomerate

Conodonts were extracted from a sample submitted by R.I. Thomson during the Geological Survey of Canada's Ancient Pacific Margin NATMAP program (Thompson et al., 2006). The sample was from limestone clasts in the basal conglomerate of the Salmon River succession, collected about 275 m northwest of sample 16PSC-207, which is from the Triassic limestone unit. This conodont collection comprises a few indeterminate neogondolellin specimens that support an age within the range of Middle-Late Triassic, Ladinian-Norian (Orchard, 2000; Daughtry and Thompson, 2004a). A re-assessment of this small collection has additionally identified a possible specimen of *Quadralella*, which suggests a Carnian age for at least one of the clasts. The fauna is revised as: *Neogondolella*? sp. indet. (3 specimens); *Quadralella*? sp. indet. (1 specimen); ramiform elements (2 specimens).

5. Detrital zircon geochronology

We collected two sandstone samples from the Salmon River succession for U-Pb detrital zircon analysis. Sample preparation and analytical work (LA-ICP-MS) was conducted at the Pacific Centre for Isotopic and Geochemical Research (PCIGR), the Department of Earth, Ocean and Atmospheric Sciences, the University of British Columbia.

5.1. Analytical procedures

Following mineral separation by standard procedures, zircons were handpicked in alcohol and mounted in epoxy, along with reference materials. Grain mounts were then wet ground with carbide abrasive paper and polished with diamond paste. Next, cathodoluminescence (CL) imaging was carried out on a Philips XL-30 scanning electron microscope (SEM) equipped with a Bruker Quanta 200 energy-dispersion X-ray microanalysis system at the Electron Microbeam/X-Ray Diffraction Facility (EMXDF). An operating voltage of 15 kV was used, with a spot diameter of 6 μm and peak count time of 30 seconds. After removal of the carbon coat the grain mount surface was washed with mild soap and rinsed with high-purity water. Prior to analysis the grain mount surface was cleaned with 3 N HNO_3 acid and again rinsed with high-purity water to

remove any surficial Pb contamination that could interfere with the early portions of the spot analyses.

Analyses were conducted using a Resonetics RESOlution M-50-LR, which contains a Class I laser device equipped with a UV excimer laser source (Coherent COMPex Pro 110, 193 nm, pulse width of 4 ns) and a two-volume cell designed and developed by Laurin Technic Pty. Ltd. (Australia). This sample chamber allowed the investigation of several grain mounts in one analytical session. The laser path was fluxed by N_2 to ensure better stability. Ablation was carried out in a cell with a volume of approximately 20 cm^3 and a He gas stream that ensured better signal stability and lower U-Pb fractionation (Eggins et al., 1998). The laser cell was connected via a Teflon squid to an Agilent 7700x quadrupole ICP-MS housed at PCIGR. A pre-ablation shot was used to ensure that the spot area on grain surface was free of contamination. Samples and reference materials were analyzed for 36 isotopes, including Pb (^{204}Pb, ^{206}Pb, ^{207}Pb, ^{208}Pb), ^{232}Th, and U (^{235}U, ^{238}U) with a dwell time of 0.02 seconds for each isotope. Pb/U and Pb/Pb ratios were determined on the same spots along with trace element concentrations. The settings for the laser were: spot size of 34 µm with a total ablation time of 30 seconds, frequency of 5 Hz, fluence of 5 J/cm^2, power of 7.8 mJ after attenuation, pit depths of approximately 15 µm, He flow rate of 800 mL/min, N_2 flow rate of 2 mL/min, and a carrier gas (Ar) flow rate of 0.57 L/min.

Reference materials were analyzed throughout the sequence to allow for drift correction and to characterize downhole fractionation for Pb/U and Pb/Pb isotopic ratios. For U-Pb analyses, natural zircon reference materials were used, including Plešovice (Sláma et al., 2008) or 91500 (Wiedenbeck et al., 1995, 2004) as the internal reference material, and both Temora2 (Black et al., 2004) and Plešovice and/or 91500 as monitoring reference materials; the zircon reference materials were placed between the unknowns. Raw data were reduced using the Iolite 3.4 extension (Paton et al., 2011) for Igor Pro™ yielding U/Pb ages, and their respective uncertainties. Final interpretation and plotting of the analytical results employed the ISOPLOT software of Ludwig (2003).

5.2. Sample 17PSC-207, basal Salmon River succession

Sample 17PSC-207 was collected from an outcrop along the Douglas Lake road (290640E, 5581299N, UTM Zone 11, NAD 83) about 30 m northwest of the Salmon River (Fig. 3). Exposed here is a well-bedded succession, dipping gently to the west, of calcite-cemented sandstones and small-pebble conglomerates, interbedded with calcareous siltstones (Fig. 6). These rocks are near the base of the Salmon River succession, less than 10 m above the basal conglomerate. The sample comes from a bed of very calcareous coarse-grained sandstone with detrital grains of plagioclase, monocrystalline quartz, polycrystalline quartz, chert, fine-grained quartz tectonite, and feldspathic volcanic rock.

Seventy-eight detrital zircon grains were analyzed from sample 17PSC-207 (Table 1, Fig. 8). Most (n=61) have Mesozoic ^{206}Pb/^{238}U ages, 6 grains are Paleozoic (503 to 323.7 Ma) and 11 grains are Paleoproterozoic (2452 to 1693 Ma). With the exception of 1 grain (233.1 Ma), the Mesozoic grains (n=60) form a tight cluster ranging from 215 to 178.3 Ma, forming a strong peak at 202 Ma on the probability density curve. More than half these grains (n=31) are Early Jurassic (201 to 178.3 Ma), and about half of these (n=14) range from 188.3 to 178.3 Ma, accounting for a secondary peak at ca. 183 Ma on the probability density curve. Lacking the analytical numbers for a statistically rigorous precise age (see Pullen et al., 2014; Coutts et al., 2019), we consider that 183 Ma is a reasonable estimate of the maximum depositional age and that it demonstrates the Salmon River succession is Jurassic.

5.3. Sample 16PSC-215, upper(?) part of Salmon River succession

Sample 16PSC-215 was collected from an isolated outcrop along the Monte-Glimpse Forest Service road (711864E, 5579575N, UTM Zone 10, NAD 83), about 4 km west of the Salmon River, in the poorly exposed western part of the Salmon River succession (Fig. 3). The outcrop is mainly green, massive to laminated, fine- to medium-grained sandstone (Fig. 7), but also includes a narrow interval of medium to dark grey laminated siltstone. The sample is medium-grained sandstone consisting mainly of plagioclase grains, accompanied by feldspathic lithic grains, hornblende, and mafic mineral or lithic grains altered to actinolite and epidote.

A small population of 17 detrital zircon grains were analyzed from sample 16PSC-215 (Table 2, Fig. 9). One of these has a ^{206}Pb/^{238}U age of 304.5 Ma, and the others (n=16) form a cluster ranging from 189 to 211.4 Ma, with a peak at 206 Ma on the probability density curve. This cluster is markedly similar to the main population of grains from sample 17PSC-207. The youngest grains (189 Ma, 189.7 Ma, 189.9 Ma, 194 Ma) contribute to a secondary peak at ca. 190 Ma, providing an estimate of the maximum depositional age. Again, although lacking the statistical rigour of large zircon sample numbers, this peak indicates that the Salmon River succession is Jurassic.

6. Discussion

6.1. Triassic rocks

Exposed along strike to the south is a belt of rocks that may be related to the limestone unit of the Salmon River study area (Fig. 2). Although mapped as Harper Ranch Group by Daughtry and Thompson (2004b), these rocks are Triassic, at least in part, because they contain Early-Middle Triassic conodonts (Thompson et al., 2006). Rocks that may correlate with the Triassic limestone unit also occur at Heffley Lake, 25 km northeast of Kamloops (Fig. 2). This unit is predominantly siltstone and argillite, but includes a limestone body that has yielded Carnian conodonts (Friedman et al., 2002). On a more regional scale, the Triassic limestone unit is part of an assemblage of Middle and Late Triassic rocks that unconformably overlie Paleozoic rocks of Quesnel terrane at scattered localities south and southeast of the Salmon River

Table 1. Zircon U-Pb laser ablation analytical data for sample 17PSC-207, Salmon River succession.

Sample no.	Isotopic Ratios							Isotopic Ages					
Analysis ID	$^{207}Pb/^{235}U$	2σ (abs)	$^{206}Pb/^{238}U$	2σ (abs)	ρ	$^{207}Pb/^{206}Pb$	2σ (abs)	$^{207}Pb/^{235}U$	2σ (Ma)	$^{206}Pb/^{238}U$	2σ (Ma)	$^{207}Pb/^{206}Pb$	2σ (Ma)
X17PSC_207_b1	0.171	0.026	0.02824	0.00077	0.0252	0.0498	0.0075	160	22	179.5	4.8	130	300
X17PSC_207_b2	7.63	0.27	0.4037	0.0049	0.2664	0.1456	0.0038	2183	31	2186	23	2287	45
X17PSC_207_b3	0.21	0.053	0.033	0.0019	0.0189	0.051	0.013	196	47	209	12	0	440
X17PSC_207_b4	0.543	0.066	0.0762	0.0023	0.1076	0.0554	0.0066	432	42	473	14	310	240
X17PSC_207_b5	0.197	0.052	0.031	0.0016	0.2907	0.048	0.012	173	43	197	10	-140	430
X17PSC_207_b6	0.173	0.026	0.0308	0.0013	0.0272	0.0504	0.0077	160	23	195.8	8.1	130	320
X17PSC_207_b7	5.13	0.28	0.3335	0.0075	0.0975	0.119	0.006	1831	48	1855	36	1911	97
X17PSC_207_b8	0.267	0.048	0.0331	0.0015	0.0537	0.064	0.012	234	37	209.8	9.6	430	350
X17PSC_207_b10	4.37	0.17	0.3004	0.0082	0.4526	0.1214	0.0047	1706	32	1693	40	1971	71
X17PSC_207_b11	0.21	0.03	0.0296	0.00086	0.1562	0.0574	0.009	196	27	188	5.4	300	290
X17PSC_207_b12	0.235	0.033	0.0331	0.0011	0.3469	0.0544	0.0073	211	27	209.8	6.7	250	270
X17PSC_207_b13	0.148	0.026	0.0301	0.0012	0.0805	0.0479	0.0088	138	23	191.4	7.7	-10	330
X17PSC_207_b14	0.169	0.025	0.02856	0.00062	0.273	0.0527	0.0075	156	22	181.5	3.9	200	290
X17PSC_207_b15	0.183	0.036	0.0297	0.0011	0.0146	0.055	0.011	168	30	188.6	6.6	220	380
X17PSC_207_b16	0.194	0.067	0.0333	0.0028	0.1035	0.045	0.016	172	57	211	17	-240	580
X17PSC_207_b17	0.176	0.024	0.02882	0.00091	0.0021	0.0556	0.0073	162	20	183.1	5.7	290	270
X17PSC_207_b18	0.186	0.02	0.0304	0.00087	0.0442	0.0482	0.0056	172	18	193	5.5	100	240
X17PSC_207_b19	0.189	0.033	0.02912	0.00092	0.0849	0.0587	0.0097	179	30	185	5.7	410	320
X17PSC_207_b20	0.215	0.027	0.0316	0.0012	0.0344	0.0536	0.0069	195	22	200.5	7.4	230	260
X17PSC_207_b21	0.211	0.034	0.0319	0.0011	0.2791	0.0536	0.0088	198	30	202.3	6.9	170	300
X17PSC_207_b22	0.24	0.036	0.0317	0.0012	0.1021	0.0602	0.0096	214	29	201.4	7.6	390	320
X17PSC_207_b23	0.213	0.038	0.0296	0.0014	0.045	0.057	0.011	191	31	188.3	9	220	350
X17PSC_207_b24	4.92	0.33	0.3178	0.0074	0.1835	0.1202	0.0074	1791	57	1778	36	1910	120
X17PSC_207_b25	0.461	0.045	0.0659	0.0021	0.2862	0.0614	0.0067	381	31	411	13	550	220
X17PSC_207_b26	0.211	0.026	0.03014	0.00082	0.1364	0.0528	0.0062	192	22	191.4	5.2	270	250
X17PSC_207_b27	4.36	0.19	0.3093	0.006	0.3135	0.1097	0.0047	1699	36	1737	29	1773	78
X17PSC_207_b28	0.174	0.034	0.0285	0.0017	0.0794	0.051	0.01	161	29	181	11	170	400
X17PSC_207_b29	0.216	0.03	0.03184	0.00097	0.1009	0.0528	0.0073	196	24	202	6.1	180	260
X17PSC_207_b30	0.214	0.032	0.031	0.0013	0.1602	0.0544	0.0082	201	30	196.5	8.4	280	320
X17PSC_207_b31	0.211	0.033	0.0317	0.0013	0.051	0.0524	0.0084	190	28	200.9	8.1	160	310
X17PSC_207_b32	0.164	0.014	0.02887	0.00093	0.132	0.0519	0.0047	153	13	183.4	5.8	220	190
X17PSC_207_b33	0.345	0.052	0.0326	0.0011	0.162	0.085	0.015	293	38	206.7	6.8	980	320
X17PSC_207_b34	0.214	0.031	0.0309	0.0013	0.1477	0.0549	0.0082	193	26	196.4	8	260	300
X17PSC_207_b35	0.249	0.027	0.03682	0.00088	0.2664	0.0548	0.0066	224	21	233.1	5.5	280	220
X17PSC_207_b37	10.29	0.33	0.4631	0.0065	0.1709	0.1731	0.0052	2457	31	2452	29	2578	52
X17PSC_207_b38	0.566	0.08	0.0736	0.0026	0.1528	0.0608	0.009	442	51	458	16	420	290
X17PSC_207_b39	0.223	0.025	0.03154	0.00087	0.0647	0.0559	0.0068	202	20	200.2	5.5	310	230
X17PSC_207_b40	0.167	0.024	0.02805	0.00081	0.1239	0.0544	0.0076	155	21	178.3	5.1	230	280
X17PSC_207_b41	4.67	0.29	0.3186	0.0086	0.3997	0.1159	0.0069	1761	56	1782	42	1850	110
X17PSC_207_b42	0.194	0.034	0.03089	0.0009	0.3047	0.0484	0.0077	176	28	196.1	5.6	0	290
X17PSC_207_b43	0.232	0.024	0.03191	0.00083	0.245	0.0596	0.0073	215	21	202.4	5.2	440	240
X17PSC_207_b44	0.191	0.037	0.0329	0.0013	0.0796	0.0457	0.0091	181	33	208.9	7.9	-80	340
X17PSC_207_b45	0.22	0.034	0.0315	0.0012	0.0653	0.0554	0.0087	198	28	199.6	7.4	250	300
X17PSC_207_b46	0.206	0.027	0.0317	0.0011	0.0233	0.0516	0.0071	188	23	200.9	6.6	150	270
X17PSC_207_b47	0.198	0.031	0.0317	0.0011	0.121	0.0491	0.008	180	26	201.3	6.9	20	290
X17PSC_207_b48	0.231	0.041	0.032	0.0014	0.1083	0.058	0.011	205	34	203.3	9	260	380
X17PSC_207_c1	0.231	0.03	0.03299	0.00095	0.0241	0.0471	0.0051	208	24	209.2	5.9	10	210
X17PSC_207_c2	0.208	0.029	0.03133	0.00097	0.217	0.0454	0.0054	189	23	198.8	6.1	-60	230
X17PSC_207_c3	6.23	0.32	0.3633	0.007	0.0019	0.119	0.0048	1999	46	2005	30	1923	73
X17PSC_207_c4	5.59	0.42	0.3385	0.0059	0.0521	0.1141	0.0049	1895	64	1879	29	1845	79
X17PSC_207_c5	0.27	0.037	0.03344	0.00096	0.287	0.0574	0.0075	238	29	212	6	350	270
X17PSC_207_c6	0.238	0.032	0.02935	0.00096	0.1573	0.0466	0.006	216	26	186.5	6	10	260
X17PSC_207_c7	0.303	0.044	0.0317	0.0016	0.5856	0.0528	0.0067	265	35	201	10	260	260
X17PSC_207_c8	5.83	0.46	0.3473	0.0091	0.0286	0.1183	0.0064	1928	69	1920	43	1900	100
X17PSC_207_c9	0.219	0.024	0.03184	0.00095	0.131	0.0524	0.0043	199	20	202	5.9	250	170
X17PSC_207_c10	0.219	0.027	0.031	0.001	0.2082	0.0523	0.007	199	22	196.6	6.5	170	250
X17PSC_207_c11	0.507	0.092	0.078	0.0029	0.2015	0.0471	0.0098	421	71	484	17	-70	350
X17PSC_207_c12	0.236	0.034	0.0322	0.001	0.0593	0.0566	0.0085	211	28	204	6.2	290	300
X17PSC_207_c13	0.618	0.077	0.0811	0.002	0.045	0.0555	0.0062	477	47	503	12	320	220

Table 1. Continued.

Sample no.	Isotopic Ratios							Isotopic Ages					
Analysis ID	$^{207}Pb/^{235}U$	2σ (abs)	$^{206}Pb/^{238}U$	2σ (abs)	ρ	$^{207}Pb/^{206}Pb$	2σ (abs)	$^{207}Pb/^{235}U$	2σ (Ma)	$^{206}Pb/^{238}U$	2σ (Ma)	$^{207}Pb/^{206}Pb$	2σ (Ma)
X17PSC_207_c14	0.241	0.028	0.03186	0.00096	0.1957	0.0561	0.0061	217	23	202.2	6	350	220
X17PSC_207_c15	0.4	0.037	0.0515	0.0013	0.0265	0.0573	0.0046	338	27	323.7	8.1	430	170
X17PSC_207_c16	0.209	0.025	0.0338	0.001	0.0942	0.0494	0.007	191	21	214.3	6.4	70	270
X17PSC_207_c17	0.205	0.021	0.0329	0.0012	0.0248	0.0484	0.0056	193	20	208.5	7.4	110	250
X17PSC_207_c19	0.23	0.03	0.032	0.0011	0.0607	0.0547	0.0065	207	24	203.3	7.2	290	250
X17PSC_207_c20	0.209	0.029	0.0317	0.0013	0.1018	0.05	0.0065	190	24	201.2	8.4	170	280
X17PSC_207_c21	0.264	0.053	0.0286	0.0011	0.0172	0.0472	0.0093	238	44	181.9	6.9	-40	340
X17PSC_207_c22	0.225	0.046	0.0328	0.0017	0.0459	0.053	0.011	199	38	208	10	110	380
X17PSC_207_c23	0.241	0.027	0.0288	0.0013	0.0786	0.0546	0.0076	218	22	183	8.3	320	290
X17PSC_207_c24	0.253	0.05	0.0339	0.0016	0.1814	0.059	0.012	221	41	215	10	290	430
X17PSC_207_c25	0.22	0.031	0.0317	0.0011	0.1787	0.0525	0.0063	199	25	201	6.7	250	250
X17PSC_207_c26	0.206	0.052	0.0294	0.0014	0.0622	0.047	0.013	187	44	186.6	8.6	-20	520
X17PSC_207_c27	0.198	0.025	0.0317	0.0011	0.1426	0.05	0.0064	181	21	201.4	6.8	150	250
X17PSC_207_c28	0.265	0.047	0.0323	0.0016	0.0987	0.066	0.011	232	37	205	10	540	360
X17PSC_207_c29	0.209	0.038	0.0329	0.0015	0.0309	0.0503	0.008	188	31	208.8	9.4	80	300
X17PSC_207_c30	5.41	0.29	0.3335	0.0078	0.0223	0.128	0.0061	1876	45	1854	38	2048	82
X17PSC_207_c31	0.254	0.049	0.0318	0.0013	7E-06	0.063	0.011	222	39	201.7	8.1	440	360
X17PSC_207_c33	0.249	0.03	0.03226	0.00075	0.0923	0.0604	0.0067	223	24	204.7	4.7	490	240
X17PSC_207_c34	0.266	0.045	0.0331	0.0014	0.3718	0.063	0.01	234	35	209.8	8.9	480	310

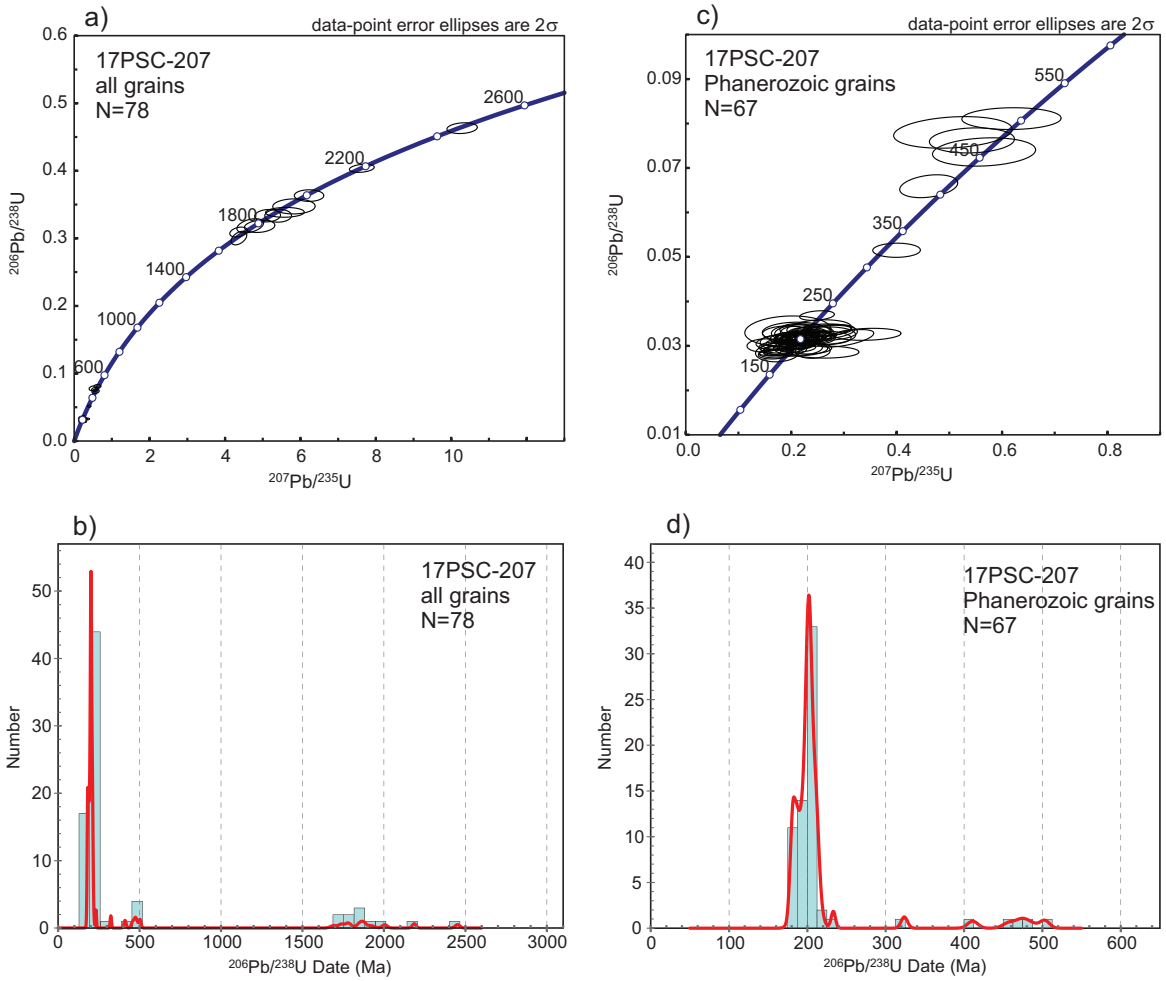

Fig. 8. U-Pb data for detrital zircons from Salmon River succession sandstone sample 17PSC-207. **a)** Concordia plot of all grains. **b)** Histogram of all grains and superimposed probability density curve. **c)** Concordia plot of Phanerozoic grains. **d)** Histogram of Phanerozoic grains with superimposed probability density curve.

Table 2. Zircon U-Pb laser ablation analytical data for sample 16PSC-215, Salmon River succession.

Sample no.	Isotopic Ratios							Isotopic Ages					
Analysis ID	$^{207}Pb/^{235}U$	2σ (abs)	$^{206}Pb/^{238}U$	2σ (abs)	ρ	$^{207}Pb/^{206}Pb$	2σ (abs)	$^{207}Pb/^{235}U$	2σ (Ma)	$^{206}Pb/^{238}U$	2σ (Ma)	$^{207}Pb/^{206}Pb$	2σ (Ma)
X16PSC_215_3	0.204	0.038	0.0312	0.0011	0.0287	0.0503	0.01	184	32	197.9	6.9	20	370
X16PSC_215_4	0.215	0.025	0.03075	0.00078	0.3225	0.052	0.0067	196	21	195.2	4.9	180	250
X16PSC_215_5	0.224	0.027	0.0326	0.00092	0.3921	0.0505	0.0062	204	24	206.8	5.7	240	270
X16PSC_215_7	0.308	0.047	0.0484	0.0012	0.218	0.0471	0.0072	274	36	304.5	7.5	90	310
X16PSC_215_12	0.23	0.029	0.03172	0.00068	0.2968	0.0543	0.0069	215	24	201.3	4.3	310	260
X16PSC_215_13	0.233	0.077	0.0298	0.0021	0.0402	0.05	0.019	204	63	189	13	180	650
X16PSC_215_14	0.24	0.041	0.03335	0.00078	0.2014	0.0526	0.0085	217	31	211.4	4.9	300	270
X16PSC_215_17	0.227	0.027	0.03252	0.00054	0.0014	0.0514	0.0061	206	22	206.3	3.4	220	240
X16PSC_215_24	0.228	0.098	0.032	0.0013	0.4768	0.0522	0.017	207	64	203	8.1	330	380
X16PSC_215_25	0.214	0.014	0.03189	0.00058	0.1868	0.0484	0.0034	198	12	202.4	3.6	130	160
X16PSC_215_28	0.204	0.032	0.0299	0.00084	0.1591	0.051	0.0083	192	29	189.9	5.3	150	340
X16PSC_215_31	0.22	0.014	0.03272	0.00065	0.0314	0.0491	0.0035	201	12	207.5	4.1	170	160
X16PSC_215_32	0.22	0.017	0.03324	0.00061	0.0226	0.0487	0.0039	203	14	210.8	3.8	120	180
X16PSC_215_33	0.203	0.041	0.0306	0.0016	0.0796	0.053	0.0099	185	35	194	10	150	390
X16PSC_215_39	0.209	0.04	0.0315	0.0012	0.0275	0.0489	0.0098	188	34	199.8	7.5	50	390
X16PSC_215_41	0.23	0.017	0.03254	0.00042	0.2826	0.0508	0.0037	211	15	206.4	2.6	230	170
X16PSC_215_45	0.2	0.019	0.02987	0.00065	0.3635	0.0483	0.0044	184	16	189.7	4	90	190

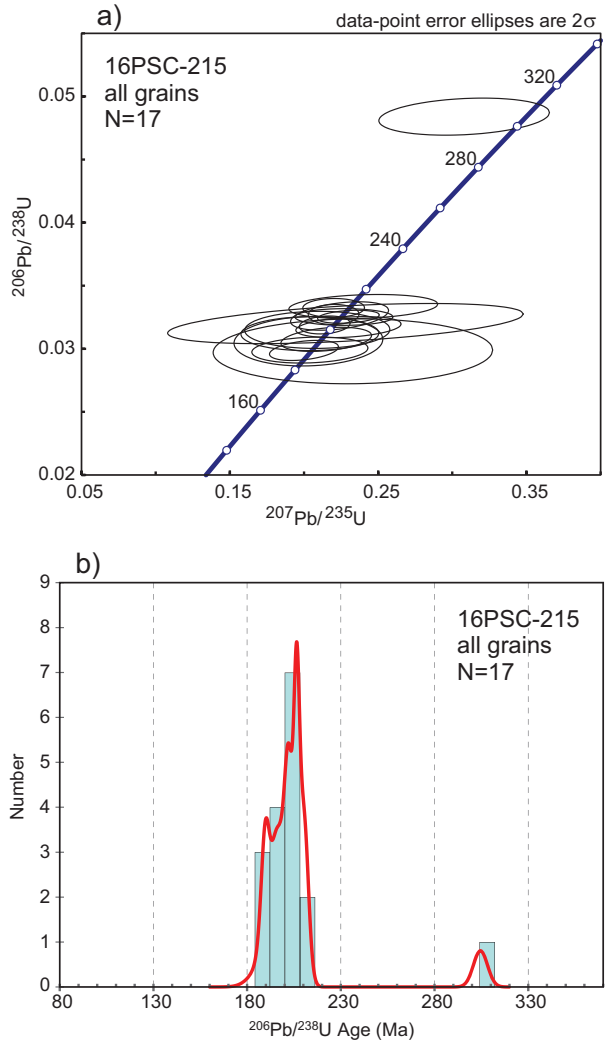

Fig. 9. U-Pb data for detrital zircons from Salmon River succession sandstone sample 16PSC-215. **a)** Concordia plot of all grains. **b)** Histogram of all grains and superimposed probability density curve.

area. These include Late Triassic rocks, mainly limestone, chert breccia, sandstone and shale, that unconformably overlie the Old Tom and Shoemaker formations near Olalla, 120 km south of the Salmon River area (Bostock, 1941; Read and Okulitch, 1977); Late Triassic limestone and siltstone of the French Mine, Hedley, Chuchuwayha, and Stemwinder formations near Hedley, 20 km west of the Olalla Triassic rocks (Ray and Dawson, 1994); and the Brooklyn Formation (Middle Triassic, mainly chert breccia, conglomerate, limestone, greenstone) that sits unconformably above the Knob Hill and Atwood groups in the Greenwood-Grand Forks area, 170 km southeast of the Salmon River area (Fyles, 1990).

6.2. Jurassic rocks

The Salmon River succession comprises siliciclastic rocks that unconformably overlie the Chapperon Group and the Triassic limestone unit. The best age constraint comes from detrital zircons extracted from sample 17PSC-207, indicating a maximum depositional age of ca.183 Ma (Early Jurassic, near the Pliensbachian/Toarcian boundary). The Salmon River succession is cut to the north by granodiorite of the Weyman Creek pluton (Fig. 2; Daughtry and Thompson, 2004a), which is undated but included in the Middle to Late Jurassic Okanagan plutonic suite (Thompson et al., 2006). If this assignment is correct, the Salmon River succession is no younger than Middle Jurassic.

Siliciclastic rocks that might correlate with the Salmon River succession are in the Ashcroft Formation, an assemblage of Early and Middle Jurassic sandstones, conglomerates, and shales that unconformably overlie Late Triassic volcanic and plutonic rocks in the western part of Nicola belt (Travers, 1978; Monger and McMillan, 1989). A more compelling correlation is with the Hall Formation, which forms the upper part of the Rossland Group in its type area, 220 km southeast of the Salmon River study area (Fig. 1; Höy and Dunne, 1997). This

correlation is based on a strong lithologic similarity, and a good match between the age of the Hall Formation (Toarcian) and the maximum depositional age established for the Salmon River succession. Most importantly, the Salmon River succession is close to a slightly older volcano-sedimentary succession (Lions Head succession, Fig. 2; Beatty et al., 2006) that is correlated with the older (Sinemurian) parts of the Rossland Group (Archibald and Elise formations), which underlie the Hall Formation in the type area of the group (Höy and Dunne, 1997).

Detrital zircons from the Salmon River succession do not identify a unique source area. The predominant Late Triassic-Early Jurassic grains could have been provided by the upper part of the Nicola Group (Late Triassic) and associated Late Triassic to Early Jurassic intrusions (Monger and McMillan, 1989; Schiarizza et al., 2013; Mihalynuk and Diakow, 2020), but the Early Jurassic component of this population could also have been provided by older parts of the Rossland Group and associated intrusions (Höy and Dunne, 1997; Beatty et al., 2006). Paleoproterozoic grains from sample 17PSC-207 (n=11, 1693 to 2452 Ma) were probably derived from the North American craton, recycled through pericratonic and continental margin sedimentary rocks, and perhaps again through Paleozoic rocks of Quesnel terrane (Mortensen et al., 2017).

6.3. Geologic domains of southern Quesnel terrane

Quesnel terrane is predominantly a Mesozoic arc complex, represented in southern British Columbia by volcanic and volcaniclastic rocks of the Nicola Group (Middle to Late Triassic) and associated Late Triassic and Early Jurassic intrusions. However, the terrane, as defined in the 1980s, also includes Paleozoic and Mesozoic rocks east of this arc complex (Monger et al., 1991). The Salmon River area is part of a geologic domain that forms the eastern part of Quesnel terrane in southern British Columbia (Fig. 1). This domain contains most of the Paleozoic rocks that have been included in Quesnel terrane, as well as Middle to Late Triassic sedimentary successions that unconformably overlie the Paleozoic rocks, and Early Jurassic volcanic-sedimentary successions (the Rossland Group and correlatives) that overlie the Paleozoic and Triassic rocks. The boundaries and coherent Mesozoic stratigraphy of this domain have not been fully appreciated because many Triassic rocks in the western part were previously included in the Nicola Group, and the full extent of the Jurassic rocks has become apparent only recently (Beatty et al., 2006; this study). The geologic history implied by relationships within the domain includes pre-Middle Triassic amalgamation of disparate Paleozoic assemblages (Okanagan and Harper Ranch subterranes of Monger et al., 1991); deposition of Middle to Late Triassic rocks unconformably above the Paleozoic rocks; uplift and erosion followed by deposition of Early Jurassic arc-like volcanic and sedimentary rocks (Rossland Group and correlatives).

To the north of the Paleozoic domain, Quesnel terrane is represented by Triassic siliciclastic rocks of the Slocan Group (Fig. 1), which were deposited mainly above pericratonic assemblages of the North American margin (Klepacki and Wheeler, 1985; Thompson et al., 2006). Volcanic rocks correlated with the Rossland Group occur locally above the Slocan Group (Thompson et al., 2006), linking the Paleozoic domain to the Slocan domain by at least the Early Jurassic. Older ties are more tenuous, because the Slocan Group is, for the most part, lithologically distinct from the Triassic rocks of the Paleozoic domain and although the Slocan Group is locally in contact with the Harper Ranch Group (Thompson et al., 2006), these contacts are not demonstrably depositional. However, if the Slocan Group and the Triassic rocks of the Paleozoic domain are linked, they would represent a stratigraphic overlap across pericratonic assemblages of the North American margin and the Paleozoic rocks of Quesnel terrane.

The Middle Triassic to Early Jurassic arc complex that forms most of Quesnel terrane is markedly distinct from the domains to the east, as exemplified by the contrasting Triassic rocks of the Nicola Group (volcanic and volcaniclastic), Slocan Group (slate, siltstone and quartz sandstone), and the Paleozoic domain (limestone and siltstone). However, Nicola rocks mapped 130 to 150 km north-northwest of the Salmon River area show some tentative links, including local exposures of Early Permian rocks, correlated with the Harper Ranch Group, in the central part of the Nicola belt, and a substantial unit of thin-bedded siltstone and quartzose siltstone (Middle to Late Triassic, Meridian Lake succession) that is lithologically similar to the Slocan Group, but is intercalated with coarse-grained volcaniclastic strata of the Nicola Group (Schiarizza et al., 2013; Schiarizza, 2019). These occurrences suggest that the basement to the Nicola Group correlates, at least in part, to rocks in the Paleozoic domain, and that the Slocan Group interfingers with Nicola rocks, as also suggested by Unterschutz et al. (2002).

7. Conclusions

Mesozoic rocks that rest unconformably above the Chapperon Group, previously considered a single Triassic unit, are now known to comprise two different units: a restricted limestone unit with Triassic conodonts; and a more extensive belt of Jurassic siliciclastic rocks (the Salmon River succession) that is tentatively correlated with the Hall Formation (Early Jurassic, Toarcian) of the Rossland Group. The geologic relationships documented near the Salmon River exemplify those in a large geologic domain that forms the eastern part of Quesnel terrane in southern British Columbia (Fig. 1). This domain comprises most of the Paleozoic rocks that have been included in Quesnel terrane, as well as Middle to Late Triassic sedimentary successions that unconformably overlie the Paleozoic rocks, and Early Jurassic volcanic-sedimentary successions (the Rossland Group and correlatives) that overlie the Paleozoic and Triassic rocks.

Acknowledgments

Isato Wada assisted with fieldwork and the collection of samples in 2016. Marghaleray Amini, June Cho, Hai Lin, Dave Newton, and Taylor Ockerman assisted with mineral separation, sample preparation and analyses at PCIGR. Lawrence Aspler reviewed the paper and made suggestions that improved it.

References cited

Beatty, T.W., Orchard, M.J., and Mustard, P.S., 2006. Geology and tectonic history of the Quesnel terrane in the area of Kamloops, British Columbia. In: Colpron, M., and Nelson, J.L., (Eds.), Paleozoic evolution and metallogeny of pericratonic terranes at the ancient pacific margin of North America, Canadian and Alaskan cordillera, Geological Association of Canada, Special Paper 45, pp. 483-504.

Black, L.P., Kamo, S.L., Allen, C.M., Davis, D.W., Aleinikoff, J.N., Valley, J.W., Mundil, R., Campbell, I.H., Korsch, R.J., Williams, I.S., and Foudoulis, C., 2004. Improved $^{206}Pb/^{238}U$ microprobe geochronology by the monitoring of a trace-element-related matrix effect; SHRIMP, ID-TIMS, ELA-ICP-MS and oxygen isotope documentation for a series of zircon standards. Chemical Geology, 205, 115-140.

Bostock, H.S., 1941. Olalla. Geological Survey of Canada, Map 628A; scale 1:63,360.

Campbell, R.B., and Okulitch, A.V., 1973. Stratigraphy and structure of the Mount Ida Group, Vernon (82L), Adams Lake (82M, W1/2) and Bonaparte (92P) map areas. In: Report of Activities, Part A, April to October 1972, Geological Survey of Canada, Paper 73-1, Part A, pp. 21-23.

Coutts, D.S., Matthews, W.A., and Hubbard, S.M., 2019. Assessment of widely used methods to derive depositional ages from detrital zircon populations. Geoscience Frontiers, 10, 1421-1435. <https://doi.org/10.1016/j.gsf.2018.11.002>

Daughtry, K.L., and Thompson, R.I., 2004a. Geology, Westwold, British Columbia. Geological Survey of Canada, Open File 4374, scale 1:50,000.

Daughtry, K.L., and Thompson, R.I., 2004b. Geology, Shorts Creek, British Columbia. Geological Survey of Canada, Open File 4373, scale 1:50,000.

Eggins, S.M., Kinsley L., and Shelley J., 1998. Deposition and element fractionation processes during atmospheric pressure laser sampling for analysis by ICP-MS. Applied Surface Science, 127-129, 278-286.

Friedman, R., Ray, G., and Webster, I., 2002. U-Pb zircon and titanite dating of intrusive rocks in the Heffley Lake area, south-central British Columbia. In: Geological Fieldwork 2001, British Columbia Ministry of Energy and Mines, British Columbia Geological Survey Paper 2002-01, pp. 109-118.

Fyles, J.T., 1990. Geology of the Greenwood-Grand Forks area, British Columbia, NTS 82E/1, 2. British Columbia Ministry of Energy, Mines and Petroleum Resources, British Columbia Geological Survey Open File 1990-25, 19 p., map scale 1:50,000.

Holland, S.S., 1976. Landforms of British Columbia, a physiographic outline. British Columbia Department of Mines and Petroleum Resources, British Columbia Geological Survey Bulletin 48, 138 p.

Höy, T., and Dunne, K.P.E., 1997. Early Jurassic Rossland Group, southern British Columbia: Part I-stratigraphy and tectonics. British Columbia Ministry of Employment and Investment, British Columbia Geological Survey Bulletin 102, 123 p.

Jones, A.G., 1959. Vernon map area, British Columbia. Geological Survey of Canada, Memoir 296, 186 p.

Klepacki, D.W., and Wheeler, J.O., 1985. Stratigraphic and structural relations of the Milford, Kaslo and Slocan groups, Goat Range, Lardeau and Nelson map areas, British Columbia. In: Current Research, Part A, Geological Survey of Canada, paper 85-1A, pp. 277-286.

Ludwig, K.R., 2003. Isoplot 3.09-A geochronological toolkit for Microsoft Excel. Berkeley Geochronology Center, The University of California at Berkeley, Special Publication No. 4.

Mihalynuk, M.G., and Diakow, L.J., 2020. Southern Nicola arc geology. British Columbia Ministry of Energy, Mines and Low Carbon Innovation, British Columbia Geological Survey Geoscience Map 2020-01, 2 sheets, scale 1:50,000.

Monger, J.W.H., and McMillan, W.J., 1989. Geology, Ashcroft, British Columbia. Geological Survey of Canada, Map 42-1989, scale 1:250,000.

Monger, J.W.H., Wheeler, J.O., Tipper, H.W., Gabrielse, H., Harms, T., Struik, L.C., Campbell, R.B., Dodds, C.J., Gehrels, G.E., and O'Brien, J., 1991. Upper Devonian to Middle Jurassic assemblages, Part B, Cordilleran Terranes. In: Gabrielse, H., and Yorath, C.J., (Eds.), Geology of the Cordilleran Orogen in Canada, Geological Survey of Canada, Geology of Canada, No. 4, pp. 281-327.

Mortensen, J.K., Lucas, K., Monger, J.W.H., and Cordey, F., 2017. Synthesis of U-Pb and fossil age, lithogeochemical and Pb-isotopic studies of the Paleozoic basement of the Quesnel terrane in south-central British Columbia and northern Washington state. In: Geoscience BC, Report 2017-1, pp. 165-188.

Nixon, G.T., and Carbno, B., 2001. Whiterocks Mountain alkaline complex, south-central British Columbia: Geology and platinum-group-element mineralization. In: Geological Fieldwork 2000, British Columbia Ministry of Energy and Mines, British Columbia Geological Survey Paper 2001-01, pp. 191-222.

Okulitch, A.V., 1979. Lithology, stratigraphy, structure and mineral occurrences of the Thompson-Shuswap-Okanagan area, British Columbia. Geological Survey of Canada, Open File 637, scale 1:250,000.

Okulitch, A.V., and Cameron, B.E.B., 1976. Stratigraphic revisions of the Nicola, Cache Creek, and Mount Ida groups, based on conodont collections from the western margin of the Shuswap metamorphic complex, south-central British Columbia. Canadian Journal of Earth Sciences, 13, 44-53.

Orchard, M.J., 2000. Report on conodonts and other microfossils, Vernon (82L), 5 samples (2 productive) collected by R.I. Thompson 1997. Geological Survey of Canada, Paleontological Report MJO-2000-14, 3 p.

Paton, C., Hellstrom, J., Paul, B., Woodhead, J., and Hergt, J., 2011. Iolite: freeware for the visualisation and processing of mass spectrometric data. Journal of Analytical Atomic Spectrometry, 26, 2508-2518.

Preto, V.A., 1964. Structural relations between the Shuswap terrane and the Cache Creek Group in southern British Columbia. M.Sc. thesis, The University of British Columbia, 87 p.

Pullen, A., Ibáñez-Mejía, M., Gehrels, G.E., Ibanez- Ibáñez-Mejía, J.C., and Pecha, M., 2014. What happens when n=1000? Creating large-n geochronological datasets with LA-ICP-MS for geologic investigations. Journal of Analytical Atomic Spectrometry, 29, 971-980.

Ray, G.E., and Dawson, G.L., 1994. The geology and mineral deposits of the Hedley gold skarn district, southern British Columbia. British Columbia Ministry of Energy, Mines and Petroleum Resources, British Columbia Geological Survey Bulletin 87, 156 p.

Read, P.B., and Okulitch, A.V., 1977. The Triassic unconformity in south-central British Columbia. Canadian Journal of Earth Sciences, 14, 606-638.

Schiarizza, P., 2017. Ongoing stratigraphic studies in the Nicola Group: Stump Lake-Salmon River area, south-central British Columbia. In: Geological Fieldwork 2016, British Columbia

Ministry of Energy and Mines, British Columbia Geological Survey Paper 2017-1, pp. 17-33.
Schiarizza, P., 2019. Geology of the Nicola Group in the Bridge Lake-Quesnel River area, south-central British Columbia. In: Geological Fieldwork 2018, British Columbia Ministry of Energy, Mines and Petroleum Resources, British Columbia Geological Survey Paper 2019-01, pp. 15-30.
Schiarizza, P., Israel, S., Heffernan, S., Boulton, A., Bligh, J., Bell, K., Bayliss, S., Macauley, J., Bluemel, B., Zuber, J., Friedman, R.M., Orchard, M.J., and Poulton, T.P., 2013. Bedrock geology between Thuya and Woodjam creeks, south-central British Columbia, NTS 92P/7, 8, 9, 10, 14, 15, 16; 93A/2, 3, 6. British Columbia Ministry of Energy, Mines and Natural Gas, British Columbia Geological Survey Open File 2013-05, 4 sheets, scale 1:100,000.
Sláma, J., Košler, J., Condon, D., and Crowley J., 2008. Plešovice zircon-a new natural reference material for U-Pb and Hf isotopic microanalysis. Chemical Geology, 249, 1-35.
Thompson, R.I., Glombick, P., Erdmer, P., Heaman, L.M., Lemieux, Y., and Daughtry, K.L., 2006. Evolution of the ancestral Pacific margin, southern Canadian Cordillera: Insights from new geologic maps. In: Colpron, M., and Nelson, J.L., (Eds.), Paleozoic evolution and metallogeny of pericratonic terranes at the ancient Pacific margin of North America, Canadian and Alaskan cordillera, Geological Association of Canada, Special Paper 45, pp. 433-482.
Travers, W.B., 1978. Overturned Nicola and Ashcroft strata and their relation to the Cache Creek Group, southwestern Intermontane Belt, British Columbia. Canadian Journal of Earth Sciences, 15, 99-116.
Unterschutz, J.L.E., Creaser, R.A., Erdmer, P., Thompson, R.I., and Daughtry, K.L., 2002. North American margin origin of Quesnel terrane strata in the southern Canadian cordillera: Inferences from geochemical and Nd isotopic characteristics of Triassic metasedimentary rocks. Geological Society of America Bulletin, 114, 462-475.
Wiedenbeck, M., Alle, P., Corfu, F., Griffin, W.L., Meier, M., Oberli, F., Quadt, A.V., Roddick, J.C., and Spiegel, W., 1995. Three natural zircon standards for U-Th-Pb, Lu-Hf, trace element and REE analyses. Geostandards Newsletter, 19, 1-23.
Wiedenbeck, M., Hanchar, J.M., Peck, W.H., Sylvester, P., Valley, J., Whitehouse, M., Kronz, A., Morishita, Y., Nasdala, L., Fiebig, F., Franchi, I., Girard, J.P., Greenwood, R.C., Hinton, R., Kita, N., Mason, P.R.D., Norman, M., Ogasawara, M., Piccoli, P.M., Rhede, D., Satoh, H., Schulz-Dobrick, B., Skår, Ø., Spicuzza, M.J., Terada, K., Tindle, K., Togashi, S., Vennemann, T., Xie, Q., and Zheng, Y.F., 2004. Further characterization of the 91500 zircon crystal. Geostandards and Geoanalytical Research, 28, 9-39.

The age and provenance of the Lay Range assemblage provides an indirect record of basement to north-central Quesnellia, British Columbia

Luke Ootes[1, a], Fil Ferri[1, 2], Dejan Milidragovic[3], and Corey Wall[4]

[1] British Columbia Geological Survey, Ministry of Energy, Mines and Low Carbon Innovation, Victoria, BC, V8W 9N3
[2] Retired, 1162 Hadfield Avenue, Victoria, BC, V9A 5N7
[3] Geological Survey of Canada, Vancouver, BC, V6B 5J3
[4] Pacific Centre for Geochemical and Isotopic Research, The University of British Columbia, Earth Sciences Building, Vancouver, BC, V6T 1Z4
[a] corresponding author: Luke.Ootes@gov.bc.ca

Recommended citation: Ootes, L., Ferri, F., Milidragovic, D., and Wall, C., 2022. The age and provenance of the Lay Range assemblage provides an indirect record of basement to north-central Quesnellia, British Columbia. In: Geological Fieldwork 2021, British Columbia Ministry of Energy, Mines and Low Carbon Innovation, British Columbia Geological Survey Paper 2022-01, pp. 31-44.

Abstract

The Lay Range assemblage, the lowest exposed lithostratigraphic unit of north-central Quesnellia, is separated into lower sedimentary and upper mafic tuff divisions. Fossil and field evidence indicates deposition of the lower sedimentary division during the Late Mississippian to Middle Pennsylvanian and of the upper mafic tuff division during the Middle Pennsylvanian to early Permian. A quartz sandstone and polymictic pebble conglomerate from the lower part of the lower sedimentary division yield detrital zircon U-Pb ages between 360 and 290 Ma (Carboniferous to early Permian), with a range of older detrital zircons from ca. 3600 to 890 Ma (Archean and Proterozoic). A small population of zircons ranges from 450 to 390 Ma (n=4; Ordovician to Devonian). The Carboniferous detrital zircons have mostly juvenile εHf(t), indicating that the parental magmas did not interact with older crust. Few zircons are more evolved and were derived from parental magmas that interacted with or melted from crust as old as middle Mesoproterozoic. The combined εHf(t) and trace element compositions of detrital zircon are consistent with formation in a juvenile arc during the Carboniferous. Comparison of Lay Range detrital zircon U-Pb, Hf, and trace element systematics indicate a similar timing of arc magmatism with eastern Stikinia and Wrangellia, but little relationship to ancient North America or Yukon-Tanana terrane. The older detrital zircons (Archean through Paleozoic) were sourced from a fringing landmass, possibly a continental oceanic plateau, that had little to no role in the petrogenesis of the Carboniferous magmas. The spread of ages in the Lay Range assemblage zircon distributions likely records multiple cycles of deposition, uplift, erosion, transport, and sedimentation. One possibility is that the fringing landmass was calved from the Neoproterozoic through Cambrian western North American passive margin.

Keywords: Quesnel terrane, Lay Range assemblage, lower sedimentary division, detrital zircon U-Pb, detrital zircon Hf, detrital zircon trace elements

1. Introduction

The Cordilleran orogen of western North America is a type example of an accretionary orogen, but the origin of many terranes (e.g., Quesnellia and Stikinia) remains enigmatic. Paired U-Pb and Lu-Hf isotopic data from detrital zircon provide otherwise inaccessible insights into the origin of source rocks, particularly those that are poorly preserved or unpreserved (e.g., Beranek et al., 2013; Malkowski and Hampton, 2014; Colpron et al., 2015; Pecha et al., 2016; Romero et al., 2020; Alberts et al., 2021; George et al., 2021; Ootes et al., in press). In many cases, detrital zircons from the lowest stratigraphic unit provide the only, and necessarily indirect, record of pre-existing basement upon which a terrane developed (e.g., Ootes et al., in press).

Quesnellia is one of the easternmost terranes of the Cordilleran orogen, commonly juxtaposed directly against rocks of Ancestral North America (Fig. 1). It consists mainly of a Mesozoic arc complex, represented by Middle Triassic to Early Jurassic volcanic, sedimentary, and intrusive rocks, but locally includes Paleozoic rocks which, in southern British Columbia, are assigned to the arc-like Harper Ranch subterrane and the oceanic Okanagan subterrane (Monger et al., 1991). In north-central British Columbia, Carboniferous to early Permian sedimentary and volcanic rocks, which closely resemble the Harper Ranch subterrane in southern British Columbia, form the basal units of Quesnellia (Monger et al., 1991; Ferri, 1997; Beatty et al., 2006). Subdivided into 'lower sedimentary' and 'upper mafic tuff' divisions (e.g., Ferri, 1997), the Lay Range assemblage has sedimentary features and fossil assemblages that are consistent with a transition from Carboniferous mainly deep-marine sedimentation to early Permian deposition of volcanosedimentary rocks (Ferri, 1997; Ferri et al., 2001).

Presented here are the first detrital zircon U-Pb, Hf, and trace element results from the lower sedimentary division of

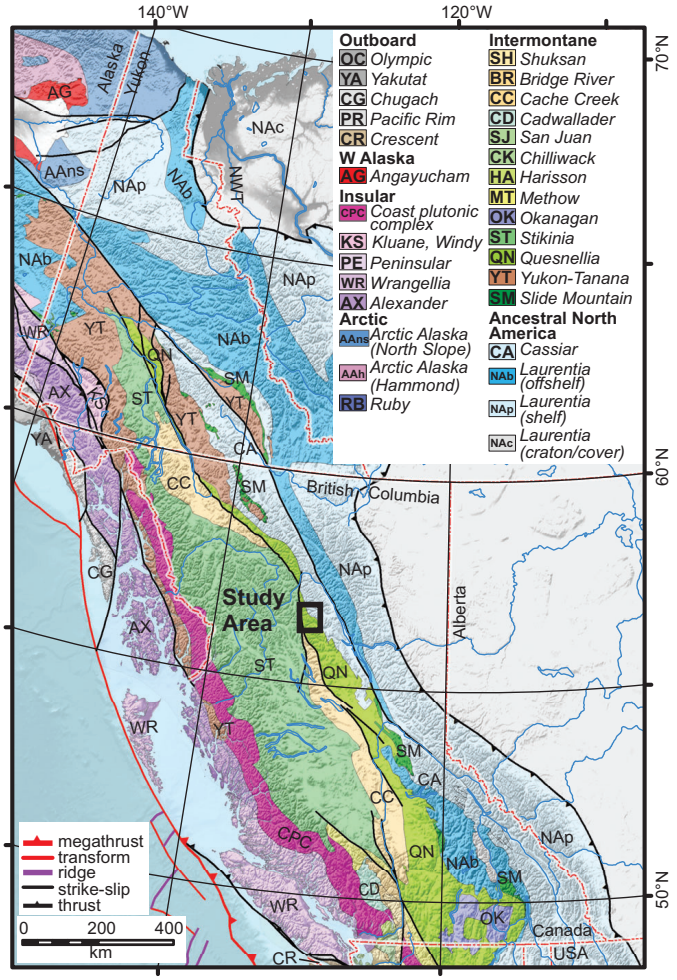

Fig. 1. Terranes of the Cordilleran orogen and location of study. Modified after Colpron (2020).

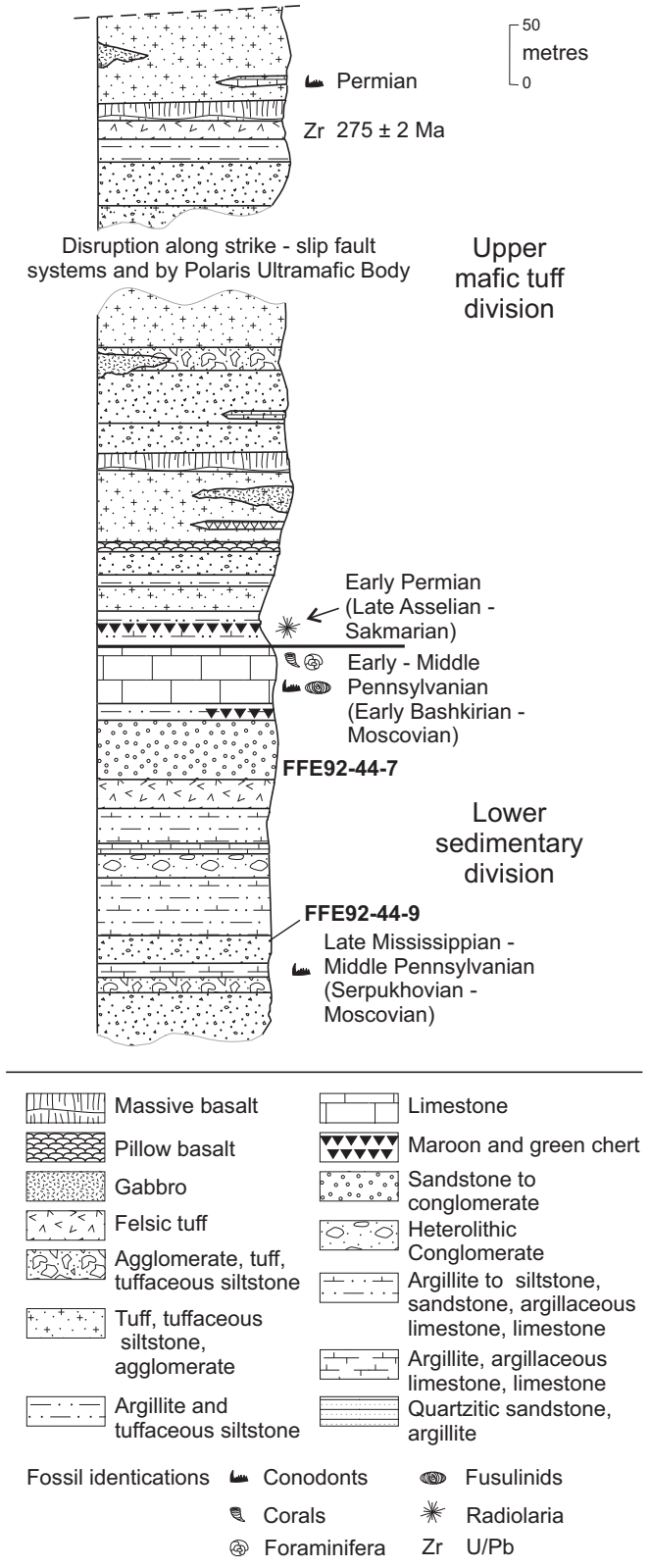

Fig. 2. Composite stratigraphy of the Lay Range assemblage. Modified after Ferri (1997).

the Lay Range assemblage in the Lay Range, which is in the traditional territory of the Tsay Keh Dene Band and Takla Lake First Nation. These results offer insights into the age and antiquity of the crust that Quesnellia developed on and allow direct comparison with similar zircon U-Pb and Hf data from Stikinia, Wrangellia, Yukon-Tanana, and cratonic North America. In its north-central segment, Quesnellia was built on an oceanic basement of juvenile volcanic arc rocks formed adjacent to a continental landmass, possibly a block calved during rifting of the western edge of North American crust covered by Neoproterozoic through Cambrian passive margin deposits.

2. Geology of the Lay Range area

The Lay Range assemblage includes Mississippian to Permian sections of predominantly sedimentary and predominantly volcanic rocks (Roots, 1954; Monger, 1973, 1977; Monger and Paterson, 1974; Ross and Monger, 1978). Ferri (1997, 2000) and Ferri et al. (2001) subdivided the Lay Range assemblage into a ‘lower sedimentary division’ and an ‘upper mafic tuff division’ (Fig. 2). Relationships between the two divisions are

best preserved in a northeasterly overturned anticline in the Lay Range mountains (Figs. 3, 4). The core of this southeast-plunging anticline, exposed across a width of about 1 km, contains the lowest rocks of the lower sedimentary division. These include chert, tuff, and siliciclastic and carbonate rocks that are tightly folded and display a strong cleavage. At the top of this succession is a fossiliferous limestone (Lower to Middle Pennsylvanian) that is overlain and underlain by a distinctive unit of maroon argillite and chert (Figs. 2, 3). This marker can be traced along much of the northeastern limb of the anticline and around its hinge zone. On the southwest limb the marker is repeated by a reverse fault but cut off by northwest-trending (strike-slip?) faults (Fig. 4).

The upper mafic tuff division overlies the maroon marker and consists of >2500 m of tuff, volcanic breccia, and volcanic flows (Figs. 2-4). Although radiolarians (fossil locality F_{21}, Fig. 3) from the base of this division are early Permian (Table 1), contact relationships with distinctive cherts in the underlying lower sedimentary division indicate continuous deposition, suggesting that the base of the upper mafic tuff division is Middle Pennsylvanian (Ferri, 2000; see below). Fossil and U-Pb geochronology from elsewhere in the unit imply that most of the volcanism defined by this unit is Permian. Southwest of the anticline, the upper mafic tuff division is only exposed across strike for 1-2 km because it is truncated by the Lay Range fault (Fig. 4). The northeast limb of the anticline consists of a 4 km-wide panel of overturned upper mafic tuff division rocks, bounded by an overturned syncline that includes the western margin of the Polaris intrusion (Fig. 3).

2.1. Lower sedimentary division

The lower sedimentary division (Figs. 2-4) consists mainly of black and grey argillite and siltstone (Fig. 5), bedded grey chert, thin-bedded arkose and quartz arenite, and chert-pebble conglomerate and breccia. The conglomerates are polymictic (Fig. 5), containing granules to cobbles of varicoloured chert, quartz, argillite, quartzite, carbonate, green tuff, and clinopyroxene-phyric volcanic rock. Less common rocks include fine- to medium-grained white quartz arenite, rhyolitic tuff, shaly or thin-bedded grey limestone, fossiliferous limestone, limy argillite, and green-grey tuffaceous rocks and volcanic sandstones. Minor, small felsic or dioritic intrusions and a narrow serpentinite body are locally in the division.

The top of the division is typically limestone that is up to 75 m thick (Figs. 2, 3). It consists of grey to white, massive to thinly bedded, bioclastic limestone, locally rich in colonial and solitary horn corals, echinoderm, and sponge material, and fusulinaceans and foraminifera (Table 1; F_1 to F_5, F_8 to F_{11}, F_{13} to F_{15}, F_{17} to F_{19} in Figure 3). The limestone is locally dolomitic and contains green tuffaceous layers and nodular masses of red or grey chert. At several localities, the limestone is gradationally underlain and overlain by distinctive packages up to 50 m thick of maroon, cream, and grey, thinly bedded argillite, siltstone, and chert (Figs. 2, 3).

2.2. Upper mafic tuff division

The most distinctive and widespread rocks of the Lay Range assemblage are green to light green and maroon, mafic volcanic rocks of the upper mafic tuff division (Figs. 2-4). The volcanic rocks include tuffs, flows, and volcanic breccias. Interbedded with the mafic volcanic rocks are subordinate green to grey argillite, siltstone, volcanic wacke and conglomerate, felsic tuff, chert, limy siltstone, and limestone. Mafic flows and large clasts commonly contain clinopyroxene and feldspar phenocrysts and amygdules. Whole rock geochemical data support the interpretation that the volcanic rocks were deposited as part of an arc sequence (Ferri, 1997).

2.3. Previous fossil and U-Pb zircon ages

Previous fossil collections and unpublished zircon U-Pb geochronology indicated that the Lay Range assemblage was deposited between the Late Mississippian and Permian (Fig. 2; Table 1). The lower sedimentary division contains Late Mississippian conodonts near the detrital zircon sample locations of this study (Fig. 2; Table 1). The upper limestone of the lower sedimentary division contains Lower to Middle Pennsylvanian (Bashkirian to Moscovian) fusulinids (Fig. 2; Table 1; Ross and Monger, 1978). Other fossils from the lower sedimentary division include corals, foraminifers and fusulinaceans that are Middle Pennsylvanian (Moscovian; Fig. 2; Table 1).

Radiolaria extracted from chert near the base of the upper mafic tuff division indicate it is early Permian (late Asselian to Sakmarian; Fig. 2; Table 1). The chert occurs only a few m above a thin limestone unit that contains Middle Pennsylvanian fusulinids (late Moscovian; Table 1; Ross and Monger, 1978). The contact between the chert and limestone is abrupt but is otherwise unremarkable; given the early Permian age of the chert, it is likely that the underlying limestone is stratigraphically equivalent to the uppermost limestone of the lower sedimentary division. This requires that a reverse fault (possibly a steepened thrust) repeats the lower sedimentary division limestone in this area (Fig. 4). Initially, the abrupt contact between limestone and maroon and green chert was interpreted as an unconformity (Ferri, 1997). However, mapping in the northern Lay Range suggests a gradational contact between limestone and overlying tuffs (Ferri, 2000). This revised interpretation makes the upper mafic tuff division as old as Middle Pennsylvanian. Conodonts are broadly Permian elsewhere in the upper mafic tuff division. The biochronological data are consistent with a 275 ±2 Ma zircon U-Pb age of a felsic tuff unit within the upper mafic tuff division in the Swannell Range (west of the study area; Ferri, unpublished data).

3. Methods

The samples for this study (Table 2) were collected during bedrock mapping (Ferri, 1997; Ferri et al., 2001) and retrieved from the British Columbia Geological Survey archive in 2021. They include a fist-sized quartz-rich sandstone (FFE92-44-7) and a fist-sized polymictic pebble conglomerate (FFE92-44-9;

Table 1. Paleontologic data from the Lay Range assemblage. All samples were taken from the lower sedimentary division except map number F21, which is from the upper mafic tuff division. UTM Zone 10, NAD 27.

Map No.	GSC Loc. No.	Field Number (Collector)	UTM X	UTM Y	Fossils	Taxa	Age	CAI	Remarks
F_1	C-37882	(J.W.H. Monger)	328230	6269750	fusulinids	*Pseudoendothyra* sp. *Profusulinella prisca* (Deprat) *Profusulinella* sp. *Fusulinella* (?) *densa* sp.	late early Moscovian (Kashirian)[1]		
F_2	C-37883	(J.W.H. Monger)	328620	6270370	fusulinids	*Pseudoendothyra timanica* Rauzer-Chernousova *Pseudostaffella gorskyi* Grozdilova and Lebedeva	early Moscovian, probably Kashirian[1]		
F_3	C-37879	(J.W.H. Monger)	328450	6268750	fusulinids	*Profusulinella prisca* sp. (Deprat) *Fusulinella* (?) *densa* sp.	late early Moscovian (Kashirian)[1]		
F_4	C-37880	(J.W.H. Monger)	327500	6269750	fusulinids	*Fusulinella decora* sp.	late Moscovian (Myachkovskian)[1]		
F_5	C-37881	(J.W.H. Monger)	327250	6270100	fusulinids	*Fusulinella decora* sp. *Wedekindellina* cf. *W. uralica* (Dutkevich)	late Moscovian (Myachkovskian)[1]		
F_6	C-37884	(J.W.H. Monger)	328200	6270100	fusulinids	*Profusulinella prisca* (Deprat) *Profusulinella ovata* Rauzer-Chernousova	late early Moscovian (Kashirian)[1]		
F_7	C-37885	(J.W.H. Monger)	327100	6270470	fusulinids	?*Profusulinella prisca* (Deprat) *Fusulinella decora* sp. *Fusulinella concava* sp. *Wedekindellina* cf. *W. uralica* (Dutkevich)	late Moscovian (Myachkovskian)[1]		
F_8	C-37886	(J.W.H. Monger)	325300	6273120	fusulinids	*Profusulinella prisca* (Deprat)	late early Moscovian (Kashirian)[1]		Position assumed to be within upper limestone of lower sedimentary division. UTMs do not correspond to map location as shown within Figure 6 of Ross and Monger (1978).
F_9	C-37887	(J.W.H. Monger)	329250	6268010	fusulinids	*Millerella* sp. *Eostaffella* sp. *Pseudoendothyra timanica* Rauzer-Chernousova *Pseudostaffella paracompressa* Safonova	early Moscovian, probably Kashirian[1]		
F_{10}	C-37888	(J.W.H. Monger)	329990	6267420	fusulinids	*Frofusulinella prisca* (Deprat) *Profusulinella arta* Leontovich *Profusulinella ovata* Rauzer-Chernousova	late early Moscovian (Kashirian)[1]		
F_{11}	C-37889	(J.W.H. Monger)	328800	6267820	fusulinids	*Profusulinella prisca* (Deprat) *Profusulinella ovata* Rauzer-Chernousova	late early Moscovian (Kashirian)[1]		
F_{12}	C-37920	(J.W.H. Monger)	326750	6270530	fusulinids	*Fusulinella decora* sp. *Fusulinella concava* sp.	late Moscovian (Myachkovskian)[1]		
F_{13}	C-189925	CRe92-26-10 (C. Rees)	329350	6268115	corals fusulinaceans	?*Lithostrotion* sp. ?*Dibunophyllum* sp. *Corwenia* sp. *Pseudostaffella* (*Semistaffella*) *variabilis* Reitlinger *Pseudoendothyra* sp. indet. *Eostaffella* sp. indet.	Late Carboniferous, early Bashkirian[2]		
F_{14}	C-189926	CRe92-26-8 (C. Rees)	329540	6268255	sponge foraminifers	*Chaetes* sp. ?*Fusulinella* sp. indet. ?*Wedekindellina* sp. indet.	Late Carboniferous, Moscovian, ?Podolian or younger[2]		The foraminifers in this sample are poorly preserved. They are definitely Moscovian in age, and are probably Podolian or younger (late Moscovian).
F_{15}	C-189924	CRe92-26-9-1 (C. Rees)	329420	6268225	coral fusulinaceans	dibunophyllinid coral indet. *Wedekindellina* sp. cf. *W. matura* Thompson	Late Carboniferous, Podolian (early late Moscovian)[2]		
F_{16}	C-208313	FFe92-44-11 (F. Ferri)	324763	6272330	conodonts, ichthyoliths	ramiform elements (4) *Gnathodus* sp. cf. *G. girtyi* Hass 1953 (6)	Early Carboniferous, Serpukhovian[3]	4.5	

Table 1. Continued.

F_{17}	C-189919	SFD92-41-12 (S.F. Dudka)	328145	6269805	foraminifers	*Fusulinella* sp. indet. ?*Profusulinella* sp. indet.	Late Carboniferous, Moscovian, ?Kashirian (late early Moscovian) or younger[2]		This sample is definitely Moscovian in age, but its exact position within the Moscovian has not been determined.
F_{18}	C-208316	SFD92-41-12 (S.F. Dudka)	338749	6268062	conodonts	ramiform elements (8) *Adetognathus*? sp. (1) *Idiognathodus* sp. (6) *Idiognathoides* sp. (11) *Neogondolella clarki* (Koike 1967) (3)	Late Carboniferous, late Bashkirian-Moscovian[3]	4.5-5.5	
F_{19}	C-189913	SFD92-41-8-3 (S.F. Dudka)	328660	6270250	corals, foraminifers	*Corwenia* sp. *Pseudostaffella* sp. ex. gr. *P. gorskyi* (Dutkevich) *Profusulinella* sp. ex. gr. *P parva* (Lee and Chen) *Eostaffella* sp. ex. gr. *E. oblonga* Ganelina *Pseudoendothyra* sp. indet.	Late Carboniferous, late Bashkirian to early Moscovian[2]		
F_{20}	C-189914	SFD92-41-9 (S.F. Dudka)	328555	6270150	echinoderm columnals	indeterminate	Ordovician to recent[2]		
F_{21}	C-189933	SFD92-46-2-4 (S.F. Dudka)	374940	6269540	radiolarians	*Pseudoalbaillella lomentaria* Ishiga and Imoto *Pseudoalbaillella* sp. cf. *scalprata* Holdsworth and Jones *Quadriremis* sp. *Quinqueremis* sp.	Early Permian; late Asselian to Sakmarian[3]		
F_{22}	C-189916	SFD92-41-14 (S.F. Dudka)	327955	6269540	sponge, echinoderm columnals, foraminifers	*Chaetetes* sp. *Fusulinella* sp.	Late Carboniferous, Moscovian[2]		The sponge, *Chaetetes*, occurs as clasts in this conglomerate and the foraminifers are in the matrix.

[1]C.A. Ross in Ross and Monger (1978)
[2]W.E. Bamber, Foraminifera by L. Rui Institute of Sedimentary and Petroleum Geology, Geological Survey of Canada; internal reports nos. C4-EWB-1993, Rui-4-1993
[3]F. Cordey, Cordilleran Division, Geological Survey of Canada

Table 2. Locations for Lay Range detrital zircon samples. UTM Zone 10, NAD 27.

Sample	UTM X	UTM Y	Rock type
FFE92-44-7	325310	6272547	Sandstone
FFE92-44-9	325148	6272391	Conglomerate

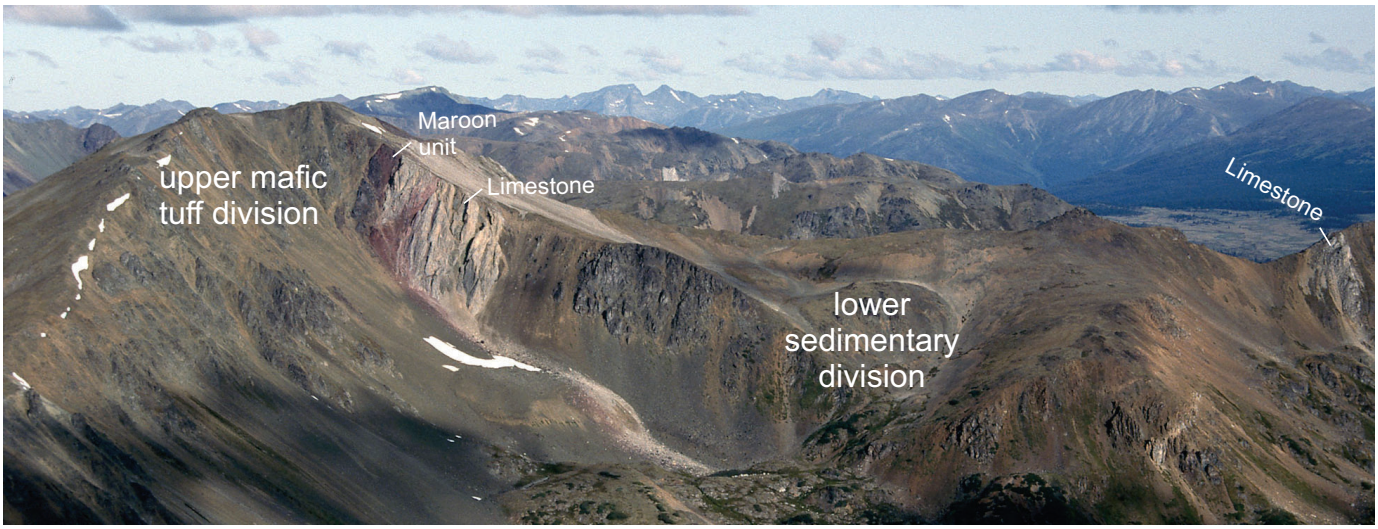

Fig. 3. The lower sedimentary and upper mafic tuff divisions of the Lay Range assemblage. In this northwest view, the lower sedimentary division is preserved in the centre of an anticline outlined by pale grey limestone (labelled) on the left and the far right of the photograph. The distinctive maroon sedimentary rocks ('maroon unit') on the left side of the photo (western limb of the fold) are overlain by the upper mafic tuff division.

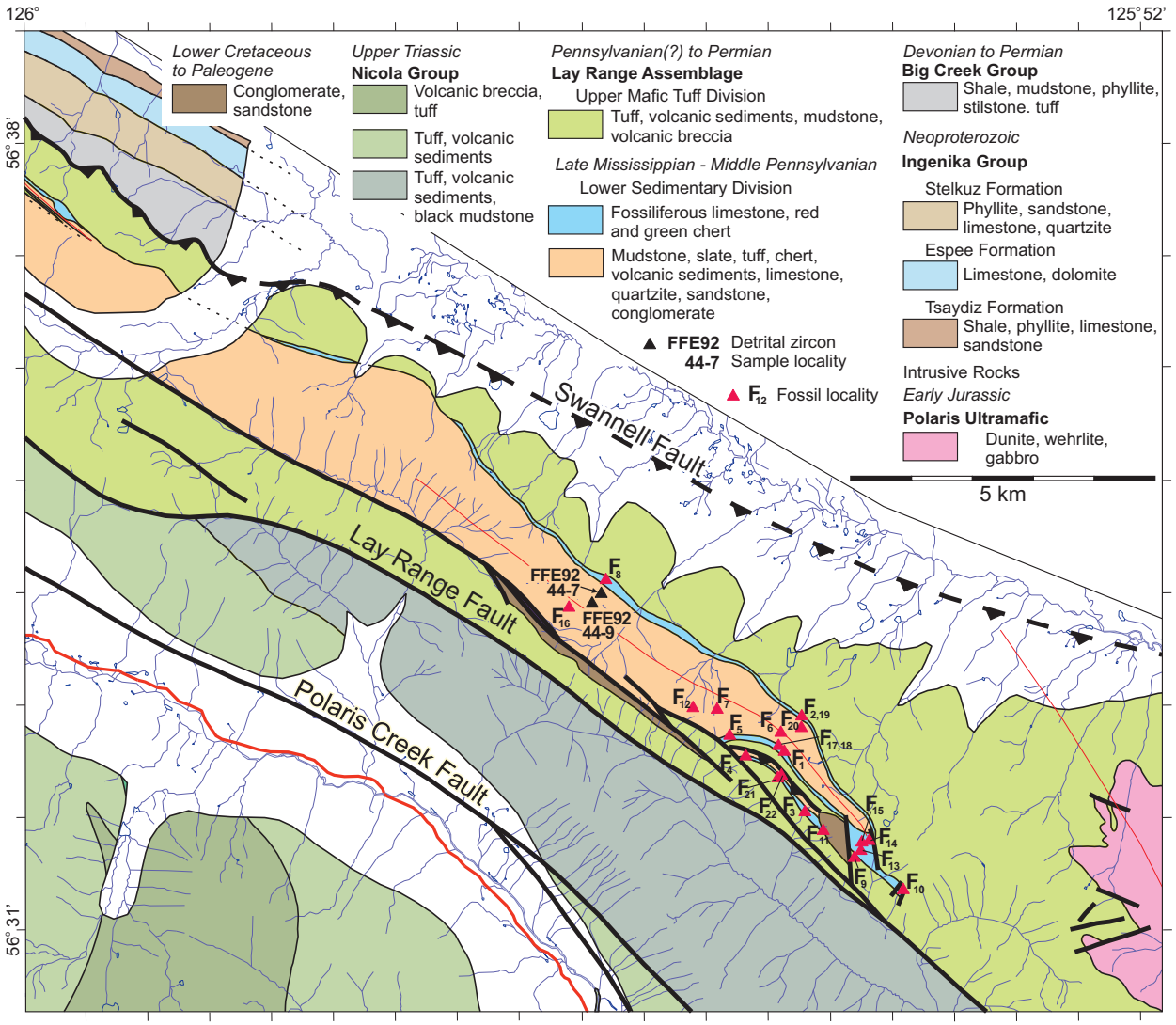

Fig. 4. Generalized geology of the study area. After Ferri (1997, 2000) and Ferri et al. (2001).

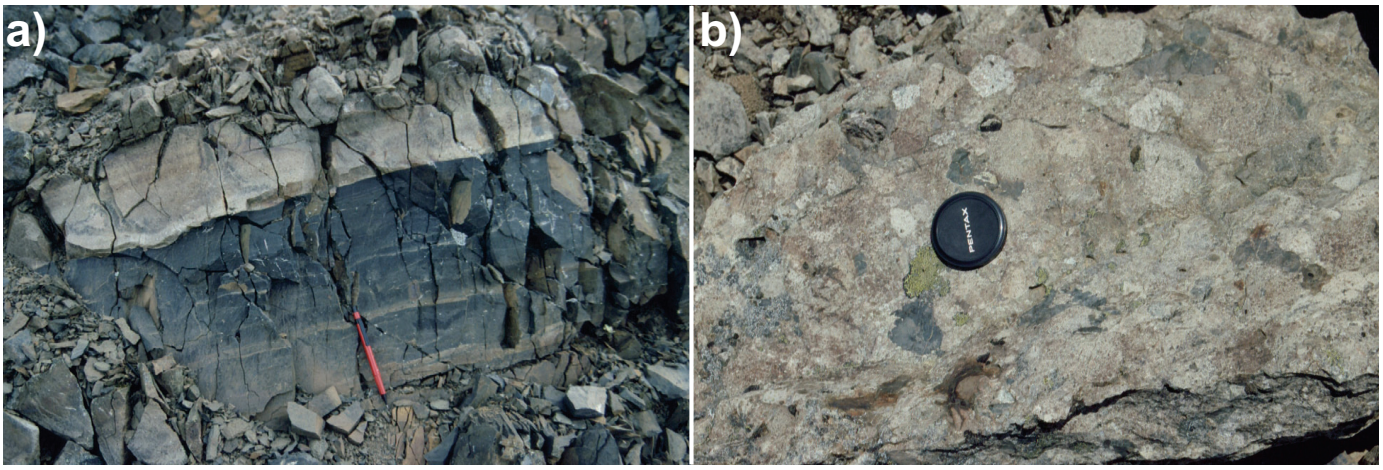

Fig. 5. a) Lay Range assemblage, lower sedimentary division. At bottom of photo, sharp-based Bouma-like fining upward sequences of graded siltstones to dark grey argillites. **b)** Lay Range assemblage lower sedimentary division. Polymictic conglomerate with subangular to subrounded chert and volcanic clasts.

Table 2) from the lower sedimentary division (Figs. 2, 4); full analytical techniques, zircon images, and results are provided in supplementary datafiles (Ootes et al., 2022).

Detrital zircon U-Pb/Hf and trace element analyses were acquired at the Pacific Centre for Isotopic and Geochemical Research at the University of British Columbia. Sample FFE92-44-7 yielded a minor amount of zircon (17) whereas sample FFE92-44-9 yielded a large number (>200) of relatively large zircon crystals (>75 mm) from conventional density and magnetic mineral separation methods. The entire zircon separate was placed in a muffle furnace at 900°C for 60 hours in quartz beakers to anneal minor radiation damage. Annealing enhances cathodoluminescence (CL) emission (Nasdala et al., 2002) and promotes more reproducible inter-element fractionation during laser ablation inductively coupled plasma mass spectrometry (LA-ICPMS; Allen and Campbell, 2012). Following annealing, individual grains were hand-picked and mounted, polished, and imaged by cathodoluminescence (CL) on a scanning electron microscope. From these compiled images, grains with consistent and clear CL patterns were selected for further isotopic analysis.

Analyses were conducted using a Resonetics RESOlution M-50-LR, which contains a Class I laser device equipped with a UV excimer laser source (Coherent COMPex Pro 110, 193 nm, pulse width of 4 ns) and a two-volume cell designed and developed by Laurin Technic Pty. Ltd. (Australia). The laser cell was connected via a Teflon squid to an Agilent 7700x quadrupole ICP-MS. A pre-ablation shot was used to ensure that the spot area on grain surface was free of contamination. Samples and reference materials were analyzed for 36 isotopes: ^{7}Li, ^{29}Si, ^{31}P, ^{43}Ca, ^{45}Sc, ^{49}Ti, Fe (^{56}Fe, ^{57}Fe), ^{89}Y, ^{91}Zr, ^{93}Nb, Mo (^{95}Mo, ^{98}Mo), ^{139}La, ^{140}Ce, ^{141}Pr, ^{146}Nd, ^{147}Sm, ^{153}Eu, ^{157}Gd, ^{159}Tb, ^{163}Dy, ^{165}Ho, ^{166}Er, ^{169}Tm, ^{172}Lu, ^{177}Hf, ^{181}Ta, ^{202}Hg, Pb (^{204}Pb, ^{206}Pb, ^{207}Pb, ^{208}Pb), ^{232}Th, and U (^{235}U, ^{238}U) with a dwell time of 0.02 seconds for each isotope. Pb/U and Pb/Pb ratios were determined on the same spots along with trace element concentration determinations. The settings included a spot size of 34 µm with a total ablation time of 30 seconds, frequency of 5 Hz, fluence of 5 J/cm^2, power of 7.8 mJ after attenuation, pit depths of approximately 15 µm, He flow rate of 800 mL/min, N_2 flow rate of 2 mL/min., and a carrier gas (Ar) flow rate of 0.57 L/min.

Data were reduced using Iolite 4 software using the UPb_Geochronology and TraceElements_IS data reduction schemes (Paton et al., 2011). After detrital zircon U-Pb and trace element analyses, zircon grains were analyzed for Lu-Hf isotopic composition. Lutetium-Hafnium isotope analyses were completed on 32 of the zircons at PCIGR using a New Wave Research, 193nm laser ablation and a Nu Plasma (NP021) MC-ICP-MS on similar CL zones as the U-Pb and trace element analyses. Data were reduced using Iolite 4 software (Paton et al., 2011) using the Hf_Isotopes data reduction scheme (Woodhead et al., 2004). Uncertainties on initial Hf ratios were propagated through Iolite and epsilon Hf values were calculated using full error propagation, outlined by Ickert (2013).

4. Results

Full analytical results upon which the following is summarized are provided as supplementary datafiles (Ootes et al., 2022). Sixteen detrital zircons from the quartz-rich sandstone sample (FFE92-44-7) were analyzed. Fourteen zircons yield Carboniferous dates (ca. 343 to 308 Ma) with a peak distribution at ca. 330 Ma (Figs. 6a, b). The youngest single zircon has a ^{206}Pb/^{238}U date of 306.4 ±10.8 Ma. The youngest statistical population (Coutts et al., 2019; Harriott et al., 2019) has a weighted mean of 325.1 ±4.2 Ma (n=5; MSWD=0.63), interpreted as the maximum deposition age of the sample. Two zircons have concordia ages of 1660 Ma and 1145 Ma. The Carboniferous zircons have a range of εHf(t) from -1.5 to +20.5 (±3.5; error reported as 2σ; Fig. 5a). The single Precambrian zircon analyzed for Lu-Hf isotopic composition has εHf(t) +6.85.

One hundred and nine detrital zircons from the polymictic pebble conglomerate sample (FFE92-44-9) were analyzed.

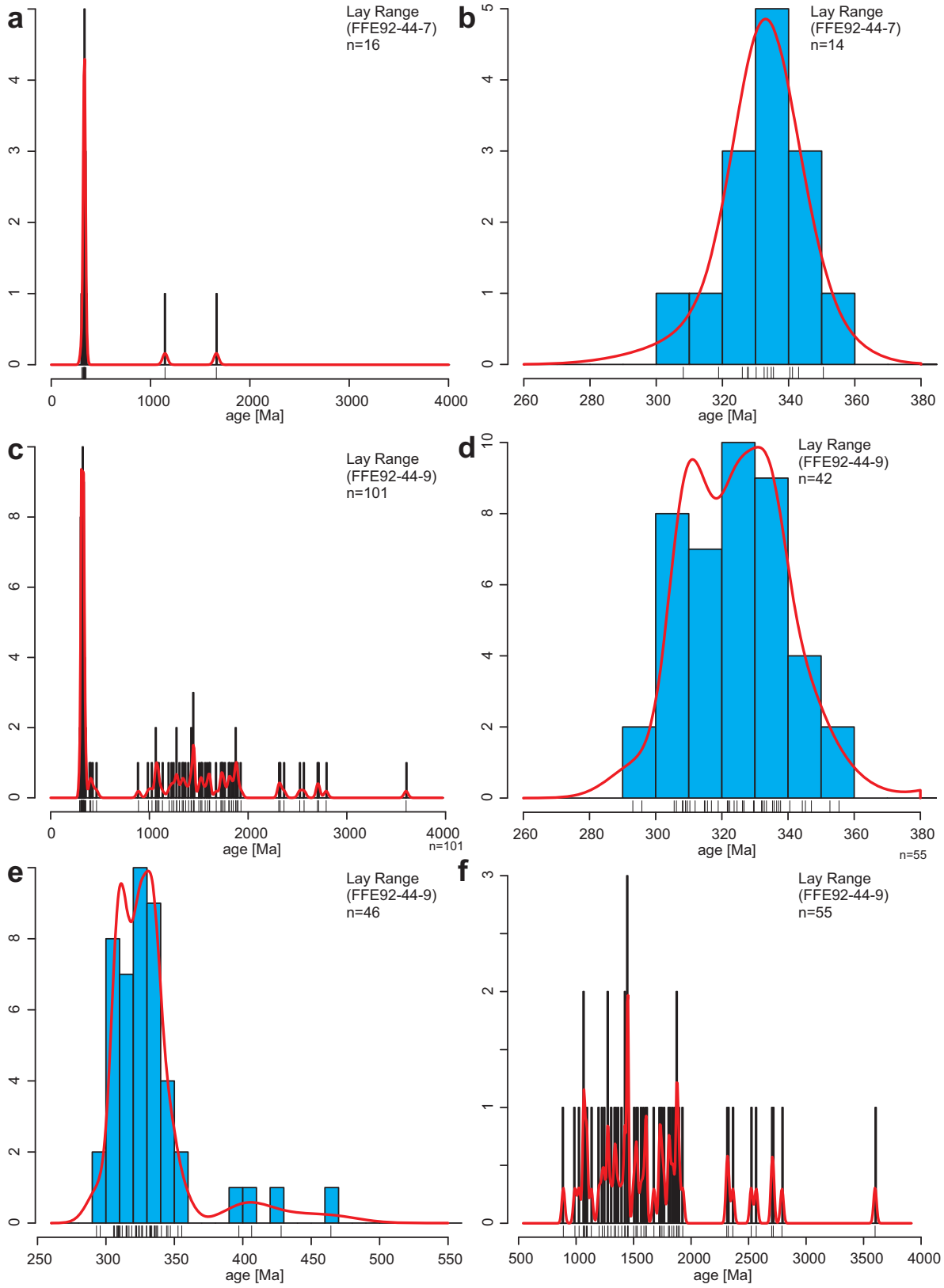

Fig. 6. Kernel density estimation (KDE) plots of detrital zircon U-Pb results from a, b) Lay Range samples FFE92-44-7 (quartz-rich sandstone, several 100 m up section) and c-f) FFE92-44-9 (polymictic conglomerate, near the base of the section). **a)** All results and **b)** Carboniferous results from FFE92-44-7. **c)** All results, **d)** Carboniferous and Permian results, **e)** all Paleozoic results, and **f)** Precambrian results from FFE92-44-9. Histogram bin widths are 10 Ma, corresponding to typical uncertainty of individual zircon U-Pb LA-ICP-MS results. Vertical ticks below the probability curves represent single zircon dates (no uncertainty). Data plotted using IsoplotR (Vermeesch, 2018).

After data reduction, P and Ti concentrations in zircon were used to qualitatively screen the data. Eight analyses were removed from the dataset because they have anomalous trace element values (Figs. 7a-c). One hundred and one analyses remained after trace element screening, indicating that ~7% of laser ablation analyses intersected mineral inclusions of apatite, titanite, or other minerals during analysis. This method independently identified analyses that have REE not typical of zircon (Fig. 7d).

Zircon grains from sample FFE92-44-9 yielded a spectrum of U-Pb ages from 3600 to 290 Ma (Fig. 6c). Forty-two zircons have $^{206}Pb/^{238}U$ dates between 360 and 290 Ma (Carboniferous to early Permian; Fig. 6d). The youngest single zircon has a $^{206}Pb/^{238}U$ date of 293.8 ±12.8 Ma and the youngest statistical population (Coutts et al., 2019; Harriott et al., 2019) has a weighted mean of 309.4 ±2.7 Ma (n=16; MSWD=0.98). This is interpreted as the maximum deposition age of the sample. Four of the zircons have unique (non-overlapping) $^{206}Pb/^{238}U$ dates from 450 to 390 Ma (Paleozoic; Fig. 6e). Fifty-five of the zircons have ages that range from 3600 to 890 Ma (Precambrian; Fig. 6f). The Carboniferous zircons have a range of εHf(t) from -6.1 to +21.9 (Fig. 8). The four Paleozoic and the Precambrian zircons have εHf(t) that range from -12.3 to +13.1 and -30 to +14, respectively.

5. Discussion

5.1. Age of the lower sedimentary division, Lay Range assemblage

Fossils preserved in the lower sedimentary division of the Lay Range assemblage are interpreted to be mostly Middle Pennsylvanian (Moscovian; 315 to 307 Ma; Table 1), but locally are as old as Late Mississippian (Serpukhovian, 331 to 323 Ma). The detrital zircon results are consistent with this interpretation, indicating maximum deposition ages between 310 to 325 Ma (Fig. 6). Nearly half (48%) of the detrital zircons from the lower sedimentary division have Carboniferous ages. A comparison of these ages with those from a quartz arenite sample from the Asitka Group, eastern Stikinia (ca. 290 Ma; Ootes et al., in press), shows strong similarities with central peaks at ca. 320 to 325 Ma (Fig. 9). Two-component finite unmixing yields nearly identical results with age peaks at ca. 315 Ma and 335-340 Ma (Fig. 9). The distribution of Carboniferous U-Pb results is broadly comparable to results reported by Mortensen et al. (2017) from the Okanagan subterrane in southern Quenesllia, British Columbia and Washington State, particularly from the Independence-Bradshaw assemblage, the Oregon claims formation, Ashnola River greywacke, the Barslow assemblage, the Attwood conglomerate, and the Anarchist gneiss; a more detailed statistical comparison cannot be carried out because raw data were not presented.

5.2. Detrital zircon εHf(t) and trace elements, lower sedimentary division

Most εHf(t) values from Carboniferous detrital zircons of the Lay Range assemblage indicate that the parental magmas were derived from a juvenile source and lacked interaction with ancient crust (Fig. 8a). A subpopulation of the Carboniferous zircon (n=6) and three of the older Paleozoic zircons have slightly more evolved εHf(t) (Fig. 8), indicating parental magmas with an enriched (crustal) component as old as middle Mesoproterozoic to Neoproterozoic; there is little evidence that the magmas yielding the Carboniferous zircons interacted with crust older than Mesoproterozoic (Fig. 8b).

Grimes et al. (2015) used igneous zircon trace elements from a number of tectonic environments to define end-member arc, mid-ocean ridge, and ocean island discrimination fields. Using one of these examples (Nb/Yb vs. U/Yb; Fig. 10), the Lay Range assemblage and Asitka Group (eastern Stikinia) Carboniferous detrital zircons overlap the magmatic arc array and mid-ocean ridge basalt (MORB) fields, but consistently plot above the mantle zircon array defined by MORB and ocean islands (Fig. 10; Grimes et al., 2015). Combined, the trace elements and juvenile εHf(t) indicate the zircons crystallized in primitive ocean arc-like magmas.

5.3. Comparison to Yukon-Tanana terrane, eastern Stikinia, and Wrangellia

The Carboniferous detrital zircon population from the Lay Range assemblage is distinct from that of the Yukon-Tanana terrane (Alaska), which has abundant juvenile to highly evolved detrital zircons of Ordovician to Devonian age (Figs. 8b, c; Pecha et al., 2016). In contrast, the U-Pb and Hf systematics of Carboniferous detrital zircons from the Lay Range assemblage overlap those from eastern Stikinia (Asitka Group; Ootes et al., in press) and Wrangellia (Figs. 8c, 11).

5.4. Provenance of detrital zircons in the lower sedimentary division, Lay Range assemblage, and Carboniferous paleogeography

With maximum depositional ages of 325-310 Ma, the lower sedimentary division of the Lay Range assemblage accumulated mainly in a deep-marine depocentre after the start of juvenile arc magmatism. By ca. 300 Ma (the maximum depositional age of the upper mafic tuff division) volcanic tuffs and flows from juvenile arc magmatism overwhelmed background sedimentation. However, although the Lay Range deposits contain mainly Carboniferous detrital zircons, they also contain a high proportion of Precambrian grains (Figs. 6, 8, 11). These grains indicate that erosion of a significantly older crustal landmass also supplied sediment. In addition, although first-cycle quartz sands can be produced by intense tropical weathering of diverse source rocks (e.g., Johnsson et al., 1991), compositionally mature sandstones in the lower sedimentary subdivision are consistent with a continental landmass (Ferri, 1997, 2000). How then can an oceanic arc, with magma sources showing evidence of minimal crustal contribution contain zircons eroded from continental crust?

We suggest that the Lay Range assemblage was deposited peripheral to a continental oceanic plateau (see Ben-Avraham and Nur, 1983) that was isolated in an oceanic setting after

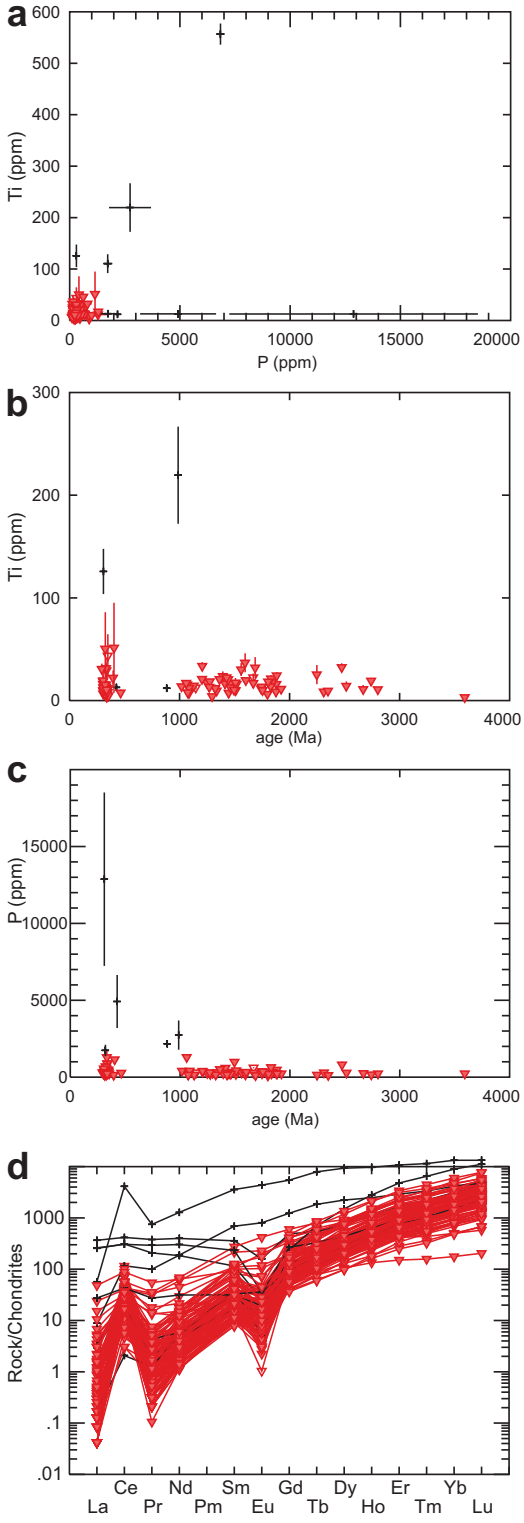

Fig. 7. Zircon trace element plots. **a)** P (ppm) vs. Ti (ppm), **b)** age (Ma) vs. Ti (ppm). **c)** age (Ma) vs. P (ppm). Red triangles are data with 'normal' trace element compositions. Black symbols (n=8) are data that were qualitatively identified as outliers whose trace element contents are inconsistent with zircon alone. **d)** Chondrite-normalized (Sun and McDonough, 1989) rare earth element concentrations in zircon. Black symbols were independently identified by qualitative observations in (a-c) and removed from the dataset. Most black symbols have REE profiles that are inconsistent with zircon (red triangles).

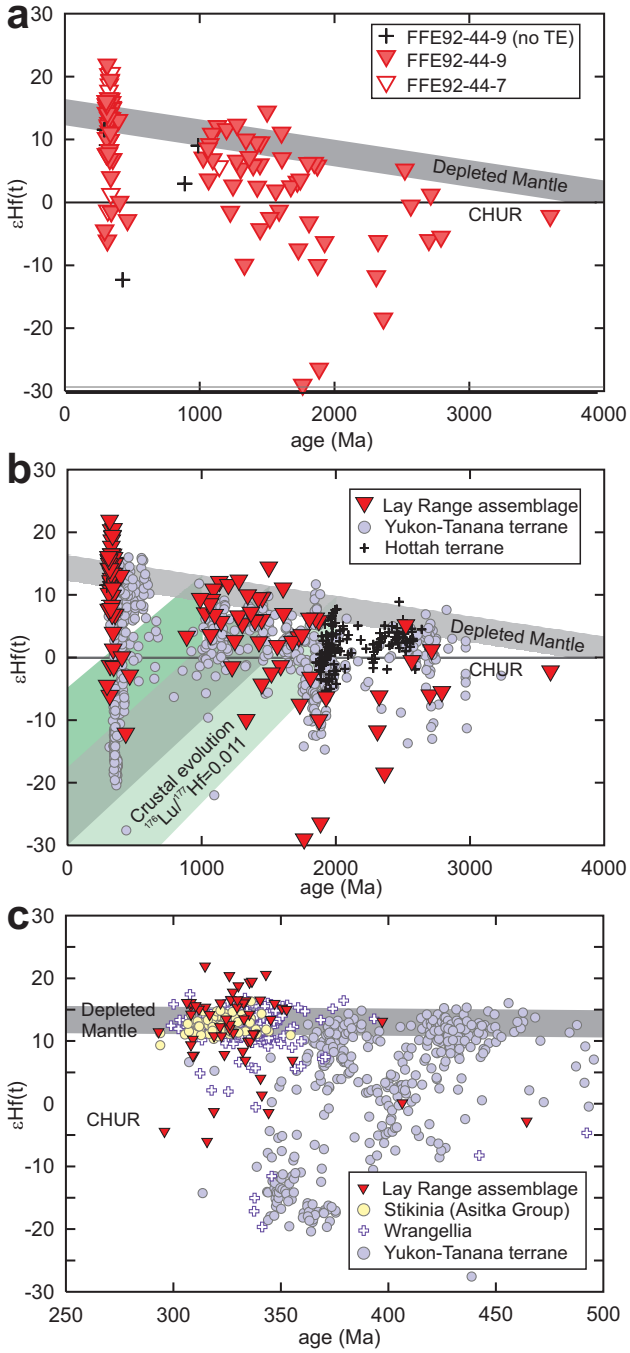

Fig. 8. Zircon U-Pb age vs. εHf(t). **a)** Detrital zircon data from the Lay Range assemblage, this study. Samples labelled 'no TE' do not have trace element data and therefore were not independently screened. Depleted Mantle curve from Chauvel and Blichert-Toft (2001). Chondrite uniform reservoir (CHUR) from Bouvier et al. (2008). **b)** Comparison of data from the Lay Range assemblage to detrital zircon data from the Yukon-Tanana terrane (Alaska; Pecha et al., 2016) and Hottah terrane, which represents >1900 Ma western Laurentia (Davis et al., 2015). Crustal evolution curves calculated using maximum and minimum Depleted Mantle values at 1000, 1500, and 2000 Ma and assuming $^{176}Lu/^{177}Hf$=0.011 (continental crust; Vervoort and Kemp, 2016). **c)** Comparison of Paleozoic detrital zircons from the Lay Range assemblage with data from the Yukon-Tanana terrane (Pecha et al., 2016), Wrangellia (Alberts et al., 2021; Malkowski and Hampton, 2014; Romero et al., 2020), and Stikinia (Ootes et al., in press).

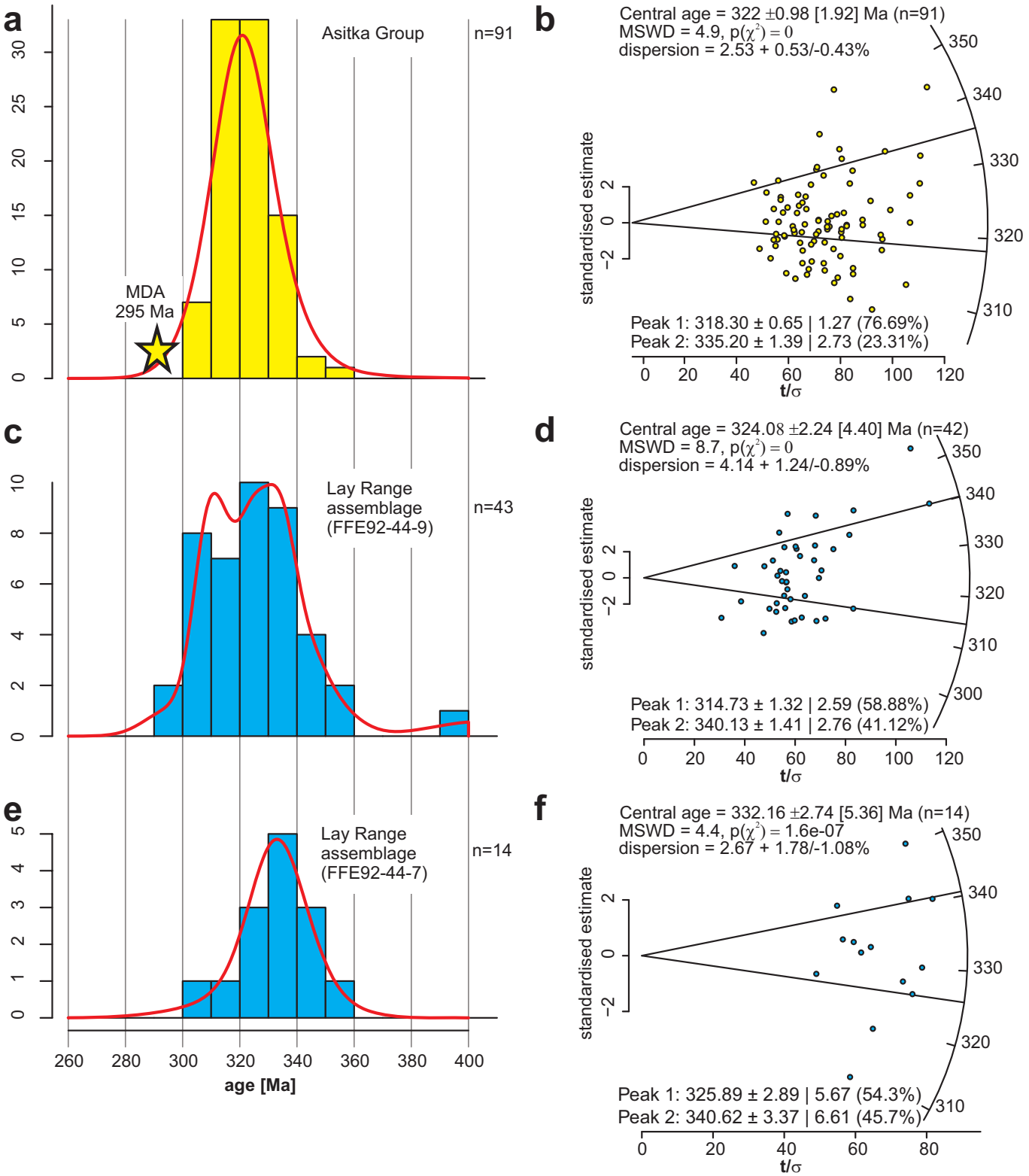

Fig. 9. Comparison of Carboniferous detrital zircon ages from Late Paleozoic rocks of the Asitka Group (eastern Stikinia) and the Lay Range assemblage. **a), c), e)** Kernel density element (KDE) plots. Maximum deposition age (MDA) for the Asitka Group determined from zircon U-Pb dating of rhyolite (Ootes et al., in press). Histogram bin widths are 10 Ma, corresponding to typical uncertainty of individual zircon U-Pb LA-ICP-MS results. **b), d), f)** Radial plots that correspond to the adjacent KDE plot. Shown are central ages (MSWD=mean square of weighted deviates). Peak 1 and Peak 2 are the result of finite unmixing models (two component) for each sample set. Data plotted using IsoplotR (Vermeesch, 2018). Data from eastern Stikinia (Asitka Group) are from Ootes et al. (in press).

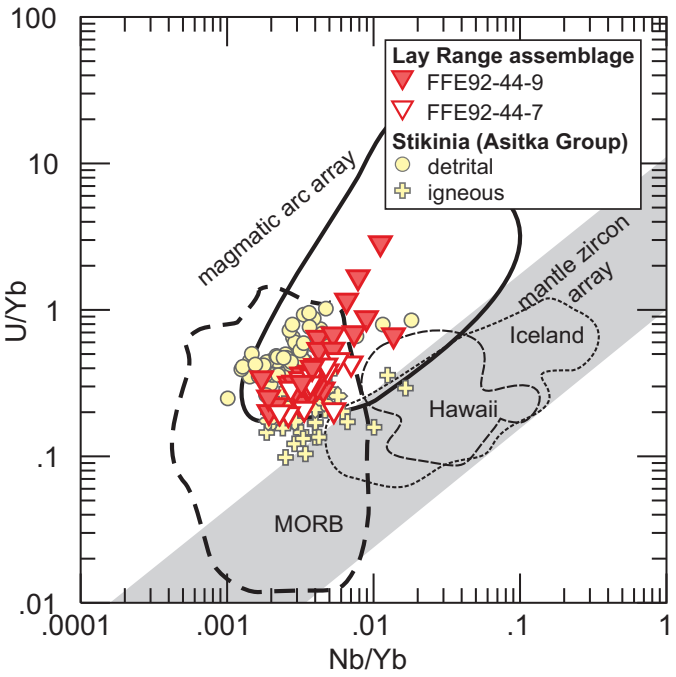

Fig. 10. Zircon Nb/Yb vs. U/Yb discrimination diagram (after Grimes et al., 2015) for detrital zircons from the Lay Range assemblage and detrital and igneous zircons from eastern Stikinia (Asitka Group; Ootes et al., in press). The Lay Range assemblage data consistently plot in the magmatic arc field above the mantle array.

being calved from a continental landmass, although we cannot rule out the possibility that the Lay Range arc developed immediately beyond the edge of a continental substrate (e.g., Ferri, 1997). If this landmass was a fragment of an older Paleozoic arc (e.g., Yukon-Tanana terrane; cf., Ferri, 1997), or a fragment of the Precambrian Shield of the North America, the Lay Range assemblage would contain diagnostic pre-Carboniferous detrital zircon population peaks, which it does not (Figs. 6f, 8a, b). Multi-cyclic reworking of older sedimentary deposits, such as described for example from the Mackenzie Mountains and Shaler supergroups (Rainbird et al., 2017) is an explanation for the range of non-overlapping Precambrian detrital zircons. We suggest that the peripheral landmass contained older sedimentary deposits that were reworked to generate second-cycle (or higher order) zircons found in the Lay Range assemblage.

Although the Mackenzie Mountains and Shaler supergroups (Meso- to Neoproterozoic) were deposited in northwest Laurentia, the characteristic Mesoproterozoic detrital zircons in these rocks (Fig. 12) were foreign to western Laurentian at the time of deposition. Grenville-aged zircons (1.5-1.0 Ga) in the Mackenzie Mountains Supergroup record a pan-continental drainage system that transported detritus eroded from the Grenville orogen more than 5000 km to the southeast (Rainbird et al., 2017). Similar population peaks in Cambrian sandstones of the Paleozoic passive margin reflect recycling of zircons that were liberated by erosion of Mackenzie Mountains Supergroup rocks (Cambrian Type II of Hadlari et al., 2012; Fig. 12).

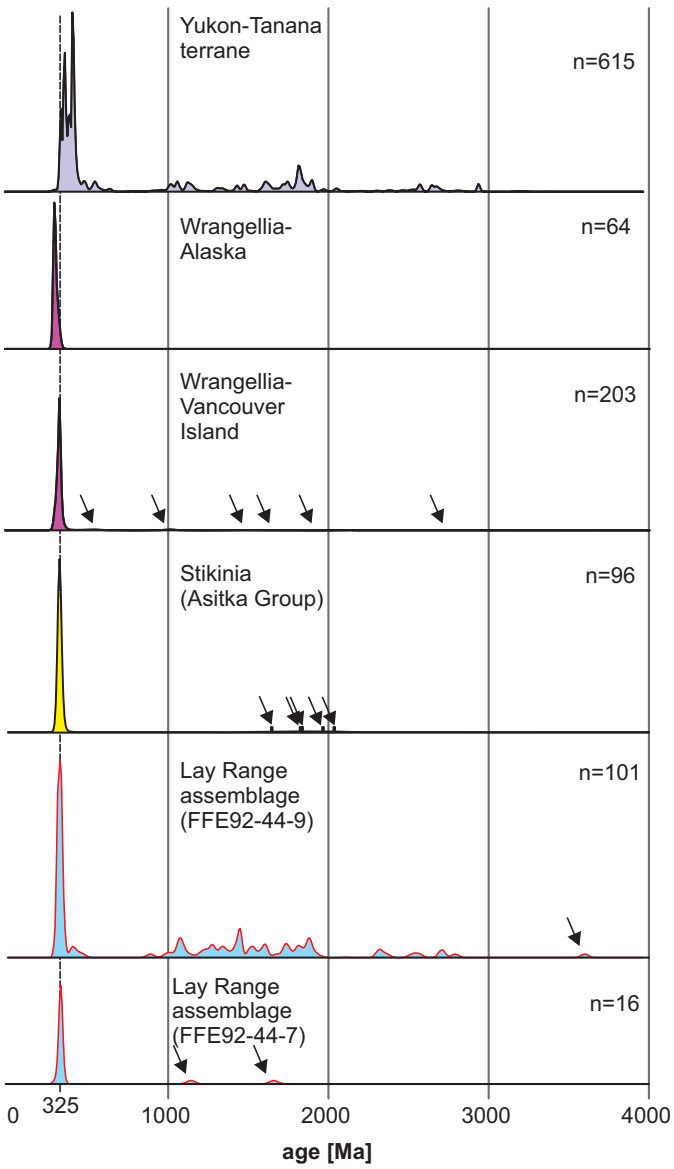

Fig. 11. Kernel density estimation plots of detrital zircon from the Yukon-Tanana terrane (Alaska, Pecha et al., 2016), Wrangellia (Alaska, Romero et al., 2020; Vancouver Island, Alberts et al., 2021), the Asitka Group of eastern Stikinia (Ootes et al., in press), and the Lay Range assemblage (this study). Arrows point to single (non-reproduced) zircon U-Pb results. Dashed vertical line at ca. 325 Ma demarcates the Carboniferous probability peak in each terrane, except Yukon-Tanana, which is older (450 to 350 Ma).

Similar recycling, with multiple episodes of deposition, uplift, erosion, and transport, likely accounts for the broad range of Precambrian detrital zircons in the Lay Range assemblage.

Possibly, Neoproterozoic through Cambrian passive margin deposits on the western margin of North America were the source of the detrital zircons. Importantly, the data (U-Pb and Hf systematics) do not support that erosion of the Yukon-Tanana terrane or Precambrian Shield provided sediment to this part of Quesnellia during the Carboniferous (cf., Ferri, 1997).

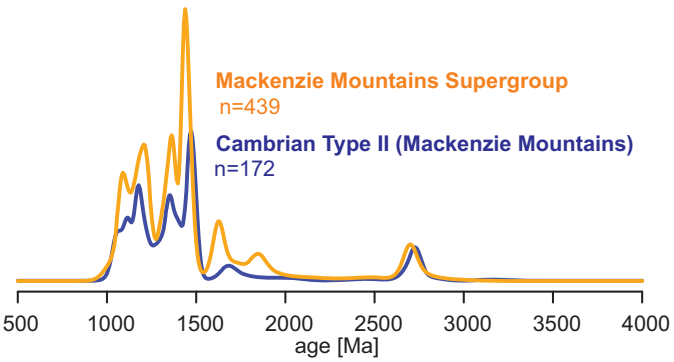

Fig. 12. Example of detrital zircons reworked through multiple sedimentary cycles. Comparison of detrital zircon probability distributions from the Mackenzie Mountains Supergroup (late Mesoproterozoic; Rainbird et al., 2017) and from Cambrian sandstones in the Mackenzie Mountains (Cambrian Type II of Hadlari et al., 2012). The Cambrian Type II sandstones display similar distributions with zircons having been derived from erosion of the Mackenzie Mountains Supergroup. Rather than representing first-cycle derivation from the original source rocks, the Cambrian Type II sandstones contain zircons that were temporarily stored in the Mackenzie Mountain Supergroup.

6. Conclusions

This study reports the biochronology and first detrital zircon U-Pb and Hf results from the Lay Range assemblage, the lowest stratigraphic unit exposed in north-central Quesnellia. Fossil evidence indicates deposition of the lower sedimentary division during the Late Mississippian to Middle Pennsylvanian and the upper mafic tuff division during the Middle Pennsylvanian to Permian. A quartz sandstone and a polymictic pebble conglomerate from the lower part of the lower sedimentary division yield detrital zircon U-Pb dates between 360 and 290 Ma (Carboniferous to early Permian), a range of older detrital zircons from 3600 to 890 Ma (Archean and Proterozoic) and a small population (n=4) from 450 to 390 Ma (Ordovician to Devonian). The εHf(t) and trace element compositions of Carboniferous detrital zircons are consistent with the parental magma having formed in a juvenile arc. Lay Range zircon U-Pb, εHf(t), and trace elements are comparable to those of the Asitka Group (eastern Stikinia) and Wrangellia but have little similarity to those of ancient North America or the Yukon-Tanana terrane. The older detrital zircons (Archean through Paleozoic) may have been sourced from a nearby continental oceanic plateau calved from a larger landmass that had little or no role in the genesis of the Carboniferous magmas. Recycling of zircons temporarily stored in older sedimentary deposits accounts for the large age spread of Precambrian detrital zircons in the Lay Range assemblage. Possibly, the postulated continental oceanic plateau may have rifted from western North American crust covered by Neoproterozoic through Cambrian passive margin deposits.

Acknowledgments

This study is a contribution to the Hogem mapping project by the British Columbia Geological Survey. This is Natural Resources Canada contribution #20210442. Reviews by P. Schiarizza and S. Regan helped improved the manuscript.

References cited

Alberts, D., Gehrels, G.E., and Nelson, J.L., 2021, U-Pb and Hf analyses of detrital zircons from Paleozoic and Cretaceous strata on Vancouver Island, British Columbia: Constraints on the Paleozoic tectonic evolution of southern Wrangellia. Lithosphere, 7866944, 20 p. <https://doi.org/10.2113/2021/7866944>

Allen, C.M., and Campbell, I.H., 2012. Identification and elimination of a matrix-induced systematic error in LA-ICP-MS $^{206}Pb/^{238}U$ dating of zircon. Chemical Geology, 332-333, 157-165. <https://doi:10.1016/j.chemgeo.2012.09.038>

Beatty, T.W., Orchard, M.J., and Mustard, P.S., 2006. Geology and tectonic history of the Quesnel terrane in the area of Kamloops, British Columbia. In Colpron, M., and Nelson, J.L., (Eds.), Paleozoic Evolution and Metallogeny of Pericratonic Terranes at the Ancient Pacific Margin of North America, Canadian and Alaskan Cordillera. Geological Association of Canada Special Paper 45, pp. 483-504.

Ben-Avraham, Z., and Nur, A., 1983. An introductory overview to the concept of displaced terranes. Canadian Journal of Earth Sciences, 20, 994-999.

Beranek, L.P., van Staal, C.R., McClelland, W.C., Israel, S., and Mihalynuk, M.G., 2013. Baltican crustal provenance for Cambrian-Ordovician sandstones of the Alexander terrane, North American Cordillera: evidence from detrital zircon U-Pb geochronology and Hf isotope geochemistry. Journal of the Geological Society, 170, 7-18.

Bouvier, A., Vervoort, J.D., and Patchett, J.P., 2008. The Lu-Hf and Sm-Nd isotopic composition of CHUR: Constraints from unequilibrated chondrites and implications for the bulk composition of terrestrial planets. Earth and Planetary Science Letters, 273, 48-57.

Chauvel, C., and Blichert-Toft, J., 2001. A hafnium isotope and trace element perspective on melting of the depleted mantle. Earth and Planetary Science Letters, 3-4, 137-151.

Colpron, M., 2020. Yukon Terranes-A digital atlas of terranes for the northern Cordillera. Yukon Geological Survey. <http://data.geology.gov.yk.ca/Compilation/2> (accessed April 2021).

Colpron, M., Nelson, J.L., and Murphy, D.C., 2007. Northern Cordilleran terranes and their interactions through time. GSA Today, 17, 4-10.

Colpron, M., Crowley, J.L., Long, D.G.F., Murphy, D.C., Beranek, L., and Bickerton, L., 2015. Birth of the northern Cordilleran orogen, as recorded by detrital zircons in Jurassic synorogenic strata and regional exhumation in Yukon. Lithosphere, 7, 541-562.

Coutts, D.S., Matthews, W.A., and Hubbard, S.M., 2019. Assessment of widely used methods to derive depositional ages from detrital zircon populations. Geoscience Frontiers, 10, 1421-1435. <https://doi.org/10.1016/j.gsf.2018.11.002>

Davis, W.J., Ootes, L., Newton, L., Jackson, V.A., and Stern, R., 2015. Characterization of the Paleoproterozoic Hottah terrane, Wopmay Orogen using multi-isotopic (U-Pb, Hf and O) detrital zircon analyses: An evaluation of linkages to northwest Laurentian Paleoproterozoic domains. Precambrian Research, 269, 296-310. <https://doi:10.1016/j.precamres.2015.08.012>

Ferri, F., 1997. Nina Creek Group and Lay Range Assemblage, north-central British Columbia: remnants of late Paleozoic oceanic and arc terranes. Canadian Journal of Earth Sciences, 34, 854-874.

Ferri, F., 2000. Devono-Mississippian Felsic Volcanism Along the Western Edge of the Cassiar Terrane, North-Central British Columbia. In: Geological Fieldwork 1999, British Columbia Ministry of Energy and Mines, Paper 2000-1, pp. 127-146.

Ferri, F., Dudka, S.F., Rees, C.J., and Meldrum, D.G., 2001. Geology of the Aiken Lake Area north-central B.C. (NTS 94C/5, 6 & 12). British Columbia Ministry of Energy and Mines, British Columbia Geological Survey Geoscience Map 2001-10, scale 1:50,000.

George, S.W.M., Nelson, J.L., Alberts, D., Greig, C.J., and Gehrels, G.E., 2021. Triassic-Jurassic accretionary history and tectonic

origin of Stikinia from U-Pb geochronology and Lu-Hf isotope analysis, British Columbia. Tectonics, 40, e2020TC006505. <https://doi.org/10.1029/2020TC006505>

Grimes, C.B., Wooden, J.L., Cheadle, M.J, and John, B.E., 2015. "Fingerprinting" tectono-magmatic provenance using trace elements in igneous zircon. Contributions to Mineralogy and Petrology, 170. <https://doi:10.1007/s00410-015-1199-3>

Hadlari, T., Davis, W.J., Dewing, K., Heaman, L.M., Lemieux, Y., Ootes, L., Pratt, B.R., and Pyle, L.J., 2012. Two detrital zircon signatures for the Cambrian passive margin of northern Laurentia highlighted by new U-Pb results from northern Canada. Geological Society of America Bulletin, 124, 1155-1168.

Harriott, T.M., Crowley, J.L., Schmitz, M.D., Wartes, M.A., and Gillis, R.J., 2019. Exploring the law of detrital zircon: LA-ICP-MS and CA-TIMS geochronology of Jurassic forearc strata, Cook Inlet, Alaska, USA. Geology, 47, 1044-1048.

Ickert, R.B., 2013. Algorithms for estimating uncertainties in initial radiogenic isotope ratios and model ages. Chemical Geology, 340, 131-138.

Johnsson, M.J., Stallard, R.F., and Lundberg, N., 1991. Controls on the composition of fluvial sands from a tropical weathering environment: Sands of the Orinoco River drainage basin, Venezuela and Columbia. Geological Society of America Bulletin, 103, 1622-1647.

Malkowski, M.A., and Hampton, B.A., 2014. Sedimentology, U-Pb detrital geochronology, and Hf isotopic analyses from Mississippian-Permian stratigraphy of the Mystic subterrane, Farewell terrane, Alaska. Lithosphere, 6, 383-398. <https://doi.org/10.1130/L365.1>

Monger, J.W.H., 1973. The Takla Group near Dewar Peak, McConnell Creek map-area (94D), British Columbia. Geological Survey of Canada Paper 74-1B, pp. 29-30.

Monger, J.W.H., 1977. The Triassic Takla Group in McConnell Creek map-area, north-central British Columbia. Geological Survey of Canada Paper 76-29, 45 p.

Monger, J.W.H., Wheeler, J.O., and Tipper, H.W., et al., 1991. Cordilleran Terranes. In: Gabrielse, H., and Yorath, C.J., (Eds.), Geology of the Cordilleran Orogen in Canada. Geological Survey of Canada, Geology of Canada, 4, 281-327.

Monger, J.W.H., and Paterson, J.A., 1974. Upper Paleozoic and Lower Mesozoic Rocks of the Omineca Mountains. Geological Survey of Canada Paper 74-1A, pp. 19-20.

Mortensen, J.K., Lucas, K., Monger, J.W.H., and Cordey, F., 2017. Synthesis of U-Pb and fossil age, lithogeochemical and Pb-isotopic studies of the Paleozoic basement of the Quesnel terrane in south-central British Columbia and northern Washington state. Geoscience BC, Report 2017-1, pp. 165-188.

Nasdala, L., Lengauer, C.L., Hanchar, J.M., Kronz, A., Wirth, R., Blanc, P., Kennedy, A.K., and Seydoux-Guillaume, A.M., 2002. Annealing radiation damage and the recovery of cathodoluminescence. Chemical Geology, 191, 121-140.

Ootes, L., Milidragovic, D., Friedman, R., Wall, C., Cordey, F., Luo, Y., Jones, G., Pearson, D.G., and Bergen, A., in press. Eastern Stikinia: No place for old basement? Geosphere.

Ootes, L., Ferri, F., Milidragovic, D., and Wall, C., Detrital zircon data from the Lay Range assemblage and Vega Creek succession, north-central Quesnel terrane 2022. British Columbia Ministry of Energy, Mines and Low Carbon Innovation, British Columbia Geological Survey GeoFile.

Paton, C., Hellstrom, J., Paul, B., Woodhead, J., and Hergt, J., 2011. Iolite: freeware for the visualization and processing of mass spectrometric data. Journal of Analytical and Atomic Spectrometry, 26, 2508-2518.

Pecha, M.E., Gehrels, G.E., McClelland, W.C., Giesler, D., White, C., and Yokelson, I., 2016. Detrital zircon U-Pb geochronology and Hf isotope geochemistry of the Yukon-Tanana terrane, Coast Mountains, southeast Alaska. Geosphere, 12, 1556-1574.

Rainbird, R.H., Rayner, N.M, Hadlari, T., Heaman, L.M., Ielpi, A., Turner, E.C., and MacNaughton, R.B., 2017. Zircon provenance data record the lateral extent of pancontinental, early Neoproterozoic rivers and erosional unroofing history of the Grenville orogen. Geological Society of America Bulletin, 129, 1408-1423.

Romero, M.C., Ridgwah, K.D., and Gehrels, G.E., 2020. Geology, U-Pb Geochronology, and Hf isotope geochemistry across the Mesozoic Alaska Range Suture Zone (South-Central Alaska): Implications for Cordilleran collisional processes and tectonic growth of North America. Tectonics, 32. <https://doi:10.1029/2019TC005946>

Roots, E.F., 1954. Geology and mineral deposits of Aiken Lake map area, British Columbia. Geological Survey of Canada, Memoir 274, 246 p.

Ross, C.A., and Monger, J.W.H., 1978. Carboniferous and Permian Fusulinaceans from the Omineca Mountains, British Columbia. In: Donnelly, V., (Ed.), Contributions to Canadian Paleontology. Geological Survey of Canada Bulletin 267, pp. 43-63.

Sun, S.S., and McDonough, W.F., 1989, Chemical and isotopic systematics of oceanic basalts: implications for mantle composition and processes. In: Saunders, A.D., and Norry, M.J., (Eds.), Magmatism in the Ocean Basins. Geological Society, London, Special Publication 42, 313-345.

Vermeesch, P., 2018, IsoplotR: a free and open toolbox for geochronology: Geoscience Frontiers, 9, 1478-1493.

Vervoort, J.D., and Kemp, A.I.S., 2016. Clarifying the zircon Hf isotope record of crust-mantle evolution. Chemical Geology, 425, 65-75.

Woodhead, J., Hergt, J., Shelley, M., Eggins, S., and Kemp, R., 2004. Zircon Hf-isotope analysis with an excimer laser, depth profiling, ablation of complex geometries, and concomitant age estimation. Chemical Geology, 209, 121-135.

Geology and geochemistry of the Kamloops Group (Eocene) in its type area, Kamloops, British Columbia

Nancy Van Wagoner[1, a] and Luke Ootes[2]

[1] Thomspon Rivers University, Department of Physical Sciences, Kamloops, BC, V2C 0C8
[2] British Columbia Geological Survey, Ministry of Energy, Mines and Low Carbon Innovation, Victoria, BC, V8W 9N3
[a] corresponding author: nvanwagoner@tru.ca

Recommended citation: Van Wagoner, N., and Ootes, L., 2022. Geology and geochemistry of the Kamloops Group (Eocene) in its type area, Kamloops, British Columbia. In: Geological Fieldwork 2021, British Columbia Ministry of Energy, Mines and Low Carbon Innovation, British Columbia Geological Survey Paper 2022-01, pp. 45-62.

Abstract

The city of Kamloops is the type locality of the eponymous Kamloops Group, a package of early Eocene (ca. 52 Ma) volcanic and lesser sedimentary rocks. In its type area, the Kamloops Group is divided into the Tranquille Formation and the overlying Dewdrop Flats Formation, each of which is separated into a number of members. Field, petrographic, and whole rock major, trace, and rare earth element data indicate that many members have comparable compositions and volcanic facies whereas others differ at different geographic locations. This difference may reflect that different locations may have been fed by different feeder vents. The volcanic rocks range from basaltic andesite to dacite; minor rhyolite occurs west of the type area in the Mount Savona Formation. The most common rock type is andesite and although some andesites have high-Mg and adakite-like geochemical features (high Sr/Y, La/Yb) these terms should not be used to imply the type of mantle contribution to this volcanic pile (e.g., slab melting). Rather, petrographic and geochemical evidence support that some of these rocks were derived from garnet-free mantle melts that mingled with garnet-free lower crust. The geochemical features are consistent with amphibole, pyroxene, and plagioclase control resulting from mantle melts mixing with lower crust.

Keywords: Kamloops Group, Eocene, volcanism, petrography, geochemistry

1. Introduction

The Kamloops Group (Eocene) of south-central British Columbia forms a portion of a discontinuous belt of graben-fill volcanic and sedimentary rocks that extends from Challis, Idaho to eastern Alaska (Fig. 1). In British Columbia, this belt overlies older accreted terranes of the intermontane region and the edge of Ancestral North America (Fig. 1; Nelson et al., 2013). Outcropping in spatially separated areas, rocks of the belt have been referred to as the Sloko Group (includes Bennet Lake and Mount Skukum volcanic complexes) and the Endako, Ootsa Lake, Kamloops, Princeton, and Penticton groups (e.g., Ickert et al., 2009; Fig. 1). The available radiometric age data indicate that volcanism occurred between 56 and 46 Ma (e.g., Ickert et al., 2009; Bordet et al., 2014).

Although the timing of Kamloops Group volcanism coincides with major global tectonic change including mantle plumes, ridge subduction, and continental collision (e.g., Gaina and Jacob, 2018) and climate change (e.g., Zachos et al., 2001), the response and/or contribution of volcanism remains unknown. In addition, the tectonic drivers of the volcanism remain controversial (Breitsprecher et al., 2003; Haeussler et al., 2003; Morris and Creaser, 2003; Bordet et al., 2014; Dostal et al., 2019; Stern and Dumitru, 2019). The Kamloops Group also appears to be underexplored for mineral deposits. For example, although an epithermal bedrock deposit was suggested as the source of placer gold in the Tranquille River and Watching Creek (Knight and McTaggart, 1988; Chapman and Mileham, 2016), which run through the type area of the Kamloops Group, such a deposit remains undiscovered. Low-sulphidation epithermal Au-Ag deposits are known in other areas of Eocene volcanism including the Skukum volcanic complex, Yukon (Love et al., 1998), the Camelsfoot Range in southern British Columbia (Blackdome mine; Schroeter, 1987), in the southern boundary region of British Columbia (Dufresne, 2015; Höy et al., 2021), and in the Republic and Toroda grabens of the Colville Group in Washington State (Ashley et al., 1990). Non-metallic mineral deposits commonly associated with Eocene rocks in southern British Columbia include coal, diatomaceous earth, kaolinite and bentonite, industrial zeolites, precious opals, and aggregates (Simandl et al., 1996; Read, 2000; Northcote, 2022).

We initiated this study, comprising bedrock mapping, geochemistry, and geochronology, to provide an understanding of the volumes, duration, and architecture of volcanism in the Kamloops Group. The volcanic and structural framework will also help assess the potential for mineralization, in particular for epithermal mineral deposits. This report presents petrographic data and summarizes geochemical data from the Kamloops Group type area, which is in the lands of the Tk'emlúps te Secwépemc First Nation, in Secwepemcúlucw, the traditional territory of the Secwépemc.

2. Study area

The type area of the Kamloops Group covers approximately 23 by 18 km (~400 km^2) near Kamloops (Fig. 2; Ewing,1981a, b, c, 1982; Van Wagoner, et al., 2021a). In the type area, the

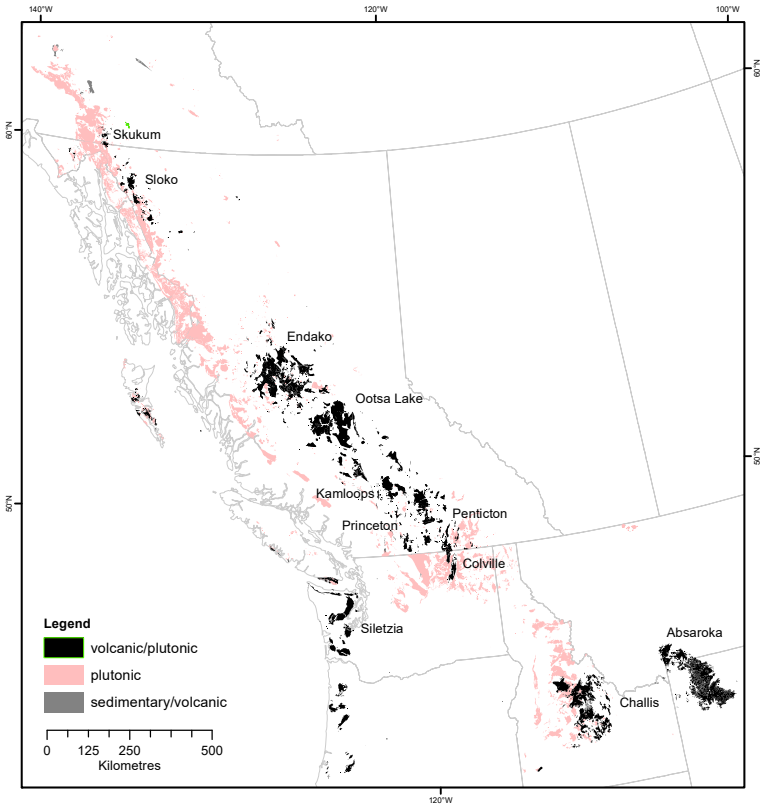

Fig. 1. Distribution of early Eocene (56-46 Ma) volcanic and plutonic complexes in the Cordilleran orogen of western Canada and northwest United States.

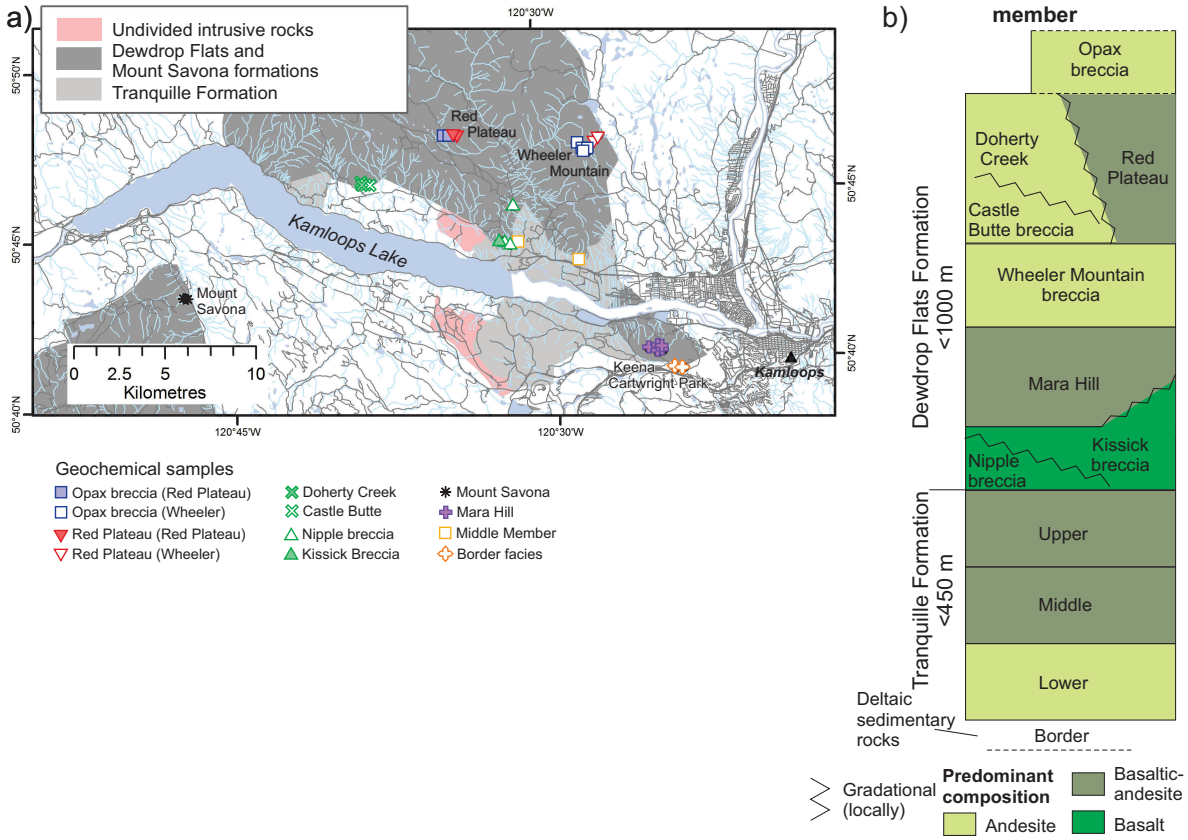

Fig. 2. a) Geological map of volcanic and lesser sedimentary rocks of the Kamloops Group, simplified after Ewing (1982). **b)** Generalized stratigraphy of the Kamloops Group (simplified after Ewing, 1981a).

rocks overlie the Nicola Group (Triassic) and are bounded on all but the north side by Nicola Group exposures. To the north, the Kamloops Group rocks continue outside the type area, forming a rectangular block that is ~25 by 16 km. For comparison with other volcanic complexes, Crater Lake (Oregon) has a diameter of ~9 km, the base of Mt. Shasta (California) has a diameter of ~10 km, and the Long Valley Caldera (California) is ~32 by 16 km (~500 km^2).

Ewing (1981a, b) divided the Kamloops Group in its type area into the lower Tranquille and the upper Dewdrop Flats formations, along with a number of informal members (Fig. 2b). The age relationships between the formations and members remains uncertain because most volcanic units are laterally discontinuous, contact relationships are rarely exposed, and volcanic facies (e.g., hyaloclastite) are not diagnostic of a particular member and are repeated throughout the sequence. In addition, some of the members have different mineralogical and geochemical characteristics at different locations.

The Kamloops Group volcanic rocks were deposited in subaerial to lacustrine environments. Subaqueous facies include pillowed flows, pillow breccias, and hyaloclastites. Interbedded with these subaqueous rocks, and more abundant near the top of the sequence, are subaerial pahoehoe and ‘A’ā flows with well-developed autobreccias, and cryptodomes with brecciated margins (Ewing 1980, 1981a, b, c, 1982; Van Wagoner et al., 2021a). Individual flows are up to several m thick, and flow sequences are up to about 600 m thick (Ewing, 1981a). Pyroclastic deposits are primarily phreatic and phreatomagmatic. Moderately to highly welded felsic tuffs are interbedded with lacustrine shales.

3. Description of sampled units

Samples were collected from north of Kamloops Lake, at Kenna Cartwright Park in the city of Kamloops, and at Mount Savona, which is 7.5 km southeast of the town of Savona and 30 km west of the Kamloops Group type area (Fig. 2). Petrographic details are summarized in Table 1.

3.1.Tranquille Formation

The Border facies (Fig. 2b) was interpreted by Ewing (1981a, b) to be at the base of the Tranquille Formation. It is exposed in the northern portion of Kenna Cartwright Park where it is in fault contact with the Kissick breccia (Fig. 2). There, the Border facies includes lenses of altered ash (bentonite), massive flows, hyaloclastite, and a reversely graded andesitic tuff breccia, interpreted as a phreatomagmatic airfall deposit (Figs. 3a-c; Van Wagoner et al., 2021a). These flows typically contain microcrysts of plagioclase and differ from other flows in the sequence by a paucity of mafic phenocrysts and pervasive alteration of plagioclase to clay minerals.

The middle member was sampled at two localities north of Kamloops Lake and is characterized by large compact pillowed flows that grade vertically and laterally to pillow breccias and hyaloclastite (Fig. 3d; Van Wagoner et al., 2021a).

3.2. Dewdrop Flats Formation

North of Kamloops Lake, the Nipple breccia forms a belt about 3.5 by 1.5 km that is the remnant of a phreatomagmatic cone and associated flows (Fig. 2). It is thickest in the northern part of the exposure where it forms a cone of vesicular to scoriaceous pyroclasts, representing a vent area (Fig. 4a). Flows from this area thin to the south. These rocks have large phenocrysts (up to 3-4 mm) of olivine, pyroxene, ±plagioclase and contain the freshest olivine in the study area (Fig. 4b).

The Kissick breccia is the name given to andesitic breccias that occur throughout the central part of the type area. These include a variety of hyaloclastite breccias, as well as breccias that formed by phreatic and phreatomagmatic eruptive processes (Van Wagoner et al., 2021a). At Kenna Cartwright Park, the Kissick breccia forms a ridge of phreatomagmatic breccias that are cored by feeder dikes and plugs (Fig. 4c), whereas at a locality north of the Kamloops Lake, where it was sampled, the unit forms the brecciated margin of a dome (Figs. 4d, e; Van Wagoner et al., 2021a).

The Mara Hill member at Kenna Cartwright Park forms a series of subaerial pahoehoe lava flows. These flows are generally 1.5 to 3 m thick but thin to anastomosing pahoehoe toes that are 3 to 20 cm thick with well-defined chill margins. These flows are distinguished from others in the type area by flow top features that include small tumuli, inflation cavities, and lava tubes (Fig. 5a) and a lack of flow-top autobreccias.

The Castle Butte breccia comprises basaltic-andesite vesicular flows and flow breccias (Fig. 5b). Within the Castle Butte breccia is a discontinuous lens of water-lain shale and sandstone beds, overlain by a 5 m thick, vaguely bedded felsic phreatomagmatic, crystal-lithic-vitric lapilli tuff, which in turn is overlain by hyaloclastite. The tuff beds are internally massive, moderately welded (Figs. 5c-f), and are the most felsic units sampled from the type area.

The Doherty Creek member comprises a series of ‘A’ā flows, flow breccias, and hyaloclastite breccias (Fig. 6a). These rocks are mineralogically similar to the Nipple breccia except that most of the olivine is entirely altered to smectite ±iddingsite and oxides (Figs. 6b-d).

The Red Plateau member was investigated on Red Plateau and on Wheeler Mountain. In both areas, the Red Plateau member is a series of ‘A’ā flows and flow breccias, but each location is mineralogically distinct. On Wheeler Mountain, the member comprises basaltic to basaltic andesite flows, flow breccias, and hyaloclastic breccias that are commonly plagioclase-phyric and rarely clinopyoxene-phyric (Figs. 7a, b). In contrast, at Red Plateau the member is more intermediate in composition (basaltic andesites and andesites) and includes hornblende as a phenocryst and microcryst phase, comprising up to about 5% in one sample (Fig. 7c). In addition, the rocks at Red Plateau typically show extensive textural evidence for complex magma chamber processes, and the only equilibrium phase appears to be clinopyroxene microcrysts. Plagioclase phenocrysts commonly have zoned, unaltered cores, surrounded by a coarse- to fine-sieve texture or dusty zone followed by an overgrowth

Table 1. Petrographic description of units sampled for geochemistry.

Formation	Member	Location	Rock type and volcanic features	Petrography
Mount Savona		Mount Savona	Rhyolitic flows and pyroclastic flows and airfall deposits	Lithic-vitric-crystal tuff with juvenile tuff fragments (to 4 cm) in a matrix of crystal vitric tuff containing 1% blocky shards and broken microlites of sanidine. The tuff fragments are similar to the matrix, but also contain compacted pumice forming a eutaxitic texture. The flow is sparsely feldspar (5%), hornblende- and biotite-phyric (3%), and flow banded due to alignment of feldspar phenocrysts.
Dewdrop Flats	Opax breccia	Red Plateau	Andesitic flow breccias and flows	Sparsely to highly vesicular. Sparsely plagioclase-phyric with <5% pyroxene and pseudomorphs of olivine microcrysts. Clinopyroxene microcrysts are euhedral to subhedral and commonly zoned. Plagioclase phenocrysts are anhedral with sieve textures, embayed edges, or rounded. Groundmass plagioclase microlites form trachytic texture.
		Wheeler Mountain	Andesitic to dacitic vesicular flow and an in situ vitric breccia	The flow is vesicular (25%), with rare skeletal plagioclase and clinopyroxene microlites in glassy to felty cryptocrystalline groundmass of plagioclase and acicular opaques with interstitial glass and clinopyroxene. The breccia is petrologically identical but is glassy and non-vesicular. Angular fragments <1 mm to several cm, commonly with oxidized rims. The rims and some entire fragments are composed of isotropic volcanic glass that contains microlites of feldspar and mafic minerals.
	Red Plateau	Red Plateau	Basaltic andesite to andesitic 'A'ā flows and flow breccias	Flows predominantly hornblende- (5%) and plagioclase- (10-15%) phyric; rare olivine (euhedral to subhedral to 0.25 mm (<1%) pseudomorphed by calcite and clay minerals. Clinopyroxene a microcryst and groundmass phase. Larger microlites are euhedral to anhedral and locally rimmed by corona of smaller crystals. Matrix glassy to hyalo-ophitic, with glass and pyroxene filling spaces between felty to trachyitic network of plagioclase microlites. In one flow, groundmass with microphenocryst beads primarily of euhedral to subhedral pyroxene and droplets and crystals of opaques. One 'A'ā flow autobreccia sample scoriaceous with opal filling the vesicles.
		Wheeler Mountain	Basaltic andesite 'A'ā flows and flow breccias	Flows are plagioclase-phyric and rarely clinopyroxene-phyric. Plagioclase phenocrysts (3-5%) are 0.3 to 3 mm, embayed, zoned, and contain melt inclusions. The groundmass is hypocrystalline with microlites of skeletal to subhedral plagioclase forming a moderate trachytic texture. Minor interstitial pyroxene, and <1% opaque minerals.
	Doherty Creek	North of Kamloops Lake	Basaltic andesite flows, flow breccias, and hyaloclastite breccia	Flows and flow breccias with 1-3mm euhedral-subhedral clinopyroxene (~7%), up to 0.5 mm euhedral to anhedral olivine phenocrysts (5%), and 0.5-1.5 mm broken and deformed plagioclase phenocrysts. The groundmass is hypocrystalline with microlites of skeletal plagioclase. Hyaloclastite breccia fragments are mineralogically similar, but matrix is largely fresh glass with incipient palagonite alteration along cracks and crystal margins.
	Castle Butte breccia	Castle Butte	Basaltic andesite flows and flow breccias, hyaloclastite, water-lain shale and sandstone, and a felsic phreatomagmatic crystal-lithic-vitric lapilli tuff	Andesitic flows are vesicular with phenocrysts and glomerocrysts (3-5%) of clinopyroxene and rare olivine pseudomorphed by iddingsite and smectite, in a pilotaxitic groundmass of randomly oriented plagioclase. Felsic tuff of magmatic vitric lapilli and pumice (45-55%), cognate andesitic fragments (~15%), and pyrogenic crystals (primarily feldspar; 5-7%) in fine ash matrix.
	Mara Hill	Kenna Cartwright Park	Subaerial basaltic andesite pahoehoe flows	Flows 1.5-3 m thick, locally thin to 3-20 cm thick pahoehoe toes. Aphyric to sparsely plagioclase phyric.

Table 1. Continued.

	Kissick breccia	North of Kamloops Lake	Basaltic andesite monolithic breccia at margin of a small dome that resulted from a mixture of magmatic and autoclastic processes.	Hypocrystalline to glassy with microlites of plagioclase (30%) forming a trachytic texture. The fragments are angular to subrounded, <0.5 mm to several cm, with smaller fragments forming the matrix breccia.
		Kenna Cartwright Park	Andesitic pillow, flow and phreatomagmatic breccias forming the remnants of cones	Breccia fragments are aphyric, microcrystalline to glassy.
	Nipple breccia	North of Kamloops Lake	Basaltic andesite, phreatomagmatic scoria cone, lava flows, and flow breccias	Typically olivine-, pyroxene-, plagioclase-phyric (3-15%). Olivine phenocrysts are euhedral to subhedral, up to 3 cm and zoned to highly embayed. Clinopyroxene euhedral to anhedral, 3-4 mm, rarely zoned. Largest plagioclase phenocrysts are zoned and display sieve textures. Groundmass glassy with microlites (3%) of plagioclase and lesser pyroxene and olivine. Microlites exhibit a trachyitic texture, commonly broken.
Tranquille	Middle	North of Kamloops Lake	Basaltic andesite, pillowed flows, pillow breccias, and hyaloclastite	Pillowed flows up to 2.5 m in diameter. Flows are aphyric to micro-plagioclase phyric. Flow margins and hyaloclastite are glassy and commonly altered to palagonite.
	Border facies	Kenna Cartwright Park	Basaltic andesite to andesite, ash (bentonite), massive flows, hyaloclasite breccias, and andesitic lapilli tuff-tuff breccia (phreatomagmatic airfall)	Flow margins and hyaloclastite fragments are glassy to hypocrystalline with microlites of plagioclase forming a trachytic texture. Flow interiors have an interstitial texture. Mafic phases are commonly altered to chlorite and calcite. Plagioclase is commonly altered to sericite.

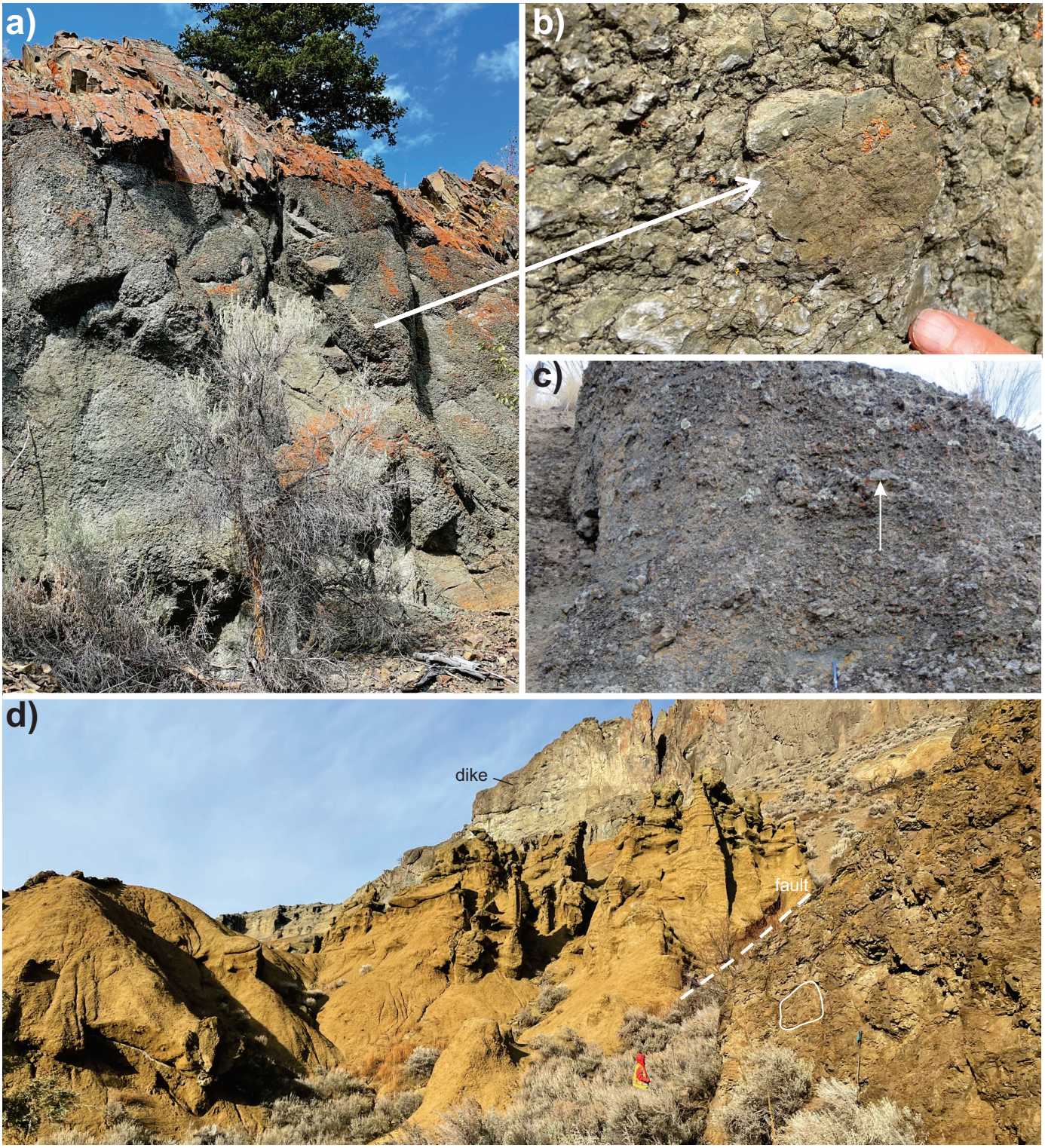

Fig. 3. a) Tranquille Formation, Border facies monolithic massive andesitic lapillistone, Kenna Cartwright Park. **b)** Close up of a) showing small bomb in a matrix of angular to subangular lapilli. **c)** Border facies lapilli tuff breccia forming a series of reversely graded beds. The arrow marks one bed. Individual fragments are primarily angular, Kenna Cartwright Park. **d)** Tranquille Formation middle member pillowed flows on right (one pillow outlined) in fault contact with upper member pyroclastic tuffs, lahars, and epiclastic sedimentary rocks that are cut by a mafic, northeast-trending, vertical dike.

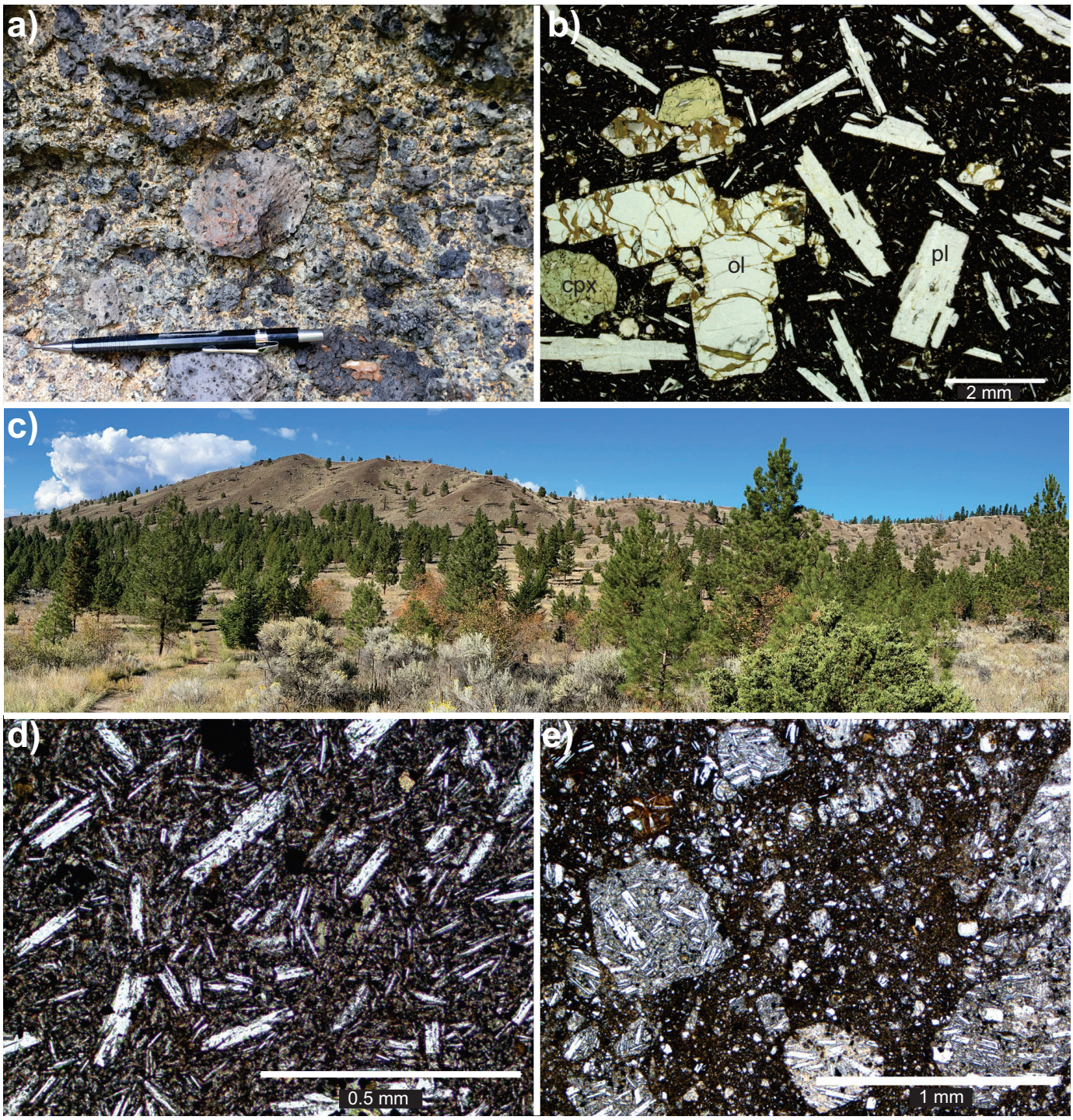

Fig. 4. a) Nipple breccia vesicular to scoriaceous magmatic pyroclasts, north of Kamloops River. **b)** Pyroclast in the Nipple breccia showing euhedral and subhedral olivine (ol), clinopyroxene (cpx), and plagioclase (pl) phenocrysts and microlites in a hypocrystalline groundmass. Plane polarized light. **c)** Ridge of the Kissick breccia at Kenna Cartwright Park. **d)** Photomicrographic from a dome that is part of the Kissick breccia north of Kamloops Lake showing microlites of plagioclase and interstitial opaque and mafic minerals in a cryptocrystalline groundmass. Cross polarized light. **e)** Kissick breccia at the margin of the dome in d). The fragments are monolithic, angular to subangular, hypocrystalline to glassy, with microlites of plagioclase forming a trachytic texture. The matrix is of smaller fragments. Cross polarized light.

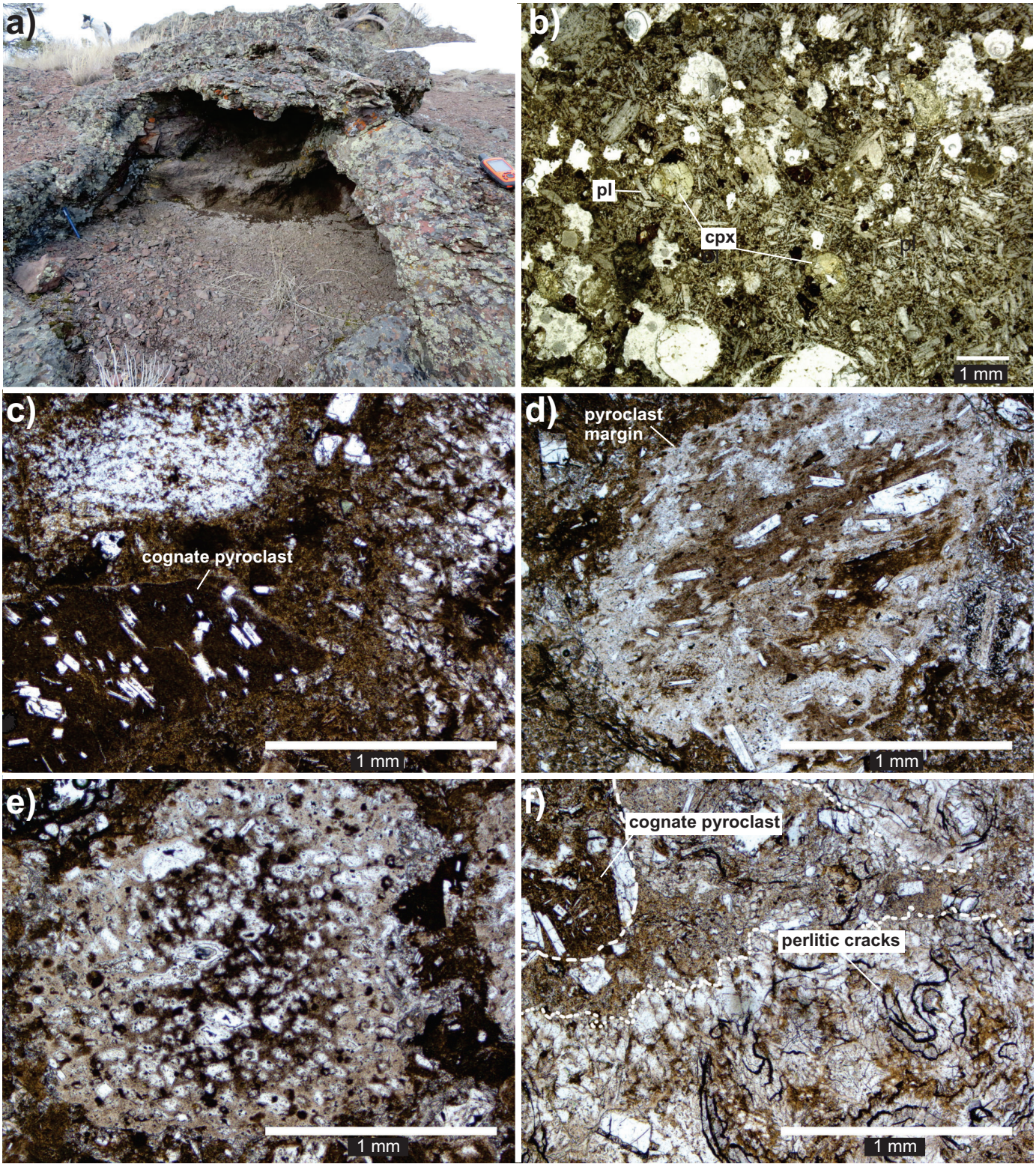

Fig. 5. a) Mara Hill member pahoehoe flow top with drain-away ledge in cavity beneath upper crust, Kenna Cartwright Park. **b)** Castle Butte member basaltic andesite autoclastic flow breccia showing a pilotaxitic groundmass texture and phenocrysts of clinopyroxene (cpx), plagioclase (pl), and oxides, north of Kamloops Lake. Clear circular shapes in the section are amygdules that are filled with calcite and analcime. Plane polarized light. **c)** Castle Butte member tuff, angular cognate pyroclast with skeletal plagioclase laths, north of Kamloops Lake. Plane polarized light. **d)** Castle Butte member tuff with magmatic pyroclast showing delicate margins and aligned plagioclase microlites, north of Kamloops Lake. Plane polarized light. **e)** Castle Butte member tuff pumice pyroclast, north of Kamloops Lake. Plane polarized light. **f)** Castle Butte member tuff vitric pyroclast, outlined in white, showing perlitic cracks, north of Kamloops Lake. Plane polarized light.

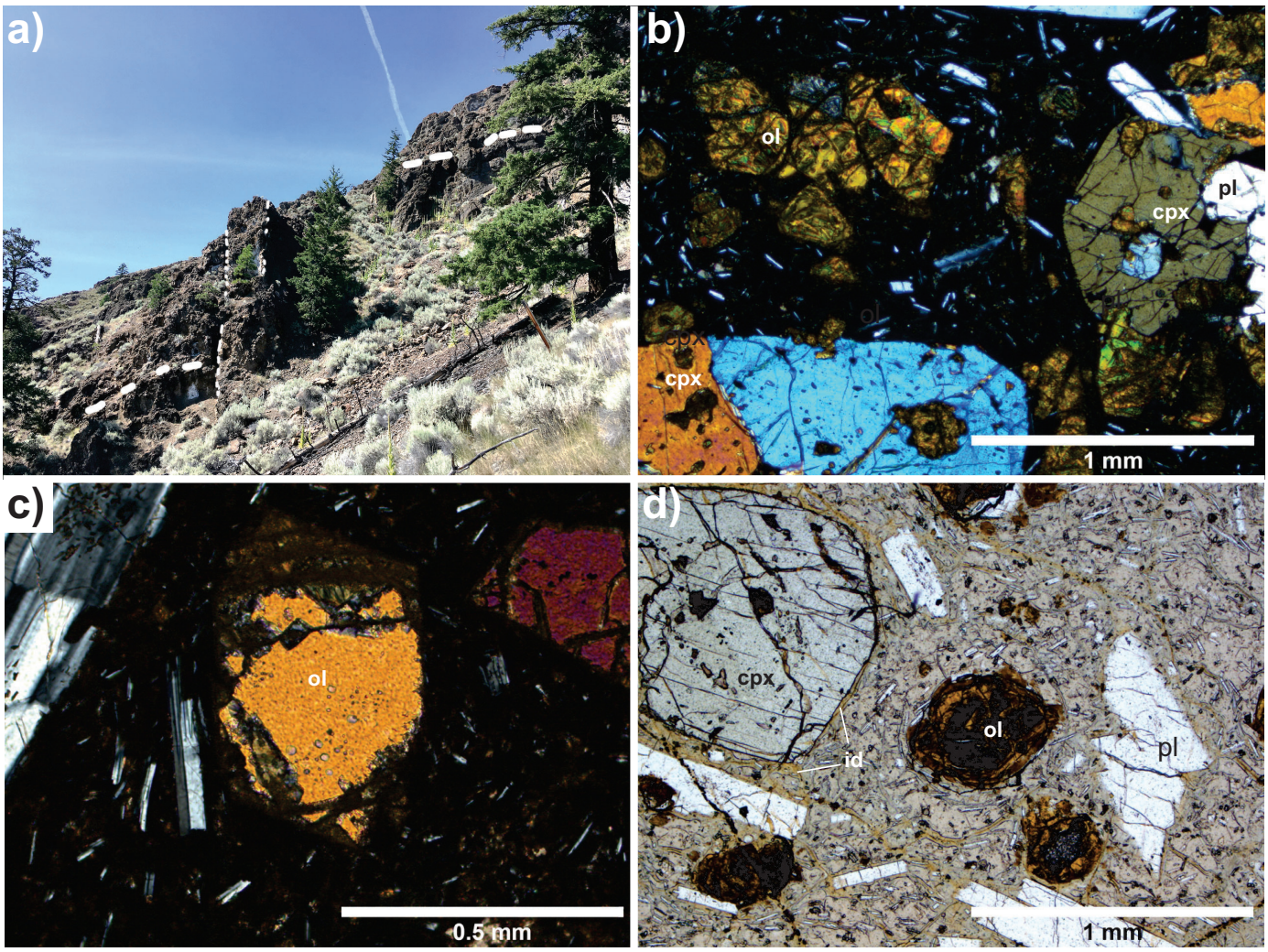

Fig. 6. Doherty Creek member, north of Kamloops Lake. **a)** Gently dipping flows and flow breccias highlighted by thick dashed line, cut by a near-vertical dike outlined by dashed lines. **b)** Fresh clinopyroxene (cpx), a glomerocryst (right) of clinopyroxene, plagioclase (pl) and altered olivine (ol), upper left. Cross polarized light. **c)** Rare fresh core of olivine. Cross polarized light. **d)** Glassy fragment of hyaloclastite, exhibiting incipient iddingsite (id) alteration along cracks and margins of phenocrysts. Cross polarized light.

rim (Fig. 7d). Amphibole (hornblende) includes both embayed and resorbed crystals, some with an inner ring of crystals and fluid inclusions (Fig. 7e). Amphibole is commonly surrounded by thick opacitic rims that have almost completely replaced the original mineral (Fig. 7c), and pyroxene microcrysts are locally surrounded by a beaded corona of micron-sized crystals (Fig. 7f).

The Opax breccia occurs near the top of Red Plateau and at the peak of Wheeler Mountain. On Red Plateau, the breccia comprises mainly andesitic flow breccias that are sparsely plagioclase-phyric and plagioclase and clinopyroxene (<1%) micro-phyric, with rare olivine that is pseudomorphed by iddingsite, clay minerals, and calcite (Figs. 8a, b). Like the underlying Red Plateau member, the large plagioclase phenocrysts display sieve textures, embayed edges and overgrowth rims (Fig. 8a). At Wheeler Mountain, the Opax breccia is andesitic to dacitic and comprises a vesicular hypocrystalline flow (Fig. 8c) and a vitric monolithic in situ hydrothermal breccia (Figs. 8d, e). The breccia at Wheeler Mountain lacks hornblende and clinopyroxene microcrysts and the disequilibrium textures observed in the feldspars at Red Plateau.

3.3. Mount Savona Formation

At Mount Savona, the Mount Savona Formation is considered the lateral equivalent of the Dewdrop Flats Formation (Ewing, 1981b). There, volcanic rocks include a rhyolitic flow (Figs. 9a, b) and tuffs (Figs. 9c, d). The flow is massive and feldspar-phyric with microcrysts of euhedral to subhedral hornblende and biotite. Flow banding is defined by the alignment of the long axes of hornblende and feldspar. (Figs. 9a, b). The tuffs are thinly bedded lithic-vitric-crystal tuffs with flow banding and massive crystal tuffs (Figs. 9c-e).

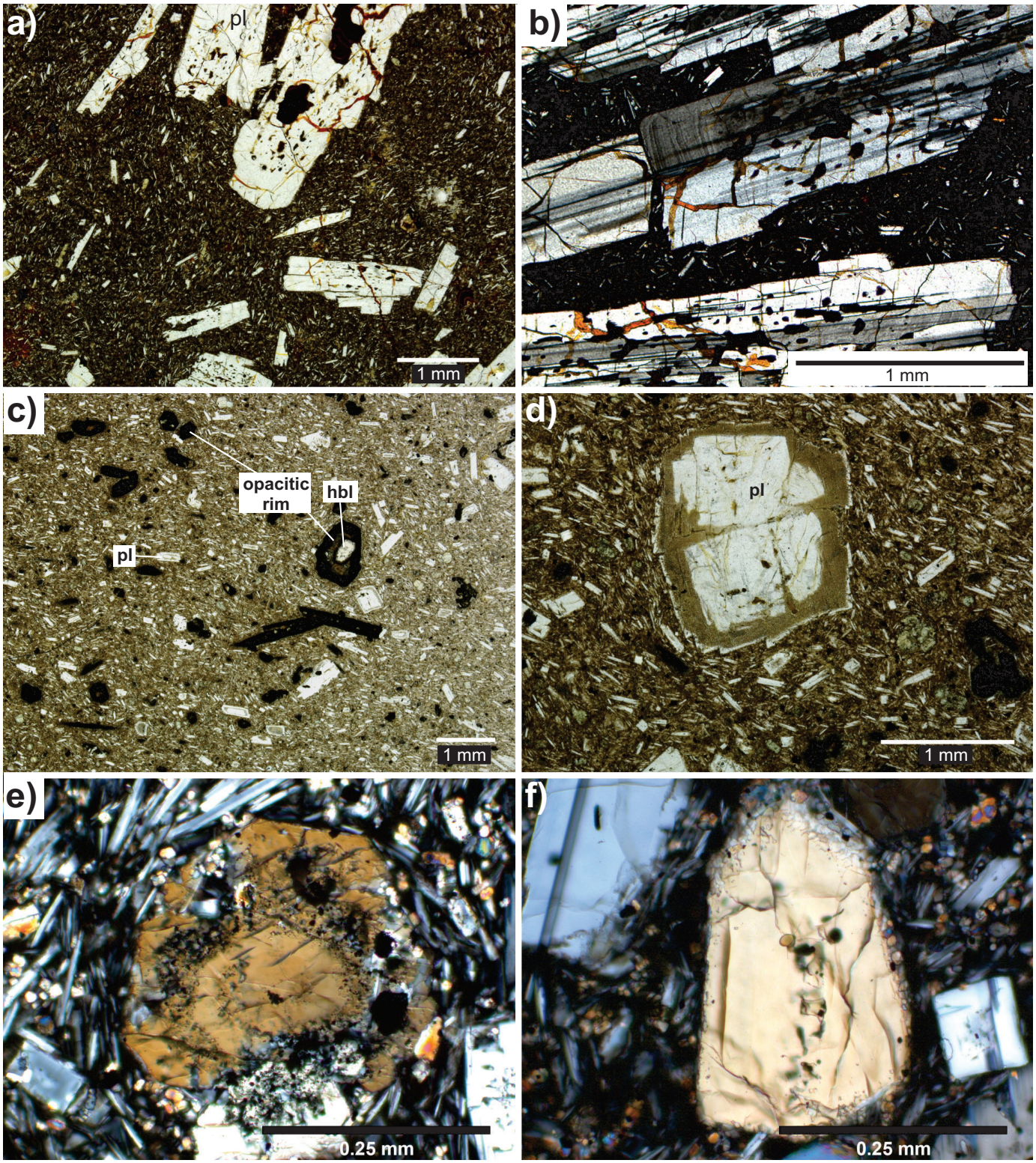

Fig. 7. a) Red Plateau member partially resorbed plagioclase exhibiting coarse sieve, or resorption texture. Groundmass includes plagioclase crystals, and microlites forming a trachytic texture, Wheeler Mountain. Plane polarized light. **b)** Red Plateau member with zoned plagioclase in the hypocrystalline groundmass, Wheeler Mountain. Cross polarized light. **c)** Red Plateau member with hornblende (hbl) surrounded by opacitic rims, Red Plateau. Plane polarized light. **d)** Red Plateau member zoned plagioclase with a fine sieve texture or dusty zone at the margin and a discontinuous overgrowth rim of annealed plagioclase, Red Plateau. Plane polarized light. **e)** Red Plateau member, originally euhedral amphibole that is partially resorbed with an internal ring of mineral and melt inclusions, Red Plateau. Cross polarized light. **f)** Red Plateau member clinopyroxene with melt, fluid, and mineral inclusions. The clinopyroxene crystal is rimmed by a corona of smaller euhedral to subhedral clinopyroxene crystals that also form a spotted texture in the groundmass, Red Plateau. Cross polarized light.

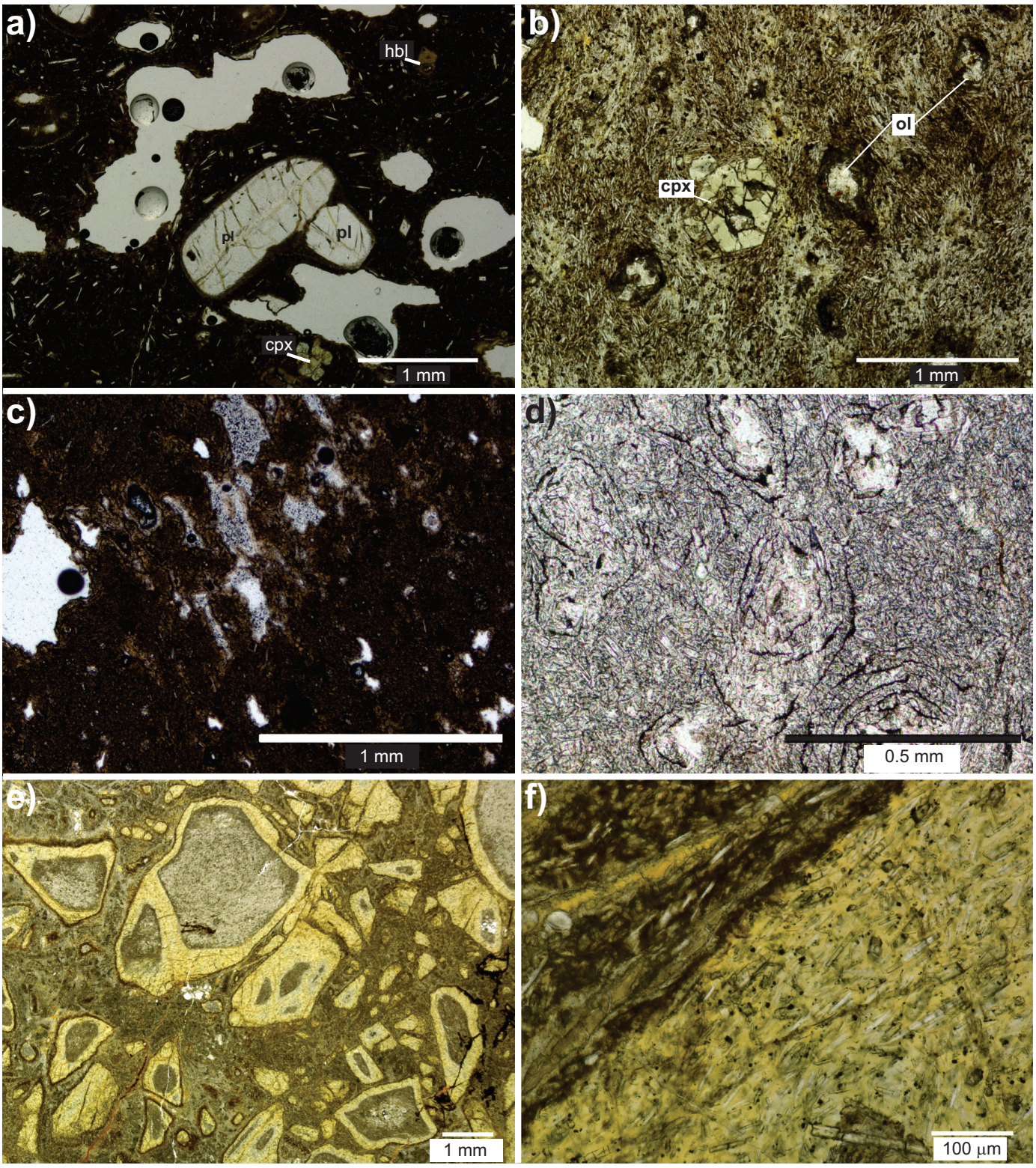

Fig. 8. Opax breccia. **a)** Vesicular andesitic flow showing rounded and resorbed plagioclase with sieve texture, a phenocryst of clinopyroxene with embayed margins, and a microlite of hornblende, Red Plateau. Plane polarized light. **b)** Euhedral clinopyroxene, plagioclase microlites forming a trachytic texture, and olivine completely altered to clay minerals and calcite (bright cores), Red Plateau**.** Plane polarized light. **c)** Vesicular, hypocrystalline flow showing very fine plagioclase microlites, Wheeler Mountain. Plane polarized light. **d)** Volcanic glass with perlitic cracks, Wheeler Mountain. Plane polarized light. **e)** Vitric breccia showing angular clasts with oxidized rims and fresh glassy margins. **f)** Closeup of e) showing microlites in a glassy matrix, Wheeler Mountain. Plane polarized light.

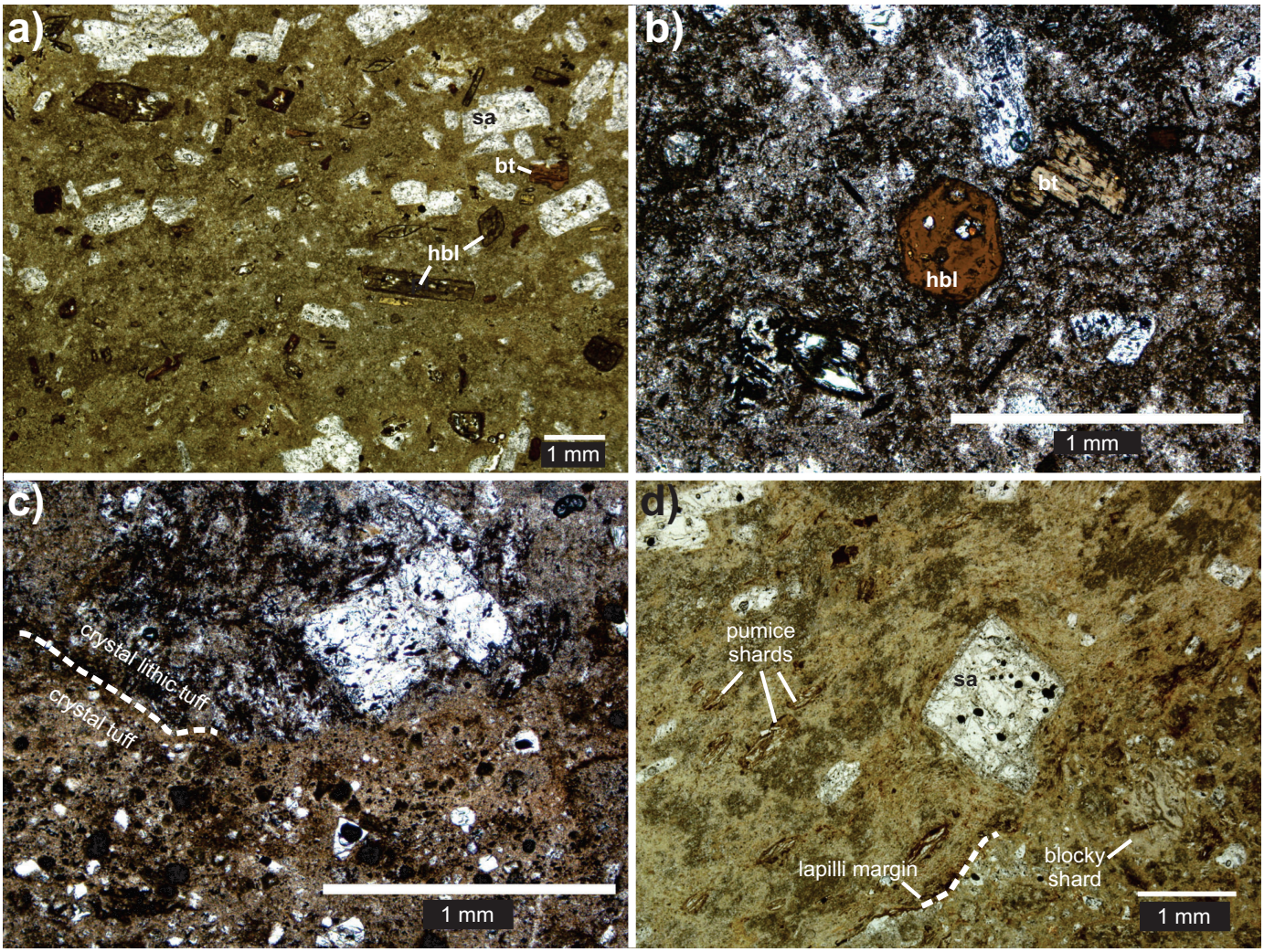

Fig. 9. Mount Savona Formation volcanic rocks. **a)** Rhyolite flow showing the main phenocryst phases of sanidine (sa), hornblende, and biotite (bt). **b)** Rhyolite flow containing euhedral biotite with mineral inclusions and euhedral hornblende. **c)** Contact between two tuff beds. **d)** Lithic fragment of a vitric-crystal tuff within a lithic-vitric-crystal tuff.

4. Geochemistry

Samples for whole rock geochemistry were collected from selected members of the Tranquille and Dewdrop Flats formations in 2019 and 2020. Massive flow units were sampled, except one of the samples from the Castle member is a heterolithic lapilli tuff that contains cognate mafic lapilli, and one sample from the Mount Savona Formation is a crystal-lithic tuff. In the case of monolithic breccias, larger fragments with minimal internal brecciation were sampled. The Mara flows from Kenna Cartwright Park (Fig. 2) were sampled in the most detail (Fig. 10). The complete dataset is provided in Van Wagoner et al. (2021b).

4.1. Methods

Clean, alteration-free samples were submitted to Activation laboratories, Ancaster, Ontario, for whole rock major, trace, and rare earth element analysis. At Actlabs, samples were crushed, mechanically split, and pulverized using mild steel. Major element oxides were determined using inductively coupled plasma optical emission spectroscopy (ICP-OES) and trace and rare earth element concentrations were determined using fusion inductively coupled plasma mass spectrometry (ICP-MS). Measurement precision was determined from duplicate analyses and accuracy was determined using certified standards provided by Actlabs and blind samples of the British Columbia Geological Survey till standard (Van Wagoner et al., 2021b). All major elements were recalculated to 100% volatile-free.

5. Results

The rocks in this study (n=32) have loss on ignition (LOI) from 1.41 to 13.12%, (average=4.2%) and geochemical data are plotted as volatile free at 100% (Fig. 10). One sample from the Red Plateau member at Wheeler Mountain was removed from the plots because the volatile-free SiO_2 (~45 wt.%) and MgO (2 wt.%) are too low and the sample consistently plots as an outlier. The rocks range from high-K calc-alkaline basalt to

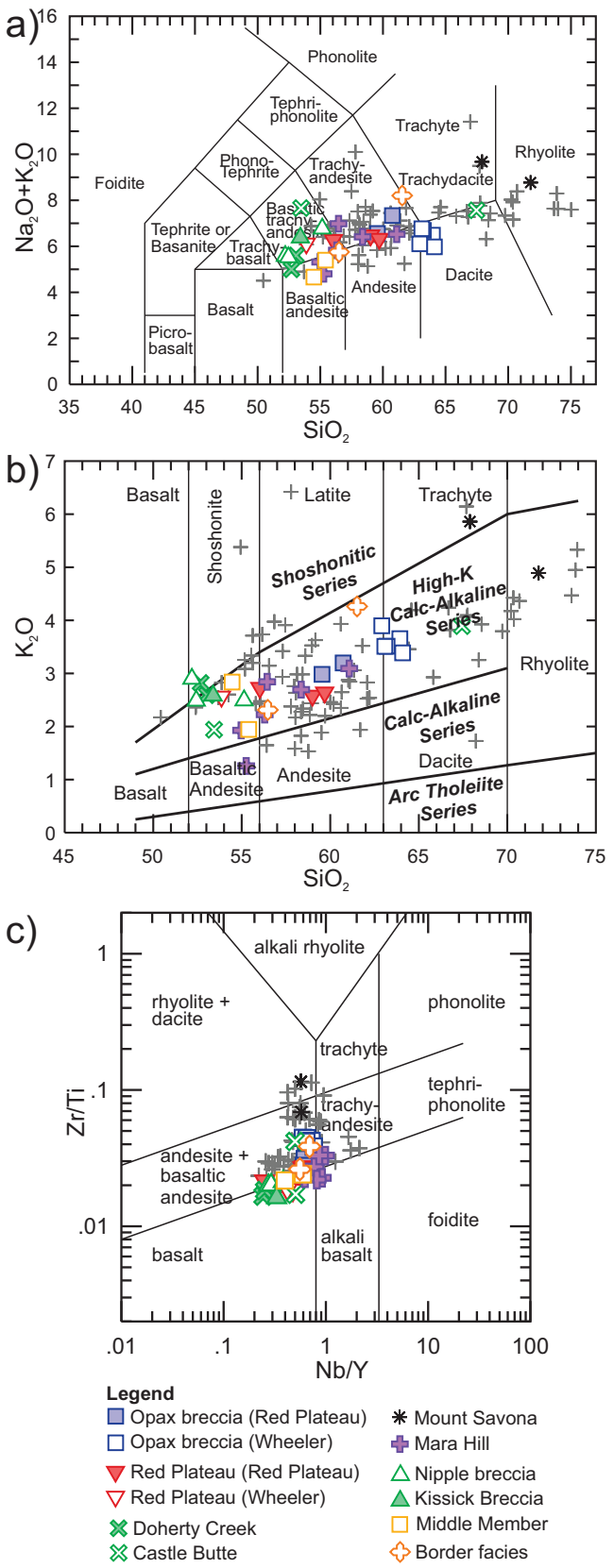

Fig. 10. a) Total alkali-silica diagram (wt.%) after Le Bas et al. (1986). Major elements calculated at 100% LOI free. **b)** SiO_2 vs. K_2O (wt.%). Fields are after Peccerillo and Taylor (1976). **c)** Nb/Y vs. Zr/Ti c diagram, after Pearce, 1996 (after Winchester and Floyd, 1977).

rhyolite with most being basaltic-andesite to andesite (Fig. 10). The most mafic rocks are from the Nipple breccia, Doherty Creek, Castle Butte, and Kissick breccia members of the Dewdrop Flats Formation, and a pillow flow from the middle member of the Tranquille Formation. The most felsic rocks are from the Mount Savona Formation west of the Kamloops Group type area. The rocks display tight trends between SiO_2 and MgO, CaO, Fe_2O_3, TiO_2, Al_2O_3, and P_2O_5 (Fig. 11). The rocks have Mg# from 30 to 63; the highest Mg#=63 is from the Nipple member and is slightly below the threshold of primitive arc magmas (Mg#=65; Fig. 12; Kelemen et al., 2003).

Relative to chondrite, the rocks are uniformly light rare earth element (LREE) enriched ($(La/Yb)_N$=6-21), with no Eu anomalies, and relatively flat middle to heavy REE ($(Dy/Yb)_n$; Fig. 13). Relative to primitive mantle, all rocks are enriched in the large ion lithophile elements (LILE), particularly fluid-mobile Ba, K, and Pb, and to a lesser extent U and Sr. The rocks have negative anomalies of some high field strength elements (HFSE; Nb, Ta. P, and Ti). The most felsic samples from Mount Savona Formation have the most pronounced negative Ti anomalies (Fig. 13c)

6. Discussion

Volcanic facies within most members of the Kamloops Group in its type area are similar at different geographic locations. However, the Red Plateau and Opax breccia members on Red Plateau are petrographically and geochemically distinct from the same members on Wheeler Mountain (Figs. 7, 8, 10, 11). The Opax breccia member at Wheeler Mountain is overall more felsic than at Red Plateau, is much finer grained, lacks clinopyroxene and olivine microlites, and has plagioclase phenocrysts with disequilibrium textures. Inversely, the Red Plateau member at Red Plateau is slightly more felsic than at Wheeler Mountain (Figs. 7, 8, 10, 11) and has hornblende and plagioclase phenocrysts with disequilibrium textures. This may indicate that each geographic location represents a unique volcanic centre.

The Castle Butte member tuffs are the most felsic rocks in the type area. Outside the type area, the Mount Savona Formation volcanic rocks comprise a felsic volcanic centre, but their contribution to tuffaceous beds elsewhere in the Kamloops Group is unclear.

The basaltic rocks have low-Mg (Mg#<65) and none of the rocks are primitive andesite (Fig. 12; Kelemen et al., 2003). Some of the Kamloops Group rocks are consistent with high-Mg andesites (Mg#50-60; Fig. 12; Kelemen et al., 2003) and some have adakitic compositions (Fig. 12; Richards and Kerrich, 2007). The terms high-Mg andesite and adakite have traditionally appealed to a tectonic process, such as slab melting (Kelemen et al., 2003; Kerrich and Richards, 2007; Zhang et al., 2019). Because the Kamloops Group volcanic rocks cover a broad compositional span that transcends the definitive fields (Fig. 12), it is best to call the rocks andesite with high-Mg or adakite-like. This terminology removes genetic connotations. The low-Mg basalts and the broad overall compositional span

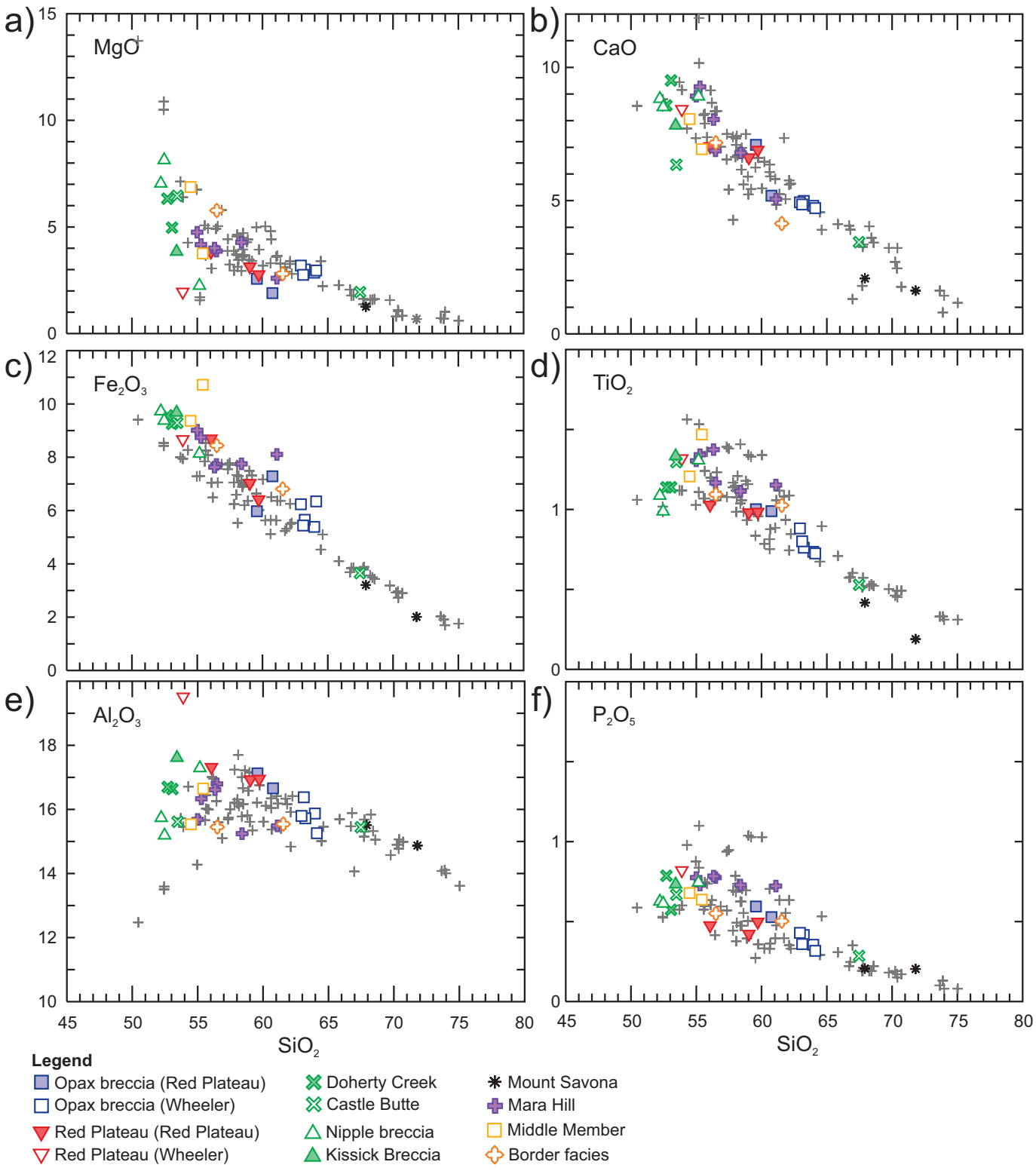

Fig. 11. Harker diagrams (wt.%). SiO_2 vs. **a)** MgO, **b)** CaO, **c)** Fe_2O_3, **d)** TiO_2, **e)** Al_2O_3, and **f)** P_2O_5.

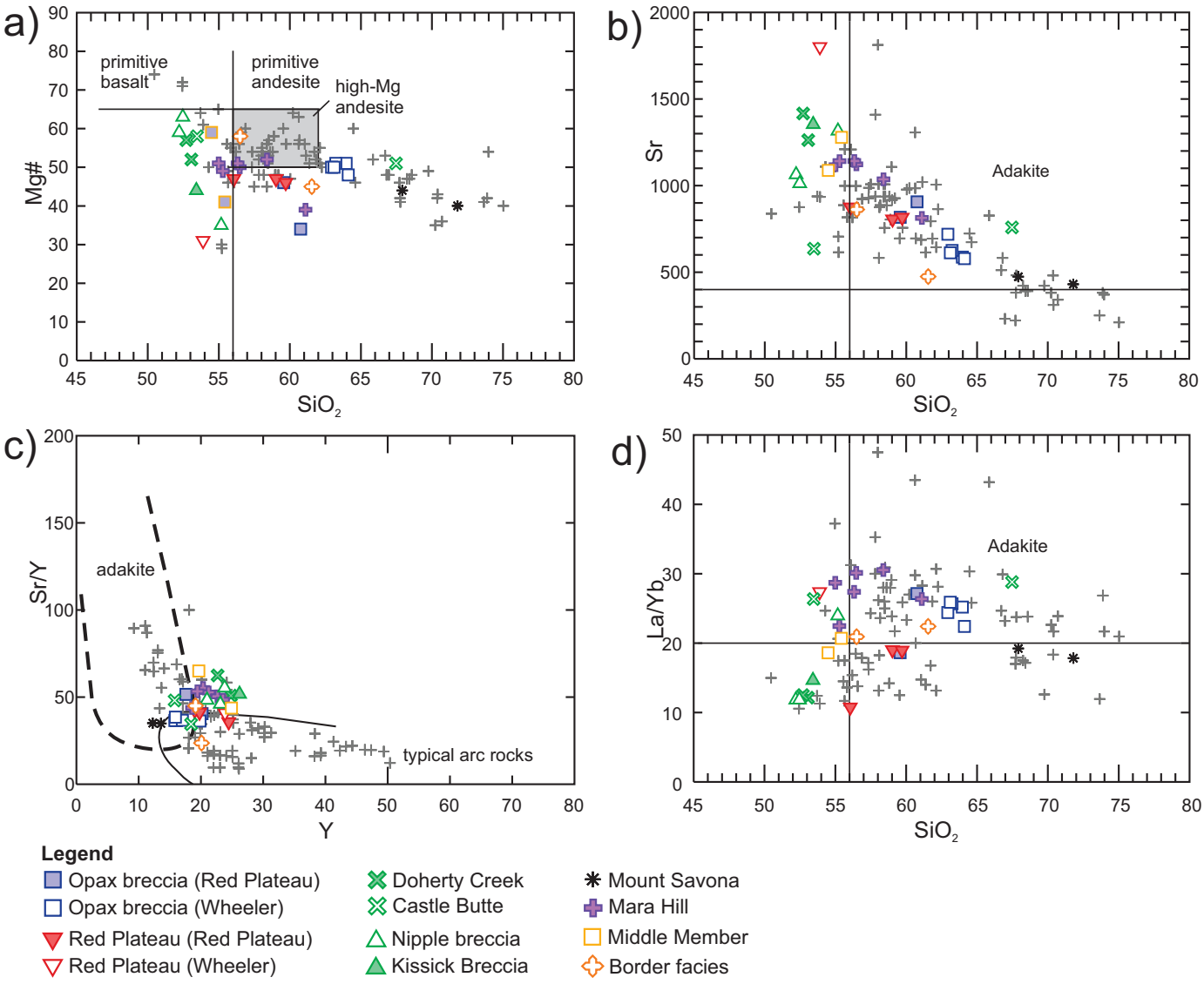

Fig. 12. a) SiO_2 (wt.%) vs. Mg#. Primitive basalt and andesite and high-Mg andesite fields from Kelemen et al. (2003). **b)** SiO_2 (wt.%) vs. Sr (ppm). **c)** Y vs. Sr/Y (ppm). **d)** SiO_2 (wt.%) vs. La/Yb. Adakite fields and typical arc field from Richards and Kerrich (2007).

indicate the volcanic rocks were likely derived from mantle magmas that hybridized with lower crust. This interpretation is supported by petrographic observations of common disequilibrium textures in phenocrysts (Figs. 7, 8a).

Many of the volcanic rocks in the Kamloops Group have plagioclase phenocrysts with disequilibrium textures (Figs. 7c, d). Such textures have been attributed to the injection and mixing of a mafic magma into a more felsic magma reservoir, particularly in andesites with high-Mg (Maro and Caffe, 2016; Conway et al., 2020; Beier et al., 2017). Parental magma mixing is also consistent with the opacitic rims that surround hornblende (Fig. 7c), which can be attributed to melt degassing or dehydration during decompression or ascent, temperature increase, and/or oxidation of the melt (e.g., Plechov et al., 2008). Similar opacitic rims textures occur in rocks from the 1956 eruption of the Bezymyannyi volcano in Kamchatka, caused by heating of the magma chamber due to injection of new magma, which triggered the eruption (Plechov et al., 2008).

Chondrite-normalized (La/Sm)n increases with increasing SiO_2, whereas (Dy/Yb)n remains relatively flat (Fig. 13). The (Dy/Yb)n is controlled by different minerals (e.g., garnet, amphibole, pyroxene) in the melt source or during fractional crystallization but the ratio does not describe the shape of the normalized middle to heavy REE pattern, which is better explained by $Dy/Dy^*(Dy/Dy^*=Dy_n/[La_n^{4/13}*Yb_n^{9/13}]$; n=chondrite normalized; Davidson et al., 2013). The shape of the normalized Kamloops Group middle to heavy REE is entirely consistent with amphibole and pyroxene control and follow a trend similar to other arcs (Figs. 13a, b; Fig. 14a).

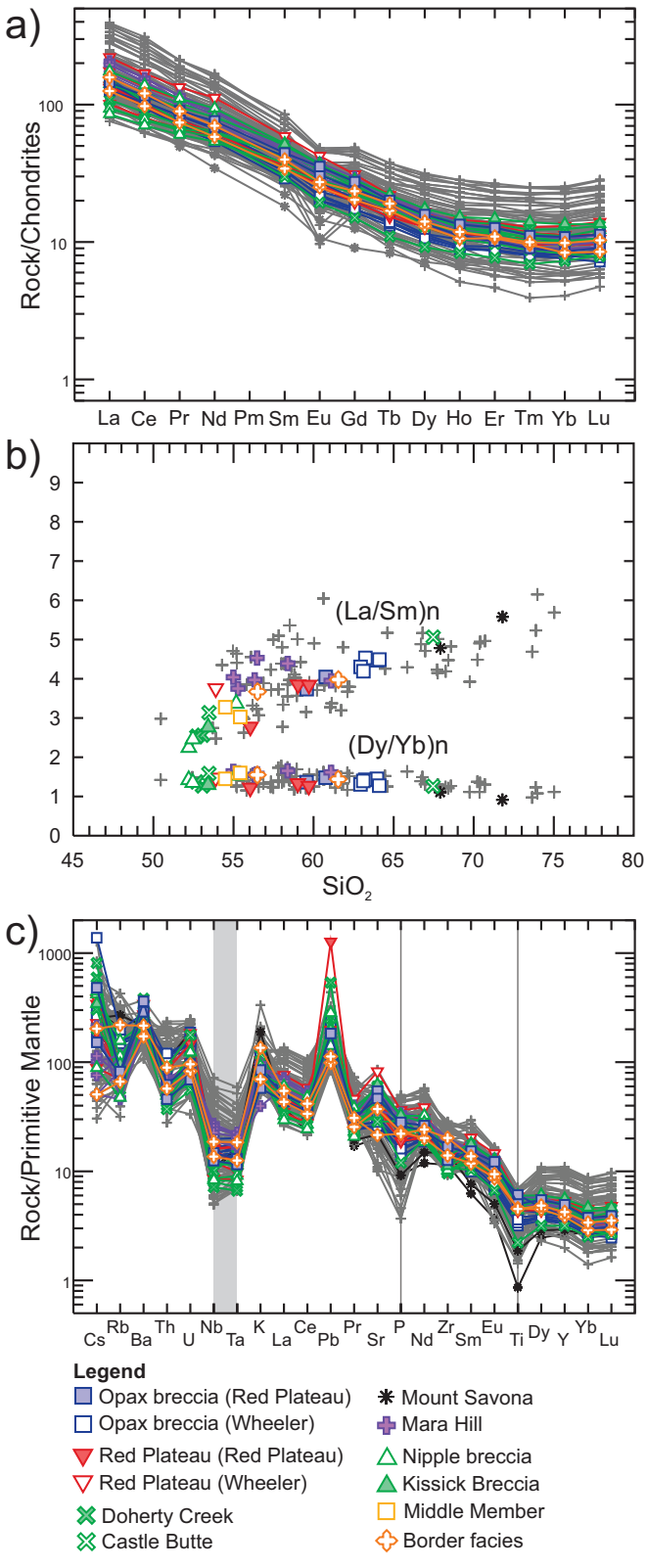

Fig. 13. a) Chondrite normalized rare earth elements. **b)** SiO_2 (wt.%) vs. chondrite normalized (La/Sm)n and (Dy/Yb)n. **c)** Primitive mantle normalized trace elements. Vertical grey bar and lines mark Nb-Ta, P, Ti anomalies. Normalizing values are from Sun and McDonough (1989).

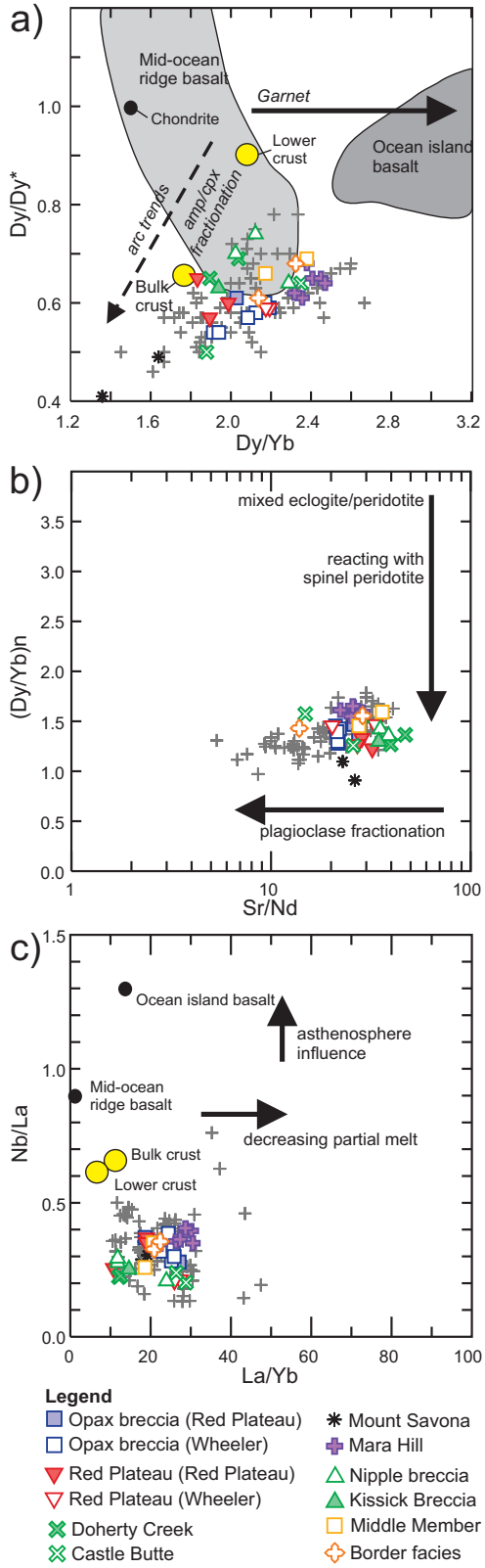

Fig. 14. a) Dy/Yb vs. Dy/Dy*. Modified after Davidson et al. (2013). **b)** Sr/Nd vs. chondrite normalized (Dy/Yb)n. Modified after Kelemen et al. (2003); chondrite from Sun and McDonough (1989). **c)** La/Yb vs. Nb/La. Mid-ocean ridge and ocean island basalt values from Sun and McDonough (1989) and crustal values from Rudnick and Fountain (1995).

There does not appear to be any garnet control on the REE, indicating that eclogite was not in the melt source, and that the parental melts were not derived from nor interacted with garnet-bearing lower crust (Figs. 14a, b). Overall, the Kamloops Group geochemistry appears to be controlled by amphibole and pyroxene and possibly by plagioclase fractionation, which explains the overall trend to lower Sr/Nd (Fig. 14c). The more mafic rocks contain the highest Sr concentrations (Fig. 12a), indicating the melt source was low in plagioclase, which would have withheld Sr during melting. This is supported by the overall lack of negative Eu anomalies in the chondrite normalized REE (Fig. 13a).

The primitive mantle normalized trace elements have negative Nb, P, and Ti anomalies (Fig. 13c) that are consistent with melts derived from a subduction-modified mantle source. The Nb/La are well below asthenosphere-derived melts, supporting a lithospheric source (Fig. 14c). Van Wagoner et al. (2021a) and others (e.g., Morris et al., 2000) contended that the Eocene magmas are not derived directly from concomitant subduction processes (cf. Ickert et al., 2009), but rather from mantle and crust that was previously subduction modified. In the Kamloops area this could be Triassic-Jurassic subduction related to the Nicola arc, or overprinting Cretaceous subduction and accretion processes. Due to the parental magma hybridization, further geochemical modelling is required to determine what mantle source was the end-member to mix with lower crust. Regarding the lower crustal end-member, geophysical evidence indicates there is a sliver of Ancestral North America near the base of the lower crust in the Kamloops area (Cook, 1995). However, whole rock Nd isotopic evidence indicates the volcanic rocks in the Savona area are juvenile (Dostal et al., 2019), supporting a mainly Quesnel terrane lower crust end-member. The petrographic and geochemical properties of the Kamloops Group volcanic rocks in this study provide an indication that bulk-rock geochemistry may not be indicative of either direct mantle melting processes or the tectonic process that caused the melting.

7. Summary

In the type area, the Kamloops Group volcanic rocks have a compositional range from basaltic andesite to dacite. The most common rock type is andesite and some have high-Mg and adakite-like geochemical features. The combination of common disequilibrium textures in plagioclase phenocrysts and geochemistry of the rocks indicate the magmas resulted from mixing of eclogite-free mantle melts with garnet-free lower crust. The geochemistry should not be used independently for tectonic discrimination as the crustal and mantle end-members require further identification.

Ongoing work for this study includes further lithostratigraphic mapping and geochemistry, high-precision geochronology, and measuring phenocryst-hosted melt inclusions in Eocene volcanic complexes in southern British Columbia. Collectively this information will help untangle the volcanogenic evolution of the Eocene volcanism, help identify volcanic centres that may control the loci of epithermal gold deposits. and estimate the contributions of volatile gases (e.g., CO_2, SO_2) to the early Eocene atmosphere.

Acknowledgments

We thank P. Schiarizza and L. Aspler for constructive reviews that helped improve the manuscript.

References cited

Ashley, R., Staatz, M.H., and Pearson, R.C., 1990. Epithermal gold deposits-Part 1. U. S. Geological Survery Bulletin, 1857-H, 31 p.

Beier, C., Haase, K.M., Brandl, P.A., and Krumm, S.H., 2017. Primitive andesites from the Taupo Volcanic Zone formed by magma mixing. Contributions to Mineralogy and Petrology, 172, 1-14. <https://doi.org/10.1007/s00410-017-1354-0>

Bordet, E., Mihalynuk, M.G., Hart, C.J.R., Mortensen, J.K., Friedman, R.M., and Gabites, J., 2014. Chronostratigraphy of Eocene volcanism, central British Columbia. Canadian Journal of Earth Sciences, 51, 56-103. <https://doi.org/10.1139/cjes-2013-0073>

Breitsprecher, K., 2002. Volcanic stratigraphy, petrology, and tectonic setting of the eastern margin of the Eocene Kamloops Group, south-central British Columbia. Unpublished B.Sc. thesis, Simon Fraser University, 257 p.

Breitsprecher, K., Thorkelson, D.J., Groome, W.G., and Dostal, J., 2003. Geochemical confirmation of the Kula-Farallon slab window beneath the Pacific Northwest in Eocene time. Geology, 31, 351-354. <https://doi.org/10.1130/0091-7613(2003)031<0351:GCOTKF>2.0.CO;2>

Chapman, R.J., and Mileham, T.J., 2016. Detrital gold grains as indicators of alkalic copper-gold porphyry mineralization. Geoscience BC Summary of Activities 2016: Minerals, Geoscience BC Report, 2016-06, 49 p.

Conway, C.E., Chamberlain, K.J., Harigane, Y., Morgan, D.J., and Wilson, C.J.N., 2020. Rapid assembly of high-Mg andesites and dacites by magma mixing at a continental arc stratovolcano. Geology, 48, 1033-1037. <https://doi.org/10.1130/G47614.1>

Cook, F.A., 1995. Lithospheric processes and products in the southern Canadian Cordillera: a Lithoprobe perspective. Canadian Journal of Earth Sciences, 32, 1803-1824.

Davidson, J., Turner, S., and Plank, T., 2013. Dy/Dy*: Variations arising from mantle sources and petrogenetic processes. Journal of Petrology, 54, 525-537. <https://doi.org/10.1093/petrology/egs076>

Dostal, J., Keppie, J.D., and Church, B.N., 2019. Generation of Eocene volcanic rocks from the Cordilleran arc of south-central British Columbia (Canada) during subduction of the Farallon and Resurrection plates and Yellowstone oceanic plateau. Geological Journal, 54, 590-604. <https://doi.org/10.1002/gj.3208>

Dufresne, M., 2015. BC Geological Survey Assessment Report for 2012 Exploration, Greenwood Property, Southern British Columbia, Canada, British Columbia Geological Survey, Assessment Report 34747, 267 p.

Ewing, T.E., 1980. Paleogene tectonic evolution of the Pacific Northwest. Journal of Geology, 88, 619-638.

Ewing, T.E., 1981a. Geology and Tectonic Setting of the Kamloops Group, South-Central British Columbia. Unpublished Ph.D. thesis. University of British Columbia, 225 p.

Ewing, T.E., 1981b. Regional stratigraphy and structural setting of the Kamloops Group, south-central British Columbia. Canadian Journal of Earth Sciences, 18, 1464-1477. <https://doi.org/10.1139/e81-137>

Ewing, T.E., 1981c. Petrology and geochemistry of the Kamloops Group volcanics, British Columbia. Canadian Journal of Earth Sciences, 18. 1478-1491. <https://doi.org/10.1139/e81-138>

Ewing, T.E., 1982. Geologic map of Tertiary rocks of the Afton-Tranquille area west of Kamloops. British Columbia. British Columbia Ministry of Energy, Mines and Petroleum Resources, British Columbia Geological Survey Preliminary Map 48, 1:50,000 scale.

Gaina, C., and Jakob, J., 2019. Global Eocene tectonic unrest: Possible causes and effects around the North American plate. Tectonophysics, 760, 136-151.

Haeussler, P.J., Bradley, D.C., Wells, R.E., and Miller, M.L., 2003. Life and death of the resurrection plate: Evidence for its existence and subduction in the northeastern Pacific in Paleocene-Eocene time. Bulletin of the Geological Society of America, 115, 867-880. <https://doi.org/10.1130/0016-7606(2003)115<0867:LADOTR>2.0.CO;2>

Höy, T., Friedman, R., and Gabites, J., 2021. Paleogene Penticton Group, Boundary area, Southern British Columbia (Parts of NTS 082E): Geochronology and implications for precious metal mineralization. Geoscience BC Summary of Activities 2020: Minerals, Geoscience BC, Report 2021-01, pp. 55-66.

Ickert, R.B., Thorkelson, D.J., Marshall, D.D., and Ullrich, T.D,. 2009. Eocene adakitic volcanism in southern British Columbia: Remelting of arc basalt above a slab window. Tectonophysics, 464, 164-185. <https://doi.org/10.1016/j.tecto.2007.10.007>

Kelemen, P.B., Hanghøj, K., and Greene A.R., 2003. One view of the geochemistry of subduction-related magmatic arcs, with an emphasis on primitive andesite and lower crust. Treatise on Geochemistry, 4, 749-806.

Knight, J., and McTaggart, K.C., 1988. Composition of gold from southwestern British Columbia: A progress report. In: Geological Fieldwork 1987, British Columbia Ministry of Employment and Investment British Columbia Geological Survey Paper 1989-01, pp. 387-394.

Le Bas, M.J., Le Maitre, R.N., Streckeisen, A., and Zanettin, B., 1986. A chemical classification of volcanic rock based on total silica diagram. Journal Petrology, 27, 745-750.

Love, D.A., Clark, A.H., Hodgson, C.J., Mortensen, J.K., Archibald, D.A., and Farrar, E., 1998. The timing of adularia-sericite-type mineralization and alunite-kaolinite-type alteration, Mount Skukum epithermal gold deposit, Yukon Territory, Canada; ^{40}Ar-^{39}Ar and U-Pb geochronology. Economic Geology, 93, 437-462.

Maro, G., and Caffe, P.J., 2016. The Cerro Bitiche andesitic field: Petrological diversity and implications for magmatic evolution of mafic volcanic centers from the northern Puna. Bulletin of Volcanology, 78. <https://doi.org/10.1007/s00445-016-1039-y>

Morris, G.A., Larson, P.B., and Hooper, P.R., 2000. 'Subduction style' magmatism in a non-subduction setting: The Colville Igneous Complex, NE Washington State, USA. Journal of Petrology, 41, 43-67. <https://doi.org/10.1093/petrology/41.1.43>

Morris, G.A., and Creaser, R.A., 2003. Crustal recycling during subduction at the Eocene Cordilleran margin of North America: A petrogenetic study from the southwestern Yukon. Canadian Journal of Earth Sciences, 40, 1805-1821. <https://doi.org/10.1139/e03-063>

Nelson, J.L., Colpron, M., and Israel, S., 2013. The Cordillera of British Columbia, Yukon and Alaska: Tectonics and metallogeny. In: Colpron, M., Bissig, T., Rusk, B.G., and Thompson, J.F., (Eds.), Tectonics, Metallogeny and Discovery: The North American Cordillera and Similar Accretionary Settings. Society of Economic Geologists Special Publication 17, Chapter 3, pp. 53-103.

Northcote, B., 2022. Exploration and mining in the South Central Region, British Columbia. In: Provincial Overview of Exploration and Mining in British Columbia, 2021. British Columbia Ministry of Energy, Mines and Low Carbon Innovation, British Columbia Geological Survey Information Circular 2022-01, in press.

Pearce, J.A., 1996. A user's guide to basalt discrimination diagrams. In: Wyman, D.A., (Ed.), Trace element geochemistry of volcanic rocks: applications for massive sulphide exploration. Geological Association of Canada, Short Course Notes, 12, pp. 79-113.

Peccerillo, A., and Taylor, S.R., 1976. Geochemistry of Eocene calc-alkaline volcanic rocks from the Kastamonu area, Northern Turkey. Contributions to Mineralogy and Petrology, 58, 63-81. <https://doi.org/10.1007/BF00384745>

Plechov, P.Y., Tsai, A.E., Shcherbakov, V.D., and Dirksen, O.V., 2008. Opacitization conditions of hornblende in Bezymyannyi volcano andesites (March 30, 1956 eruption). Petrology, 16, 19-35. <https://doi.org/10.1134/s0869591108010025>

Read, P.B., 2000. Industrial minerals in the Cenozoic rocks of southern British Columbia. British Columbia Ministry of Energy and Mines, Chapter 7, 53-86.

Richards, J.P., and Kerrich, R., 2007. Adakite-like rocks: Their diverse origins and questionable role in metallogenesis. Economic Geology, 102, 537-576.

Schroeter, T.G., 1987. Brief studies of selected gold deposits in southern British Columbia. In: Geological Fieldwork 1986, British Columbia Ministry of Energy, Mines and Petroleum Resources, British Columbia Geological Survey Paper 1987-1, pp. 15-22.

Simandl, G., 2009. Nonmetallic minerals other than coal: Industrial minerals, gemstones and aggregate in British Columbia, Canada. Ministry of Energy, Mines and Petroleum Resources, British Columbia Geological Survey, Paper 2009-2, 37 p.

Stern, R.J., and Dumitru, T.A., 2019. Eocene initiation of the Cascadia subduction zone: A second example of plume-induced subduction initiation? Geosphere, 15, 659-681. <https://doi.org/10.1130/GES02050.1>

Sun, S.S., and McDonough, W.F., 1989. Chemical and isotopic systematics of oceanic basalts: implications for mantle composition and processes. In: Saunders, A.D., and Norry, M.J., (Eds.), Magmatism in the Ocean Basins. Geological Society, London, Special Publication 42, pp. 313-345.

Van Wagoner, N., Ootes, L., and Thomson-Gladish, J., 2021a. Volcanism and geochemistry of the Kamloops Group, south-central British Columbia. In: Geological Fieldwork 2020, British Columbia Ministry of Energy, Mines and Low Carbon Innovation, British Columbia Geological Survey Paper 2021-01, pp. 65-88.

Van Wagoner, N., Ootes, L., and Sutcliffe, B., 2021b. Geochemical data from the Kamloops Group. British Columbia Ministry of Energy, Mines and Low Carbon Innovation, British Columbia Geological Survey GeoFile 2021-16, 2 p.

Winchester, J.A., and Floyd, P.A., 1977. Geochemical discrimination of different magma series and their differentiation product using immobile elements. Chemical Geology, 20, 325-343. <http://dx.doi.org/10.1016/0009-2541(77)90057-2>

Zachos, J., Pagani, H., Sloan, L., Thomas, E., and Billups, K., 2001. Trends, rhythms, and aberrations in global climate 65 Ma to present. Science, 292, 686-693. <https://doi.org/10.1126/science.1059412>

Zhang, L., Li., S., and Zhao, Q., 2019. A review of research on adakites. International Geology Review, 63, 47-64. <https://doi.org/10.1080/00206814.2019.1702592>

Revised stratigraphy and geochronology of the Hazelton Group, host rocks for volcanogenic mineralization in the Kitsault River area, northwestern British Columbia

Rebecca C. Hunter[1, a], Christopher F.B. Sebert[2], Richard Friedman[3], and Corey Wall[3]

[1] British Columbia Geological Survey, Ministry of Energy, Mines and Low Carbon Innovation, Victoria, BC, V8W 9N3
[2] Dolly Varden Silver Corporation, Vancouver, BC, V7X 1E5
[3] Pacific Centre for Isotopic and Geochemical Research, Department of Earth, Ocean and Atmospheric Sciences, The University of British Columbia, Vancouver, BC, V6T 1Z4
[a] corresponding author: Rebecca.Hunter@gov.bc.ca

Recommended citation: Hunter, R.C., Sebert, C.F.B., Friedman, R., and Wall, C., 2022. Revised stratigraphy and geochronology of the Hazelton Group, host rocks for volcanogenic mineralization in the Kitsault River area, northwest British Columbia. In: Geological Fieldwork 2021, British Columbia Ministry of Energy, Mines and Low Carbon Innovation, British Columbia Geological Survey Paper 2022-01, pp. 63-81.

Abstract

The Kitsault River area, at the southern end of the 'Golden Triangle', hosts numerous Ag-rich volcanogenic massive sulphide (VMS) and epithermal-type deposits similar to those of the Eskay rift ca. 150 km to the northwest. Resolving the age and affinity of late Early to Middle Jurassic volcano-sedimentary Hazelton Group host rocks is key to understanding the metallogeny of the Kitsault River area. Based on field and new U-Pb zircon geochronological data we identify six Hazelton Group facies in the Kitsault area. The lower Hazelton Group consists of facies 1, a coarse-grained basal unit of sedimentary rocks with a maximum depositional age of ca. 206-204 Ma; facies 2, a volcano-sedimentary package with abundant limestone, tuff and lapilli tuff to tuff breccia with augite-phyric clasts and a crystallization age of ca. 201 Ma; facies 3, an andesitic lapilli tuff to tuff breccia package with abundant exotic clasts (chert, limestone) and epiclastic beds, and facies 4, an andesitic lapilli tuff to tuff breccia unit with volcanic-derived clasts and rare sedimentary beds with a crystallization age of ca. 193 Ma. Upper Hazelton Group strata consist of facies 5, a unit of fine grained tuffaceous and epiclastic rocks of rhyodacite to basalt composition with a maximum depositional age of 188 to 178 Ma and facies 6, a unit of interbedded feldspathic wacke and tuff with a maximum depositional age of ca. 168 Ma. The VMS and VMS-related epithermal occurrences in the Kitsault River area are in rocks of the upper Hazelton Group. The new maximum depositional age (ca. 188 Ma) of epiclastic rocks from the Sault Zn-Pb-Ag-Sr showing suggests that the VMS mineralization in the Kitsault River area may be slightly older than the ca. 174 Ma Au-rich VMS systems of the Eskay rift and indicates that significant precious metal-bearing VMS and/or epithermal-type systems formed well outside the main Eskay rift corridor in mainly volcaniclastic rocks.

Keywords: Kitsault River, Hazelton Group, Stikinia, Jurassic, U-Pb zircon geochronology, VMS, Eskay rift, Golden Triangle, silver, gold

1. Introduction

Deciphering the stratigraphic and timing relationships of rocks deposited in volcano-sedimentary regions is challenging because of abrupt vertical and lateral variability, high rate of deposition and erosion, and disruption by synvolcanic structures (e.g., Gibson et al., 1999; Marti et al., 2018). To establish such relationships in regions of prolonged volcanic activity, detailed mapping and facies analysis supplemented by abundant geochronological sampling are needed.

The Kitsault River area is ca. 50 km southeast of Stewart along the west-central margin of Stikinia (Fig. 1) and at the southern end of the Iskut-Stewart mineral belt, which forms part of the informally named 'Golden Triangle' (Fig. 2). It is within the traditional lands of the Nisga'a, Gitanyow, Tsetsaut Skii Km Lax Ha, and Metlakatla First Nations. The area hosts significant Ag-rich volcanogenic massive sulphide (VMS) deposits and showings (e.g., Dolly Varden, Torbrit, Wolf, Sault) in late Early to Middle Jurassic volcano-sedimentary rocks of the upper Hazelton Group. The host rocks were originally included in a lower Hazelton Group intermediate volcanic unit (lJHvc Fig. 3; Alldrick et al., 1986). A ca. 193 Ma U-Pb zircon age on a dacite in the footwall of the Sault showing (Mortensen and Kirkham, 1992) is consistent with ages in the lower Hazelton Group (Johnny Mountain dacite; Nelson et al., 2018). However, an upper Hazelton rhyolitic lapilli tuff from the Wolf deposit area yielded a preliminary CA-TIMS crystallization age of ca. 178 Ma (Hunter and van Straaten, 2020). This significantly younger age suggests that some or all the host rocks may be part of the upper Hazelton Group, coeval with the Iskut River Formation in the Eskay rift (Gagnon et al., 2012). Resolving the age and affinity of the host rocks is key to understanding the metallogeny of the Kitsault River area.

In this paper we refined the stratigraphy of the Hazelton Group based on mapping in the Kitsault River area and present three new CA-TIMS and three LA-ICPMS U-Pb zircon ages. These additional data help to decipher the timing of volcanism and sedimentation that were ultimately responsible for VMS- and/or epithermal mineralizing systems in the Kitsault River

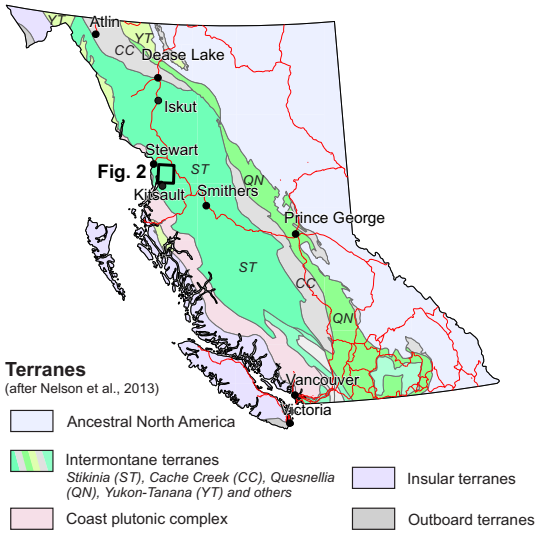

Fig. 1. Simplified terrane map of British Columbia (after Nelson et al., 2013) and location of Kitsault study area.

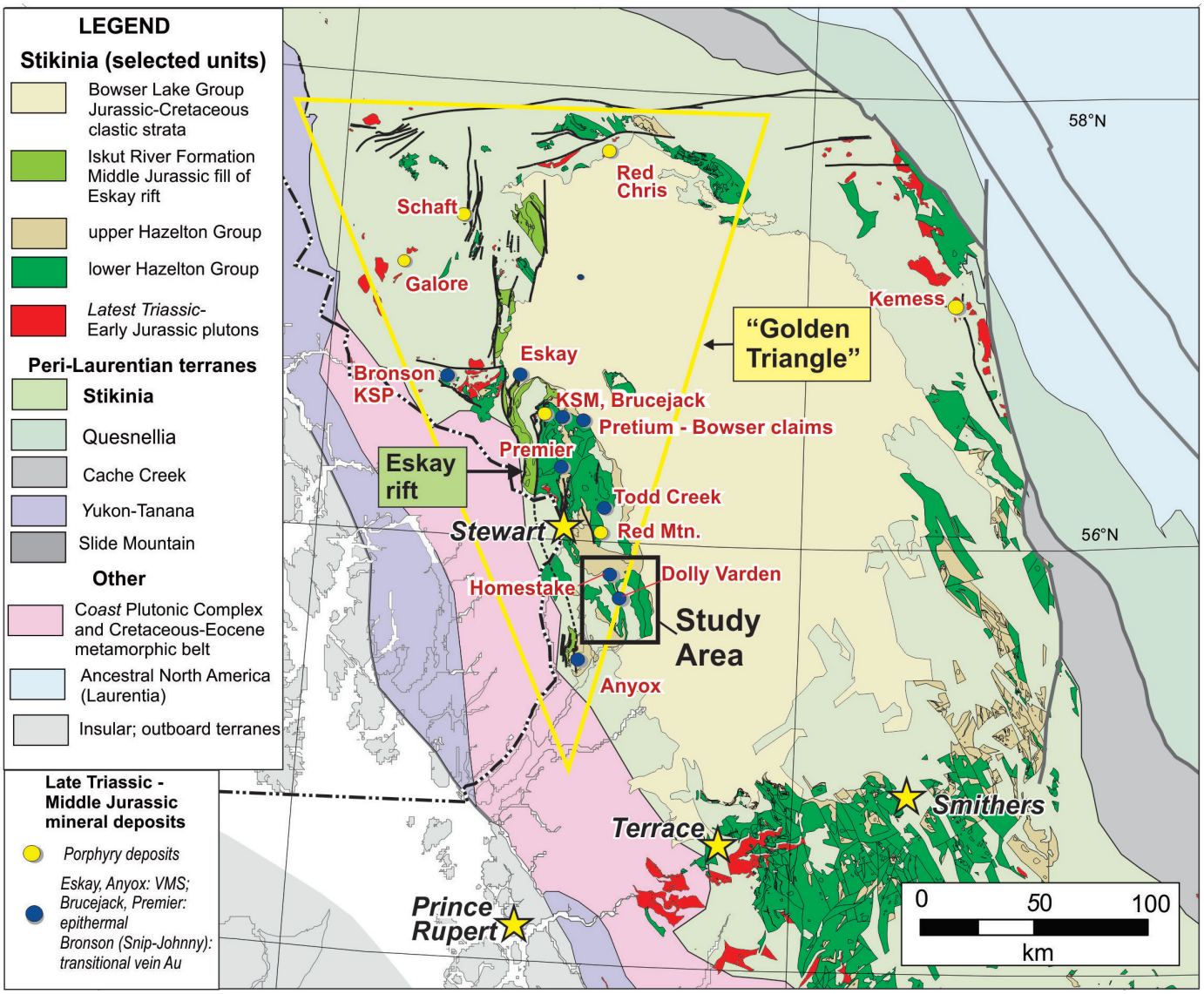

Fig. 2. Kitsault River study area with respect to major Late Triassic to Middle Jurassic mineral deposits in northwestern Stikinia (after Nelson et al., 2018).

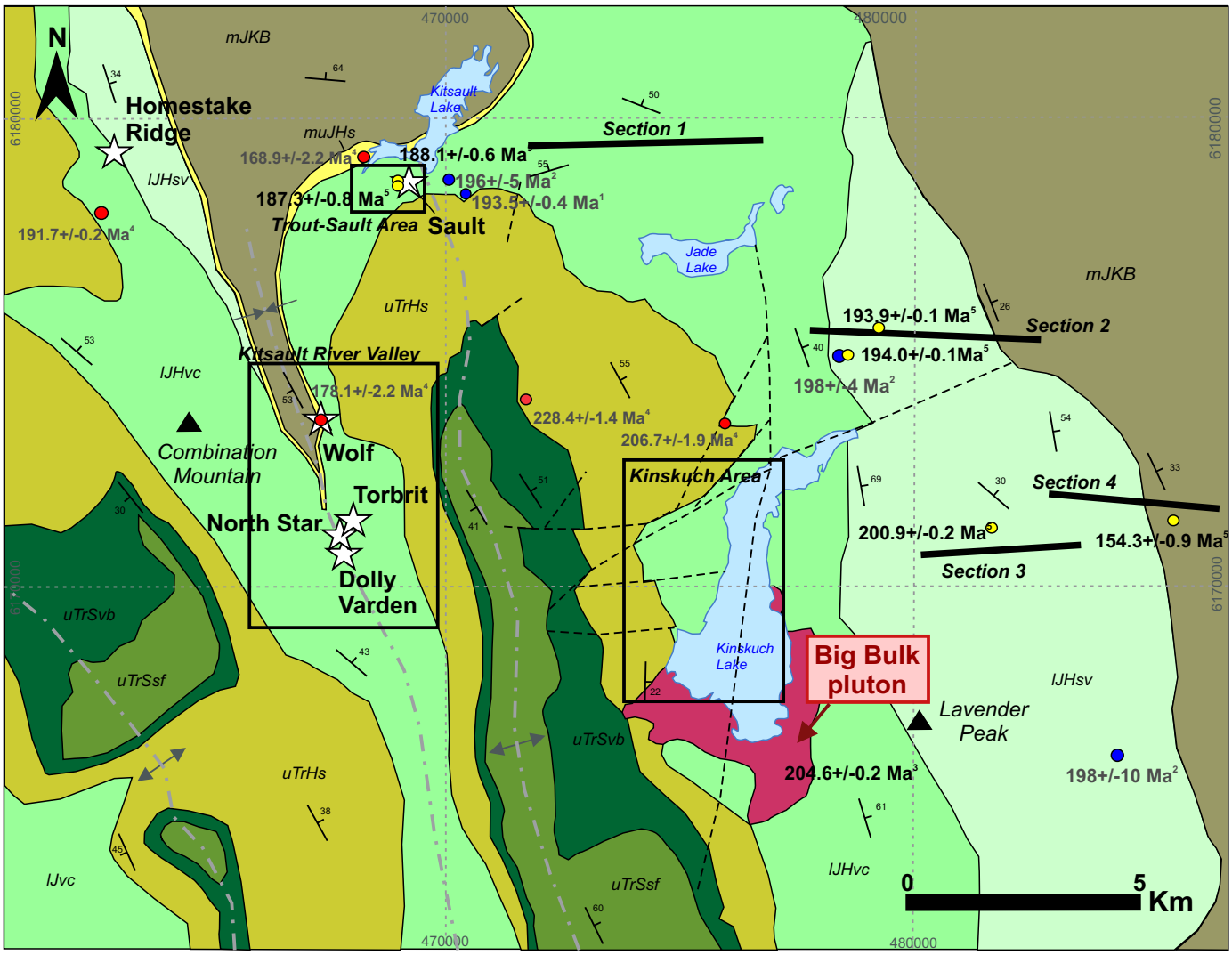

Legend

Bowser Lake Group (Middle Jurassic)

- mJKB — mudstone, sandstone, chert pebble conglomerate

Hazelton Group (Lower-Middle Jurassic)

- muJHs — upper sedimentary unit - Quock Fm.
- lJHsv — epiclastic and felsic volcanic unit
- lJHvc — intermediate volcanic unit
- uTrHs — middle sedimentary unit (transitional)

Stuhini Group (Upper Triassic)

- uTrSvb — mafic volcanic unit
- uTrSsf — lower sedimentary unit

- This study
- Hunter and van Straaten, 2020
- Historical ages
- Deposits
- Faults
- Axial trace
- Bedding

Fig. 3. Simplified geology of the Kitsault River area (after Alldrick et al., 1986; MacIntyre et al., 1994). Sources of geochronology: [1]Mortensen and Kirkham, 1992; [2]Greig and Gehrels, 1995; [3]Miller et al., 2020; [4]Hunter and van Straaten, 2020; [5] this study. Stratigraphic subdivisions are those of Alldrick et al., 1986 (cf. Table 1, Fig. 4).

area. Although the Kitsault River area lies approximately 30 km east of the projected extent of the Eskay rift, new data suggest that VMS and VMS feeder mineralization may be both Eskay rift equivalent and older.

2. Regional geology

Stikinia, a polyphase island arc terrane, is made up of the Stikine assemblage (Devonian to Mississippian; Anderson, 1989; Greig, 1992; Logan et al., 2000), the Stuhini and Takla groups (Middle to Late Triassic; Monger, 1977; Brown et al., 1996), and the Hazelton Group (latest Triassic to Middle Jurassic; Marsden and Thorkelson, 1992; Gagnon et al., 2012; Nelson et al., 2018).

The Stuhini Group consists of augite-rich basalt to basaltic andesite, crystal-lithic lapilli tuff, and epiclastic strata including greywacke, siltstone, tuff, and limestone (Brown et al., 1996). The Hazelton Group overlies the Stuhini Group and older rocks along a regional unconformity (Greig, 2014; Nelson and Kyba, 2014) and is an extensive package of volcanic and sedimentary rocks (Marsden and Thorkelson, 1992; Gagnon et al., 2012; Nelson et al., 2018). Regionally, the lower Hazelton Group comprises siliciclastic rocks of the Jack Formation (cobble to boulder granitoid-clast conglomerate, granulestone, arkosic sandstone, and thinly bedded siltstone and mudstone), the Snippaker unit (sandstone, polymictic conglomerate, siltstone and mudstone), and the Klastline and Betty Creek formations, including the Unuk River andesite unit (andesitic and lesser felsic volcaniclastic rocks; Gagnon et al., 2012; Nelson et al., 2018 and references therein). The upper Hazelton Group consists of sedimentary rocks of the Spatsizi Formation (volcanic-derived sandstone, conglomerate, mudstone, siltstone and limestone) and Quock Formation (siliceous mudstone and pale felsic tuff), subaerial dacite and rhyolite flows of the Mount Dilworth Formation, and bimodal volcanic and sedimentary rocks of the Iskut River Formation (Gagnon et al., 2012; Nelson et al., 2018). The Bowser Lake Group (Middle Jurassic to Middle Cretaceous) overlies the Hazelton Group and consists of marine and nonmarine sandstones, siltstones, and conglomerates (Tipper and Richards, 1976; Eisbacher, 1981; Evenchick and Thorkelson, 2005; Evenchick et al., 2007).

The study area hosts porphyry (e.g., Big Bulk), precious and base metal-rich epithermal (e.g., Homestake Ridge), and VMS (e.g., Dolly Varden, Torbrit, Wolf) deposits and showings, which formed in volcano-sedimentary successions of the Hazelton Group and associated plutonic rocks of Stikinia (Fig. 2; Höy, 1991; Childe, 1997; Nelson et al., 2013; Logan and Mihalynuk, 2014; Barresi et al., 2015; Nelson et al., 2018). The Big Bulk porphyry Cu showing, spatially and temporally related to the sub-Hazelton unconformity, formed during the Rhaetian (Miller et al., 2020; Hunter and van Straaten, 2020). Major porphyry deposits (Cu-Au-Ag-Mo) of the Stewart-Iskut district such as the KSM (Kerr-Sulphurets-Mitchell), Brucejack, Silbak-Premier, Big Missouri, Scottie Gold, and Red Mountain deposits, similarly formed during the Latest Triassic to Early Jurassic (Nelson and Kyba, 2014). The Homestake Ridge epithermal deposit possibly formed in the Early Jurassic (Hunter and van Straaten, 2020) which, if true, would make it synchronous with deposition of the Betty Creek Formation. Most of the major VMS deposits (e.g., Eskay Creek, Anyox) of the Stewart-Iskut district are in upper Hazelton Group rocks (Lower to Middle Jurassic) of the Iskut River Formation in the Eskay rift (Barresi et al., 2015). However, several VMS deposits and showings are in mixed sedimentary to intermediate to felsic pyroclastic rocks 10s of kilometres outside the Eskay rift (e.g., Dolly Varden, Wolf, Torbrit, Todd Creek, Pretium-Bowser project showings, Premier-Silver Hill; Hunter and van Straaten, 2020).

3. Geology of the Kitsault area

In the Kitsault area, Triassic to Cretaceous volcano-sedimentary rocks of the Stuhini, Hazelton and Bowser Lake groups form continuous, tightly folded, north-northwest-trending anticline-syncline pairs (Fig. 3; Alldrick et al., 1986; Dawson and Alldrick, 1986; Greig, 1991; Evenchick et al., 2008. Alldrick et al. (1986) loosely subdivided the area into two broad Stuhini Group volcano-sedimentary units, a middle sedimentary unit, and two Hazelton Group units, including an intermediate volcanic rock unit and an epiclastic and felsic volcanic unit that grades upward into sedimentary strata of the Bowser Lake Group (Fig. 3; Table 1).

The Stuhini Group, the oldest unit in the area consists of black siltstone, mudstone, feldspathic wacke, conglomerate, basalt, pyroclastic rock and local limestone. Alldrick et al. (1986) and Devlin (1987) separated the Stuhini Group into a ‘lower sedimentary unit’ and a ‘mafic volcanic unit’ (units uTrSsf and uTrSvb, Fig. 3).

The lowest part of the Hazelton Group section as mapped by Alldrick et al. (1986) is a basal unit consisting of siltstone, sandstone, wacke, conglomerate, and volcanic breccia containing limestone clasts (unit uTrHs, Fig. 3). Detrital zircons from basal Hazelton Group volcanic-derived sandstone and polymictic pebble conglomerate yielded preliminary maximum depositional ages of 228.4 ±1.4 Ma and 206.7 ±1.9 Ma (Hunter and van Straaten, 2020). Recent work in the Kinskuch Lake area showed that this basal unit is more extensive than mapped by Alldrick et al. (1986) and includes impressive megaclast-bearing conglomerate (with clasts up to 120 m) that formed along prominent northeast-trending faults (Kinskuch conglomerates; Miller et al., 2020). These faults were active as early as the latest Triassic and display strike-slip to oblique slip movement, interpreted to have resulted in local zones of extension and small, pull-apart basins (Miller et al., 2020). The emplacement of the Big Bulk porphyry stock (Fig. 3; 204.61 ±0.18 Ma) and associated Cu-Au mineralization is interpreted to coincide this period of extension (Miller et al., 2020). Late Triassic normal faulting and deposition of coarse conglomerates during the transition from the Stuhini Group to the Hazelton Group is reported throughout the Stewart-Iskut district (Nelson and Kyba, 2014; Kyba and Nelson, 2015; Febbo et al., 2019).

Table 1. Evolution of lithostratigraphic subdivisions in the Kitsault area, including informal units used in this study.

		Alldrick et al., 1986	**Hunter and van Straaten (2020)**	**This study**
Bowser Lake Group		Bowser Lake Group (mJKB)	Bowser Lake Group	Bowser Lake Group
upper Hazelton Group	Quock Formation	upper sedimentary unit (muJHS)		facies 6
				facies 5 (Kitsault unit)
	Spatsizi Formation			
lower Hazelton Group	Betty Creek Formation; includes Unuk River andesite unit	epiclastic and felsic volcanic unit (lJHsv) intermediate volcanic unit (lJHvc)	facies 3, sub-facies 3a; facies 1 and 2	facies 3 and 4 sub-facies 4a
		middle sedimentary unit (uTrHs) (transitional)	sub-facies 3b	facies 1 and 2 (Kinskuch unit)
Stuhini Group		mafic volcanic unit (uTrSvb) lower sedimentary unit (uTrSsf)		

The basal Hazelton Group unit is overlain by a thick section of andesitic pyroclastic rocks (lapilli tuff to tuff breccia), and lesser lenses of mudstone, limestone, and chert referred to as the 'intermediate volcanic unit' (lJHvc, Fig. 3) by Alldrick et al. (1986). Dacite-andesite flows to lapilli tuff to tuff breccia from this unit provided ages between 198 Ma and 193 Ma (Mortensen and Kirkham, 1992; Greig and Gehrels, 1995). This unit is broadly equivalent to the Unuk River andesite of the Betty Creek Formation as defined in the McTagg anticlinorium (Lewis, 2013; Gagnon et al., 2012; Nelson et al., 2018; Hunter and van Straaten, 2020).

At the base of the upper Hazelton Group is a unit of volcanic breccia, sandstone, conglomerate, lesser dacite and andesite flows, pyroclastic rocks, and minor siltstone and limestone that Alldrick et al. (1986) referred to as the 'epiclastic and felsic volcanic unit' (unit lJHsv, Fig. 3). The upper Hazelton Group pyroclastic and epiclastic rocks are inferred to record shallow-water sedimentation punctuated by gravity slide-generated mass flow (McCuaig and Sebert, 2017). Although this unit is predominantly andesitic (McCuaig and Sebert, 2017), the compositions range from basalt to rhyolite. A rhyolitic lapilli tuff collected from drill core at the Wolf deposit provided a LA-ICP-MS U-Pb zircon age of 178 ±2.2 Ma. South of Kitsault Lake, a distinct horizon of epiclastic strata extends for ca. 5 km and is host to the Sault showing (Fig. 3). The horizon is a 20-100 m thick, northeast-trending, bedded zone of calcareous and locally graphitic sedimentary and felsic volcaniclastic rock that likely represents a hiatus in Hazelton Group volcanism. Overlying the 'epiclastic and felsic volcanic unit' is an 'upper sedimentary unit' of fossiliferous greywacke with belemnites and bivalves, black siltstone, sandstone, limestone, and arkose (Fig. 3; Alldrick et al., 1986). A volcanic-derived sandstone with belemnite casts provided a maximum deposition age of 168.9 ±2.2 Ma (Hunter and van Straaten, 2020), which suggests the 'upper sedimentary unit is likely a part of the Quock Formation (Hunter and van Straaten, 2020).The Bower Lake Group gradationally overlies the upper Hazelton Group strata and consists of interbedded siltstone, sandstone and chert-pebble conglomerate (Alldrick et al., 1986; Hunter and van Straaten, 2020).

4. Updated preliminary lithostratigraphy of the Hazelton Group

Below we update facies assignments used by Hunter and van Straaten (2020) and reconsider the stratigraphy proposed by Alldrick et al. (1986) for the Hazelton Group in the Kitsault area (Fig. 4, Table 1).

4.1. Lower Hazelton Group

4.1.1. Facies 1; Volcanic-derived sandstone, conglomerate, and mega-conglomerate

Based on detailed mapping by Miller et al. (2020), we redefine facies 1 (cf. Hunter and van Straaten, 2020; Table 1) the very basal unit of the Hazelton Group in the Kitsault River area (Fig. 4). It consists of massive to weakly stratified pebble to large boulder, polymictic conglomerate (Kinskuch conglomerate) with rounded to angular clasts, locally interbedded with and incised by coarse-grained feldspathic sandstone with lithic fragments and tuff (Fig. 5a; Miller et al., 2020). Clasts range up to 120 m and include sandstone, mudstone, limestone, chert, and volcanic rock-derived clasts of Stuhini Group augite-phyric basalt and Hazelton Group hornblende-plagioclase-phyric andesite (Miller et al., 2020). Maximum depositional ages yielded by U-Pb analysis of detrital zircons from a basal Hazelton Group volcanic-derived sandstone (ca. 228.4 ±1.4 Ma) and a polymictic pebble conglomerate (206.7 ±1.9 Ma), and a U-Pb zircon crystallization age from a porphyry diorite stock dated at 204.6 ±0.18 Ma constrain facies 1 to the Rhaetian (Hunter and van Straaten, 2020; Miller et al., 2020).

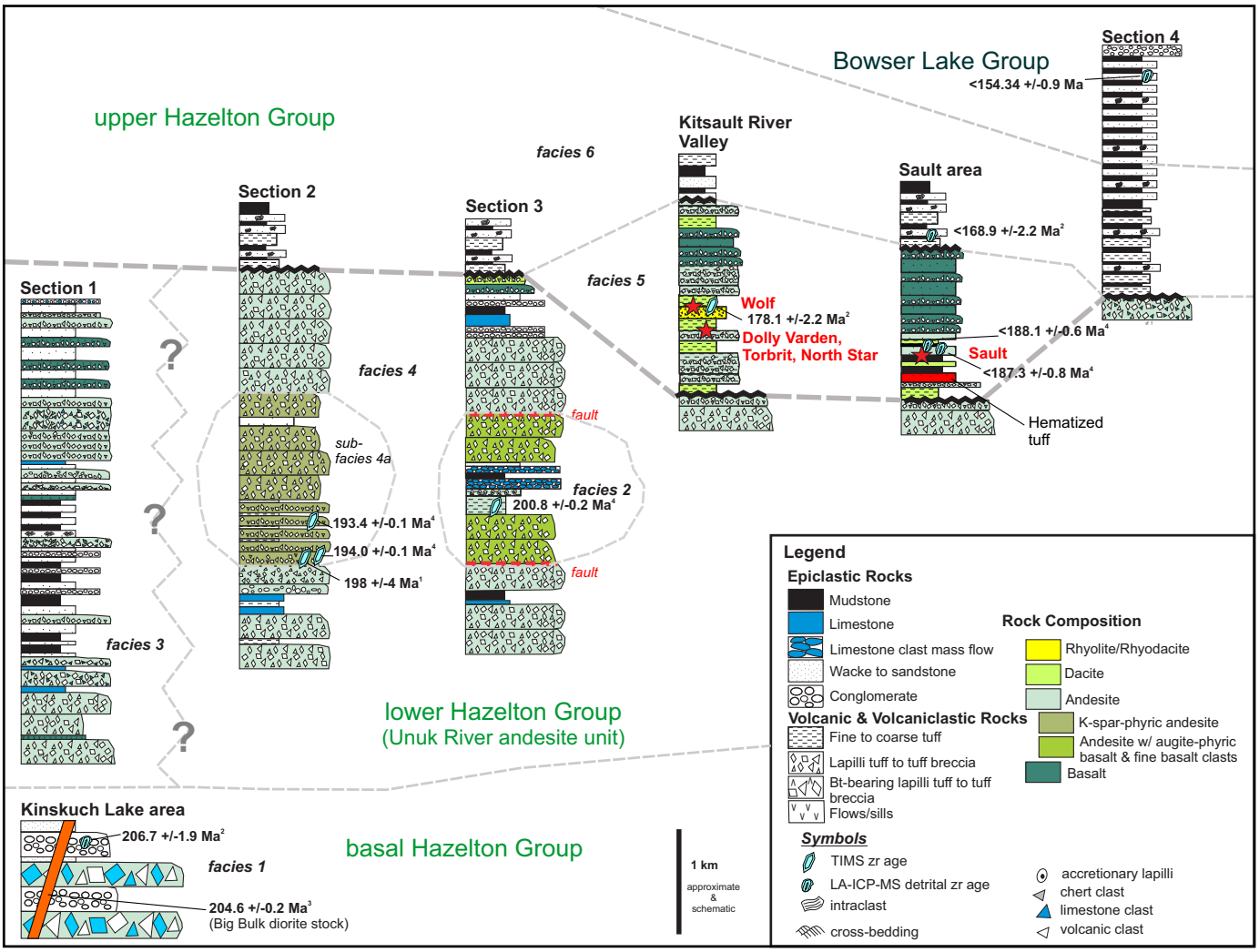

Fig. 4. Updated stratigraphy and lithostratigraphic correlations in the Kitsault River area. Sections are schematic composites compiled from map data. U-Pb zircon ages are from [1]Greig and Gehrels (1995), [2]Hunter and van Straaten (2020), [3]Miller et al. (2020), and [4]this study. See Fig. 3 for locations.

4.1.2. Facies 2; Hornblende-plagioclase-phyric volcanic rocks, tuff, sandstone, conglomerate, and limestone

Facies 2 (redefined from facies 3 of Hunter and van Straaten, 2020; Table 1) is exposed along a prominent north-trending ridge between glacier-covered valleys 3.7 km east of Kinskuch Lake (Fig. 3). It consists of lapilli tuff, lapillistone, and tuff breccia, and rocks such as limestone, limestone clast-rich conglomerate, conglomerate, fine-grained sandstone, and mudstone (Figs. 4, 5b). The tuff breccias locally contain abundant augite-phyric basalt, and hornblende-plagioclase-phyric volcanic clasts. Although basal and upper contacts were not observed, the unit shares similarities to rocks described by Miller et al. (2020) that lie above the Kinskuch conglomerate. A tuff sample yielded an inferred depositional age of ca. 201 Ma (see below).

4.1.3. Facies 3; Hornblende-plagioclase-phyric pyroclastic and epiclastic facies

Facies 3 (grouped facies 1 and 2 in Hunter and van Straaten, 2020; Table 1) consists of poorly sorted lapilli tuff to tuff breccia with subrounded to subangular hornblende-plagioclase-phyric clasts, plus limestone and chert clasts in a hornblende-plagioclase-crystal-bearing matrix (Fig. 4). The lapilli tuff to tuff breccia is intercalated with extensive thick recessive beds of siltstone and fine-grained feldspathic sandstone in repeating fining-upward sequences with 10-50 m-thick micritic limestone, feldspathic sandstone, and conglomerate and rare chert (Fig. 5c). The facies contains local 50-100 m thick beds of biotite-bearing, matrix- to clast-supported lapilli tuff to tuff breccia with subrounded to subangular 3 mm to 10 cm biotite-plagioclase-phyric clasts in a biotite and plagioclase crystal-bearing matrix. A 5 m thick, coherent, augite-plagioclase-phyric unit is near the base of the unit.

4.1.4. Facies 4; hornblende-plagioclase-phyric volcanic facies

Facies 4 is a thick to very thick-bedded, hornblende-plagioclase lapilli tuff, lapillistone, tuff breccia and pyroclastic

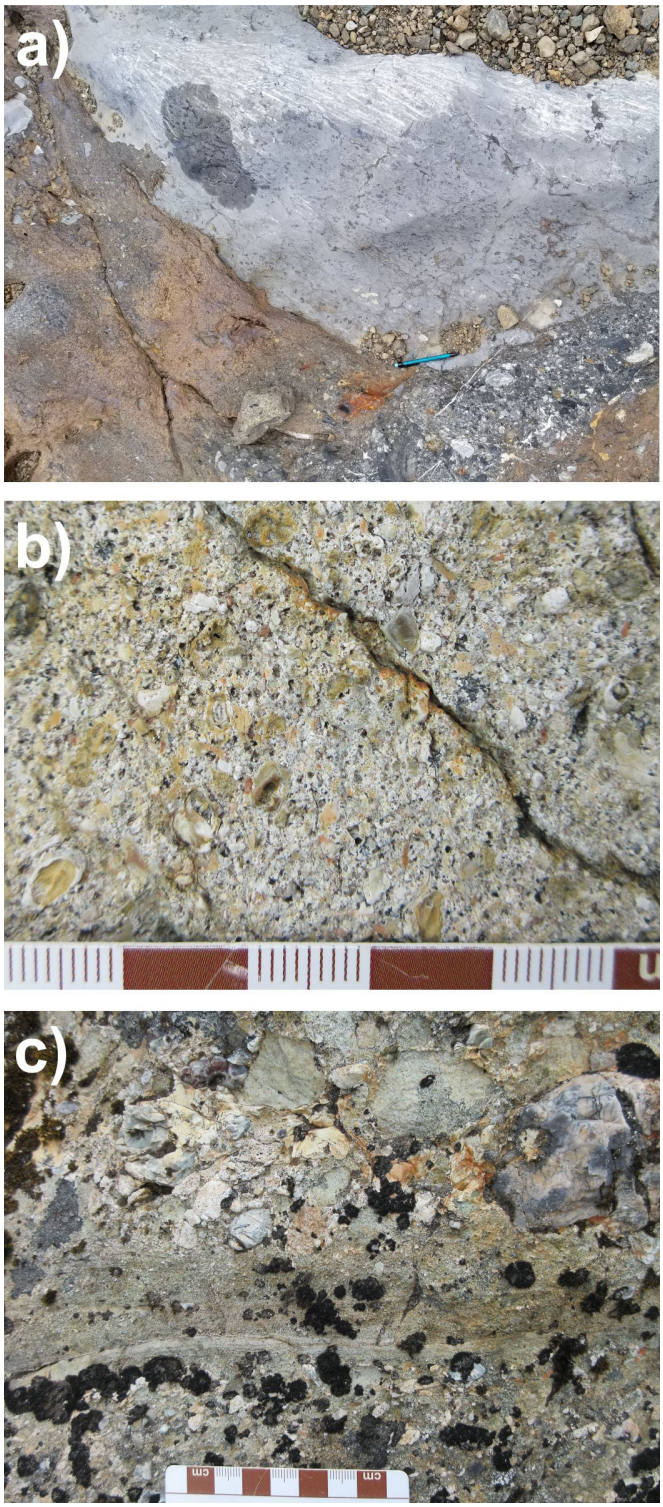

Fig. 5. Representative photographs of facies 1, 2 and 3. **a)** Facies 1, Kinskuch conglomerate with grey limestone megaclast resting within irregularly interbedded coarse-grained sandstone and limestone-chert pebble conglomerate (UTM 475174E; 6170818N). **b)** Facies 2, clast-supported lapillistone with abundant accretionary lapilli (UTM 480620E; 6170990N). **c)** Facies 3, beds of clast- to matrix-supported polymictic conglomerate with rounded to subrounded clasts of chert, fine-grained tuff, and various plagioclase porphyritic fragments separated by a volcanic-derived sandstone layer (UTM 474247E; 6179466N). UTM: NAD 83, Zone 9.

breccia (Fig. 4). It contains subangular to subrounded, moderately to poorly sorted clasts that range from 0.4 to 60 cm in a fine- to coarse-ash matrix containing 2-5% hornblende and abundant plagioclase crystals (Fig. 6a). Volcanic clasts are predominant and consist of hornblende- and plagioclase-phyric (1-5 mm) fragments with varying phenocryst percentages (3-20%); aphyric volcanic and limestone clasts are local. The unit varies from matrix- to clast-supported and is massive to weakly graded. Locally, laterally discontinuous beds up to 2 m thick of graded coarse- to fine-tuff separate layers of lapilli tuff to tuff breccia. Locally interbedded with the polymictic lapilli tuff to tuff breccia are maroon, poorly sorted, thick-bedded, largely monomictic, matrix-supported lapilli tuff to tuff breccia with clasts that display ameboid to wispy cuspate-lobate clast boundaries.

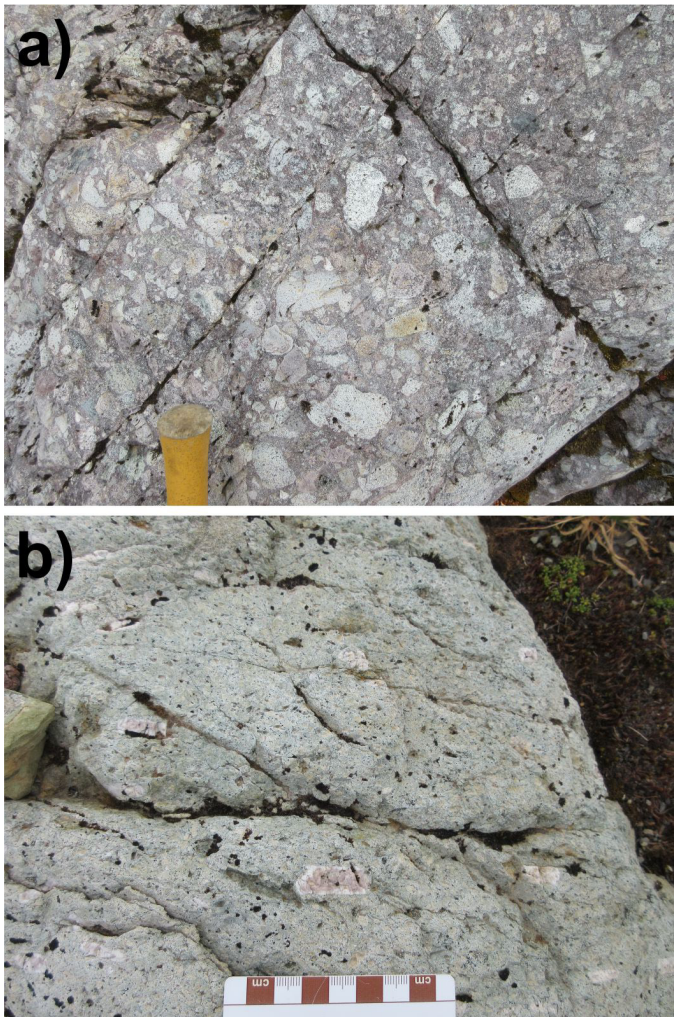

Fig. 6. Lower Hazelton Group facies 4 rocks. **a)** Clast-supported lapillistone to lapilli tuff with subrounded to subangular hornblende-feldspar-phyric clasts with variable hornblende and plagioclase percentages (UTM 479119E; 6172627N). **b)** Hornblende-plagioclase-K-feldspar porphyry with zoned K-feldspar crystals up to 3 cm long aligned along bedding (UTM 479658E; 6175426N). UTM: NAD 83, Zone 9.

4.1.4.1. Sub-facies 4a; K-Feldspar and plagioclase porphyry and crystal tuff

Sub-facies 4a, originally placed in sub-facies 3a in Hunter and van Straaten (2020), is a distinct K-feldspar, hornblende, and plagioclase porphyry and crystal tuff exposed northeast of Kinskuch Lake and in a small (ca. 5 m) area north of Lavender Peak (Fig. 4). The unit varies from a massive, to flow-banded coherent rock, to plagioclase- and K-feldspar-bearing crystal tuff with K-feldspar crystals aligned along bedding (Fig. 6b; Hunter and van Straaten, 2020). The main exposure consists of a discontinuous unit that appears to be partially intercalated with facies 4 lapilli tuff to tuff breccia but contact relationships are obscured by weak to moderate disseminated sericite, limonite, and pyrite alteration. Zircons from a sub-facies 4a sample yielded a crystallization age of ca. 193 Ma (see below).

4.2. Upper Hazelton Group

4.2.1. Facies 5; Intermediate to mafic tuff, volcanic sandstone, local rhyolite to rhyolite tuff

Facies 5, in the Kitsault Valley and near the Sault showing ('intermediate volcanic unit' lJHvc of Fig. 3), consists of interbedded pyroclastic (tuff, lapilli tuff, crystal tuff, local tuff breccia) and more voluminous epiclastic sandstone to small pebble conglomerate (reworked tuff, lapilli tuff) with a combination of volcanic and sedimentary clast types (Figs. 4, 7a; McCuaig and Sebert, 2017). The unit is mainly andesitic but varies from basaltic to dacitic and locally, rhyolitic (McCuaig and Sebert, 2017). Minor rhyolites to rhyodacite tuffs are at the Wolf deposit and in the footwall of the Sault showing (McCuaig and Sebert, 2017). A rhyolitic lapilli tuff from the Wolf deposit yielded a preliminary CA-TIMS crystallization age of 178 ±2.2 Ma (Hunter and van Straaten, 2020). The main basaltic section is exposed in the hanging wall of the Dolly Varden, Torbrit, North Star and Sault deposits and showings (McCuaig and Sebert, 2017). These basaltic rocks consist mainly of intercalated tuff and lapilli tuff to volcanic sandstone and conglomerate with variable amounts of volcanic-derived lithic clasts and vitric lapilli (Fig. 7b). The basaltic units appear to be discontinuous and their contacts with both the underlying volcaniclastic rocks and overlying sedimentary rocks have not been observed. Detrital zircons from a sandstone near the base of the section at the Sault showing yielded a maximum depositional age of ca. 187 Ma; another sample taken 50 m away yielded a maximum depositional age of ca. 188 Ma (see below). These comparatively young ages suggest that this sequence is in the upper Hazelton Group.

4.2.2. Facies 6; Interbedded feldspathic wacke, siltstone, tuff, minor black mudstone, limestone

Extensive, planar-bedded mudstone (locally black), siliceous siltstone, feldspathic wacke, limestone, and fine tuff to lapilli tuff is at the top of the Hazelton Group. The unit appears to have gradational contacts with underlying Hazelton Group volcano-sedimentary rocks and overlying Bowser Lake Group sedimentary rocks. The unit is distinguished by light-brown weathering tuff beds that are 3-20 cm thick and consist of fine to coarse ash and 1-3 mm wispy lapilli. The tuff beds are intercalated with the mudstone-siltstone-sandstone beds (Fig. 7c) and decrease in number up section (Fig. 4). Local muddy limestone beds at the base of the unit contain rare belemnite casts. Detrital zircons from a sandstone near the southeast arm of Kitsault Lake (Fig. 3) yielded a preliminary maximum depositional age of 168.9 ±2.2 Ma (Bajocian or younger; Hunter and van Straaten, 2020). Facies 6 is interpreted to be a part of the Quock Formation as described by Gagnon et al. (2012).

4.3. Bowser Lake Group

4.3.1. Interbedded feldspathic wacke, mudstone, and chert clast-bearing pebble conglomerate

Using criteria similar to Evenchick et al. (2010), the disappearance of facies 6 tuffaceous beds and the appearance of chert-pebble conglomerate are taken to mark the base of the Bowser Lake Group. In the Kitsault River area, the Bowser Lake Group consists of interbedded grey to brown, laminated- to medium-bedded, fine- to medium-grained feldspathic wacke and mudstone with local beds of chert-pebble conglomerate (Figs. 4, 7d). Load casts and flame structures are well developed, and 1-5 cm subrounded mudstone intraclasts are developed throughout the unit. The chert-pebble conglomerate forms metre-scale beds containing subrounded granules and pebbles in a coarse sandstone matrix. A sandstone sample yielded a maximum depositional age of ca. 154 Ma (see below).

5. Geochronology

Presented here are the analytical results from three Laser Ablation Inductively Coupled Plasma Mass Spectrometry (LA-ICPMS) and three Chemical Abrasion Thermal Ionization Mass Spectrometry (CA-TIMS) U-Pb zircon samples (Fig. 3). The samples, collected in 2019 and 2020, were analyzed at the Pacific Centre for Isotopic and Geochemical Research (The University of British Columbia). The complete analytical dataset for the CA-TIMS and LA-ICP-MS analyses will be presented elsewhere (Hunter et al., 2022).

5.1. Analytical procedures

5.1.1. LA-ICP-MS methods

Rock samples that underwent standard mineral separation procedures zircons were handpicked in alcohol and mounted in epoxy, along with reference materials. Grain mounts were wet ground with carbide abrasive paper and polished with diamond paste. Cathodoluminescence (CL) imaging was carried out on a Philips XL-30 scanning electron microscope (SEM) equipped with a Bruker Quanta 200 energy-dispersion X-ray microanalysis system at the Electron Microbeam/X-Ray Diffraction Facility (EMXDF) at the University of British Columbia. An operating voltage of 15 kV was used, with a spot diameter of 6 μm and peak count time of 17-27 seconds. After removal of the carbon coat the grain mount surface was washed with mild soap and rinsed with high purity water. Before

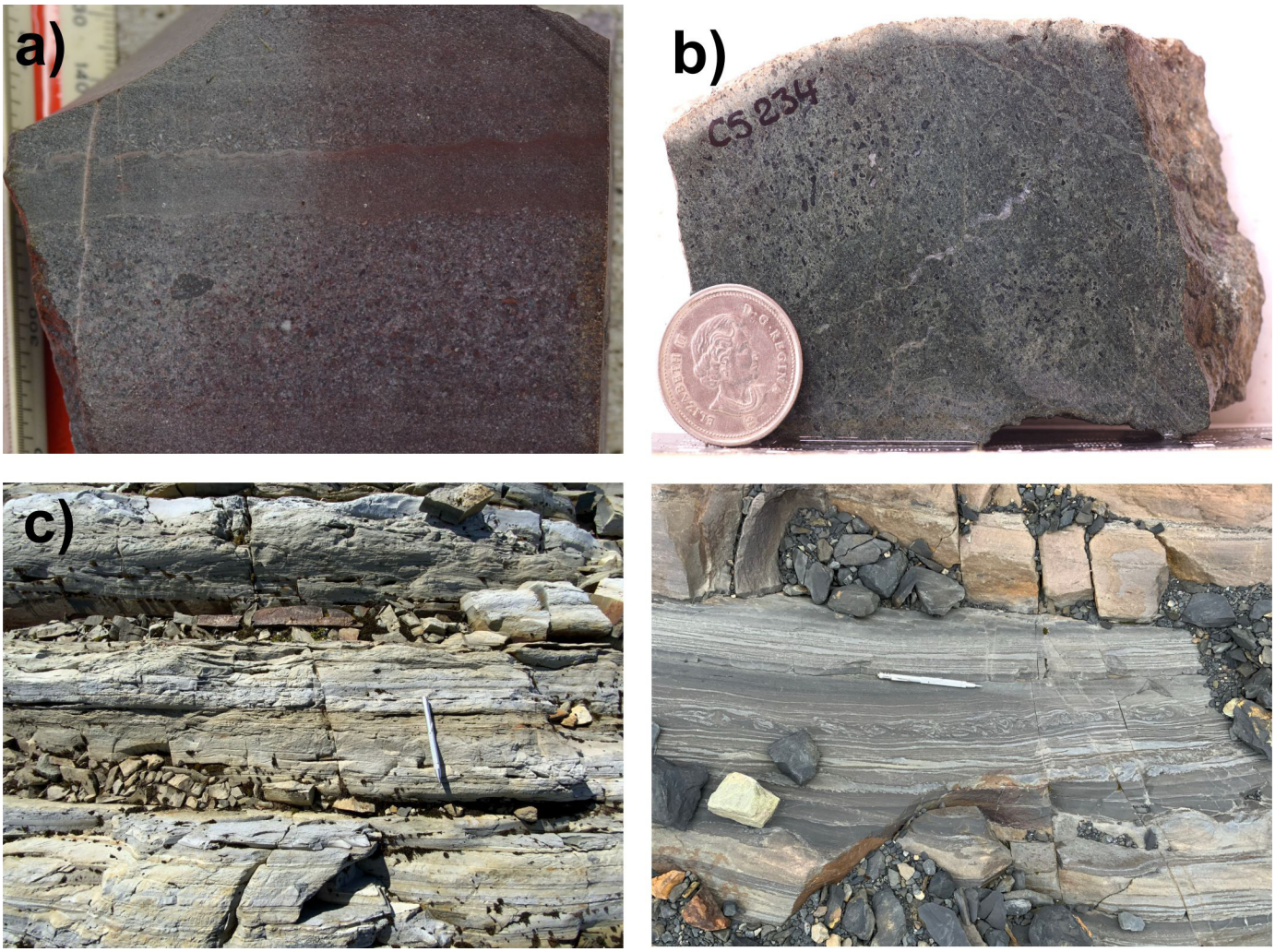

Fig. 7. Representative photos of upper Hazelton Group and Bowser Lake Group units. **a)** Facies 5, well-bedded, fine to very coarse-grained epiclastic sandstone with small volcanic-derived pebbles northwest of the Wolf deposit (UTM 467281E; 6173275N. **b)** Facies 5, dark green mafic lapilli tuff with pebble-sized glassy and weakly amygdaloidal clasts in a crystal- and ash-rich matrix (UTM 467801E; 6178200N). **c)** Facies 6, interbedded fine and course tuff (UTM 462065E; 6159694N). **d)** Bowser Lake Group, finely interlayered mudstone and siltstone (dark toned) and fine-grained sandstone (light toned) with soft-sediment deformation (UTM 463493E; 6183729N). UTM: NAD 83, Zone 9.

analysis the grain mount surface was cleaned with 3 N HNO_3 acid and again rinsed with high purity water to remove any surficial Pb contamination that could interfere with the early portions of the spot analyses.

Analyses were conducted using a Resonetics RESOlution M-50-LR, which contains a Class I laser device equipped with a UV excimer laser source (Coherent COMPex Pro 110, 193 nm, pulse width of 4 ns) and a two-volume cell designed and developed by Laurin Technic Pty. Ltd. (Australia). This sample chamber allowed investigating several grain mounts in one analytical session. The laser path was fluxed by N_2 to ensure better stability. Ablation was carried out in a cell with a volume of approximately 20 cm^3 and a He gas stream that ensured better signal stability and lower U-Pb fractionation (Eggins et al., 1998). The laser cell was connected via a Teflon squid to an Agilent 7700x quadrupole ICP-MS housed at PCIGR. A pre-ablation shot was used to ensure that the spot area on grain surface was contamination-free. Samples and reference materials were analyzed for 36 isotopes: ^{7}Li, ^{29}Si, ^{31}P, ^{43}Ca, ^{45}Sc, ^{49}Ti, Fe (^{56}Fe, ^{57}Fe), ^{89}Y, ^{91}Zr, ^{93}Nb, ^{95}Mo, ^{98}Mo, ^{139}La, ^{140}Ce, 141Pr, ^{146}Nd, 147Sm, ^{153}Eu, ^{157}Gd, ^{159}Tb, ^{163}Dy, ^{165}Ho, ^{166}Er, ^{169}Tm, ^{172}Lu, ^{177}Hf, ^{181}Ta, ^{202}Hg, Pb (^{204}Pb, ^{206}Pb, ^{207}Pb, ^{208}Pb), ^{232}Th, and U (^{235}U, ^{238}U) with a dwell time of 0.02 seconds for each isotope. Pb/U and Pb/Pb ratios were determined on the same spots along with trace element concentration determinations. These isotopes were selected based on their relatively high natural abundances and absence of interferences. The settings for the laser were: spot size of 34 µm with a total ablation time of 30 seconds, frequency of 5 Hz, fluence of 5 J/cm^2, power of 7.8 mJ after attenuation, pit depths of approximately 15 µm, He flow rate of 800 mL/min, N_2 flow rate of 2 mL/min, and a carrier gas (Ar) flow rate of 0.57 L/min.

Reference materials were analyzed throughout the sequence to allow for drift correction and to characterize downhole fractionation for Pb/U and Pb/Pb isotopic ratios. For trace

elements, NIST 612 glass was used for both drift correction and trace element calibration, with sample spacing between every five to eight unknowns, and ^{90}Zr was used as the internal standard assuming stoichiometric values for zircon. NIST 610 glass was analyzed after each NIST 612 analysis and used as a monitor reference material for trace elements. For U-Pb analyses, natural zircon reference materials were used, including Plešovice (Sláma et al., 2008; 337.13 ±0.33 Ma) or 91500 (Wiedenbeck et al., 1995; 2004; 1062.4 ±0.4 Ma, $^{206}Pb/^{238}U$ date) as the internal reference material, and both Temora2 (Black et al., 2004; 416.78 ±0.33 Ma) and Plešovice and/or 91500 as monitoring reference materials; the zircon reference materials were placed between the unknowns in a similar fashion as the NIST glasses. Raw data were reduced using the Iolite 3.4 extension (Paton et al., 2011) for Igor ProTM yielding concentration values, Pb/U and Pb/Pb dates, and their respective propagated uncertainties. For all LA-ICPMS analyses, we excluded individual grain ages with <0.05 probability of concordance (calculated using the Isoplot routine of Ludwig, 2012). We calculated preliminary maximum depositional ages for detrital zircon samples using the youngest statistical population (YSP) in a probability density plot (PDP) constructed in Isoplot (Ludwig, 2012), which follows the methods of Herriott et al. (2019).

5.1.2. CA-TIMS methods

CA-TIMS procedures described here are modified from Mundil et al. (2004), Mattinson (2005) and Scoates and Friedman (2008). After rock samples underwent standard mineral separation procedures, zircons were handpicked in alcohol. The clearest, crack- and inclusion-free grains were selected, photographed and then annealed in quartz glass crucibles at 900°C for 60 hours. Selected individual annealed grains are transferred into clean 300 mL PFA microcapsules (crucibles) and ultrapure HF (up to 50% strength, 500 mL) and HNO_3 (up to 14 N, 50 mL) were added for chemical abrasion leaching step. They were placed in 125 mL PTFE liners (up to 15 per liner) and about 2 mL HF and 0.2 mL HNO_3 of the same strength as acid in beakers containing samples were added to the liners. The liners were then slid into stainless steel Parr™ high pressure dissolution devices, which were sealed and brought up to a maximum of 190°C for 8-16 hours (typically 175°C for 12 hours). Beakers are removed from liners and zircon is separated from leachate. Zircons were rinsed with >18 MΩ.cm water and sub-boiled acetone. Then 200 mL of sub-boiled 6N HCl was added and beakers were set on a hotplate at 80-130°C for 30 minutes and again rinsed with water and acetone. Masses were estimated from the dimensions (volumes) of grains. For full dissolution in same microcapsules (crucibles), about 50 mL 50% HF and 5 mL 14 N HNO_3 were added and each was spiked with a $^{233-235}U$-^{205}Pb tracer solution (EARTHTIME ET535), capped and again placed in a Parr liner (up to 15 microcapsules per liner). HF and nitric acids in a 10:1 ratio, respectively, were added to the liner, which was then placed in Parr high pressure device and dissolution was achieved at 220°C for 40 hours. The resulting solutions were dried on a hotplate at 130°C, 50 mL 6N HCl was added to microcapsules and fluorides were dissolved in high pressure Parr devices for 12 hours at 180°C. HCl solutions were transferred into clean 7 mL PFA beakers and dried with 2 mL of 0.5 N H_3PO_4. Samples were loaded onto degassed, zone-refined Re filaments in 2 mL of silicic acid emitter (Gerstenberger and Haase, 1997).

Isotopic ratios were measured with single collector VG 54R thermal ionization mass spectrometers equipped with analogue Daly photomultipliers. Analytical blanks were 0.1 pg for U and up to 1 pg for Pb. U fractionation was determined directly on individual runs using the EARTHTIME ET535 mixed $^{233-235}U$-^{205}Pb isotopic tracer and Pb isotopic ratios were corrected for fractionation of 0.40 ±0.04%/amu, based on replicate analyses of NBS-982 reference material and the values recommended by Thirlwall (2000). Data reduction employed the excel-based program of Schmitz and Schoene (2007). Unless otherwise noted all errors were quoted at the 2 sigma or 95% level of confidence. Isotopic dates are calculated with the decay constants l_{238}=1.55125E-10 and l_{235}=9.8485E-10 (Jaffe et al., 1971) and a $^{238}U/^{235}U$ ratio of 137.88. EARTHTIME U-Pb synthetic solutions were analyzed on an on-going basis to monitor the accuracy of results. Standard concordia diagrams were constructed and regression intercepts, weighted averages calculated with Isoplot (Ludwig, 2003; 2012).

5.2. Results

5.2.1. Sample 19RHU-10-2a, fine tuff from facies 2 (CA-TIMS)

The sample from facies 2 was collected 3.7 km east of Kinskuch Lake along a prominent outcrop ridge with almost near continuous exposure (Fig. 3). The sample is from an 8.5 m thick fine tuff that is interbedded with coarse tuff on the mm- to cm-scale (Fig. 8a). This unit is conformably underlain and overlain by m-scale beds of muddy limestone to calcareous mudstone, medium-grained sandstone, as well as tuff, lapilli tuff (locally containing accretionary lapilli) and tuff breccia locally containing augite-phyric and basalt clasts. Nineteen anhedral to subhedral zircons were extracted from the sample and five of these were selected for CA-TIMS analysis. They range in size from 100 to 150 µm and have 1:2 aspect ratios. Out of the five analyzed zircons, one provided a $^{206}Pb/^{238}U$ date of 201.24 Ma ±0.24 Ma and is inferred to be a xenocryst or antecryst. The remaining four grains overlap on concordia (Fig. 9a) and have a weighted mean $^{206}Pb/^{238}U$ age of 200.85 ±0.15 Ma (MSWD=1.63), which is inferred to be the depositional age of the tuff (Fig. 9b).

5.2.2. Sample 19RHU-1-1, potassium feldspar-phyric andesite from sub-facies 4a (CA-TIMS)

Sample 19RHU-1-1 was collected from sub-facies 4a northeast of Kinskuch Lake (Fig. 3). It is a coherent, medium-grained andesite and consists primarily of plagioclase, 3% hornblende and 2-3% potassium feldspar phenocrysts between 1 and 3 cm in size (Fig. 8b). It surrounded by m-scale beds

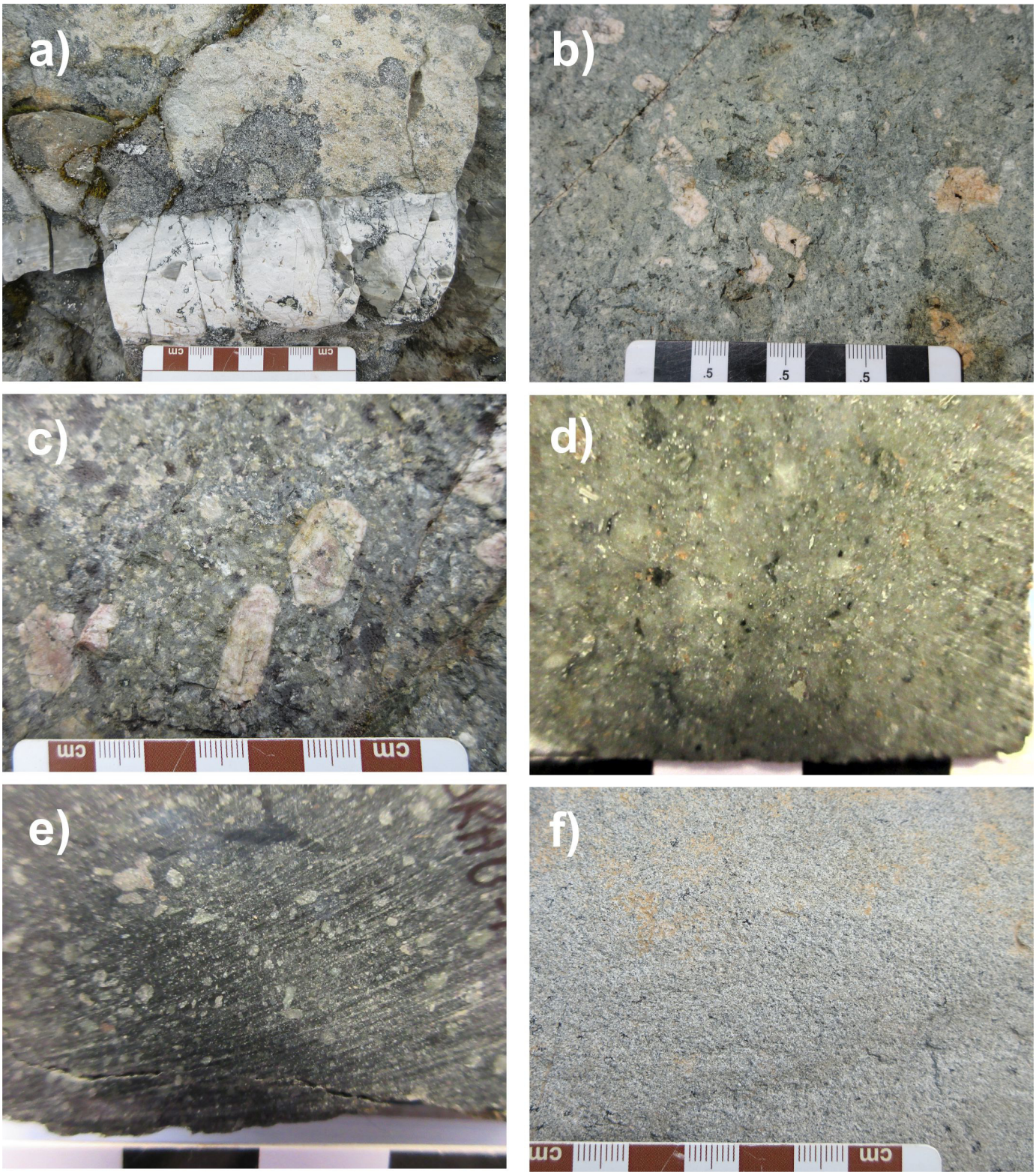

Fig. 8. Photographs of geochronological samples. **a)** Facies 2, sample 19RHU-10-2a, white weathering fine tuff bed interbedded with coarse to fine lapilli tuff (UTM 480620E; 6170990N). **b)** Sub-facies 4a sample 19RHU-1-1, massive, K-feldspar-plagioclase-hornblende-phyric andesite porphyry with cm phenocrysts of K-feldspar (UTM 479953E; 6175692N). **c)** Sub-facies 4a sample 19RHU-4-2, same as above with K-feldspar phenocrysts up to 3 cm long (UTM 478931E; 6175118N). **d)** Facies 5 sample 20RHU-1-14, light green, crystal tuff to lapilli tuff with 1-3 mm black vitric lapilli (UTM 469159E; 6178502N). **e)** Facies 5 sample 20RHU-1-16 , dark gray, poorly-sorted, graphitic fine-grained sandstone with 2-3 mm blocky plagioclase fragments and irregular 1-3 mm dark gray vitric clasts (UTM 469160E; 6178519N). **f)** Bowser Lake Group sample 19RHU-16-1, white weathering, coarse-grained feldspathic wacke (UTM 485465E; 6171061N). UTM: NAD 83, Zone 9.

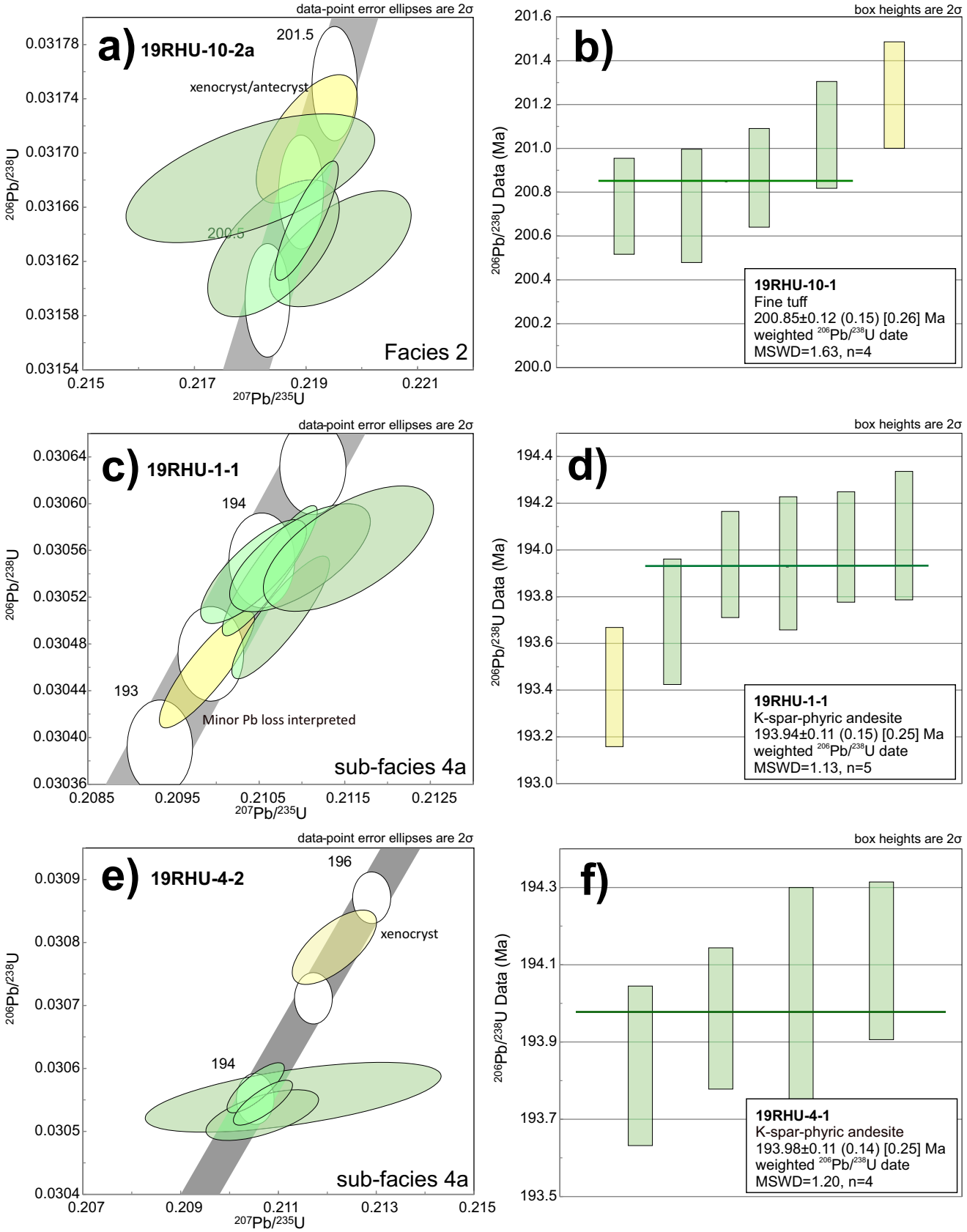

Fig. 9. CA-TIMS analyses plots of zircons. **a)** Concordia plot of zircons from sample 19RHU-10-2a. **b)** $^{206}Pb/^{238}U$ ages and calculated mean age for sample 19RHU-10-2a. **c)** Concordia plot of zircons from sample 19RHU-1-1. **d)** $^{206}Pb/^{238}U$ ages and calculated mean age for sample 19RHU-1-1. **e)** Concordia plot of zircons from sample 19RHU-4-2. **f)** $^{206}Pb/^{238}U$ ages and calculated mean age for sample 19RHU-4-2.

of lapilli tuff to tuff breccia with hornblende-plagioclase-phyric fragments. The contact area varies from abrupt with overprinting strong limonite and sulphide alteration, and in other localities, the porphyry appears gradational and transitions into a potassium-feldspar-phyric lapilli tuff to tuff breccia. Forty-one subhedral to euhedral zircons were extracted from the sample and six of these were selected for CA-TIMS analysis. The zircons are 100 to 200 μm in length with 1:1 to 1:2 aspect ratios. Five of six grains analyzed are mutually overlapping on concordia and yield a weighted mean $^{206}Pb/^{238}U$ age of 193.93 ±0.11 Ma (MSWD=1.13), which is interpreted to be the crystallization age of the sample (Figs. 9c, d). A single zircon overlaps concordia with a slightly younger $^{206}Pb/^{238}U$ date of 193.42 ±0.11 Ma, is inferred to have undergone minor Pb loss (Fig. 9c).

5.2.3. Sample 19RHU-4-2, potassium feldspar-phyric andesite from sub-facies 4a (CA-TIMS)

A second potassium-feldspar-phyric andesite was collected from sub-facies 4a northeast of Kinskuch Lake (Fig. 3). It is a coherent andesite and contains 3-5%, 1-4 cm phenocrysts of potassium feldspar in a plagioclase-rich groundmass with 3% hornblende (Fig. 8c). The andesite is adjacent to hornblende-plagioclase-phyric andesite lapilli tuff to tuff breccia, but contact relationships are obscured by moderate limonite and sulphide alteration. Thirty-nine subhedral to euhedral zircons were extracted from the sample having sizes between 100 and 200 μm and 1:2 to 1:3 aspect ratios. Five zircons were selected for CA-TIMS analysis. One grain overlaps concordia with an older $^{206}Pb/^{238}U$ date of 195.51 ±0.30 Ma and is inferred to be a xenocryst (Fig. 9e). Four grains are mutually overlapping on concordia and provide a weighted mean $^{206}Pb/^{238}U$ age of 193.98 ±0.11 Ma (MSWD=1.20), which is interpreted to be the crystallization age of the sample (Fig. 9f).

5.2.4. Sample 20RHU-1-14, volcanic sandstone from facies 5 (LA-ICPMS)

From facies 5, this sample was collected 600 m south of Kitsault Lake (Fig. 3). It is from a light green, weakly foliated, clast-supported, carbonaceous volcanic sandstone with subangular plagioclase and crystal tuff fragments near the base of the section at the Sault showing (Fig. 8d). Zircon grains are largely subrounded, partially fragmented, and have aspect ratios of 1:1 to 1:2, with long dimensions ranging from 100-200 um. Most $^{206}Pb/^{238}U$ dates span ca. 178-212 Ma (n=108) with a single primary peak at 191 Ma; two older zircons have $^{206}Pb/^{238}U$ dates of ca. 361 Ma and 373 Ma (Fig. 10a). The youngest statistical population provided a mean age of 187.33 ±0.83 Ma (MSWD=1.00; n=31), which is interpreted to be the maximum depositional age (Fig. 10b).

5.2.5. Sample 20RHU-1-16, graphitic, calcareous volcanic sandstone from facies 5 (LA-ICPMS)

The facies 5 sample was also collected south of Kitsault Lake, 17 m north of 20RHU-1-14 (Fig. 3). It is a graphite-bearing, calcareous, poorly sorted, volcanic sandstone with 1-3 mm subangular clasts of plagioclase and plagioclase crystal tuff and lesser black wispy vitric fragments (Fig. 8e). It has a moderate foliation defined by graphite. Zircon grains are mainly subrounded, fragmented to subhedral, and have aspect ratios of 1:1 to 3:1, with long dimensions varying from 100-250 um. Most $^{206}Pb/^{238}U$ dates span 203.4-182.7 Ma (n=103) with a broad age peak defined at 190.0 Ma (Fig. 10c). The youngest statistical population yielded a mean age of 188.08 ±0.59 Ma (MSWD=0.99; n=61), which is interpreted to be the maximum depositional age (Fig. 10d).

5.2.6. Sample 19RHU-16-1, feldspathic wacke from Bowser Lake Group (LA-ICPMS)

This feldspathic wacke sample was taken from the Bowser Lake Group, 8.5 km east of Kinskuch Lake (Fig. 3). It is from a section of fine- to medium-grained feldspathic wacke and very fine-grained, laminated, graphite-bearing gray to black siltstone interbedded on the 0.5 to 1 m scale (Fig. 8f). The sample has three distinct $^{206}Pb/^{238}U$ probability peaks spanning the Late Triassic to Late Jurassic at ca. 197 Ma, 187 Ma, and 156 Ma (Fig. 10e). One concordant zircon provided a Carboniferous $^{206}Pb/^{238}U$ date at ca. 306 Ma. The youngest statistical population provided a mean age of 154.31 ±0.93 Ma (MSWD=1.00; n=16), which is interpreted to be the maximum depositional age (Fig. 10f). This age is well within the Bowser Lake Group time frame.

6. Discussion

6.1. Lithostratigraphic and geochronological considerations

As documented previously, a maximum depositional age of 206.7 ±1.4 Ma (Hunter and van Straaten, 2020) and a crystallization age of 204.6 ±0.18 Ma (Miller et al., 2020) indicate that the onset of Hazelton Group deposition was during the Rhaetian and that deposition of facies 1 was coeval with or older than facies 2. Rocks that Alldrick et al. (1986) referred to as the 'middle sedimentary unit' appear to form the basal Hazelton Group (facies 1 and 2) and rocks of the 'intermediate volcanic unit' are more accurately placed in the lower Hazelton Group (facies 3 and 4; i.e., part of the Betty Creek Formation-Unuk River andesite unit; Table 1). The 'epiclastic and felsic volcanic unit' of Alldrick et al. (1986) is problematic because the main exposures east of Kinskuch Lake and northwest of the Kitsault River Valley (Fig. 3) are largely intermediate volcaniclastic rocks of facies 4 with local exposures of predominantly epiclastic units similar to units found in facies 3. We therefore interpret that the 'epiclastic and felsic volcanic unit' defined by Alldrick et al. (1986) does not form a discrete unit that can be mapped consistently across the area.

The fine tuff sampled within facies 2 provided a crystallization age of 200.9 ±0.2 Ma (Hettangian) and indicates that it is older than the thick ca. 193 Ma (Facies 4, sub-facies 4a) andesitic units and is younger than the inferred age of the basal Hazelton Group. It is interbedded with abundant limestone, as well as augite-phyric tuff breccia, which further suggests that this unit

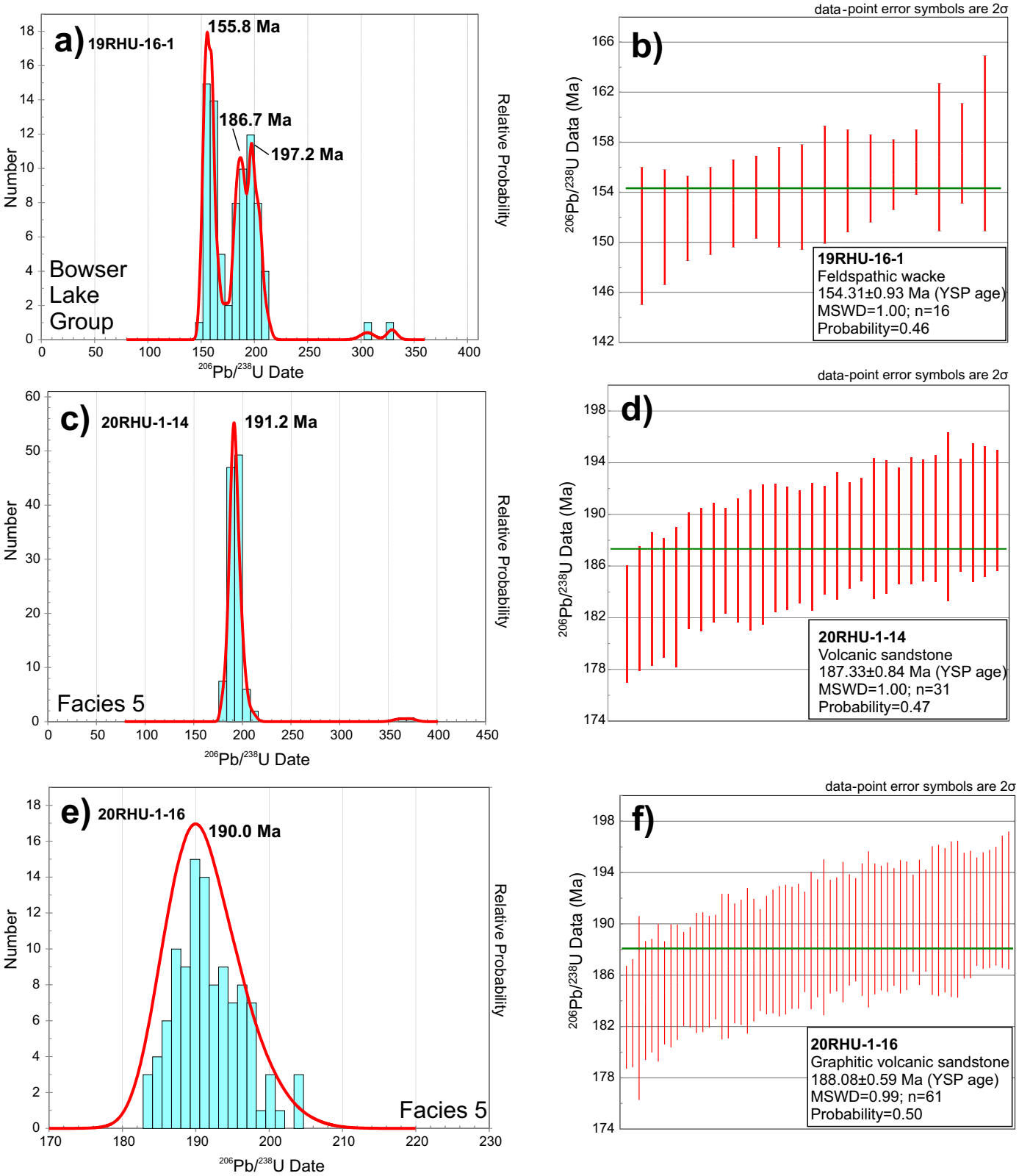

Fig. 10. LA-ICP-MS analyses plots of zircons. **a)** $^{206}Pb/^{238}U$ probability density plot showing the main probability age peaks for sample 19RHU-16-1. **b)** $^{206}Pb/^{238}U$ ages and calculated mean age for the youngest statistical population for sample 19RHU-16-1. **c)** $^{206}Pb/^{238}U$ probability density plot from showing the main probability age peaks for sample 20RHU-1-14. **d)** $^{206}Pb/^{238}U$ ages and calculated mean age for the youngest statistical population for sample 20RHU-1-14. **e)** $^{206}Pb/^{238}U$ probability density plot from showing the main probability age peaks for sample 20RHU-1-16. **f)** $^{206}Pb/^{238}U$ ages and calculated mean age for the youngest statistical population for sample 20RHU-1-16.

likely represents more of the basal Hazelton Group deposited before the thick andesitic pyroclastic flows of facies 4 that make up the bulk of the lower Hazelton Group. The ridge that these rocks are exposed along could represent a localized upthrown block of the basal Hazelton group east of Kinskuch Lake. Thus far, the basal Hazelton Group contact with the Stuhini Group in the Kitsault area appears much more gradational and contrasts to the sharp, inferred erosional contacts observed in the Snippaker area and the McTagg anticlinorium (Nelson and Kyba, 2014; Kyba and Nelson, 2015). Because facies 1 and 2 represent a unique and mappable lithostratigraphic unit, we suggest that together they form part what we refer to as the 'Kinskuch unit', which includes the 'Kinskuch conglomerates' of Miller et al. (2020; Table 1).

Facies 3 consists of abundant hornblende-plagioclase-phyric andesite interbedded with epiclastic rocks (limestone, siltstone, sandstone, conglomerate). The pyroclastic rocks also contain abundant limestone and chert clasts, in contrast to facies 4, which contains almost entirely volcanic-derived clasts. Although the age of facies 3 has not been determined, a U-Pb zircon age of 193.5 ±0.4 Ma was obtained from a felsic volcanic unit below the Sault showing (Mortensen and Kirkham, 1992) that could be a part of facies 3. Accordingly, facies 3 may be laterally equivalent to facies 4 and represent sedimentation in a relatively deep-marine setting distal to the main eruption centre(s). Alternatively, if the dated felsic volcanic unit is not apart of facies 3, then it could either be younger than facies 4 and represent an interim period between basal Hazelton sedimentation and the deposition of the thick andesitic pyroclastic flows of facies 4, or older and represent a gradual shift of facies 3 to more epiclastic sedimentation as the andesitic volcanism waned. Two K-feldspar-phyric andesite samples from Facies 4a have crystallization ages at ca. 193 Ma, placing facies 4 within the age range of the Unuk River andesite unit of the Betty Creek Formation (Gagnon et al., 2012; Nelson et al., 2013). The very coarse-grained K-feldspar megacrysts and locally massive texture indicate that facies 4a may represent feeder sub-volcanic intrusions to volcanism responsible for the thick andesitic lapilli tuff to tuff breccia rocks of Facies 4. Alternatively, the plagioclase and K-feldspar-phyric sub-facies 4a may represent intrusions similar to the Premier diorite to monzonite intrusions (Febbo et al., 2015) that host the Au-Cu porphyry Mitchell and Sulphurets deposits. U-Pb zircon ages from diorite plutons with K-feldspar phenocrysts in the Sulphurets suite have similar Lower Jurassic ages of 196 ±2.9 Ma, 192.2 ±2.8 Ma and 189 ±2.8 Ma (Febbo et al., 2015).

Near the Sault showing, two epiclastic samples from facies 5 provided similar ca. 188 Ma maximum depositional ages. The epiclastic strata are underlain by feldspar-phyric lapilli tuff inferred to be facies 3 or 4 that have been loosely dated at ca. 196 Ma and ca. 193 Ma (Fig. 3; Mortensen and Kirkham, 1992; Greig and Gehrels, 1995). The difference in age may indicate a significant break in sedimentation from the Sinemurian (facies 3 and 4 lapilli tuff) to the Pleinsbachian or younger (facies 5 epiclastic units) in the Sault showing area. The abundance of carbonate rocks in units at the Sault showing could suggest equivalence to the Spatsizi Formation, which is distributed throughout the Stewart-Iskut district. The remaining pyroclastic to epiclastic strata of facies 5 are not documented elsewhere in the Stewart-Iskut district and are unlike rocks of the Iskut River Formation, which host large VMS-type mineralization systems. We suggest that facies 5 constitutes a new mappable lithostratigraphic unit, referred to as the 'Kitsault unit' in Table 1, and that it forms part of the upper Hazelton Group outside of the main Eskay rift.

6.2. Implications for Kitsault River area mineralization systems and expression of VMS and VMS-related mineralization external to the main Eskay rift

The Kitsault River area hosts numerous stratabound to vein infill Ag-rich Pb-Zn deposits and showings such as Dolly Varden, Torbrit, North Star, Wolf, and Sault (Hanson, 1922; Black, 1951; Campbell, 1959; Dawson and Alldrick et al., 1986; Devlin and Godwin, 1986; Pinsent, 2001; Dunn and Pinsent, 2002), which have been interpreted variously as: epithermal vein-related (Grove, 1986); stratabound VMS (Devlin and Godwin, 1985; Devlin, 1987); shallow subaqueous hot spring (Dunn and Pinsent, 2002); or hybrid VMS-epithermal (Hunter and van Straaten, 2020). Additional descriptions of the Dolly Varden, Torbrit, North Star and Wolf deposits can be found in Hunter and van Straaten (2020). The deposits and showings are along, or peripheral to major northwest- and northeast-trending faults with inferred normal and strike-slip movement (Devlin and Godwin, 1986; McCuaig and Sebert, 2017).

The Sault showing is a small exhalative zone that is thought to be broadly correlative to the Dolly Varden deposits (McCuaig and Sebert, 2017). It consists of stratiform Zn-Pb-Ag-Sr mineralization that forms disrupted laminae of pyrite, sphalerite, celestite, and galena at the base of an approximately 50 m thick calcareous and locally graphitic sedimentary to volcaniclastic section consisting of interbedded mudstone, sandstone, muddy limestone, chert, and tuff to fine lapilli tuff layers, including a unit described as a metalliferous carbonate diamictite (Tupper and McCartney, 1990; Mortensen and Kirkham, 1992; Pinsent, 2001). The showing is overlain by a basaltic to andesitic tuffaceous rock with minor epiclastic beds and underlain by andesitic lapilli tuff to tuff breccia with local epiclastic sequences (Tupper and McCartney, 1990). The best mineralized diamond drill hole intersection contained 1.3% Zn, 0.12% Pb, 26.5 g/t Ag and 10 ppb Au along 4.95 m coincident with fault rock and minor carbonate and quartz veins (Tupper and McCartney, 1990). Alteration associated with the mineralized zones consist of ankerite, silica, pyrite and weak sericite and clay (Tupper and McCartney, 1990).

The ca. 178 Ma felsic tuffaceous sandstone dated at Wolf (Hunter and van Straaten, 2020), shows that at least some of the mineralization in the Kitsault River area is cogenetic with VMS deposits in the upper part of the Hazelton Group elsewhere, such as at Eskay Creek and Anyox (Alldrick, 1993; Smith,

1993; Barrett and Sherlock, 1996; Evenchick and McNicoll, 2002; MacDonald et al., 1996a; Macdonald et al., 1996b; Roth et al., 1999; Sherlock et al., 1999; Barresi and Dostal, 2005). In contrast, the new maximum depositional age of ca. 188 Ma for epiclastic rocks at the Sault showing could indicate that some of the Ag-rich mineralization systems are slightly older.

The Eskay Creek deposit encompasses several stratiform to discordant Au-Ag-Pb-Zn-Cu zones with disseminated, massive to semi-massive sulphides and sulphosalts with varying amounts of barite (Sherlock et al., 1999) and is inferred to have formed as shallow-water VMS or as a hybrid VMS-epithermal system (Roth et al., 1999; Galley et al., 2007) with bimodal volcanism (Barrie and Hannington, 1999; Franklin et al., 2005). The Ag-rich nature of the Kitsault River area deposits, which lack significant Au enrichment, is unique. Higher Ag and Pb values in VMS settings are generally in areas that host more sedimentary rocks, such as the bimodal-siliciclastic VMS-type (Barrie and Hannington, 1999; Franklin et al., 2005; Hannington et al., 2005). However, the Kitsault River area lacks significant turbiditic deposits. In contrast to the Besshi deposits in Japan or Windy Craggy in British Columbia (Peter and Scott, 1999), the Kitsault deposits are hosted largely in intermediate to dacitic epiclastic to fine pyroclastic rocks between a lower package of andesitic lapilli tuff to tuff breccia and an upper package of calc-alkaline fine-grained mafic pyroclastic rocks.

Coupled with Ag-rich mineralization, the lithologic characteristics of the Kitsault area suggest that it either represents a new, underexplored VMS deposit type or a hybrid VMS-epithermal system. Other Au-Ag-rich VMS-type mineralization in late Early to Middle Jurassic Hazelton Group rocks includes new discoveries southeast of the Brucejack Mine (Pretium Resources Inc., 2021; Brueckner et al., 2021), north of the Premier deposit at Silver Hill (Ascot Resources Ltd., 2020), and 30 km northeast of Stewart at Todd Creek (ArcWest Exploration Inc., 2019). These examples demonstrate the vast VMS-type mineralization potential of the Hazelton Group outside of the traditional Eskay rift. Additional bedrock mapping, targeted age dating and geochemical analysis will be vital to understand the upper Hazelton Group and its prospectivity for these new or hybrid VMS mineralization systems.

7. Conclusions

Updating the pioneering stratigraphic assignments in the Kitsault area by Alldrick et al. (1986), we divide the Hazelton Group into six facies and one sub-facies. Facies 1, with maximum depositional ages of ca. 206-204 Ma, consists of volcanic-derived sandstone, conglomerate, and megaclast-bearing conglomerate that forms the basal part of the lower Hazelton Group. Facies 2 comprises augite- and hornblende-plagioclase-phyric volcanic rocks, tuff, sandstone, conglomerate, and limestone. A fine tuff within this facies has a depositional age of 200.9 ±0.2 Ma making it slightly younger than the basal Hazelton Group. Facies 1 and 2 form part of a lithostratigraphic unit that we refer to as the 'Kinskuch unit'. Facies 3 consists of hornblende-plagioclase-phyric pyroclastic rocks with significant exotic clasts (limestone, chert), and interbedded siltstone, sandstone, conglomerate, and limestone. Facies 4 is mainly lapilli tuff to tuff breccia containing volcanic-derived, hornblende-plagioclase-phyric clasts with minor tuff, sandstone, and limestone interbeds. Two samples of K-feldspar porphyry (sub-facies 4a) to flow-banded tuff within Facies 4 yielded ca. 193 Ma crystallization ages. Facies 3 is inferred to be slightly younger, slightly older, or a distal equivalent to facies 4. The upper Hazelton Group begins with facies 5 and consists mainly of mafic to intermediate tuff, volcanic sandstone, and dacite to dacite tuff. The age of facies 5 is constrained by maximum depositional ages of ca. 188 Ma for volcanic sandstone units from the Sault showing and a ca. 178 Ma rhyolite lapilli tuff from the Wolf deposit. Facies 5 forms part of a newly named lithostratigraphic unit we refer to as the 'Kitsault unit' and likely localized expressions of the Spatsizi Formation. With a maximum deposition age of ca. 168 Ma, facies 6 consists of interbedded feldspathic wacke and fine lapilli tuff to tuff with lesser limestone and black mudstone. Facies 6 grades into interbedded feldspathic wacke, mudstone and chert clast-bearing pebble conglomerate of the Bowser Lake Group, with a maximum depositional age of ca. 154 Ma. Preliminary stratigraphic and geochronological results suggest that VMS type mineralization in the Kitsault River area has a potential age range from ca. 188 to ca. 178 Ma, which may indicate that the mineralization systems could be older than the Au-rich VMS systems in the Eskay rift. Future mapping-based studies in the Kitsault River area will be vital to better resolve the stratigraphy, timing, and geochemistry of the Hazelton Group and its important mineralizing systems.

Acknowledgments

We thank Dolly Varden Silver Corporation, in particular Rob van Egmond, Amanda Bennett, and Charlie Fleenor, for their logistical support, and their hospitality while we stayed in the Alice Arm Camp. We thank Summit Helicopters and their pilots for getting us out to and back from the field throughout the summer. Emily Miller is thanked for the use of some of her M.Sc. thesis photos and information. Cheerful and dedicated field assistance was provided by Ben Coats. Hai Lin, Taylor Ockerman and Marghaleray Animi are thanked for their work in preparation and analysis of the geochronological samples. Insightful reviews by JoAnne Nelson, Jeff Chiarenzelli, and Lawrence Aspler significantly improved this manuscript.

References cited

Anderson, R.G., 1989. A stratigraphic, plutonic and structural framework for the Iskut map area, northwestern British Columbia. In: Current Research, Part E, Geological Survey of Canada, Paper 89-1, pp. 145-154.

ArcWest Exploration Inc., 2019. ArcWest Exploration Inc. expands Yellow Bowl porphyry copper-gold target, Todd Creek project. <https://arcwestexploration.com/2019/11/27/arcwest-exploration-inc-expands-yellow-bowl-porphyry-copper-gold-target-todd-creek-project/>, last accessed December 2021.

Alldrick, D.J., 1993. Geology and metallogeny of the Stewart mining

camp, northwestern British Columbia. British Columbia Ministry of Energy, Mines and Petroleum Resources, British Columbia Geological Survey Bulletin 85, 105 p.

Alldrick, D.J., Dawson, G.L., Bosher, J.A., and Webster, I.C.L., 1986. Geology of the Kitsault River area (NTS 103P). British Columbia Ministry of Energy, Mines and Petroleum Resources, British Columbia Geological Survey Open File 1986-02, 1:50,000 scale.

Ascot Resources Ltd., 2020. Ascot announces its initial 2020 exploration program including high-grade silver mineralization at Silver Hill. <https://ascotgold.com/news-releases/2020/ascot-announces-its-initial-2020-exploration-program-including-high-grade-silver-mineralization-at-silver-hill/>, last accessed December 2021.

Barresi, T., and Dostal, J., 2005. Geochemistry and petrography of upper Hazelton Group volcanics: VHMS-favourable stratigraphy in the Iskut River and Telegraph Creek map areas, northwestern British Columbia. In: Geological Fieldwork 2004, British Columbia Ministry of Energy and Mines, British Columbia Geological Survey Paper 2005-1, pp. 39-47.

Barresi, T., Nelson, J.L., and Dostal, J., 2015. Geochemical constraints on magmatic and metallogenic processes: Iskut River Formation, volcanogenic massive sulfide-hosting basalts, NW British Columbia, Canada. Canadian Journal of Earth Sciences, 52, 1-20.

Barrett, T.J., and Sherlock, R.L., 1996. Geology, lithogeochemistry and volcanic setting of the Eskay Creek Au-Ag-Cu-Zn deposit, northwestern British Columbia. Exploration and Mining Geology, 5, 339-368.

Barrie, C.T., and Hannington, M.D., 1999. Classification of volcanic-associated massive sulfide deposits based on host-rock composition. In: Barrie, C.T., and Hannington, M.D., (Eds.), Volcanic-associated massive sulfide deposits: processes and examples in modern and ancient settings, Reviews in Economic Geology, 8, Society of Economic Geologists, Inc, pp. 1-11.

Black, J.M., 1951. Geology and mineral occurrences of the Upper Kitsault Valley. In: British Columbia Ministry of Energy Mines and Petroleum Resources, British Columbia Geological Survey Annual Report, pp. A76-A83.

Black, L.P., Kamo, S.L., Allen, C.M., Davis, D.W., Aleinikoff, J.N., Valley, J.W., Mundil, R., Campbell, I.H., Korsch, R.J, Williams, I.S., and Foudoulis, C., 2004. Improved $^{206}Pb/^{238}U$ microprobe geochronology by the monitoring of a trace-element-related matrix effect; SHRIMP, ID-TIMS, ELA-ICP-MS and oxygen isotope documentation for a series of zircon standards. Chemical Geology 205, 115-140.

Brown, D.A., Gunning, M.H., and Greig, C.J., 1996. The Stikine project: Geology of western Telegraph Creek map area, northwestern British Columbia. British Columbia Ministry of Employment and Investment, British Columbia Geological Survey Bulletin 95, 130 p.

Brueckner, S.M., Johnson, G., Wafforn, S., Gibson, H., Sherlock, R., Anstey, C., and McNaughton, K., 2021. Potential for volcanogenic massive sulfide mineralization at the A6 anomaly, northwest British Columbia, Canada: Stratigraphy, lithogeochemistry, and alteration mineralogy and chemistry. Minerals, 11, 867.

Campbell, F.A., 1959. The geology of Torbrit Silver Mine, British Columbia. Economic Geology, 54, 1461-1495.

Carter, N.C., 1981. Porphyry copper and molybdenum deposits, west-central British Columbia. British Columbia Ministry of Energy Mines and Petroleum Resources, British Columbia Geological Survey Bulletin 64, 81 p.

Childe, F.C., 1997. Timing and tectonic setting of volcanogenic massive sulphide deposits in British Columbia: constraints from U-Pb geochronology, radiogenic isotopes, and geochemistry. Unpublished Ph.D. thesis, The University of British Columbia, Vancouver, B.C., Canada.

Dawson, G.L., and Alldrick, D.J., 1986. Geology and mineral deposits of the Kitsault Valley. In: Geological Fieldwork 1985, British Columbia Ministry of Energy, Mines and Petroleum Resources, British Columbia Geological Survey Paper 1986-1, pp. 219-224.

Devlin, B.D., 1987. Geology and genesis of the Dolly Varden silver camp, Alice Arm area, northwestern British Columbia. Unpublished M.Sc. thesis, The University of British Columbia, Vancouver, B.C., Canada.

Devlin, B.D., and Godwin, C.I., 1986. Geology of the Dolly Varden camp, Alice Arm area. In: Geological Fieldwork 1985, British Columbia Ministry of Energy, Mines and Petroleum Resources, British Columbia Geological Survey Paper 1986-1, pp. 327-330.

Dunne, K.P.E., and Pinsent, R.H., 2002. Depositional setting of silver-rich quartz-sulphate-carbonate deposits of the upper Kitsault River area, northwest British Columbia. In: Geological Fieldwork 2001, British Columbia Ministry of Energy, Mines and Petroleum Resources, British Columbia Geological Survey Paper 2002-01, pp. 177-196.

Eggins, S.M., Kinsley, L., and Shelley, J., 1998. Deposition and element fractionation processes during atmospheric pressure laser sampling for analysis by ICP-MS. Applied Surface Science 127-129, 278-286.

Eisbacher, G.H., 1981. Late Mesozoic-Paleogene Bowser Basin molasse and Cordilleran tectonics, western Canada. In: Miall, A. D. (Ed.), Sedimentation and Tectonics in Alluvial Basins, Geological Association of Canada Special Paper 23, pp. 125-151.

Evenchick, C.A., and McNicoll, V.J., 2002. Stratigraphy, structure, and geochronology of the Anyox Pendant, northwest British Columbia, and implications for mineral exploration. Canadian Journal of Earth Sciences, 39, 1313-1332.

Evenchick, C.A., and Thorkelson, D.J., 2005. Geology of the Spatsizi River map area, north-central British Columbia. Geological Survey of Canada Bulletin 577, 276 p.

Evenchick, C.A., McMechan, M.E., McNicoll, V.J., and Carr, S.D., 2007. A synthesis of the Jurassic-Cretaceous tectonic evolution of the central and southeastern Canadian Cordillera: Exploring links across the orogen. In: Sears, J.W., Harms, T.A. and Evenchick, C.A., (Eds.), Whence the mountains? Inquiries in the evolution of orogenic systems: A volume in honor or Raymond A. Price, Geological Society of America Special Paper 433, pp. 117-145.

Evenchick, C.A., Mustard, P.S., Greig, C.J., McMechan, M.E., Ritcey, D.H., Smith, G.T., and Ferri, F., 2008. Geology, Nass River, British Columbia. Geological Survey of Canada, Open File 5705, 1:125,000 scale.

Evenchick, C.A., Poulon, T.P., and McNicoll, V.J., 2010. Nature and significance of the diachronous contact between the Hazelton and Bowser Lake groups (Jurassic), north-central British Columbia. Bulletin of Canadian Petroleum Geology, 58, 235-267.

Febbo, G.E., Kennedy, L.A., Savell, M., Creaser, R.A., and Friedman, R.M., 2015. Geology of the Mitchell Au-Cu-Ag-Mo porphyry deposits, northwestern British Columbia, Canada. In: Geological Fieldwork 2014, British Columbia Ministry of Energy, Mines and Petroleum Resources, British Columbia Geological Survey Paper 2015-1, pp. 59-86.

Febbo, G.E., Kennedy, L.A., Nelson, J.L., Savell, M.J., Campbell, M.E., Creaser, R.A., Friedman, R.M., van Straaten, B.I., and Stein, H.J., 2019. The evolution and structural modifications of the supergiant Mitchell Au-Cu porphyry, northwestern British Columbia. Economic Geology, 114, 303-324.

Franklin, J.M., Gibson, H.L., Jonasson, I.R., and Galley, A.G., 2005. Volcanogenic massive sulfide deposits. In: Hedenquist, J.W., Thompson, J.F.H., Goldfarb, R.J., and Richards, J.P., (Eds.), Economic Geology 100th Anniversary Volume, The Economic Geology Publishing Company, pp. 523-560.

Gagnon, J.-F., Barresi, T., Waldron, J.W.F., Nelson, J.L., Poulton, T.P., and Cordey, F., 2012. Stratigraphy of the upper Hazelton

Group and the Jurassic evolution of the Stikine terrane, British Columbia. Canadian Journal of Earth Sciences, 49, 1027-1052.

Galley, A.G., Hannington, M.D., and Jonasson, M., 2007. Volcanogenic massive sulphide deposits. In: Goodfellow, W.D., (Ed.), Mineral deposits of Canada: A synthesis of major deposit types, district metallogeny, the evolution of geological provinces, and exploration methods, Geological Association of Canada, Mineral Deposits Division, Special Publication 5, pp. 141-161.

Gerstenberger, H., and Haase, G., 1997. A Highly effective emitter substance for mass spectrometric Pb isotopic ratio determinations. Chemical Geology 136, 309-312.

Greig, C.J., 1991. Stratigraphic and structural relations along the west-central margin of the Bowser Basin, Oweegee and Kinskuch areas, northwestern British Columbia. In: Current Research, Part A, Geological Survey of Canada Paper 91-1A, pp. 197-205.

Greig, C.J., 1992. Jurassic and Cretaceous plutonic and structural styles of the Eagle Plutonic Complex, southwestern British Columbia, and their regional significance. Canadian Journal of Earth Sciences, 29, 793-811.

Greig, C.J., and Gehrels, G.E., 1995. U-Pb zircon geochronology of Lower Jurassic and Paleozoic Stikinian strata and Tertiary intrusions, northwestern British Columbia. Canadian Journal of Earth Sciences, 32, 1155-1171.

Gibson, H.L., Morton, R.L., and Hudak, G.J., (1999). Submarine volcanic processes, deposits and environments favorable for the location of volcanic-associated massive sulfide deposits. In: Barrie, C.T., and Hannington, M.D., (Eds.), Volcanic-associated massive sulfide deposits: processes and examples in modern and ancient settings, Reviews in Economic Geology, 8, pp. 13-51.

Grove, E.W., 1986. Geology and mineral deposits of the Stewart area, British Columbia. British Columbia Ministry of Energy, Mines and Petroleum Resources, British Columbia Geological Survey Bulletin 58, 219 p.

Hannington, M.D., De Ronde, C.E.J., and Petersen, S., 2005. Sea-floor tectonics and submarine hydrothermal systems. In: Hedenquist, J.W., Thompson, J.F.H., Goldfarb, R.J., and Richards, J.P., (Eds.), Economic Geology 100th Anniversary Volume, The Economic Geology Publishing Company, pp. 111-141.

Hanson, G., 1922. Upper Kitsault Valley, British Columbia. In: Geological Survey of Canada, Summary Report Part A, pp. 7-21.

Herriott, T.M., Crowley, J.L., Schmitz, M.D., Wartes, M.A., and Gillis, R.J., 2019. Exploring the law of detrital zircon: LA-ICP-MS and CA-TIMS geochronology of Jurassic forearc strata, Cook Inlet, Alaska, USA. Geology, 47, 1044-1048.

Höy, T., 1991. Volcanogenic massive sulphide deposits in British Columbia. In: McMillan, W.J., (Ed.), Ore Deposits, Tectonics and Metallogeny in the Canadian Cordillera, British Columbia Ministry of Energy, Mines and Petroleum Resources, British Columbia Geological Survey Paper 1991-4, pp. 89-124.

Hunter, R.C., and van Straaten, B.I., 2020. Preliminary stratigraphy and geochronology of the Hazelton Group, Kitsault River area, Stikine terrane, northwest British Columbia. In: Geological Fieldwork 2019, British Columbia Ministry of Energy, Mines and Petroleum Resources, British Columbia Geological Survey Paper 2020-01, pp. 101-118.

Hunter, R.C., Sebert, C.F.B., Friedman, R., and Wall, C., 2022. Geochronological data from the Kitsault River area: 2019 and 2020 field seasons. Ministry of Energy, Mines and Low Carbon Innovation, British Columbia Geological Survey, GeoFile.

Jaffey, A.H., Flynn, K.F., Glendenin, L.E., Bentley, W.C., and Essling, A.M., 1971. Precision measurement of half-lives and specific activities of ^{235}U and ^{238}U. Physical Review C, 4, 1889-1906.

Kyba, J., and Nelson, J.L., 2015. Stratigraphic and tectonic framework of the Kyber-Sericite-Pins mineralized trend, lower Iskut River, northwest British Columbia. In: Geological Fieldwork 2014, British Columbia Ministry of Energy, Mines and Petroleum Resources, British Columbia Geological Survey Paper 2015-01, pp. 41-58.

Logan, J.M., and Mihalynuk, M.G., 2014. Tectonic controls on Early Mesozoic paired alkaline porphyry deposit belts (Cu-Au ±Ag-Pt-Pd-Mo) within the Canadian Cordillera. Economic Geology, 109, 827-858.

Logan, J.M., Drobe, J.R., and McClelland, W.C., 2000. Geology of the Forrest Kerr-Mess Creek area, northwestern British Columbia. British Columbia Ministry of Energy, Mines and Petroleum Resources, British Columbia Geological Survey Bulletin 104, 132 p.

Ludwig, K.R., 2003. Isoplot 3.00, A Geochronological Toolkit for Microsoft Excel. University of California at Berkeley. kludwig@bgc.org/isoplot

Ludwig, K.R., 2012. Isoplot 3.75. A geochronological toolkit for Microsoft Excel. Special Publication, Berkley Geochronology Center, 75 p.

Marsden, H., and Thorkelson, D.J., 1992. Geology of the Hazelton volcanic belt in British Columbia: Implications for the Early to Middle Jurassic evolution of Stikinia. Tectonics, 11, 1266-1287.

Marti, J., Groppelli, G., and Brum da Silveira, A., 2018. Volcanic stratigraphy: A review. Journal of Volcanology and Geothermal Research 357, 68-91.

Mattinson, J.M., 2005. Zircon U-Pb chemical abrasion ("CA-TIMS") method: Combined annealing and multi-step partial dissolution analysis for improved precision and accuracy of zircon ages. Chemical Geology 220, pp. 47-66.

McCuaig, M., and Sebert, C., 2017. 2016 Technical Report for the Dolly Varden Property, Skeena Mining Division. British Columbia Ministry of Energy, Mines and Petroleum Resources Assessment Report 36934.

Macdonald, A.J., Lewis, P.D., Thompson, J.F.H., Nadaraju, G., Bartsch, R., Bridge, D.J., Rhys, D.A., Roth, T., Kaip, A., Godwin, C.I., and Sinclair, A.J., 1996a. Metallogeny of an Early to Middle Jurassic arc, Iskut River area, northwestern British Columbia. Economic Geology, 91, 1098-1114.

MacDonald, R.W.J., Barrett, T.J., and Sherlock, R.L., 1996b. Geology and lithogeochemistry at the Hidden Creek massive sulfide deposit, Anyox, west-central British Columbia. Exploration and Mining Geology, 5, 369-398.

MacIntyre, D., Ash, C., and Britton, J., 1994. Geological compilation Skeena-Nass area, west central British Columbia. In: British Columbia Ministry of Energy, Mines and Petroleum Resources, British Columbia Geological Survey Open File 1994-14, 1:250,000 scale.

Miller, E.A., Kennedy, L.A., and van Straaten, B.I., 2020. Geology of the Kinskuch Lake area and Big Bulk porphyry prospect: Syn-depositional faulting and local basin formation during the Rhaetian (latest Triassic) transition from the Stuhini to the Hazelton Group. In: Geological Fieldwork 2019, British Columbia Ministry of Energy, Mines and Petroleum Resources, British Columbia Geological Survey Paper 2020-01, pp. 77-99.

Monger, J.W.H., 1977. The Triassic Takla Group in McConnell Creek map-area, north central British Columbia. Geological Survey of Canada Paper 76-29, 45 p.

Mortensen, J.K., and Kirkham, R.V., 1992. A U-Pb zircon age for host rocks of a syngenetic strontium(-zinc) occurrence in the Kitsault Lake area, west-central British Columbia. In: Radiogenic Age and Isotopic Studies, Report 5, Geological Survey of Canada, Paper 91.2, pp. 181-185.

Mundil, R., Ludwig, K.R., Metcalfe, I., and Renne, P.R., 2004. Age and timing of the Permian Mass Extinctions: U/Pb Dating of Closed-System Zircons, Science 305, 1760-1763.

Nelson, J.L., and Kyba, J., 2014. Structural and stratigraphic control of porphyry and related mineralization in the Treaty Glacier-KSM-Brucejack-Stewart trend of western Stikinia. In: Geological Fieldwork 2013, British Columbia Ministry of Energy, Mines and

Petroleum Resources, British Columbia Geological Survey Paper 2014-01, pp. 111-140.

Nelson, J.L., Colpron, M., and Israel, S., 2013. The Cordillera of British Columbia, Yukon and Alaska: Tectonics and metallogeny. In: Colpron, M., Bissig, T., Rusk, B.G., and Thompson, J., (Eds.), Tectonics, Metallogeny and Discovery: The North American Cordillera and Similar Accretionary Settings, Society of Economic Geologists Special Publication 17, pp. 53-110.

Nelson, J.L., Waldron, J., van Straaten, B.I., Zagorevski, A., and Rees, C., 2018. Revised stratigraphy of the Hazelton Group in the Iskut River region, northwestern British Columbia. In: Geological Fieldwork 2017, British Columbia Ministry of Energy, Mines and Petroleum Resources, British Columbia Geological Survey Paper 2018-1, pp. 15-38.

Paton, C., Hellstrom, J., Paul, B., Woodhead, J., and Hergt, J., 2011. Iolite: Freeware for the visualization and processing of mass spectrometric data. Journal of Analytical Atomic Spectometry 26, 2508-2518.

Peter, J.M., and Scott, S.D., 1999. Windy Craggy, northwestern British Columbia: The world's largest Besshi-type deposit. In: Barrie, C.T., and Hannington, M.D., (Eds.), Volcanic-associated massive sulfide deposits: processes and examples in modern and ancient settings, Reviews in Economic Geology, 8, Society of Economic Geologists, Inc., pp. 261-295.

Pinsent, R.H., 2001. Mineral deposits of the upper Kitsault River area, British Columbia. In: Geological Fieldwork 2000, British Columbia Ministry of Energy and Mines, British Columbia Geological Survey Paper 2001-1, pp. 313-326.

Pretium Resources Inc., 2021. Exploration - Near-mine and regional exploration. <https://www.pretivm.com/exploration/Near-mine-and-Regional-Exploration/default.aspx>, last accessed December 2021.

Roth, T., Thompson, J.F.H., and Barrett, T.J., 1999. The precious metal-rich Eskay Creek deposit, northwestern British Columbia. In: Barrie, C.T., and Hannington, M.D., (Eds.), Volcanic-associated massive sulfide deposits: processes and examples in modern and ancient setting, Reviews in Economic Geology 8, pp. 357-374.

Schmitz, M.D., and Schoene, B., 2007. Derivation of isotope ratios, errors, and error correlations for U-Pb geochronology using ^{205}Pb-^{235}U-(^{233}U)-spiked isotope dilution thermal ionization mass spectrometric data. Geochemistry, Geophysics, Geosystems, 8, <https://doi.org/10.1029/2006GC001492>

Scoates, J.S., and Friedman, R.M., 2008. Precise age of the platinuferous Merensky Reef, Bushveld Complex, South Africa, by the U-Pb ID-TIMS chemical abrasion ID-TIMS technique, Economic Geology, 103, 465-471.

Sherlock, R.L., Roth, T., Spooner, E.T.C., and Bray, C.J., 1999. Origin of the Eskay Creek precious metal-rich volcanogenic massive sulfide deposit; fluid inclusion and stable isotope evidence. Economic Geology, 94, 803-824.

Sláma, J., Košler, J., Condon, D., and Crowley, J., 2008. Plešovice zircon-A new natural reference material for U-Pb and Hf isotopic microanalysis. Chemical Geology 249, 1-35.

Smith, A.D., 1993. Geochemistry and tectonic setting of volcanics from the Anyox mining camp, British Columbia. Canadian Journal of Earth Sciences, 30, 48-59.

Thirlwall, M.F., 2000. Inter-laboratory and other errors in Pb isotope analyses investigated using a ^{207}Pb-^{204}Pb double spike. Chemical Geology 163, 299-322.

Tipper, H.W., and Richards, T.A., 1976. Jurassic stratigraphy and history of north-central British Columbia. Geological Survey of Canada Bulletin 270, 82 p.

Tupper, D.W., and McCartney, I.D., 1990. Geological, geochemical and diamond drilling report on the Kits-Jade project, Kitsault Lake area, British Columbia. Ministry of Energy, Mines and Petroleum Resources, British Columbia Geological Survey Assessment Report 20167, 23 p.

Wiedenbeck, M., Alle, P., Corfu, F., Griffin, W.L., Meier, M., Oberli, F., Quadt, A.V., Roddick, J.C., and Spiegel, W., 1995. Three natural zircon standards for U-Th-Pb, Lu-Hf, trace element and REE analyses. Geostandards Newsletter 19, 1-23.

Wiedenbeck, M., Hanchar, J.M., Peck, W.H., Sylvester, P., Valley, J., Whitehouse, M., Kronz, A., Morishita, Y., Nasdala, L., Fiebig, F., Franchi, I., Girard, J.P., Greenwood, R.C., Hinton, R., Kita, N., Mason, P.R.D., Norman, M., Ogasawara, M., Piccoli, P.M., Rhede, D., Satoh, H., Schulz-Dobrick, B., Skår, Ø., Spicuzza, M.J., Terada, K., Tindle, K., Togashi, S., Vennemann, T., Xie, Q., and Zheng, Y.F., 2004. Further characterization of the 91500 zircon crystal. Geostandards and Geoanalytical Research 28, 9-39.

Revised stratigraphy of the Stuhini and Hazelton groups and LA-ICP-MS zircon geochronology of the Scottie gold mine area, northwestern British Columbia

Ben Stanley [1, a] and JoAnne Nelson[2]

[1] Scottie Resources Corp., 905-1111 West Hastings Street, Vancouver, BC, V6E 2J3
[2] Emeritus Scientist, British Columbia Geological Survey, Ministry of Energy, Mines and Low Carbon Innovation, Victoria, BC, V8W 9N3
[a] corresponding author: Stanley@seracx.com

Recommended citation: Stanley, B., and Nelson, J., 2022. Revised stratigraphy of the Stuhini and Hazelton groups and LA-ICP-MS zircon geochronology of the Scottie gold mine area, northwestern British Columbia. In: Geological Fieldwork 2021, British Columbia Ministry of Energy, Mines and Low Carbon Innovation, British Columbia Geological Survey Paper 2022-01, pp. 83-102.

Abstract

The past-producing Scottie gold mine lies within the Stewart mining camp, in the southern part of a prolific mineral district in northwestern British Columbia popularly known as the 'Golden Triangle'. The Golden Triangle includes Cu-Au porphyries (e.g., Red Chris, KSM), epithermal gold deposits (e.g., Brucejack, Scottie Gold) and VMS deposits (e.g., Eskay Creek, Granduc, Anyox). They are hosted by, and causally related to, Upper Triassic through Middle Jurassic volcano-sedimentary strata of the Stuhini and Hazelton groups and/or comagmatic subvolcanic intrusions, and many are spatially related to the unconformable contact between the Stuhini Group and overlying Hazelton Group. In this study, detailed geological mapping, supported by geochemistry and LA-ICP-MS zircon geochronology of volcanic and sedimentary units, establish a stratigraphic section through the upper Stuhini and lower Hazelton groups in the Scottie gold mine area.

Recognized for the first time in this study, the Stuhini Group in the Stewart mining camp includes a lower unit of interlayered argillite, limestone, plagioclase-rich fine-grained sandstone and felsic tuff, which grades up-section into an upper volcanic unit of augite-phyric trachyandesite (latite) breccias, flows and flow-breccias, and felsic (trachyte) flows, lapilli- and crystal lithic tuffs. Geochemically the volcanic rocks are highly potassic, of shoshonitic affinity. Zircons from a crystal tuff near the base of the upper volcanic unit yielded a Youngest Statistical Population (YSP) weighted average of 214.2 ±1.0 Ma, considered the age of crystallization.

Hazelton Group stratigraphy in the Stewart mining camp is comparable to but distinct from that in the McTagg anticlinorium. The stratigraphically lowest unit in the Hazelton Group forms an isolated exposure of beige siltstone with lesser interbeds of sandstone and mudstone, apparently overlying sedimentary strata of the lower Stuhini Group unit across an ice-covered contact. Zircons from a siltstone in this unit yielded a YSP weighted average age of 201.0 ±5.2 Ma, which we interpret as the maximum age for the onset of Hazelton Group deposition in this area. It coincides with a ca. 200.5 Ma U-Pb zircon age of the nearby Tennyson porphyry, interpreted as comagmatic with early Hazelton volcanism, and with the Hettangian-Sinemurian faunal age of the Jack Formation at the base of the Hazelton Group on the flanks of the McTagg anticlinorium, 20 kilometres to the north. In the eastern half of the map area, steeply dipping strata of the Betty Creek Formation (lower Hazelton Group) paraconformably overlie the upper Stuhini volcanic unit. The Betty Creek Formation includes two intervals of feldspar-hornblende-phyric andesitic flows, tuffs, breccias, and conglomerates of the Unuk River andesite unit, separated by a siltstone unit that contains a Pliensbachian(?) ammonite mold and has yielded a YSP weighted average of 190.6 ±1.7 Ma. These ages correspond to the latter stages of Betty Creek volcanism on the flanks of the McTagg anticlinorium.

The highly diverse metallogeny of the Golden Triangle resulted from collision-driven processes during Stuhini and Hazelton arc and back-arc development. The New Britain arc and Bismarck plate provide a modern analogue of collision-related arc and back-arc reorganization, which has given rise to both alkalic Cu-Au porphyries (Lihir) and seabed massive sulphide deposits (Manus basin). The upper volcanic unit in the Stuhini Group, described here, provides new evidence of shoshonitic volcanism at the transition from main-stage Stuhini arc-back-arc activity into post-collision (Galore suite) magmatism.

Keywords: Scottie gold mine, Stewart mining camp, Stuhini Group, Hazelton Group, detrital zircon geochronology, lithogeochemistry, shoshonite

1. Introduction

The Golden Triangle is the popular name for a large, prolific mineral district in northwestern British Columbia, in which Cu-Au and Cu-Mo porphyries, precious metal vein systems, and volcanogenic massive sulphide deposits are hosted by Late Triassic to Middle Jurassic volcano-sedimentary successions and cogenetic intrusions (Fig. 1 inset; Nelson and van Straaten, 2021). The stratigraphic setting of these deposits is a key aspect of their metallogeny, with many of them within 2 km of the unconformable contact between the Stuhini Group and overlying uppermost Triassic to Jurassic rocks of the Hazelton Group. In the last decades, discovery and development of the Brucejack gold mine and the KSM (Kerr-Sulphurets-Mitchell) Cu-Au porphyry resource in the McTagg anticlinorium (Fig. 1) has been accompanied by intensive geological study by government and university researchers. Detailed geological

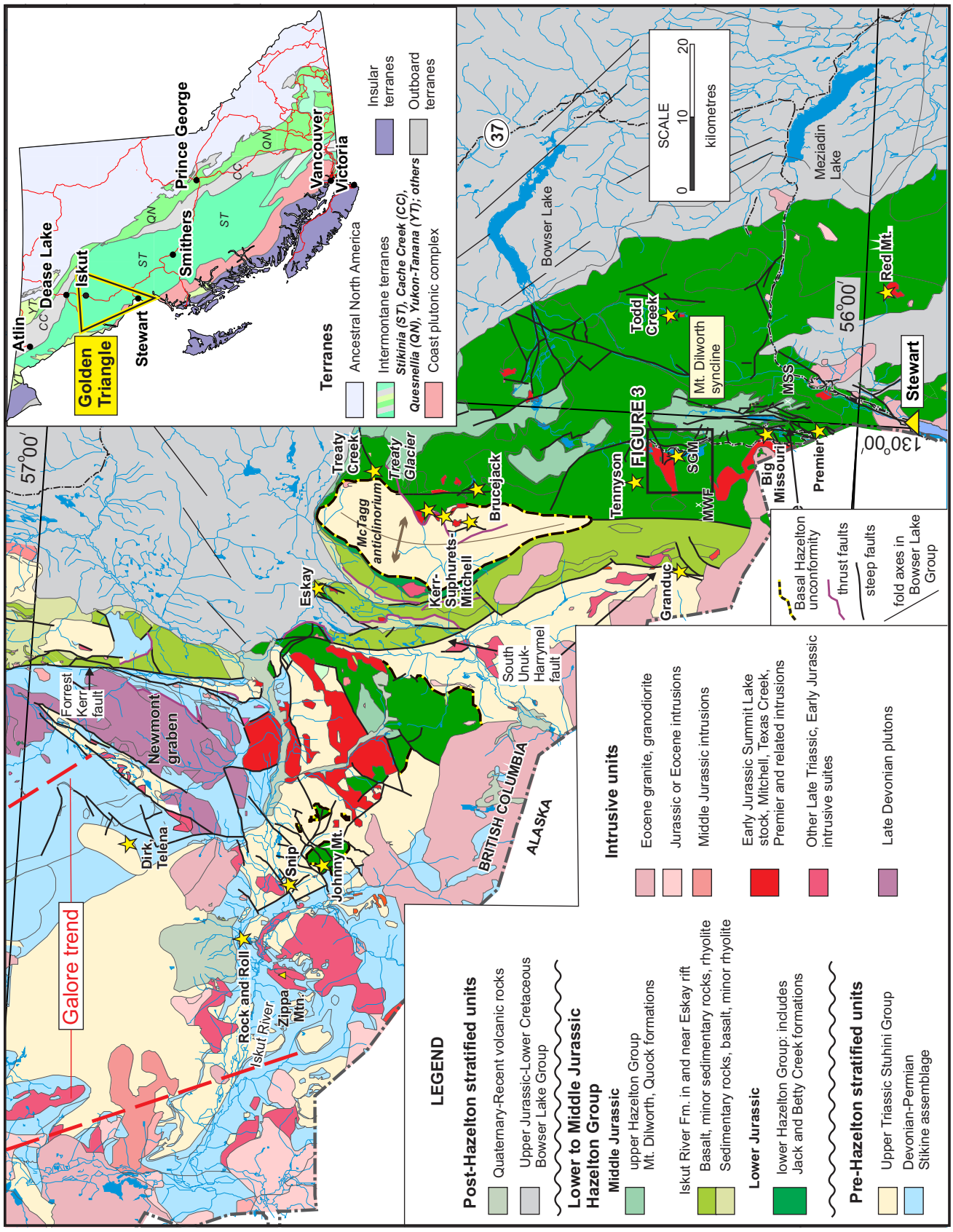

Fig. 1. Regional setting of the Scottie gold mine area in the southern Iskut River region of northwestern British Columbia. Inset, generalized terrane map and position at southern tip of the Golden Triangle. SGM = Scottie Gold Mine; MWF = Mt. White-Fraser; MSS = Mt. Shorty-Stevenson.

mapping, stratigraphic, and geochronological studies have shown important temporal and spatial relationships between Cu-porphyry and precious metal vein mineralization, Triassic-Jurassic intrusions, the sub-Hazelton Group unconformity surface, and favourable stratigraphic settings in the Hazelton Group (Lewis, 2013; Nelson and Kyba, 2014; Febbo et al., 2015; Tombe et al., 2018; Nelson et al., 2018; Fig. 1). In turn, these regional studies have led to terrane-scale tectonic and metallogenetic syntheses that depict evolving arc-back-arc configurations during terrane accretion to the North American margin (Nelson and van Straaten, 2021; Nelson et al., 2022, in press).

Before the present study, comparable stratigraphic and geochronological constraints have not been available for the Stewart mining camp, south of the McTagg anticlinorium (Fig. 1). The area has not been systematically mapped or studied since the 1980s. This contribution, based on detailed geological mapping of the Scottie gold mine area, documents for the first time a stratigraphic section of the upper Stuhini and lower Hazelton groups in the Stewart mining camp, with temporal constraints provided by LA-ICP-MS geochronology. It describes a previously unrecognized volcanic unit of shoshonite affinity in the upper part of the Stuhini Group, locates what may be the basal Hazelton unconformity, and aligns Hazelton Group stratigraphic subdivisions in this area with those established in the McTagg anticlinorium by Lewis (2013) and Nelson et al. (2018). These new observations clarify the tectonic history of the Stewart mining camp during the crucial transition between Stuhini and Hazelton arc and back-arc configurations. The Scottie property is within the traditional lands of the Nisga'a First Nation.

2. Regional geology

The study area lies within Stikinia, a multiphase arc-back-arc terrane constructed between the Late Devonian and Early Jurassic (Fig. 1; e.g., Nelson and van Straaten, 2021). Three unconformity-bounded island arc volcano-sedimentary successions are recognized: 1) the Stikine assemblage (upper Paleozoic; Logan et al., 2000; Gunning et al., 2006); 2) the Stuhini and Takla groups (Middle to Upper Triassic); and 3) the Hazelton Group (uppermost Triassic to Middle Jurassic; Nelson et al., 2018). Coeval and comagmatic Mesozoic arc-related intrusive suites include Late Triassic Stuhini Group equivalents (Stikine and Galore suites) and latest Triassic (Tatogga suite) and Early Jurassic (Texas Creek suite) Hazelton Group equivalents (Alldrick, 1993; Nelson et al., 2018; Nelson and van Straaten, 2021).

The main axis of Stuhini Group magmatism is defined by thick accumulations of mafic to intermediate volcanic rocks along the Stikine arch region of northern Stikinia (Brown et al., 1996; van Straaten and Wearmouth, 2019) and accompanying ca. 229-216 Ma Stikine suite plutons that form an easterly trend along the arch (Nelson and van Straaten, 2021). In contrast, Stuhini Group sections farther south, in the McTagg anticlinorium and Stewart mining camp (Fig. 1), comprise mainly sedimentary units and augite-phyric to aphanitic basalts (Massey et al., 2005; Lewis, 2013), which Nelson and van Straaten (2021) infer were deposited in a marine back-arc basin.

The Stuhini Group near the Granduc volcanogenic massive sulphide deposit in the western part of the Stewart mining camp (Fig. 1) comprises phyllite and meta-clastic strata with thinner mafic interlayers that may be extrusive, intrusive or both (Lewis, 2013). A sheared mafic unit in the footwall of the Granduc deposit yielded a U-Pb zircon age of 222 ±1 Ma, based on three concordant fractions (Childe, 1997). Detrital zircons from a heterolithic breccia in the hanging wall of the deposit gave an interpreted MDA (Maximum Depositional Age) of ca. 208 Ma (Mihalynuk et al., 2019), reinterpreted as 213.3 +6.0/-4.8 Ma, with exclusion of a single ca. 194 Ma youngest grain (Nelson and van Straaten, 2021). Based on the existing age constraints on Granduc (between 222 and 208 Ma) the volcanogenic mineralization either formed in a back-arc setting during main Stuhini arc-building at 229-216 Ma (Nelson and van Straaten, 2021), or after subduction ceased. The younger age is more likely, because the hanging wall breccia unit contains mineralized clasts that were interpreted as intraclasts (Mihalynuk et al., 2019).

A distinctive north-trending magmatic belt, the Galore trend, developed in western Stikinia between 212 and 203 Ma (Fig. 1; Nelson and van Straaten, 2021; Nelson et al., 2022 in press). The Galore plutonic suite that defines this trend is typified by small plutons and stocks of predominantly alkaline affinity. Comagmatic volcanic units include shoshonitic basalts and alkali-enriched pyroclastic deposits (Logan and Koyanagi, 1994). The southernmost known exposures of the Galore belt, in the lower Iskut River region, are: 1) the Zippa Mountain gabbro-syenite pluton (Fig. 1; Coulson et al., 1999, 2007); 2) small, ca. 214-203 Ma, mildly alkalic porphyritic stocks and diatremes and biotite-K-feldspar-bearing tuff and volcanic breccias interpreted as their extrusive equivalents, near the Dirk and Telena mineral occurrences (Fig. 1; Mihalynuk et al., 2011, 2012; Nelson and van Straaten, 2021) and 3) small Late Triassic syenite plutons in the Newmont graben (Fig. 1; Logan et al., 2000).

Stuhini arc and post-arc magmatic activity ceased by the latest Triassic due to collision of northern Stikinia and the pericratonic Yukon-Tanana terrane, which led to uplift and variable deformation throughout the terrane (Nelson and van Straaten, 2021; Nelson et al., 2022, in press). The base of the lower Hazelton Group is a regional unconformity that was initially recognized in the 1990s (e.g., Henderson et al., 1992; Brown et al., 1996; Logan et al., 2000) and has since become increasingly well documented (Greig, 2014; Nelson and Kyba, 2014; Kyba and Nelson, 2015; Febbo et al., 2019; Miller et al., 2020). The lower Hazelton Group (Rhaetian-Pliensbachian) represents the development of the Hazelton arc and its back-arc (Nelson et al., 2018). It is overlain by post-arc sedimentary and volcanic strata of the upper Hazelton Group (Pliensbachian-Callovian) including units of regional extent on the periphery

of the Bowser Basin and the volcano-sedimentary fill of the Eskay rift (Gagnon et al., 2012).

On the flanks of the McTagg anticlinorium (Fig. 1), the Stuhini Group-Hazelton Group contact is an angular unconformity (Nelson and Kyba, 2014), with the lowest unit in the Hazelton Group, the Jack Formation (Hettangian-Sinemurian), lying on previously tilted and, in some localities, folded Stuhini Group rocks (Fig. 2; Henderson et al., 1992; Lewis, 2013). The Jack Formation is a unique sedimentary sequence that is compositionally mature relative to the Stuhini Group and apparently restricted to the McTagg area. It consists of cobble to boulder, highly rounded granitoid-clast conglomerate, quartz-bearing arkosic sandstone, granulestone, thinly bedded siltstones and mudstones and, west of the McTagg anticlinorium, a middle volcaniclastic unit (Nelson and Kyba, 2014).

The Jack Formation is overlain by the main volcanic unit of the lower Hazelton Group, the Betty Creek Formation (Lewis, 2013). The base of the Betty Creek Formation above

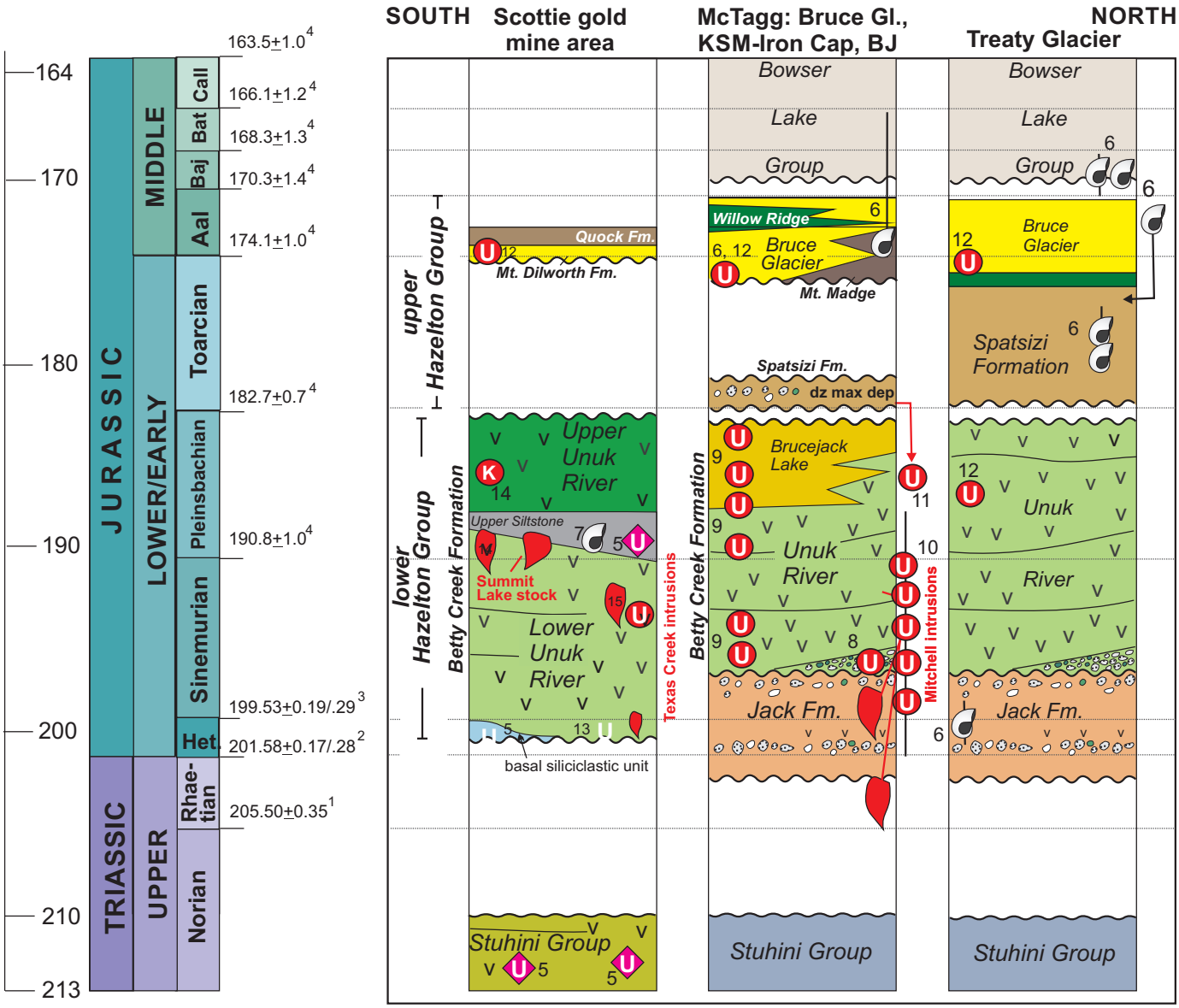

Fig. 2. Stratigraphic columns representing the Hazelton Group in the Scottie gold mine-McTagg-Treaty area, southern Iskut River region. Numbers reference sources for fossil and radiometric ages. **1.** Norian-Rhaetian boundary (Wotzlaw et al., 2014); **2.** Rhaetian-Hettangian boundary (Schaltegger et al., 2008); **3.** Hettangian-Sinemurian boundary (Schaltegger et al., 2008); **4.** Cohen et al., (2013); **5.** ca. 214.2 Ma, 211.9 Ma, 201.0 Ma, and 190.6 Ma U-Pb zircon (this study); **6.** biochronologic and geochronologic compilations of Lewis (2013) based on Nadaraju (1993) and Nadaraju and Lewis (2001). **7.** Pleinsbachian ammonite fossil mold (this study) **8.** ca. 197 Ma, U-Pb zircon (Nelson, et al., 2021); **9.** MacDonald (1993) and Greig (2013); **10.** 198-189 Ma U-Pb zircon (Febbo et al., 2019); **11.** ca. 186 Ma youngest detrital zircon population (Nelson et al., 2021); **12.** Cutts et al. (2015); **13.** ca. 200.5 Ma U-Pb zircon (van Straaten et al., 2014); **14.** ca.190.6 Ma U-Pb zircon (Lepore, 2006); **15.** ca. 192.8 Ma U-Pb zircon (Alldrick, 1993).

the Jack Formation is sharp and ranges from paraconformable to unconformable. It represents an abrupt transition from siliclastic sedimentation to predominantly andesitic pyroclastic volcanism and epiclastic sedimentation (Nelson et al., 2018). Uranium-lead ages place the base of the Betty Creek Formation in the mid-Sinemurian (ca. 197 Ma), slightly younger than the youngest Jack Formation, indicating an abrupt onset of andesitic volcanism (Nelson et al., 2018). The Betty Creek Formation has been divided into three lithologically based, informal units (Fig. 2; Nelson et al., 2018). The Unuk River andesite unit is the most widespread and voluminous, extending from the Stewart mining camp into the McTagg area and west into the lower Iskut region. The Johnny Mountain dacite unit (ca. 194 Ma, Lewis, 2013) only occurs on Johnny Mountain (Fig. 1), and the Brucejack Lake felsic unit (ca. 185-178 Ma; Lewis, 2013) only occurs in the Brucejack area east of the McTagg anticlinorium. They represent local felsic centres within a regional andesitic volcanic field.

3. Previous work in the Stewart mining camp

Because of its accessibility from tidewater, the earliest mineral prospecting and small-scale mining in what would become known as the Golden Triangle began in the Stewart area in the early 1900s (Alldrick, 1993). By the 1980s, significant epithermal gold resources were identified at Scottie Gold (BC MINFILE 104B 034), Premier (BC MINFILE 104B 054), and adjacent Big Missouri (BC MINFILE 105B 045, 46). Scottie Gold was mined between 1981 and 1984, producing 2.98 million grams of gold and 1.63 million grams of silver. Premier was mined between 1989 and 1996; Big Missouri 1927-1942 and briefly 1988-89.

Geological mapping of the Stewart mining camp was conducted in the 1980s during the peak phase of mining and exploration activity (Alldrick, 1993). This work assigned all volcano-sedimentary units in the Stewart area to the Hazelton Group, in ascending order: alternating intermediate green volcanic and marine sedimentary beds of the Unuk River Formation; maroon and green volcaniclastic strata of the Betty Creek Formation; and dacitic tuffs of the Mt. Dilworth Formation (Alldrick, 1993). No Stuhini Group strata were recognized. The Unuk River Formation was subdivided into six members, in ascending order: lower andesite, lower siltstone, middle andesite, upper siltstone, upper andesite, and plagioclase-potassium feldspar-hornblende crystal-lithic tuffs and flows of the Premier porphyry member (Alldrick, 1993). The base of the overlying Betty Creek Formation was primarily defined by a change of colour in the andesitic volcaniclastic rocks from dark green to maroon and green (Alldrick, 1993).

Later workers pointed out that no clear, regionally applicable lithologic distinction exists between the Betty Creek and Unuk River formations, and that the variation of rock colouring records diagenesis, and occurs at all stratigraphic levels in the andesitic sequence (Lewis et al., 2001). Currently, all volcanic rocks in the lower Hazelton Group between Stewart and the Iskut River are included in the Betty Creek Formation (Lewis, 2013; Nelson et al., 2018). The andesitic volcanic and epiclastic sequences in the Stewart mining camp belong to the informal Unuk River andesite unit of the Betty Creek Formation (Lewis, 2013). The siltstone members of Alldrick (1993) were not addressed, because they do not occur in Betty Creek sections in the McTagg area where the revised stratigraphic schema was developed. The Mt. Dilworth Formation, which overlies the Betty Creek Formation, is Middle Jurassic (Cutts et al., 2015) and is part of the upper Hazelton Group (Gagnon et al., 2012).

4. Supracrustal rocks in the Scottie area: Stuhini and Hazelton groups

4.1. Stuhini Group

In the study area, the lowest Stuhini Group unit exposed consists of interlayered argillite, limestone, plagioclase-rich fine-grained sandstones, and felsic tuffs (Fig. 3); the base of this unit has not been observed. It grades up-section into an upper unit of alkalic volcanic breccias, flows and tuffs.

4.1.1. Lower fine-grained sedimentary-tuff unit

The lowest Stuhini Group unit in the study area outcrops along a 4 km-long ridge south of August mountain, and in a discontinuous belt extending north from the Lost Railway area (Fig. 3). It consists of dark grey, carbonaceous argillite with lesser light-toned, plagioclase-rich fine-grained sandstone, very fine grained felsic tuff interbeds, and discontinuous grey limestone lozenges up to 10s of m long (Fig. 4a). In some exposures, these rock types are interlayered on a cm to m scale. Sodium cobaltinitrite staining of a sample from a 2 m-thick sandstone bed indicates a low content of potassium feldspar (Fig. 4b). The sandstone contains angular to subangular grains of plagioclase (45%), quartz (20%), potassium feldspar (15%), and lesser relict mafic grains (Fig. 4c).

In the Domino area (Fig. 3), fine-grained dark grey argillites are interbedded with volcanic breccias and flows of the upper volcanic unit. These interbeds decrease in number and disappear up-section at the expense of purely volcanic beds, indicating a transitional contact with respect to the upper volcanic unit.

4.1.2. Upper volcanic unit

Alkalic volcanic and volcaniclastic deposits of this unit form a north-northwest trending belt extending from the eastern slopes of August mountain through Summit Mountain and continuing to the Domino area, in part covered by glaciers (Fig. 3). In this belt, light-toned augite-phyric trachyandesite-(latite) breccias, flows and flow-breccias, felsic flows, and lapilli tuffs interfinger with laminated felsic (trachyte) crystal lithic tuffs (Fig. 5; McPhie, 1993). Breccias of this unit overlie dark-toned argillaceous strata of the lower fine-grained sedimentary-tuff unit near the southern Berendon Glacier fork and east of August mountain (Fig. 3). The coarse-grained volcaniclastic units are typically monomictic, consisting of lapilli to bomb fragments embedded in a finely comminuted matrix of the same composition (Fig. 5a). Large, well-formed, fresh augite phenocrysts are abundant in the clasts. Less common polymictic

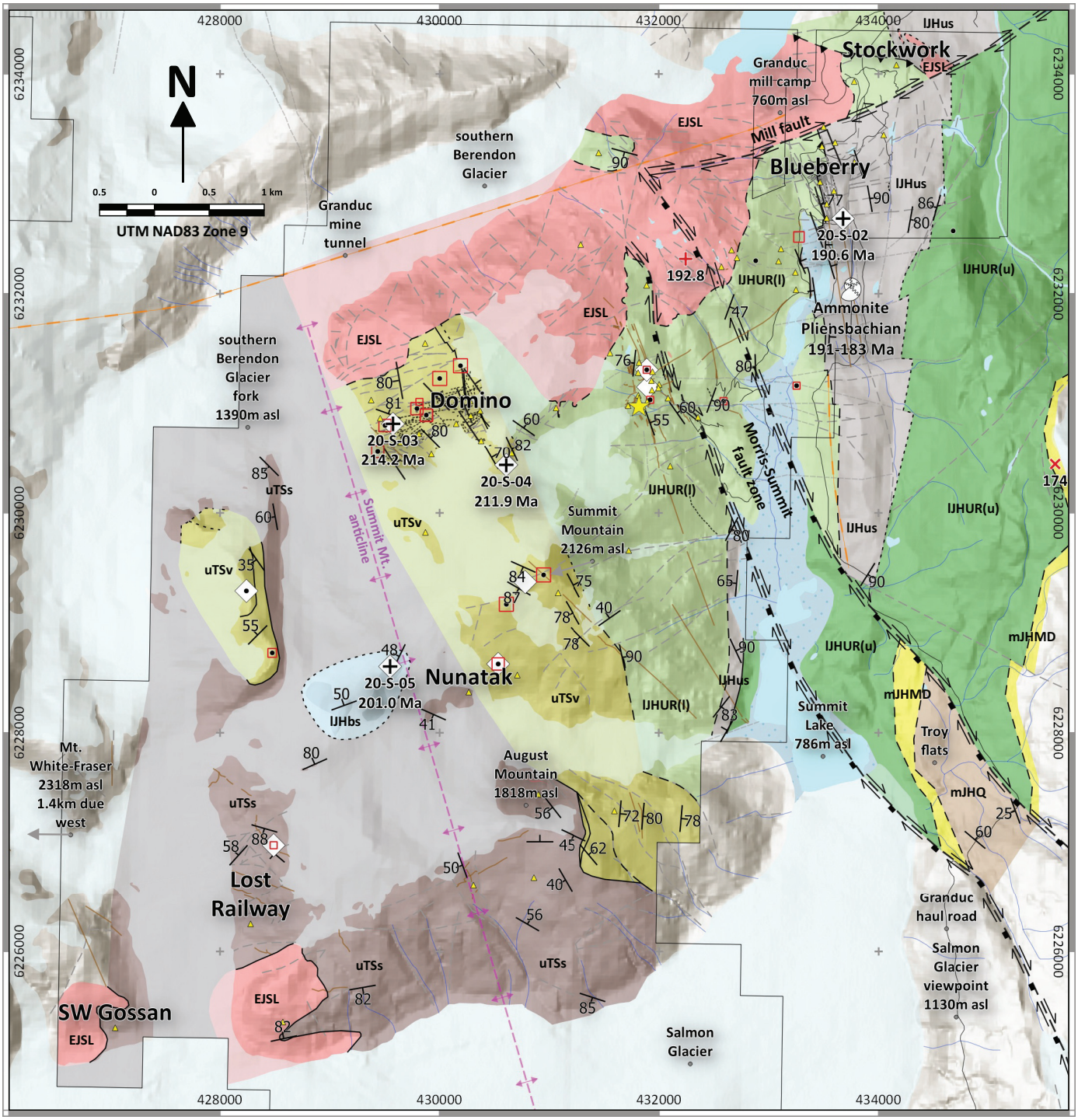

Fig. 3. Geology of the Scottie gold mine area.

varieties contain subangular to subrounded fragments of similar composition to the matrix but with a range of volcanic and hypabyssal textures. Some contain clasts of argillite and lesser chert, which may represent scavenged colluvial fragments. A set of 12 samples from this unit show a strong response to sodium cobaltinitrite staining, indicating high potassium feldspar and compositions in the field of trachyandesite (latite, based on subequal percentages of plagioclase and potassium feldspar; Lemaitre et al., 2002) and possibly trachyte (Figs. 3, 5b). Potassium feldspar, probably sanidine, forms very fine-grained aggregates along with variable amounts of plagioclase as igneous matrix to breccia and tuff clasts.

A crystal-lithic tuff bed near the base of the unit (20-S-03, Fig. 3) shows graded bedding and cross bedding that indicate younging towards the northeast (to top of photo Fig. 5c). The bed contains angular potassium-feldspar-rich lithic fragments

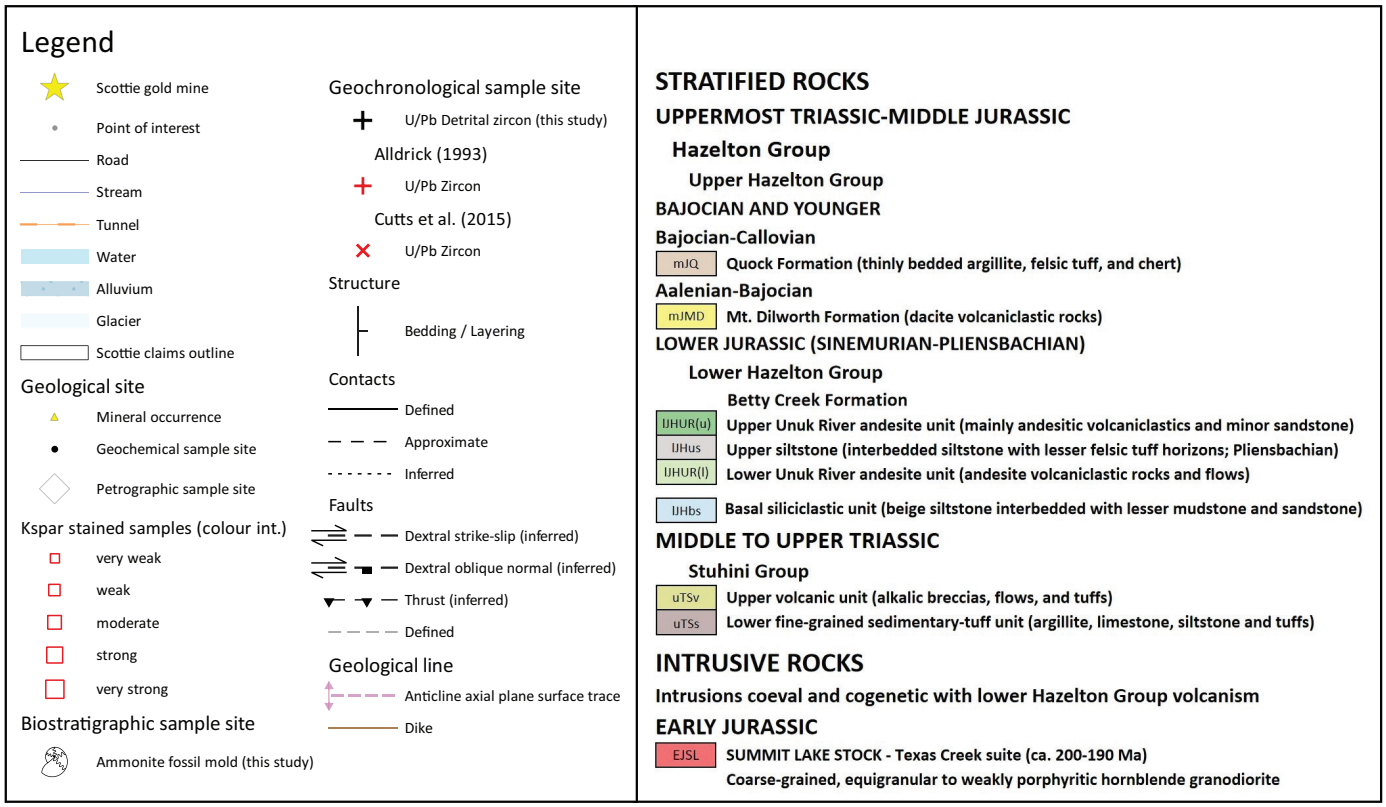

Fig. 3. Continued. Legend.

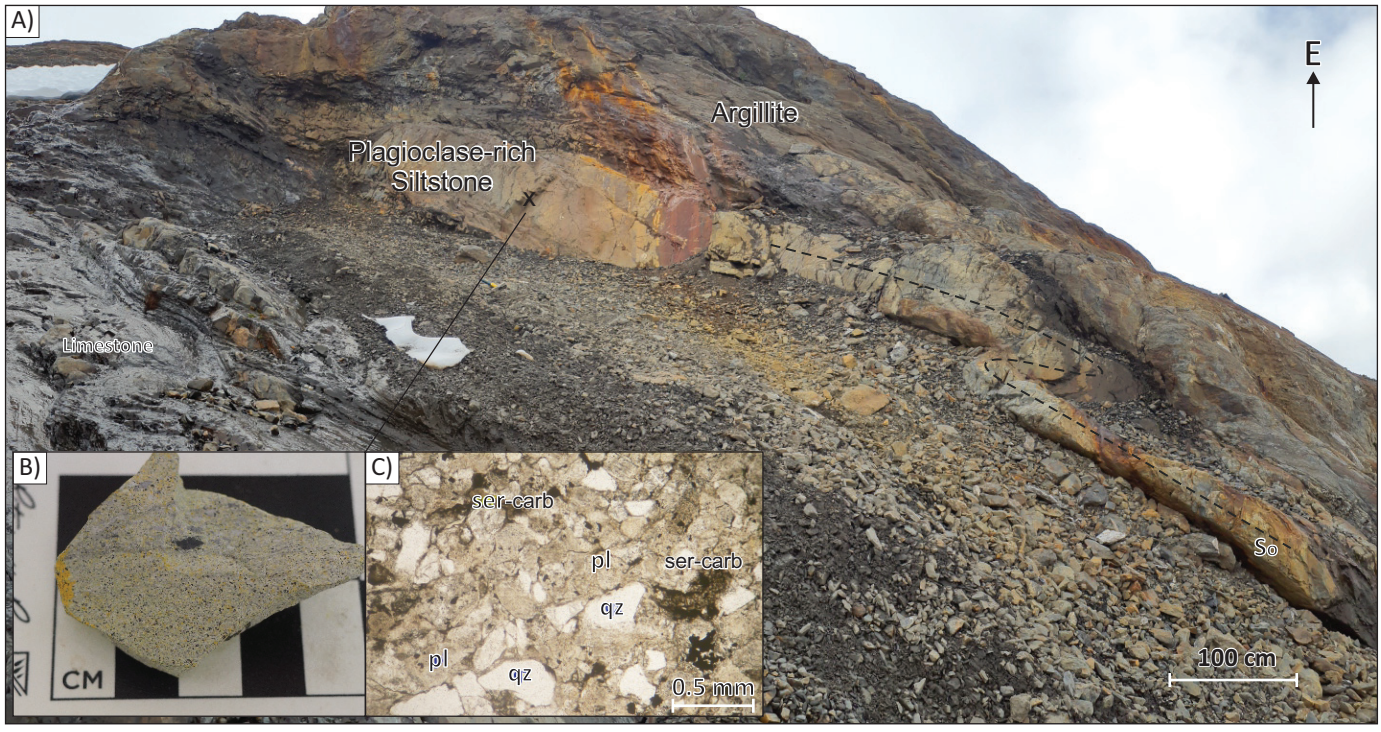

Fig. 4. Stuhini Group lower fine-grained sedimentary-tuff unit in the Lost Railway area (UTM 428488E, 6226977N). **a)** Interbedded argillite, with a prominent plagioclase-rich, fine-grained sandstone bed, and limestone. South-vergent tight fold in sandstone. **b)** Sodium cobaltinitrite stained fine-grained sandstone, showing weak response. **c)** Photomicrograph of plagioclase-rich, fine-grained sandstone, plane-polarized light. Small patches of secondary sericite and carbonate. pl = plagioclase; qz = quartz; ser-carb = sericite + carbonate.

Fig. 5. Stuhini Group, augite-bearing alkalic volcanic rocks of upper volcanic unit. **a)** Matrix-supported latite volcanic breccia, north of Domino area (UTM 430001E, 6231228N). **b)** Sodium cobaltinitrite-stained hand sample of breccia in a) indicates abundant matrix potassium feldspar. **c)** Interbedded beige parallel- and cross-stratified latite crystal-lithic tuff and lapilli tuff. U-Pb detrital zircon LA-ICPMS sample site 20-S-03 (UTM 429535E, 6230888N). MDA = 214.2 ±1.0 Ma (see below). **d)** Photomicrograph displays augite-plagioclase-phyric lithic fragment with potassium- and plagioclase feldspar-rich matrix. Crossed polarizers. **e)** Interval of laminated augite-rich crystal-lithic tuffs interbedded with lapilli tuff. U-Pb detrital zircon LA-ICPMS sample site 20-S-04 (UTM 430607E, 6230437N); U-Pb crystallization age = 211.9 ±3.6 Ma (see below). **f)** Photomicrograph of fragment from laminated tuff displays large, embayed augite phenocryst in plagioclase-rich matrix with interstitial potassium feldspar. Crossed polarizers. **g)** Large, fresh euhedral and broken augite phenocrysts. Crossed polarizers. aug = augite, plag = plagioclase, Kspar = potassium feldspar.

(50%), broken plagioclase (20%), and augite (5%) crystal clasts (Fig. 5d). Although compositionally similar, lithic clasts in this tuff exhibit a wide range of igneous textures, from holocrystalline with well-formed matrix plagioclase and interstitial potassium feldspar (Fig. 5d) to nearly aphanitic. The top of the volcanic unit is marked by very coarse, light-toned augite-phyric volcaniclastic rocks (Figs. 5a, b, e, f). A crystal-lithic tuff interbedded with lapilli tuff (Fig. 5e; 20-S-4, Fig. 3) contains densely packed augite-phyric plagioclase-rich lithic fragments (Fig. 5f) and euhedral to broken, fresh augite phenocrysts (Fig. 5g), with a few dark green-pleochroic hornblende crystal clasts. Plagioclase does not form phenocrysts in this sample. Lithic clasts are all augite-phyric, but show different matrix textures ranging from felted plagioclase and anhedral interstitial potassium feldspar (Fig. 5f), to nearly glassy. Some augite crystals in the igneous matrix show embayed margins (Fig. 5f) that may reflect partial resorption by the melt.

4.2. Lower Hazelton Group

A nunatak in the west-central part of the map area forms an isolated exposure of basal Hazelton Group siltstone, sandstone, and mudstone, surrounded by Stuhini Group strata (Fig. 3). The eastern half of the map area is underlain by a thick, east-younging section of the Betty Creek Formation of the lower Hazelton Group. The section there comprises two units of feldspar-hornblende-phyric andesitic flows, tuffs, breccias, and conglomerates assigned to the Unuk River andesite unit of the Betty Creek Formation, following the lithologically based usage of Nelson et al. (2018), and an intervening siltstone unit (Figs. 2, 3). Siltstones have not been previously recognized as components of the Betty Creek Formation (Lewis, 2013, Nelson et al., 2018). Alldrick (1993) included the siltstone in the Unuk River Formation; however subsequent workers have restricted the term 'Unuk River' to denote andesitic lithofacies within the Betty Creek Formation (Lewis, 2013; Nelson et al., 2018). In this report we assign it the informal name of "upper siltstone unit", based on its assigned name in Alldrick (1993).

East of the map area, the Betty Creek Formation is overlain by felsic tuffs of the Mount Dilworth Formation (upper Hazelton Group, Middle Jurassic), west of Troy flats and along the flanks of the north trending Mount Shorty-Stevenson ridgeline (Figs. 1-3; Alldrick, 1993).

4.2.1. Basal siliciclastic rocks

West of Nunatak (Fig. 3), the lowermost Hazelton unit forms an outlier surrounded by the lower fine-grained sedimentary-tuff unit of the Stuhini Group and extensively covered by glaciers. The outlier consists of beige siltstone with lesser interbeds of sandstone and mudstone (Fig. 6). The siltstone consists of sericite-altered plagioclase grains with subordinate subrounded to subangular quartz grains (Fig. 6b). Because the upper volcanic unit of the Stuhini Group is missing, the glacier-covered basal contact of this siliclastic unit may record the regionally developed sub-Hazelton Group unconformity.

4.2.2. Betty Creek Formation

4.2.2.1. Lower Unuk River andesite unit

A thick andesitic succession overlies the upper Stuhini Group volcanic unit on the eastern slope of Summit Mountain, extending into the Blueberry area (Fig. 3). It consists predominantly of matrix-supported plagioclase-hornblende-phyric andesite breccias and flows, with little or no matrix potassium feldspar (Fig. 7). Coherent and volcaniclastic eruptive units interfinger and grade into one another at outcrop scale. Volcanic breccias typically contain lapilli to bomb fragments (Figs. 7a, c) of similar composition to the matrix. Clasts are angular and irregular. Fragments of augite-phyric latite and argillite occur locally. Rare pyroxene phenocrysts are much smaller than those in the underlying upper Stuhini volcanic unit. Generally, layering in this unit appears subparallel to its lower contact and with layering in subjacent rocks of the upper Stuhini Group volcanic unit. We interpret this contact as a paraconformity.

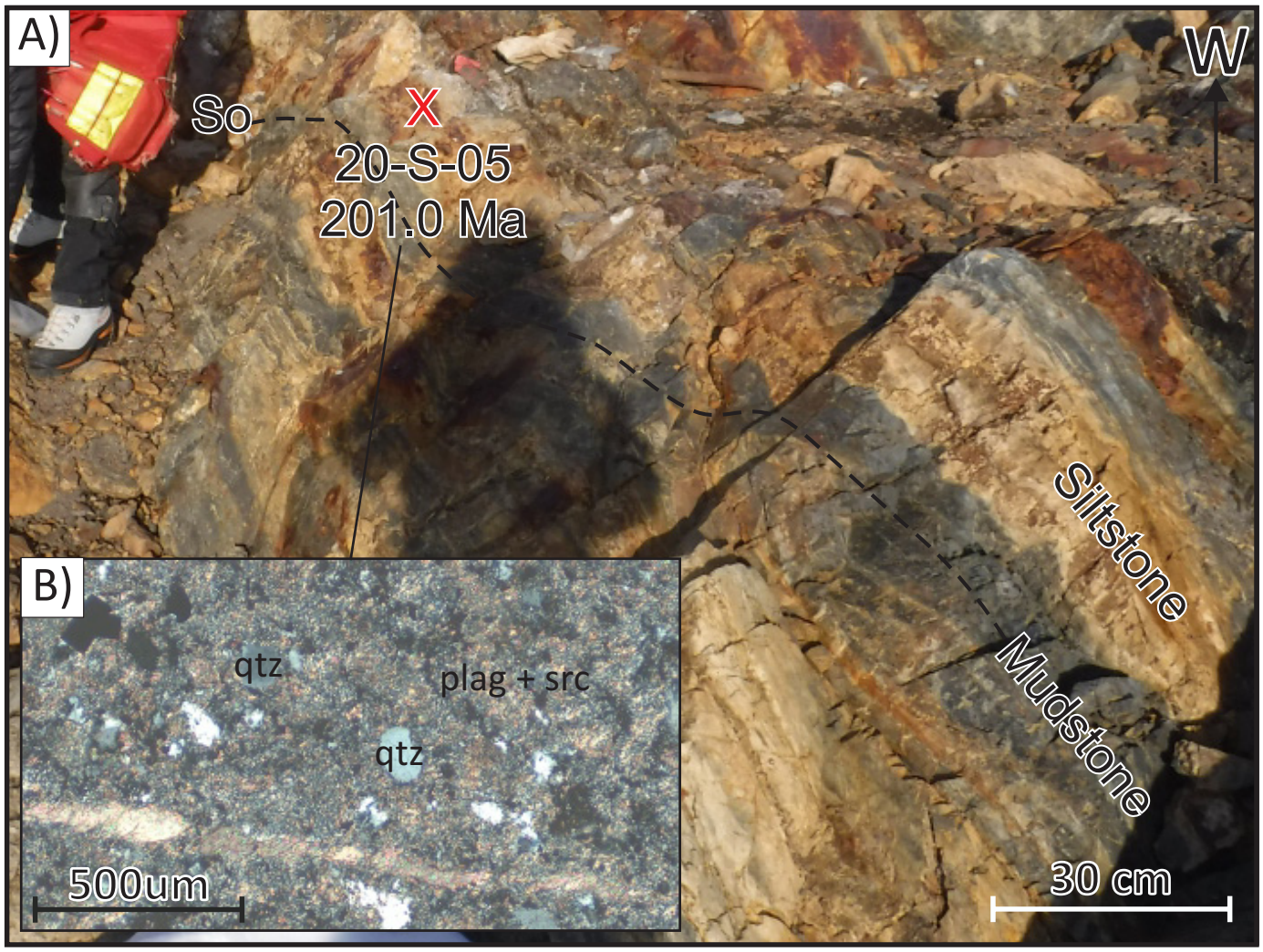

Fig. 6. Lower Hazelton Group, basal siliciclastic rocks. **a)** Siltstone and mudstone beds; U-Pb detrital zircon sample site 20-S-5, west of Nunatak area (UTM 429549E, 6228603N). MDA = 201.0 ±5.2 Ma (see below). **b)** Photomicrograph of sample 20-S-5 displays mainly heavily sericitized detrital plagioclase grains with scattered angular to subrounded quartz. Crossed polarizers. Qtz = quartz, plag + src = sericite-altered plagioclase.

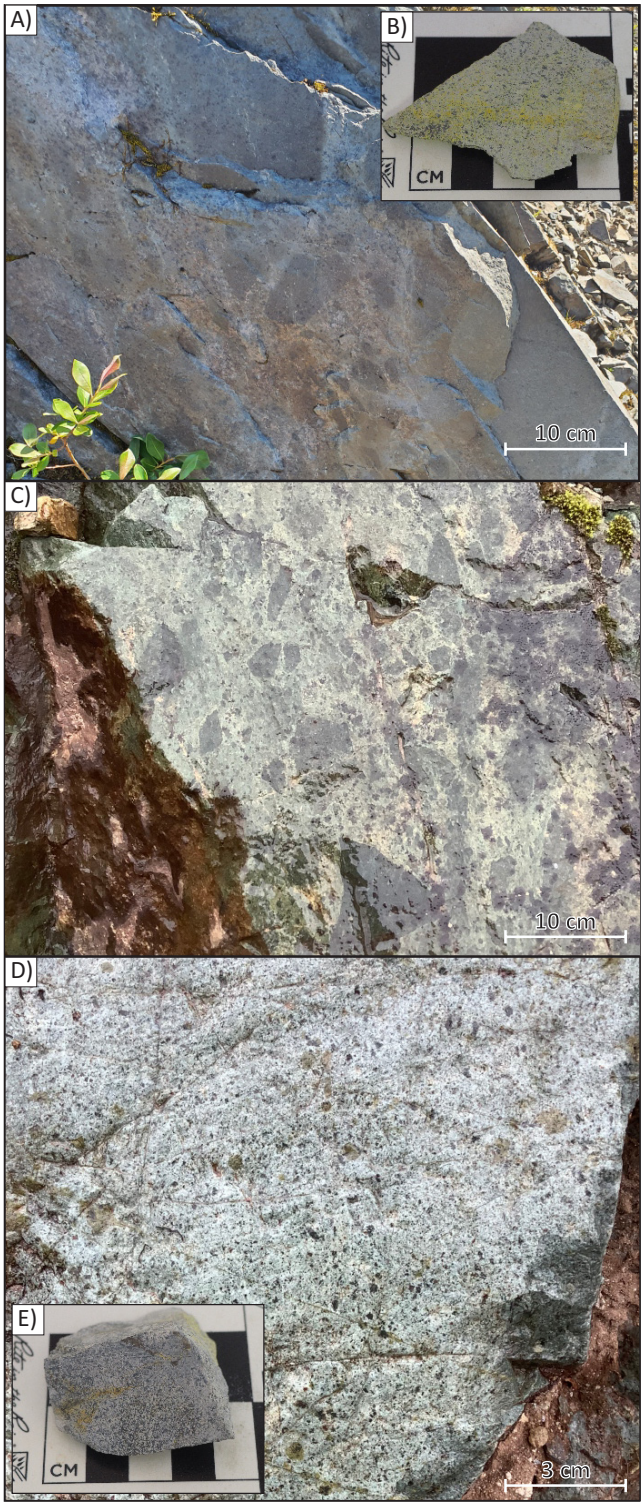

Fig. 7. Lower Hazelton Group, Betty Creek Formation, lower Unuk River unit andesites. **a)** Monomictic, matrix-supported, hornblende-phyric andesitic volcanic breccia, 1.4 km east of the Scottie gold mine area (UTM 433255E, 6231163N). **b)** Breccia matrix hand sample very weakly stained by sodium cobaltinitrite. **c)** Monomictic matrix-supported andesite volcanic breccia from 1 km east of the Scottie gold mine area (UTM 432881E, 6231341N). **d)** Weakly sericite altered, hornblende-phyric andesite flow from the Scottie gold mine area (UTM 431923E, 6231034N). **e)** Very weakly sodium cobaltinitrite-stained hand sample of flow in d).

4.2.2.2. Upper siltstone unit

Grey feldspar-rich siltstones outcrop in a north-striking, northerly thickening sequence east of and stratigraphically above the lower Unuk River andesite unit (Figs. 3, 8). These strata have sub-vertical dips and contain mud rip-up clasts, flame structures, load casts, and graded- and cross-bedding structures that consistently indicate younging to the east. A sample from this unit (Fig. 8b) contains subangular grains of potassium feldspar (30%), fine-grained potassium feldspar-rich lithic grains (20%), plagioclase (25%), and quartz (5%). Carbonate minerals (5%) occur as patches in the matrix. Towards the upper half of the siltstone unit, thin (<5 m), internally-laminated felsic ash tuff beds interfinger with siltstone beds.

In its southernmost exposure west of Summit Lake, the unit is approximately 130 m thick (Fig. 3), whereas at its northern extent in the Blueberry area 6 km along strike, it may be as much as 1200 m thick. The upper contact with andesites of the upper Unuk River unit lies under Quaternary cover. An ammonite fossil mold has been tentatively assigned a Pliensbachian age (M. Golding, personal communication 2021, based on identification by Terry Poulton).

4.2.2.3. Upper Unuk River andesite unit

Light to dark green and maroon andesitic breccias and tuffs overlie the upper siltstone unit on the eastern side of the map area (Figs. 3, 9). Small hornblende and plagioclase phenocrysts are common in this unit. Most breccias are monomictic and

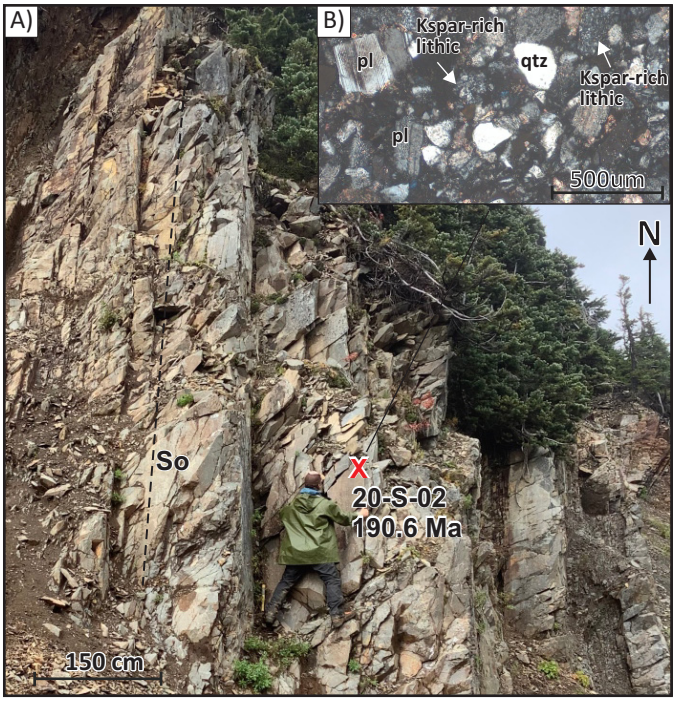

Fig. 8. a) Lower Hazelton Group, Betty Creek Formation, upper siltstone unit and U-Pb detrital zircon sample site 20-S-2 from the Blueberry area (UTM 433678E, 6232684N). MDA = 190.6 ±1.7 Ma (see below). **b)** Photomicrograph of sample 20-S-2, illustrating abundant feldspar and sparse quartz. Kspar = potassium feldspar, plag = plagioclase, qtz = quartz.

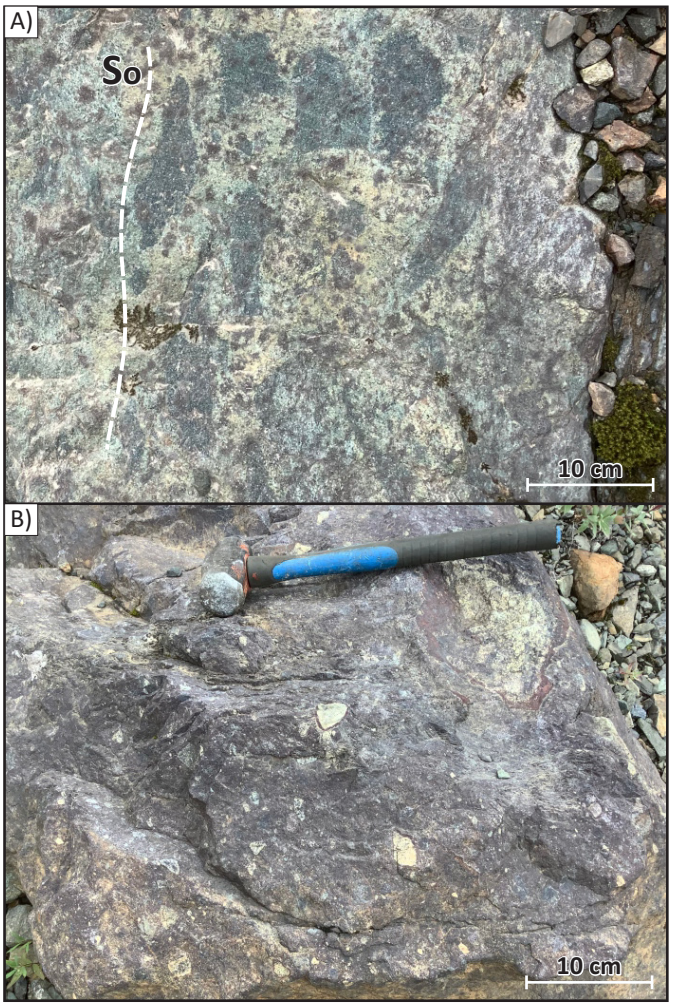

Fig. 9. Upper Unuk River unit andesites. **a)** Matrix-supported green and maroon volcanic breccia, 1.3 km east-southeast of the Blueberry area (UTM 434680E, 6232572N). **b)** Maroon matrix-supported volcanic breccia with feldspar-phyric clasts, 1.5 km east-southeast of the Blueberry area (UTM 434793E, 6232514N).

matrix-supported (Figs. 9a, b); locally, apparent long axes align to define a crude layering (Fig. 9a). In some breccias, angular lapilli to bomb fragments of laminated felsic tuff are similar in colour and texture to felsic volcanic interbeds in the upper siltstone unit to the west, and are interpreted as accidental clasts derived from them. The andesitic sequence contains minor sandstone interbeds with mud rip-up clasts; cross-bedding and graded bedding indicate younging to the east.

5. Intrusive rocks: Summit Lake stock, Texas Creek plutonic suite

Within the Stewart mining camp, the Texas Creek plutonic suite (ca. 202-190 Ma) consists of the Texas Creek batholith, the Summit Lake stock, Premier porphyry dikes, and a variety of related dikes and sills (Alldrick, 1993; Anderson, 1993). The Texas Creek batholith and Premier porphyry dikes outcrop 10 km south of the study area, near the past-producing Premier mine (Fig. 1). There, gold-silver mineralization and associated alteration zoning patterns are spatially related to plutons of the Texas Creek suite and Premier porphyry dikes (Bird et al., 2020). Major element analysis of the Summit Lake stock, Texas Creek batholith, and Premier porphyry dikes indicates that the suite is subalkaline, calc-alkaline in composition with elevated potassium contents (Alldrick, 1993). Discriminant diagrams also show that Texas Creek intrusions are chemically similar to, and likely comagmatic with, Hazelton Group volcanic rocks (Alldrick, 1993).

The Summit Lake stock outcrops as an elongate northeast trending (~7 km long) body at the northern extent of the study area (Fig. 3). It consists of medium- to coarse-grained equigranular to porphyritic potassium-feldspar and hornblende granodiorite to tonalite (Alldrick, 1993). Less common weakly foliated, mafic enclave-bearing phases are interpreted as older phases of the stock (Alldrick, 1993). The stock cuts across northwest-trending strata of the upper volcanic unit of the Stuhini Group and the lower Unuk River andesite unit. Northeast of the main stock, a small, probably related body cuts the upper siltstone unit (Fig. 3).

Regionally, U-Pb ages of Texas Creek suite intermediate porphyritic intrusions (Mitchell suite at KSM and Lehto suite in the Snippaker area; Fig. 1) are coeval with Unuk River unit andesites (Fig. 2; Febbo et al., 2015; Kyba and Nelson, 2015; Febbo, 2016; Nelson et al., 2018). In the Scottie area, the stock returned a 192.8 ±2 Ma U-Pb age (Fig. 2; Alldrick, 1993). North of the study area, on the Tennyson claims, an early Texas Creek suite intrusion yielded a U-Pb zircon age of 200.5 ±0.8 Ma (van Straaten et al., 2014), and a dike is 190.6 ±1.3 Ma (LA-ICP-MS U-Pb zircon, Lepore, 2006).

6. Structural geology

The main structural element in the map area is a regional-scale fold, the Summit Mountain anticline, which is cored by Stuhini Group rocks (Fig. 3). The anticline trends north-northwest and is asymmetric, verging to the east-northeast. It displays a subvertical to steeply east-dipping eastern limb of eastward-younging Hazelton Group rocks and a moderately southwest-dipping western limb defined by Hazelton Group units that cap the Mt. White-Fraser ridgeline, 2 km west of the study area. This major fold forms an anticline-syncline pair with the Mount Dilworth syncline farther east (Alldrick, 1993). These structures are first-order features of the Early Cretaceous Skeena fold and thrust belt (Evenchick, 2001).

Two northwest-trending, west-side down dextral-oblique normal faults (Morris-Summit fault zone) extend from the southeast corner of the map area and appear to cut the Summit Lake stock. In the northeast corner of the map area, the Mill fault, a major east-northeast-trending dextral strike-slip structure, also appears to cut the Summit Lake stock. Stuhini and Hazelton group strata are also cut by relatively minor northwest- and east-trending cross faults (Fig. 3).

7. Geochemistry

Eighteen representative samples from volcanic-volcaniclastic

units were collected across the study area for whole-rock geochemical analysis. Twelve samples were collected from the upper Stuhini volcanic unit, five samples from the lower Unuk River andesite unit and one sample from the upper Unuk River andesite unit (Table 1; sample locations on Fig. 3). During sample collection every effort was taken to avoid altered rock. A diamond saw was used to trim and remove veins and to minimize weathering. Major elements for most samples were analyzed at Australian Laboratory Services (ALS; Terrace, BC, laboratory) using ICP-Atomic emission spectrometric methods; two samples were analyzed at Société Générale de Surveillance (SGS; Burnaby, BC, laboratory) using ICP-optical emission spectrometric methods; in each case following lithium metaborate fusion and nitric acid digestion. The summary of major element geochemical results in Table 1 shows total weight percent values (between 91.2 and 101.6 wt.%) and loss on ignition values (between 1.8 and 5.6 wt.%). Full analytical datasets and background information are presented in Stanley and Nelson (2022).

7.1. Results

7.1.1. Upper volcanic unit, Stuhini Group

In the field, rocks of the upper volcanic unit appear as mainly large-augite-phyric trachyandesite (latite) to aphyric trachyte volcanic breccias, flows, and tuffs (Fig. 5). All twelve samples plot in the alkaline field, ranging from basaltic trachy-andesite, trachy-andesite, phono-tephrite, tephri-phonolite, to phonolite compositions on the total alkali versus silica discrimination diagram (TAS; Fig. 10a), and all samples, except D707510 and D707513, plot within the shoshonite series, ranging from absarokite, shoshonite, to banakite compositions on the potassium versus silica discrimination diagram (Fig. 10b). The abundance of augite phenocrysts in most of these rocks may skew the analytical compositions to lower silica contents and lead to clustering in the basaltic trachy-andesite field as opposed to their field identification as predominantly latites. Lemaitre et al. (2002) noted that the TAS diagram is intended as an interpretive tool for aphanitic volcanic rocks because crystal accumulation may produce spurious results. For this reason, field classification of these rocks should take precedence. Their highly potassic, shoshonitic geochemical character agrees with field identification of abundant igneous potassium feldspar.

7.1.2. Unuk River andesite unit, Hazelton Group

The Unuk River andesite unit consists mainly of matrix-supported feldspar-hornblende-phyric andesite breccias and less common coherent andesites interpreted as flows. The augite phenocrysts in this unit are subordinate to plagioclase and hornblende and are smaller than those in the upper volcanic unit of the Stuhini Group. Four samples plot within the alkaline field (basaltic trachy-andesite) adjacent the subalkaline boundary, and two plot within the subalkaline field (basalt and basaltic trachy-andesite) of the TAS discrimination diagram (Fig. 10a). On the K_2O vs. SiO_2 diagram, two samples plot within the shoshonite series (range from absarokite-shoshonite), two in the high potassium calc-alkaline series, and two in the calc-alkaline series (Fig. 10b).

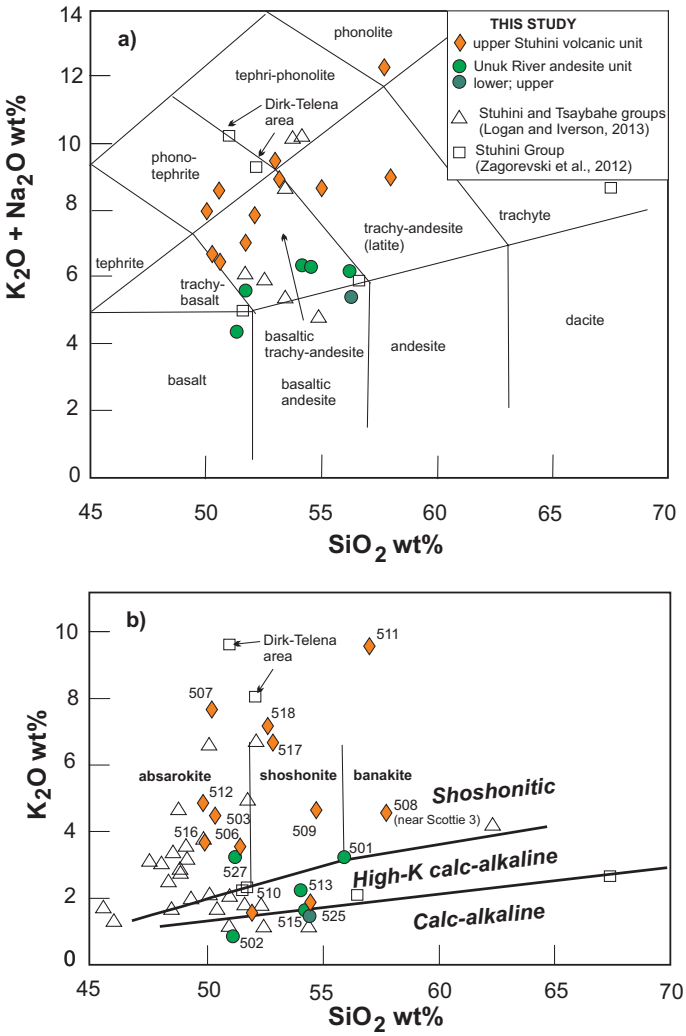

Fig. 10. a) Total alkalis vs. silica (Le Bas et al., 1986) rock type discrimination plot. Alkaline and subalkaline/tholeiitic fields after Irvine and Baragar (1971). Values are recalculated from Table 2 data to account for loss on ignition (e.g., SiO_2*100/(Total-Loss on ignition). **b)** Classification plot based on SiO_2 vs. K_2O (after Peccerillo and Taylor, 1976; Morrison, 1980), used to distinguish shoshonitic, high-K calc-alkaline, calc-alkaline and tholeiitic series rocks. Values are recalculated from Table 2 data to account for loss on ignition (e.g., SiO_2*100/(Total-Loss on ignition). Legend as in a).

8. Detrital zircon geochronology

We collected four samples for laser ablation-inductively coupled plasma-mass spectrometry (LA-ICP-MS) analysis: two from the upper alkalic volcanic unit of the Stuhini Group; one from the basal siliciclastic unit of the Hazelton Group; and one from the upper siltstone unit, Betty Creek Formation (Table 2). The analyses were carried out at the Pacific Centre for Isotopic and Geochemical Research (PCIGR), University of British Columbia, using a Resonetics RESOlution M-50-LR. The full analytical details, complete dataset, and data processing methods are presented in Stanley and Nelson (2022).

Table 1. Whole rock geochemical results from the Scottie gold mine area. All locations are NAD 83 Zone 9; samples D707527 and D707525 were analyzed at SGS Laboratories, all others were analyzed at ALS laboratories.

Sample	D707503	D707506	D707507	D707508	D707509	D707510	D707511	D707512	D707513
Group	Stuhini	Stuhini	Stuhini	Stuhini	Stuhini	Stuhini	Stuhini	Stuhini	Stuhini
Unit	upper volcanic unit	upper volcanic unit	upper volcanic unit	upper volcanic unit	upper volcanic unit	upper volcanic unit	upper volcanic unit	upper volcanic unit	upper volcanic unit
Rock Type	Augite-phyric latite breccia	Augite-phyric latite breccia	Augite-phyric latite breccia	Latite tuff	Trachyte	Felsic tuff	Felsic tuff	Latite	Latite
Easting	430190	429794	430001	429503	429437	429881	429879	428240	428476
Northing	6231344	6230954	6231228	6230801	6230560	6230893	6230895	6229290	6228726
SiO_2 (wt.%)	48.1	50.8	46.7	57.2	53.6	47.3	56.7	48.3	51.8
Al_2O_3 (wt.%)	15.35	16.8	15.2	17.1	17.1	17.15	19.25	17.4	17.1
Fe_2O_3 (wt.%)	10.3	9.15	8.76	6.24	8.36	9.21	6.55	9.56	10.2
CaO (wt.%)	8.75	5.71	7.3	4.32	4.28	5.2	1.07	6.36	4.15
MgO (wt.%)	5.19	7.72	5.17	3.88	4.04	3.24	1.87	6.07	4.25
Na_2O (wt.%)	1.94	3.41	0.86	4.38	3.88	5.78	2.54	3.03	4.25
K_2O (wt.%)	4.34	3.58	7.19	4.56	4.57	1.44	9.6	4.8	1.79
TiO_2 (wt.%)	0.88	0.76	0.67	0.74	1.04	0.75	0.6	0.74	0.9
MnO (wt.%)	0.21	0.18	0.21	0.1	0.21	0.21	0.14	0.18	0.18
P_2O_5 (wt.%)	0.36	0.31	0.38	0.28	0.41	0.6	0.2	0.31	0.36
LOI	2.4	2.86	4.29	2.26	2.43	4.26	1.75	4.18	4.96
Total	98.07	101.62	97.25	101.45	100.33	95.44	101.29	101.24	100.23

From each sample, 79 grains were hand-picked and mounted for analysis, except for 20-S-4, which yielded only three zircon grains. Probability density and histogram plots of detrital zircon ages were generated using the Isoplot 3.70 and 4.15 add-in for Microsoft Excel (Ludwig, 2008). Maximum Depositional Ages (MDA) were assigned based on Youngest Statistical Populations (YSP), according to the method of Coutts et al. (2019). To identify multiple source populations, we applied the Unmix routine in Isoplot 3.70 (Ludwig, 2008).

8.1. Stuhini Group, upper volcanic unit, samples 20-S-3 and 20-S-4

Sample 20-S-3 is of an interbedded latite crystal tuff and lapilli tuff 500 m west of the Domino area, near the interpreted base of the unit (Figs. 3, 5c). The main peak in the probability plot is ca. 219 Ma, with a younger shoulder at ca. 214 Ma (Fig. 11a, Table 2). It also contains a single Paleozoic grain, ca. 381.5 Ma (Stanley and Nelson, 2021). Although the youngest grain is 204.9 ±4.7 Ma, it is highly discordant (9.4%) and we attribute its young age to lead loss. The Youngest Statistical Population has a weighted average of 214.2 ±1.0 Ma based on 27 grains (Fig. 11b). We interpret this as the crystallization age of the tuff. The prominent older peak (ca. 219 Ma) is attributed to recycling of older Stuhini Group and Stikine plutonic suite zircons.

Sample 20-S-4 is of an augite-phyric latite crystal-lithic lithic

Table 1. Continued.

Sample	D707516	D707517	D707518	D707501	D707502	D707504	D707515	D707527	D707525
Group	Stuhini	Stuhini	Stuhini	Hazelton	Hazelton	Hazelton	Hazelton	Hazelton	Hazelton
Unit	upper volcanic unit	upper volcanic unit	upper volcanic unit	lower Unuk River andesite	lower Unuk River andesite	lower Unuk River andesite	lower Unuk River andesite	lower Unuk River andesite	upper Unuk River andesite
Rock Type	Augite-phyric trachyte breccia	Augite-phyric crystal tuff	Latite tuff	Hbl-phyric andesite breccia	Hbl-phyric andesite	Andesite breccia	Hbl-plag-phyric dacite	Hbl-Fsp-phyric andesite	Andesite
Easting	430534	430608	430947	432590	431923	433255	431891	432883	434680
Northing	6228626	6229168	6229436	6231022	6231034	6231163	6231307	6232300	6232572
SiO_2 (wt.%)	48	50.6	45.6	55.1	48.5	47.9	53	51.18	54.36
Al_2O_3 (wt.%)	16.2	16	16.4	16.6	14.9	14.95	16.2	16.43	18.26
Fe_2O_3 (wt.%)	9.56	8.86	7.48	9.39	12.15	9.51	4.32	10.65	8.55
CaO (wt.%)	5.54	5.26	3.14	5.56	7.7	4.35	11.3	8.41	6.05
MgO (wt.%)	8.92	4.86	4.24	4.2	5.83	4.78	5.21	5.46	3.04
Na_2O (wt.%)	2.93	2.11	1.95	2.82	3.31	3.63	4.6	2.34	3.84
K_2O (wt.%)	3.59	6.46	6.24	3.22	0.88	2.01	1.66	3.27	1.53
TiO_2 (wt.%)	0.74	0.76	0.63	0.81	0.85	0.72	0.77	0.79	0.69
MnO (wt.%)	0.13	0.17	0.13	0.19	0.2	0.17	0.11	0.11	0.22
P_2O_5 (wt.%)	0.3	0.39	0.46	0.28	0.37	0.37	0.41	0.44	0.32
LOI	2.79	2.61	4.52	2.22	3.74	4.12	2.47	1.98	5.63
Total	99.03	98.49	91.17	100.73	98.59	92.77	100.19	101.06	102.49

tuff from the top of the volcanic unit, north of Summit Mountain (Figs. 3, 5e). It only yielded three zircon grains, all of which are concordant (Fig. 11c). A weighted average of the youngest two grains is 211.9 ±3.6 Ma (Table 2), which is tentatively considered the crystallization age of the tuff. Although based on sparse data, this age overlaps within error the more robust age derived from sample 20-S-3. Thus, alkalic volcanism at ca. 214 Ma was the last event recorded by the Stuhini Group in the Scottie area.

8.2. Lower Hazelton Group

8.2.1. Basal siliciclastic rocks, sample 20-S-5

Sample 20-S-5 is of a siltstone from west of the Nunatak area (Figs. 3, 6). Zircon analyses show a main probability density peak of ca. 219 Ma, with subordinate peaks at ca. 201, 214, and 232 Ma (Fig. 12a). The Youngest Statistical Population of four grains has a weighted average age of 201.0 ±5.2 Ma (Table 2), interpreted as the maximum depositional age. The older populations show input from main-stage Stuhini Group and Stikine suite sources and from the immediately underlying uppermost Stuhini Group volcanic unit.

8.2.2. Betty Creek Formation, upper siltstone unit, sample 20-S-2

Sample 20-S-2 is from a well-sorted potassium feldspar-rich siltstone bed in the Blueberry area (Figs. 3, 8a, b). Zircon

Table 2. Summary of results from LA-ICP-MS U-Pb zircon analysis for samples from Scottie gold mine area. All locations are NAD 83 Zone 9.
N = Grains analyzed (total); N1 = Concordant grains (<10% discordant).

Sample ID	Unit	Easting	Northing	Description	N	N1	Youngest grain	Youngest Statistical Population	Probability density peaks	Unmix ages (fractions)
20-S-3	Stuhini Group, upper volcanic unit	429535	6230888	Beige laminated latite crystal-lithic tuff. Kspar-rich, plagioclase + augite-phyric lithics; plagioclase and augite crystal clasts	78	65	204.9 ±4.7 Ma 9.40% discordant; does not form coherent population with older grains	**214.2 ±1.0 Ma** (27 grains, except youngest; MSWD=0.89, prob=0.63): **volcanic crystallization age**	215 Ma 219 Ma 244 Ma	207.4 ±5.5 Ma (.04) 214.52 ±1.9 Ma (.36) 221.22 ±1.8 Ma (.45) 230.5 ±3.8 Ma (.14) 243.7 ±7.3 Ma (.02) relative misfit = 0.705
20-S-4	Stuhini Group, upper volcanic unit	430607	6230437	Laminated latite tuff with augite-phyric lithic clasts	3	3	**211.9 ±3.6 Ma** (youngest 2 of 3 total grains) **volcanic crystallization age**	n/a	n/a	n/a
20-S-5	Hazelton Group basal clastic unit	429549	6228603	Siltstone from mudstone-siltstone-fine sandstone sequence	79	67	198.5 ±4.7 Ma	**201.0 ±5.2 Ma** (4 grains, MSDW=0.16, prob=0.92) **MDA**	201 Ma 215 Ma 220 Ma 234 Ma	201.4 ±3.1 Ma (.06) 210.9 ±5.3 Ma (.16) 214.6 ±4.3 Ma (.31) 221.7 ±2 Ma (.38) 232.3 ±4.5 Ma (.09) relative misfit = 0.617
20-S-2	Hazelton Group, Betty Creek Fm., upper siltstone unit	433678	6232684	Light grey homogenous siltstone	79	76	189.7 ±3.7 Ma	**190.6 ±1.7 Ma** (youngest 4 grains, MSWD=0.104 prob=0.96) **MDA**	190.5 Ma 198-203 Ma 216 Ma 243 Ma	197.83 ±1.3 Ma (.20) 204.92 ±2.7 Ma (.23) 216.46 ±1.1 Ma (.47) 226.6 ±2.6 Ma (.10) relative misfit = 0.366

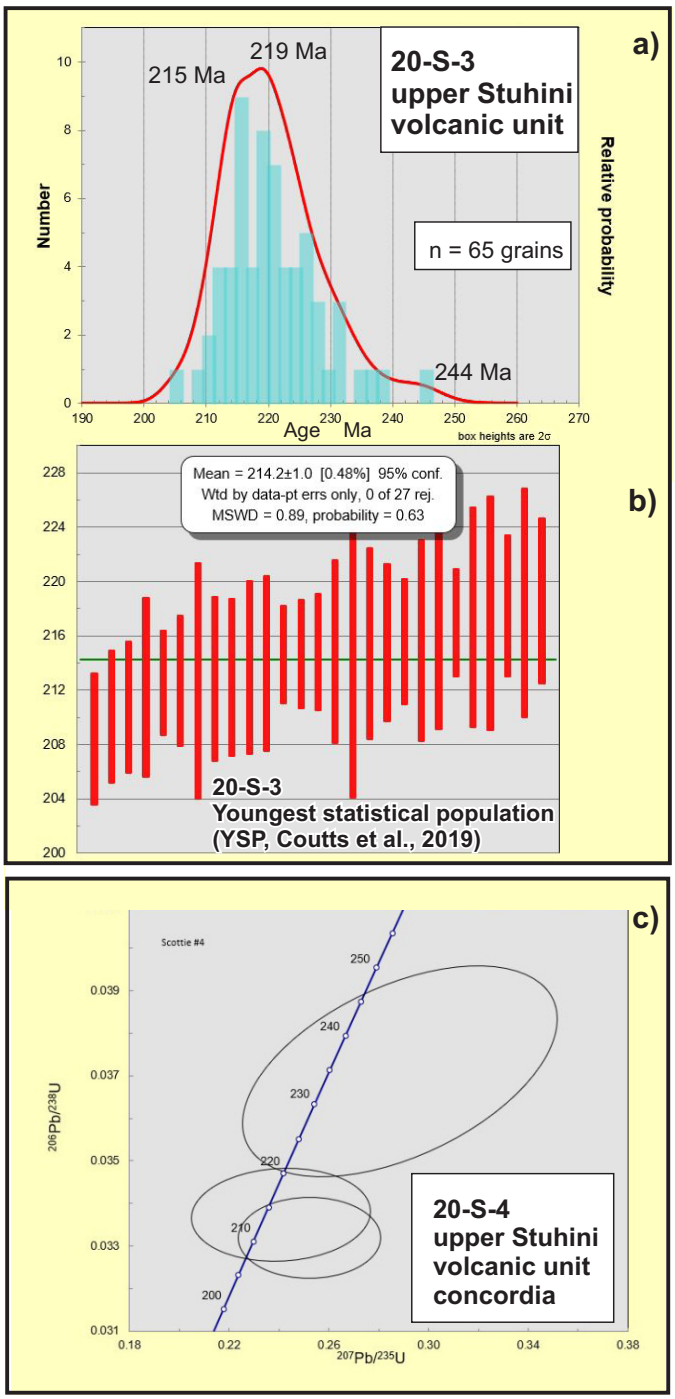

Fig. 11. Detrital zircon data for upper Stuhini Group alkalic volcanic unit. **a)** Probability density plot for 20-S-3. **b)** Weighted average for Youngest Statistical Population of 27 grains in sample 20-S-3. **c)** Concordia plot for 3 grains recovered from 20-S-4.

analyses display a prominent combined population density peak ca. 216-226 Ma, with lesser peaks ca. 190.5, 201, and 243 Ma (Fig. 12b). It also contains three Paleozoic grains with ages of 248.5, 283.1, and 317.5 Ma (Stanley and Nelson, 2021). The Youngest Statistical Population of four grains has a weighted average of 190.6 ±1.7 Ma (Table 2), which we interpret to be the maximum depositional age for this unit. It agrees with

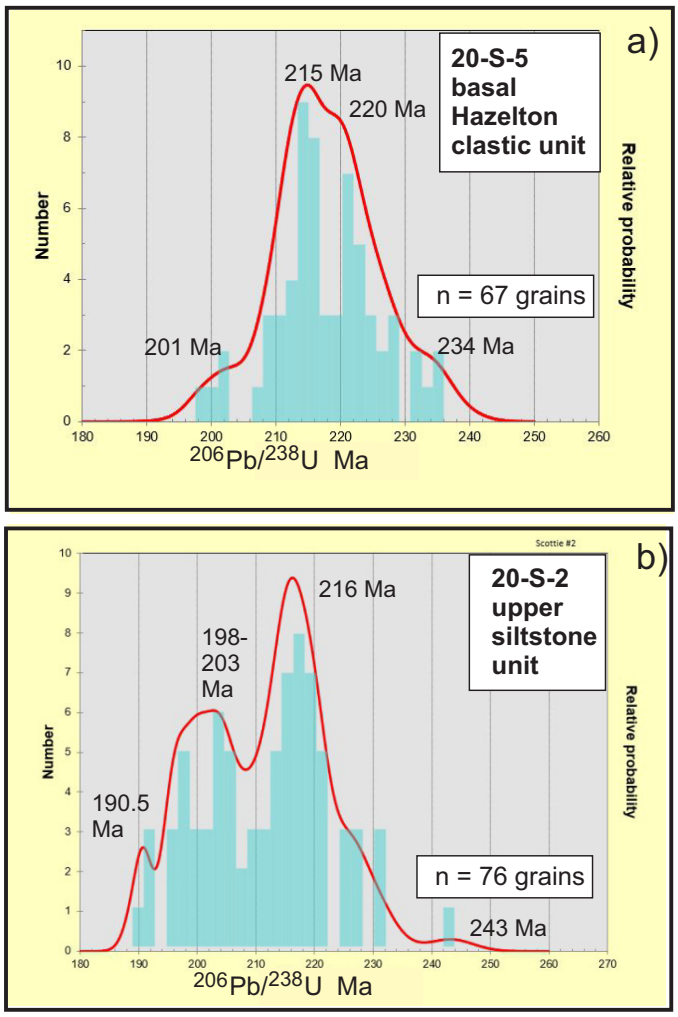

Fig. 12. Zircon age probability plots for lower Hazelton Group. **a)** Probability density plot for siltstone of basal siliciclastic unit. **b)** Probability density plot for upper siltstone unit, Betty Creek Formation.

the Pliensbachian age of enclosed ammonites. The prominent Late Triassic peak provides evidence for continued supply of detritus from Stuhini Group and Stikine suite sources in the Early Jurassic, likely derived from erosion of nearby uplifts.

9. Discussion

9.1. Revised stratigraphy of the Scottie gold mine area and Stewart mining camp

This study has shown that units belonging to the Stuhini Group are present in the Stewart mining camp, underlying previously recognized lower Hazelton Group strata (Alldrick, 1993). It presents a revision of Hazelton Group stratigraphic nomenclature for the Scottie area that aligns with current terminology for strata flanking the McTagg anticlinorium (Lewis, 2013; Nelson et al., 2018).

The lower fine-grained sedimentary-tuff unit of the Stuhini Group resembles argillite-siltstone-sandstone units in the core of the McTagg anticlinorium and near Granduc (Lewis, 2013). The upper volcanic unit gradationally overlies the dark-

coloured sedimentary strata, forming the highest stratigraphic level of the Stuhini Group in the Scottie area. The youngest zircon population from a crystal-lithic tuff near the base of the unit is 214.2 ±1.0 Ma, or Late Norian.

Interbedded siltstone, sandstone and mudstone form the lowest Hazelton Group unit in the area. The basal contact of this unit with the underlying lower sedimentary-tuff unit of the Stuhini Group is covered. Because the upper Stuhini volcanic unit is missing at this locality the contact may be an unconformity. The maximum depositional age of the basal Hazelton unit (ca. 201 Ma) is close to the Triassic-Jurassic boundary (Cohen et al., 2013), similar in age to the Jack Formation (Hettangian-Sinemurian) in the McTagg anticlinorium (Fig. 2). Because the basal unit is much finer grained than the Jack Formation, it may be a distal equivalent. Notably, the unit is at least 10 m.y. younger than the upper volcanic unit of the Stuhini Group, indicating a significant hiatus between Stuhini and Hazelton deposition in the Scottie area.

The main section of the Hazelton Group overlies the upper volcanic unit of the Stuhini Group on the eastern limb of the Summit Mountain anticline. Eastward younging directions are observed in both units. Most of the contact is ice-covered or inaccessible. It is most likely paraconformable, given the >10 m.y. depositional hiatus between youngest Stuhini and oldest Hazelton units. All strata in the main Hazelton sequence are assigned to the Betty Creek Formation. The lower and upper andesite units belong to the lithologically defined Unuk River andesite unit. Lithological equivalents of the intervening siltstone unit do not occur in the McTagg area, where current Betty Creek stratigraphy has been defined (Lewis, 2013, Nelson et al., 2018). We refer to it informally as the "upper siltstone unit", following Alldrick (1993). Future workers in the Stewart camp may choose to assign this lithofacies a topographically based name.

9.2. Regional significance of the upper volcanic unit, Stuhini Group

The upper volcanic unit is unusual because of its age (ca. 214 Ma) which is relatively young for the Stuhini Group (mainly Carnian-Norian faunal ages; associated plutons 229-216 Ma), and because of its strongly alkalic, shoshonitic geochemistry (Fig. 10). In general, Stuhini volcanic rocks are of high-K calc-alkaline to moderately shoshonitic character (Fig. 10b; Logan and Iverson, 2013). Very high, variable potassium contents are only seen in minor latite porphyries in the Dease Lake area (Logan and Iverson, 2013), in alkalic rocks from near the Dirk-Telena prospects in the lower Iskut area (Fig. 10b; Zagorevski et al., 2012), and in volcanic and intrusive rocks near the Galore Cu-Au porphyry deposit (Logan and Koyanagi, 1994). The sample suite from the upper volcanic unit of the Stuhini Group in the Scottie area ranges into these extremely potassic compositions.

The upper volcanic unit is approximately age-equivalent to: 1) the hanging wall breccia at the Granduc volcanogenic deposit (Mihalynuk at al., 2019); and 2) the alkalic volcanic/high-level intrusive complex that hosts the Dirk and Telena showings in the lower Iskut River area (Fig. 1; Mihalynuk et al., 2011, 2012). Together, these rocks offer insights into possible tectonic and magmatic regimes in the Iskut region of Stikinia near the close of Stuhini volcanism. The Dirk-Telena alkalic igneous suite, the Zippa Mountain gabbro-syenite complex and the Newmont graben syenites are the southernmost expressions of the alkalic Galore trend (Fig. 1), which has been interpreted as a structurally controlled, post-subduction magmatic belt (Nelson and van Straaten, 2021). Granduc is adjacent to the north-striking, regional South-Unuk-Harrymel fault (Fig. 1), which forms the western margin of the Eskay rift (Middle Jurassic), and may mark the location of an earlier, syn-Stuhini back-arc or post-arc rift that hosted Granduc. The upper volcanic unit in the Scottie area, 18 km east of Granduc, shows that alkalic magmatism and formation of seabed massive sulphides in localized rift basins may have overlapped in time and space during the transitional period between Stuhini and Hazelton arc development. The modern Bismarck plate provides a possible analogy (Nelson et al., 2022, in press). Collision with the Australian plate in Papua New Guinea caused rotation of the Bismarck plate and development of complex back-arc rift (Manus basin) and fault geometries within it (Brandl et al., 2020). Seabed massive sulphides are currently forming in the Manus basin, while in another part of the back arc region (Tabar-Lihir-Tabar-Feni island chain), structurally controlled shoshonitic volcanism is accompanied by porphyry and epithermal mineralization (Brandl et al., 2020). The unusual and varied metal endowment of the Golden Triangle appears to be the product of an evolving arc-collisional environment that is only beginning to be understood. Observations of the Scottie gold mine area presented herein are a contribution to this ongoing work.

10. Conclusions

This study of the Scottie gold mine area has established a stratigraphic section of the Stuhini and Hazelton groups in the Stewart mining camp, 20 kilometres south of sections previously described on the flanks of the McTagg anticlinorium (Lewis, 2013; Nelson and Kyba, 2014). A mainly sedimentary unit in the Stuhini Group, similar to units seen in the McTagg area, is succeeded gradationally by ca. 214 Ma shoshonitic volcanic breccias, tuffs and flows. The base of the Hazelton Group is interpreted as unconformable and corresponds to a >10 m.y. depositional hiatus. The oldest Hazelton unit is a thin, local siliciclastic outlier that has a ca. 201 Ma maximum depositional age. Separately, a steeply east-dipping section of the Betty Creek Formation comprises two intervals of the Unuk River andesite unit and an intervening siltstone, the "upper siltstone unit" of Alldrick (1993). The upper siltstone unit has a ca. 191 Ma maximum depositional age and contains a Pliensbachian(?) ammonite mold. The stratigraphic section described here enables comparison of the early Mesozoic geological history of the Stewart mining camp with other regions of northwestern Stikinia and aids in tectonic reconstructions.

Acknowledgments

The management, board of directors, and employees of Scottie are thanked for their support over the past three years. This project would not have been possible without the collaboration of Thomas Mumford, Daniel Guestrin, and Jon Rigg of Scottie Resources Corp. LA-ICP-MS detrital zircon analysis was performed by Richard Friedman at the Pacific Centre for Isotopic and Geochronological Research (PCIGR) at the University of British Columbia. Careful reviews by Bram van Straaten and Rebecca Hunter have significantly improved this paper.

References cited

Alldrick, D.J., 1993. Geology and metallogeny of the Stewart mining camp, northwestern British Columbia (104B, 103O). British Columbia Ministry of Energy, Mines and Petroleum Resources, British Columbia Geological Survey Bulletin 85, 105 p.

Anderson, R.G., 1993. A Mesozoic stratigraphic and plutonic framework for northwestern Stikine (Iskut River area), northwestern British Columbia. In: Dunne, G.C. and McDougall, K.A., (Eds.), Mesozoic paleogeography of the western United States, II. Society of Economic Paleontologists and Mineralogists, Pacific Section, 71, pp. 477-494.

Bird, S., Arseneau G., Petrovic, A., Palkovits, F., Fogarty, J., Jensen, S., Masson, B., Marsland, R., Teymouri, S., Grills, F., and Savage, K., 2020. Premier & Red Mountain gold project. Feasibility study NI 43-101 Technical Report. Prepared for Ascot Resources Ltd., 607 p. <https://ascotgold.com/site/assets/files/4831/premier-and-red-mountain-gold-project-ni43-101-final-report-compressed.pdf>

Brandl, P.A., Hannington, M.D., Geerson, J., Peterson, S., and Gennerich, H-H., 2020. The submarine tectono-magmatic framework of Cu-Au endowment in the Tabar-to-Feni island chain, PNG. Ore Geology Reviews, 121, 103491. <https://doi.org/10.1016/j.oregeorev.2020.103491>

Brown, D.A., Gunning, M.H., and Greig, C.J., 1996. The Stikine project: Geology of western Telegraph Creek map area, northwestern British Columbia (NTS 104G/5, 6, 11W, 12 and 13). British Columbia Ministry of Energy, Mines and Petroleum Resources, British Columbia Geological Survey Bulletin 95, 176 p.

Childe, F., 1997. Timing and tectonic setting of volcanogenic massive sulphide deposits in British Columbia: Constraints from U-Pb geochronology, radiogenic isotopes and geochemistry. Unpublished Ph.D. thesis, The University of British Columbia, 319 p.

Cohen, K.M., Finney, S.C., Gibbard, P.L., and Fan, J.-X., 2013. The ICS International Chronostratigraphic Chart. Episodes, 36, 199-204 (updated version 2021/10, <https://stratigraphy.org/ICSchart/ChronostratChart2021-10.pdf>)

Coulson, I.M., Russell, J.K., and Dipple, G.M., 1999. Origins of the Zippa Mountain pluton: A Late Triassic, arc-derived, ultrapotassic magma from the Canadian Cordillera. Canadian Journal of Earth Sciences, 36, 1415-1434. <https://doi:10.1139/e99-045>

Coulson, I.M., Westphal, M., Anderson, R.G., and Kyser, T.K., 2007. Concomitant skarn and syenitic magma evolution at the margins of the Zippa Mountain pluton. Mineralogy and Petrology, 90, 199-221. <https://doi:10.1007/s00710-006-0178-9>

Coutts, D.S., Mathews, W.A., and Hubbard, S.M., 2019. Assessment of widely used methods to derive depositional ages from detrital zircon populations. Geoscience Frontiers 10, 1241-1435. <https://doi.org/10.1016/j.gsf.2018.11.002>

Cutts, J.A., McNicoll, V.J., Zagorevski, A., Anderson, R.G., and Martin, K., 2015. U-Pb geochronology of the Hazelton Group in the McTagg anticlinorium, Iskut River area, northwestern British Columbia. In: Geological Fieldwork 2014, British Columbia Ministry of Energy and Mines, British Columbia Geological Survey Paper 2015-1, pp. 87-102.

Evenchick, C.A., 1991. Structural relationships of the Skeena Fold Belt west of the Bowser Basin, northwest British Columbia. Canadian Journal of Earth Sciences, 28, 973-983.

Febbo, G.E., Kennedy, L.A., Savell, M., Creaser, R.A., and Friedman, R.M., 2015. Geology of the Mitchell Au-Cu-Ag-Mo porphyry deposit, northwestern British Columbia, Canada. In: Geological Fieldwork 2014, British Columbia Ministry of Energy and Mines, British Columbia Geological Survey Paper 2015-1, pp. 59-86.

Febbo, G.E., Kennedy, L.A., Nelson, J.L., Savell, M.J., Campbell, M.E., Creaser, R.A., Friedman, R.M., van Straaten, B.I., and Stein, J.J., 2019. The evolution and structural modification of the supergiant Mitchell Au-Cu porphyry, northwestern British Columbia. Economic Geology, 114, 303-324.

Gagnon, J.F., Barresi, T., Waldron, J.W.F., Nelson, J.L., Poulton, T.P., and Cordey, F., 2012. Stratigraphy of the upper Hazelton Group and Jurassic evolution of the Stikine terrane, British Columbia. Canadian Journal of Earth Sciences, 49, 1027-1052.

Greig, C., 2014. Latest Triassic-earliest Jurassic contractional deformation, uplift and erosion in Stikinia, NW BC. Geological Society of America Abstracts with Programs, 46, p. 588.

Gunning, M.H., Hodder, R.W.H., and Nelson, J.L., 2006. Contrasting volcanic styles within the Paleozoic Stikine assemblage, western Stikine terrane, northwestern British Columbia. In: Colpron, M., and Nelson, J.L., (Eds)., Paleozoic Evolution and Metallogeny of Pericratonic Terranes at the Ancient Pacific Margin of North America, Canadian and Alaskan Cordillera. Geological Association of Canada, Special Paper 45, pp. 201-227.

Henderson, J.R., Kirkham, R.V., Henderson, M.N., Payne, J.G., Wright, T.O., and Wright, R.L., 1992. Stratigraphy and structure of the Sulphurets area, British Columbia, In: Current Research, Part A, Geological Survey of Canada Paper 92-1A, pp. 323-332.

Kyba, J., and Nelson, J., 2015. Stratigraphic and tectonic framework of the Khyber-Sericite-Pins mineralized trend, lower Iskut River, northwest British Columbia. In: Geological Fieldwork 2014, British Columbia Ministry of Energy and Mines, British Columbia Geological Survey Paper 2015-1, pp. 41-58.

Irvine, T.N., and Baragar, W.R.A., 1971. A guide to the chemical classification of the common volcanic rocks. Canadian Journal of Earth Sciences, 8, 523-548.

Le Bas, M.J., Le Maitre, R.W., Streckheisen, A., and Zanettin, B., 1986. A chemical classification of volcanic rocks based on the total alkali-silica diagram. Journal of Petrology, 27, 745-750.

Le Maitre, R.W., Streckeisen, A., Zanettin, B., Le Bas, M.J., Bonin, B., Bateman, P., and Lameyre, J., 2002. Igneous Rocks. A Classification and Glossary of Terms, 2. Cambridge University Press, 236 p.

Lepore, W.A., 2006. Temporal, isotopic, geochemical and structural studies of magmatism and associated mineralization within the Early to Middle Jurassic Hazelton Group on the Tide property, northwestern BC, Canada. Unpublished B.Sc. thesis, The University of British Columbia, 53 p.

Lewis, P.D., MacDonald, A.J., and Bartsch, R.D., 2001. Hazelton Group/Bowser Lake Group stratigraphy in the Iskut River area: Progress and problems. In Metallogenesis of the Iskut River area, northwestern British Columbia, Mineral Research Unit Special Publication, Number 1, Chapter 2, pp. 9-30, The University of British Columbia.

Lewis, P.D., 2013. Iskut River area geology, northwest British Columbia (104B/08, 09, 10 & part of 104B/01, 07, 11). Geoscience BC Report 2013-05.

Logan, J.M., and Iverson, O., 2013. Dease Lake Geoscience Project: Geochemical characteristics of Tsaybahe, Stuhini and Hazelton volcanic rocks, northwestern British Columbia (NTS 104I, J).

In: Geoscience BC Summary of Activities 2012, Geoscience BC Report 20-13-1, pp. 11-32.

Logan, J.M., and Koyanagi, V.M., 1994. Geology and mineral deposits of the Galore Creek area (104G/3, 4). British Columbia Ministry of Energy, Mines and Petroleum Resources, British Columbia Geological Survey Bulletin 92, 95 p.

Logan, J.M., Drobe, J.R., and McClelland, W.C., 2000. Geology of the Forrest Kerr-Mess Creek area, northwestern British Columbia, British Columbia Ministry of Energy and Mines, British ColumbiaGeological Survey Bulletin 104, 164 p.

Ludwig, K., 2008. User's manual for Isoplot 3.70-a geochronological toolkit for Microsoft Excel. Berkeley Geochronology Center Special Publication 4, 76 p.

MacDonald, A.J., 1993. Lithostratigraphy and geochronometry, Brucejack Lake, northwestern British Columbia (104B/08E). In: Geological Fieldwork 1992, British Columbia Ministry of Energy and Mines, British Columbia Geological Survey Paper 1993-1, pp. 315-323.

MacDonald, S., 2021. Ore characterization of a mesothermal gold deposit in northwestern British Columbia. Unpublished B.Sc. Thesis, Kingston, Ontario, Queen's University, 63 p.

McPhie, J., 1993. Volcanic textures: A guide to the interpretation of textures in volcanic rocks. Centre for Ore Deposit and Exploration Studies, University of Tasmania, 198 p.

Mihalynuk, M.G., Logan, J.M., Zagorevski, A., and Joyce, N., 2011. Geology and mineralization of the Hoodoo Mountain area (NTS 104B/14E). In: Geological Fieldwork 2010, British Columbia Ministry of Energy and Mines, British Columbia Geological Survey, Paper 2011-01, pp. 37-64.

Mihalynuk, M.G., Zagorevski, A., and Cordey, F., 2012. Geology of the Hoodoo Mountain area (NTS 104B/14W). In: Geological Fieldwork 2011, British Columbia Ministry of Energy, Mines and Natural Gas, British Columbia Geological Survey, Paper 2012-01, pp. 45-68.

Mihalynuk, M.G., Zagorevski, A., Logan, J.M., Friedman, R.M., and Johnston, S.T., 2019. Age constraints for rocks hosting massive sulphide mineralization at Rock and Roll and Granduc deposits between Iskut and Stewart, British Columbia. In: Geological Fieldwork 2018, British Columbia Ministry of Energy, Mines and Petroleum Resources, British Columbia Geological Survey Paper 2019-01, pp. 97-111.

Miller, E.A., Kennedy, L.A., and van Straaten, B.I., 2020. Geology of the Kinskuch Lake area and Big Bulk porphyry prospect, northwestern British Columbia: Syn-depositional faulting and basin formation during the Rhaetian (latest Triassic) transition from the Stuhini to the Hazelton Group. In: Geological Fieldwork 2019, British Columbia Ministry of Energy, Mines and Petroleum Resources, British Columbia Geological Survey Paper 2020-01, pp. 77-99.

Morrison, G.W., 1980. Characteristics and tectonic setting of the shoshonite rock association. Lithos, 13, 97-108.

Nadaraju, G., 1993. Triassic-Jurassic biochronology of the eastern Iskut River map area, northwestern British Columbia. Unpublished. M.Sc. thesis, The University of British Columbia, 258 p.

Nadaraju, G., and Lewis, P.D., 2001. Biochronology data set, Chapter 8. In: Lewis, P.D., Toma, A., and Tosdal, R.M., (Eds.), Metallogenesis of the Iskut River area, northwestern British Columbia. Mineral Deposit Research Unit, Special Publication Number 1, pp. 9-30.

Nelson, J.L., and Kyba, J., 2014. Structural and stratigraphic control if porphyry and related mineralization in the Treaty Glacier-KSM-Brucejack-Stewart trend of northwestern Stikinia. In: Geological Fieldwork 2013, British Columbia Ministry of Energy, Mines and Natural Gas, British Columbia Geological Survey Paper 2014-1, pp. 111-140.

Nelson, J.L., and van Straaten, B., 2021. Recurrent syn- to post-subduction mineralization along deep crustal corridors in the Iskut-Stewart-Kitsault region of western Stikinia, northwestern British Columbia. In: Sharman, E.R., Lang, J.R., and Chapman, J.B., (Eds.), Porphyry Deposits of the Northwestern Cordillera of North America: A 25-Year Update: Canadian Institute of Mining and Metallurgy Special Volume 57, pp. 194-211.

Nelson, J.L., Colpron, M., and Israel, S., 2013. The Cordillera of British Columbia, Yukon and Alaska: Tectonics and metallogeny. In: Colpron, M., Bissig, T., Rusk, B.G., and Thompson, J.F., (Eds.), Tectonics, Metallogeny and Discovery: The North American Cordillera and Similar Accretionary Settings. Society of Economic Geologists Special Publication 17, Chapter 3, pp. 53-103.

Nelson, J., Waldron, J., van Straaten, B., Zagorevski, A., and Rees, C., 2018. Revised stratigraphy of the Hazelton Group in the Iskut River region, northwestern British Columbia. In: Geological Fieldwork 2017, British Columbia Ministry of Energy, Mines and Petroleum Resources, British Columbia Geological Survey, Paper 2018-1, pp. 15-38.

Nelson, J.L., Friedman, R., and van Straaten, B., 2021. LA-ICP-MS and TIMS U-Pb data files from the Iskut project (Dease Lake to Kitsault): British Columbia Ministry of Energy, Mines and Low Carbon Innovation, British Columbia Geological Survey GeoFile 2021-10, 13 p.

Nelson, J.L., van Straaten, B., and Friedman, R., 2022. Latest Triassic-Early Jurassic Stikine-Yukon-Tanana terrane collision and the onset of accretion in the Canadian Cordillera: insights from Hazelton Group detrital zircon provenance and arc-back-arc configuration. Geosphere, in press.

Pecerrillo, A., and Taylor, S.R., 1976. Geochemistry of Eocene calc-alkaline volcanic rocks from the Kastamonu area, northern Turkey. Contributions to Mineralogy and Petrology, 58, 63-81.

Schaltegger, U., Guex, J., Bartolini, A., Schoene, B., and Ovtcharova, M., 2008. Precise U-Pb age constraints for end-Triassic mass extinction, its correlation to volcanism and Hettangian post-extinction recovery. Earth Planetary Science Letters 267, 266-275.

Stanley, B., and Nelson, J.L., 2022. LA-ICP-MS U-Pb data files, detrital zircon geochronology, and geochemistry of the Stuhini and Hazelton groups, Scottie gold mine area, northwestern British Columbia. British Columbia Ministry of Energy, Mines and Low Carbon Innovation, British Columbia Geological Survey GeoFile.

Tombe, S.P., Richards, J.P., Greig, C.J., Board, W.S., Creaser, R.A., Muehlenbachs, K.A., Larson, P.B., DuFrane, S.A., and Spell, T., 2018. Origin of the high-grade Early Jurassic Brucejack epithermal Au-Ag deposits, Sulphurets Mining Camp, northwestern British Columbia. Ore Geology Reviews, 95, 480-517.

van Straaten, B.I., and Wearmouth, C., 2019. Geology of the Latham and Pallen Creek area, northwestern British Columbia: Distinguishing the Tsaybahe Group, Stuhini Group, and Hazelton Group, and the onset of Triassic arc volcanism in northern Stikinia. In: Geological Fieldwork 2018, British Columbia Ministry of Energy, Mines and Petroleum Resources, British Columbia Geological Survey Paper 2019-01, pp. 79-96.

van Straaten, B.I., McLeish, D.F., and Harding, B.E., 2014. Diamond drilling, geological, geochemical, and geophysical work on the Tennyson property. British Columbia Ministry of Energy and Mines, Assessment Report 34816.

Wotzlaw, J-F., Goex, J., Bartolini, A., Galley, Y., Krystyn, L., McRoberts, C.A., Taylor, D., Schoene, B., and Schalteffer, U., 2014. Towards accurate numerical calibration of the Late Triassic: High-precision U-Pb geochronology constraints on the duration of the Rhaetian. Geology 42, 571-574.

Zagorevski, A., Mihalynuk, M.G., and Logan, J.M., 2012. Geochemical characteristics of Mississippian to Pliensbachian volcanic and hypabyssal rocks in the Hoodoo Mountain area (NTS

104B/14E). In: Geological Fieldwork 2011, British Columbia Ministry of Energy, Mines and Natural Gas, British Columbia Geological Survey, Paper 2012-01, pp. 121-133.

Mapping ultramafic cumulates at the Tulameen ultramafic-mafic Alaskan-type intrusion, south-central British Columbia, aided by remotely piloted aircraft system photogrammetry

Dylan W. Spence[1, a], Henry Crawford[2], James S. Scoates[1], James A. Nott[1], Graham T. Nixon[3], and Dejan Milidragovic[3, 4]

[1] Pacific Centre for Isotopic and Geochemical Research, Department of Earth, Ocean and Atmospheric Sciences, University of British Columbia, Vancouver, BC, V6T 1Z4
[2] Department of Earth, Ocean and Atmospheric Sciences, University of British Columbia, Vancouver, BC, V6T 1Z4
[3] British Columbia Geological Survey, Ministry of Energy, Mines and Low Carbon Innovation, Victoria, BC, V8W 9N3
[4] Geological Survey of Canada, Vancouver, BC, V6B 5J3
[a] corresponding author: dspence@eoas.ubc.ca

Recommended citation: Spence, D.W., Crawford, H., Scoates, J.S., Nott, J.A., Nixon, G.T., and Milidragovic, D., 2022. Mapping ultramafic cumulates at the Tulameen ultramafic-mafic Alaskan-type intrusion, south-central British Columbia, aided by remotely piloted aircraft system photogrammetry. In: Geological Fieldwork 2021, British Columbia Ministry of Energy, Mines and Low Carbon Innovation, British Columbia Geological Survey Paper 2022-01, pp. 103-122.

Abstract

The Tulameen intrusion (Late Triassic), an 18 by 6 km ultramafic-mafic body in the Quesnel terrane of southern British Columbia, is hosted by metavolcanic and metasedimentary rocks of the Nicola Group (Upper Triassic). The intrusion is zoned, with a dunite core passing outwards through olivine clinopyroxenite and clinopyroxenite, to hornblende clinopyroxenite and hornblendite at the margin. It contains widespread gabbroic rocks and a dioritic-syenodioritic phase along the southeastern margin. Detailed mapping along a >4 km transect of near-continuous exposure in the Tulameen River during a period of low water level was assisted by a remotely piloted aircraft system (RPAS). Overlapping, high-resolution digital imagery acquired by the RPAS was used to create 3-dimensional (3D) models, digital elevation models, and orthomosaics using Structure-from-Motion (SfM) photogrammetry. The transect along the Tulameen River includes dunite, chromitite, olivine clinopyroxenite, hornblende clinopyroxenite, gabbro, and minor olivine wehrlite. These rocks are cut by layered gabbro-diorite tabular bodies and fine-grained mafic to intermediate dikes. Contacts between the major map units are predominantly north-trending shear zones. Primary intrusive contacts are rarely exposed, and are typically limited to olivine clinopyroxenite, hornblende clinopyroxenite, and gabbro. Zones of intermingled ultramafic cumulates defined by entrained and variably deformed enclaves of dunite and olivine wehrlite in olivine clinopyroxenite are typical of the section. These zones are interpreted to record magma recharge and remobilization of crystal-rich magma mushes across a range of physical and rheological conditions.

Keywords: Alaskan-type, ultramafic-mafic intrusion, Tulameen intrusion, remotely piloted aircraft system (RPAS), photogrammetry, dunite, olivine clinopyroxenite

1. Introduction

The products of subduction zone magmatism include diverse volcanic and plutonic rocks. Alaskan-type, or Ural-Alaskan-type, ultramafic-mafic intrusions, such as the Tulameen intrusion (Late Triassic) in southern British Columbia (Fig. 1), are volumetrically minor, yet petrologically important, members of subduction zone magmatism (Findlay, 1969; Irvine, 1974; Nixon et al., 1997). These ultramafic-mafic rocks, characterized by a lack of orthopyroxene (Fig. 2), are cumulates that form by segregation and accumulation of crystals in a magma chamber. The Tulameen Alaskan-type intrusion is zoned (Fig. 3), with a dunite core passing outwards through olivine clinopyroxenite to hornblende clinopyroxenite and hornblendite at the margin (Findlay, 1963, 1969). Gabbroic rocks are concentrated in the eastern, central, and south-central parts of the intrusion, and a voluminous dioritic-syenodioritic phase occupies the southeastern margin (Fig. 3). Convergent margin-related ultramafic-mafic intrusions in British Columbia are known for magmatic Ni-Cu-PGE mineralization (Scheel et al., 2009; Nixon et al., 2015; Manor et al., 2016, 2017; Jackson-Brown, 2017; Nixon et al., 2020). The emplacement and crystallization of the Tulameen intrusion, which contains newly discovered magmatic copper sulphide mineralization in the Champion zone (Nixon et al., 2020), coincides with the most prolific time of copper-gold porphyry mineralization in British Columbia (Logan and Mihalynuk, 2014).

Many plutonic rocks in the middle to upper crust are formed through the incremental emplacement and amalgamation of smaller volume magma batches (e.g., Matzel et al., 2006; Schoene et al., 2012; Annen et al., 2015; Mungall et al., 2016;

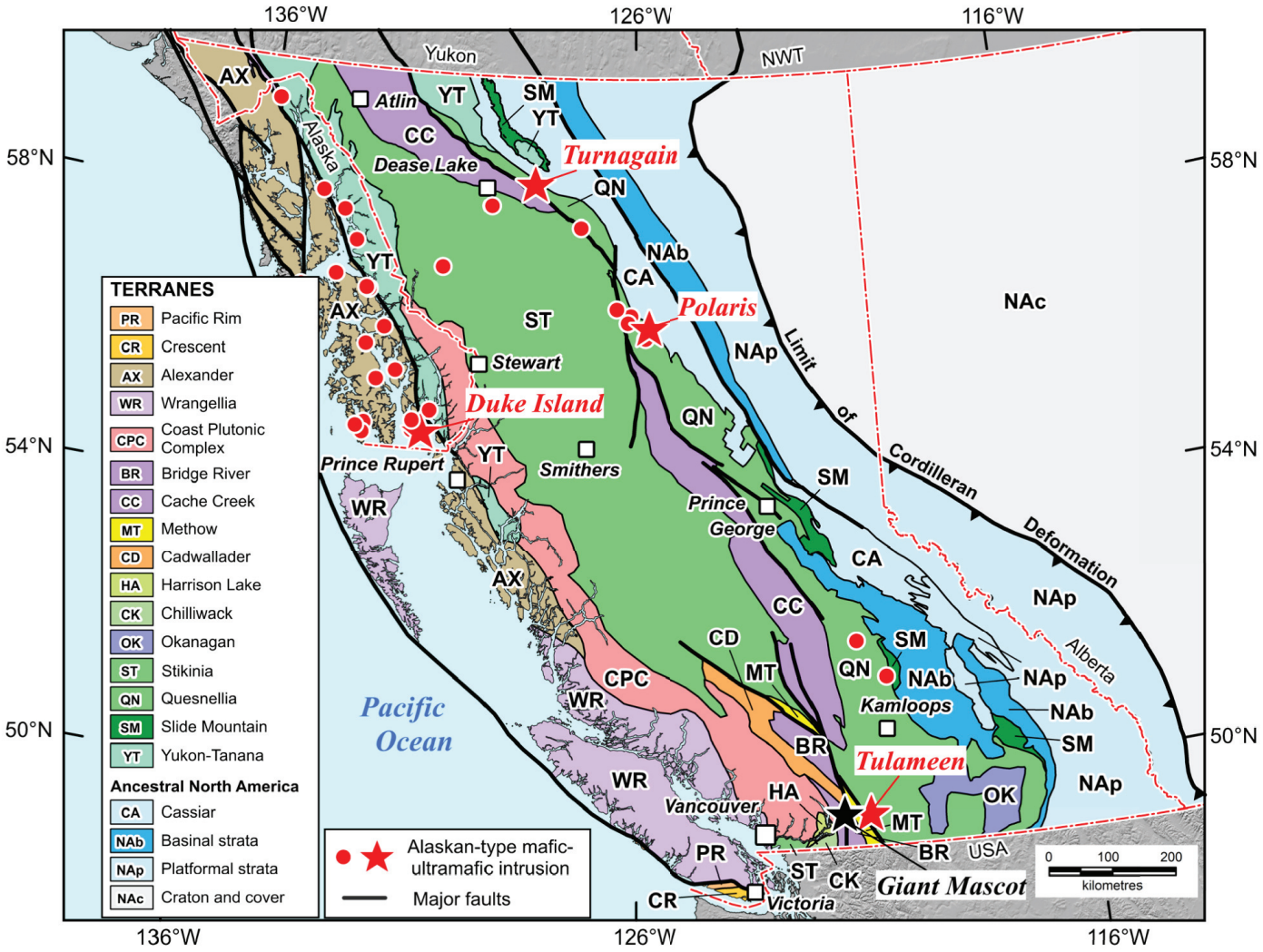

Fig. 1. Terrane map of British Columbia and southeastern Alaska (after Colpron and Nelson, 2011) showing the distribution of Alaskan-type ultramafic-mafic intrusions (after Himmelberg and Loney, 1995; Nixon et al., 1997). The Tulameen, Polaris, Turnagain, and Duke Island Alaskan-type intrusions are highlighted by red-filled stars and all other Alaskan-type intrusions are shown as red-filled circles. The Giant Mascot (Late Cretaceous) orthopyroxene-bearing intrusion and associated Ni-Cu-PGE deposit is shown for reference; black-filled star (Manor et al., 2016, 2017).

Wall et al., 2018; Yao et al., 2021; Scoates et al., 2021). Diverse textural and mineralogical features in individual intrusive bodies, which have been attributed to crystal-rich magma mixing, has garnered attention in felsic plutonic systems (e.g., Paterson, 2009; Weinberg et al., 2021), and mixing of crystal-rich magmas has been explored through numerical simulations in mafic plutonic systems (Bergantz et al., 2015; Schleicher et al., 2016). However, with the notable exception of work by Nixon et al. (2020), who recognized the effects of remobilized ultramafic cumulates in the Tulameen intrusion, and Nott et al. (2020a, 2020b), who gave detailed descriptions providing evidence for local disaggregation and remobilization of semi-consolidated ultramafic cumulates at the Polaris Alaskan-type intrusion, there has been little direct application to mafic intrusions in the rock record.

The Tulameen Alaskan-type intrusion contains a sequence along the Tulameen River of predominantly olivine clinopyroxenite with entrained and deformed blocks of dunite and wehrlite. This chaotic association of cumulates was interpreted as a 'syn-magmatic avalanche deposit' (Nixon et al., 2020). Because of good access and excellent exposure, the Tulameen River is an ideal setting to investigate mixing of crystal-rich mafic magmas. In the summer of 2021, during a period of exceptionally low water levels, we carried out detailed mapping and sampling of ultramafic rocks exposed along the Tulameen River. We augmented traditional field mapping by using a remotely piloted aircraft system (RPAS) with an onboard digital RGB camera. Imagery of the study area was used to process 3D models, digital elevation models, and orthomosaics. In this contribution, we present the preliminary results of this mapping by describing the main rock types exposed along the Tulameen River and their interrelationships. The field site is on the traditional territories of the Nlaka'pamux and Syilx Okanagan nations.

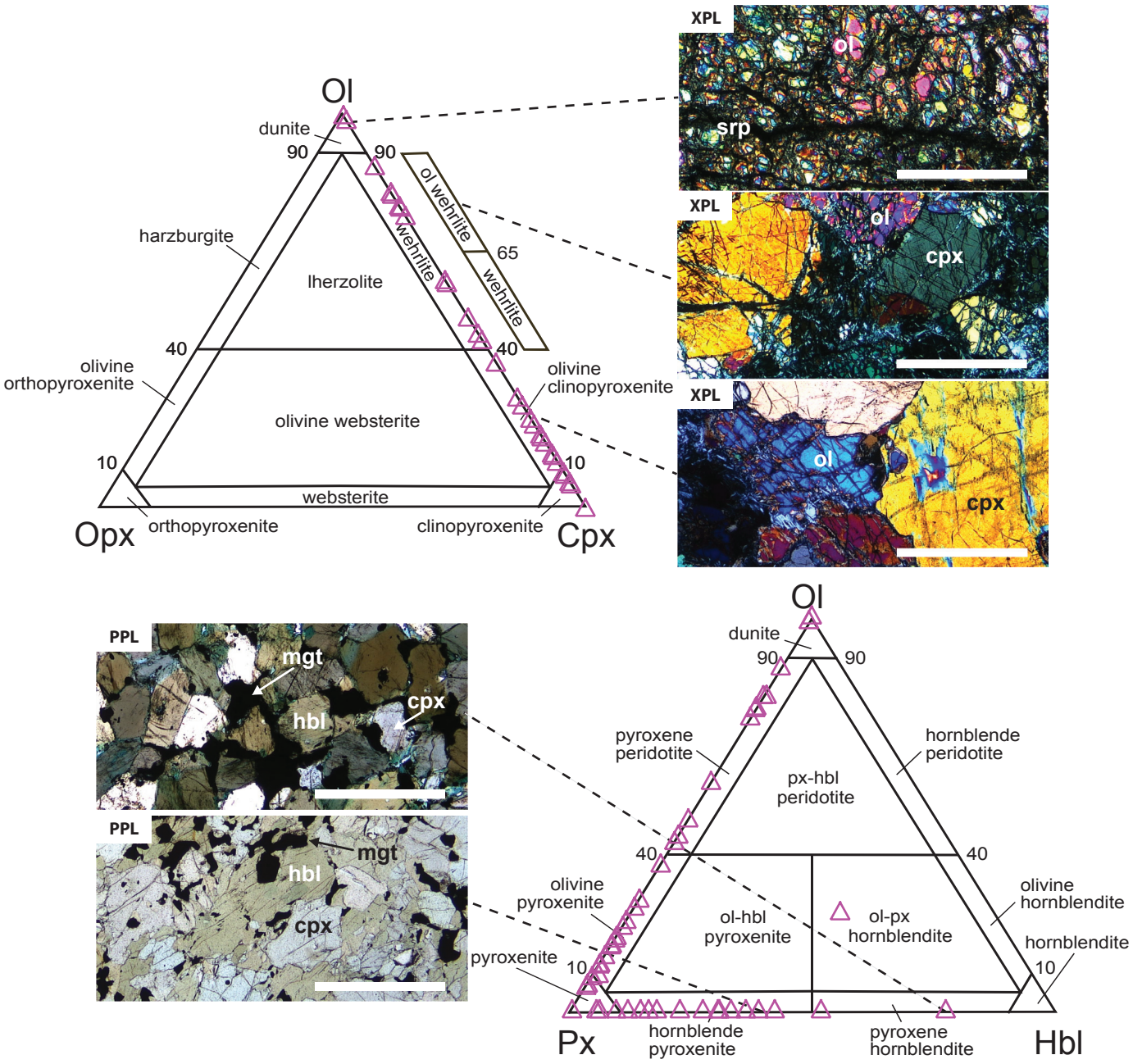

Fig. 2. IUGS ternary classification of ultramafic rocks (Le Maitre, 1989) with unofficial sub-classifications of olivine wehrlite and wehrlite and modal analyses for typical ultramafic rocks in the Tulameen intrusion (Findlay, 1963) illustrating the characteristic lack of orthopyroxene in Alaskan-type intrusions (adapted from Nixon et al., 2015). Representative photomicrographs of selected rock types from the Tulameen intrusion in cross-polarized light (XPL) or plane-polarized light (PPL). Scale bars are 1 mm. Abbreviations: cpx = clinopyroxene; hbl = hornblende; mgt = magnetite; ol = olivine; px = pyroxene; srp = serpentine.

2. Previous work

First mentioned the early 1900s (e.g., Kemp, 1902), the Tulameen intrusion is recognized as the source of platinum for nearby placer deposits. Comprehensive geology and economic mineral reports were provided by Camsell (1913) and Rice (1947). The first detailed accounts of the geology and petrology of the Tulameen intrusion were by Findlay (1963, 1969) followed by St. Louis et al. (1986), Nixon and Rublee (1988), Nixon (1990), and Rublee (1989, 1994). The last decade has seen an increased focus on mapping convergent margin ultramafic intrusions due to their Ni-Cu-PGE mineralization potential (e.g., Manor et al., 2014; Nixon et al., 2017; Nixon, 2018; Nott et al., 2020b). The most recent map of the Tulameen Alaskan-type intrusion by Nixon (2018) modified the original mapping of Findlay (1963) and subsequent mapping by Nixon et al. (1997). Ongoing work on the Tulameen intrusion includes

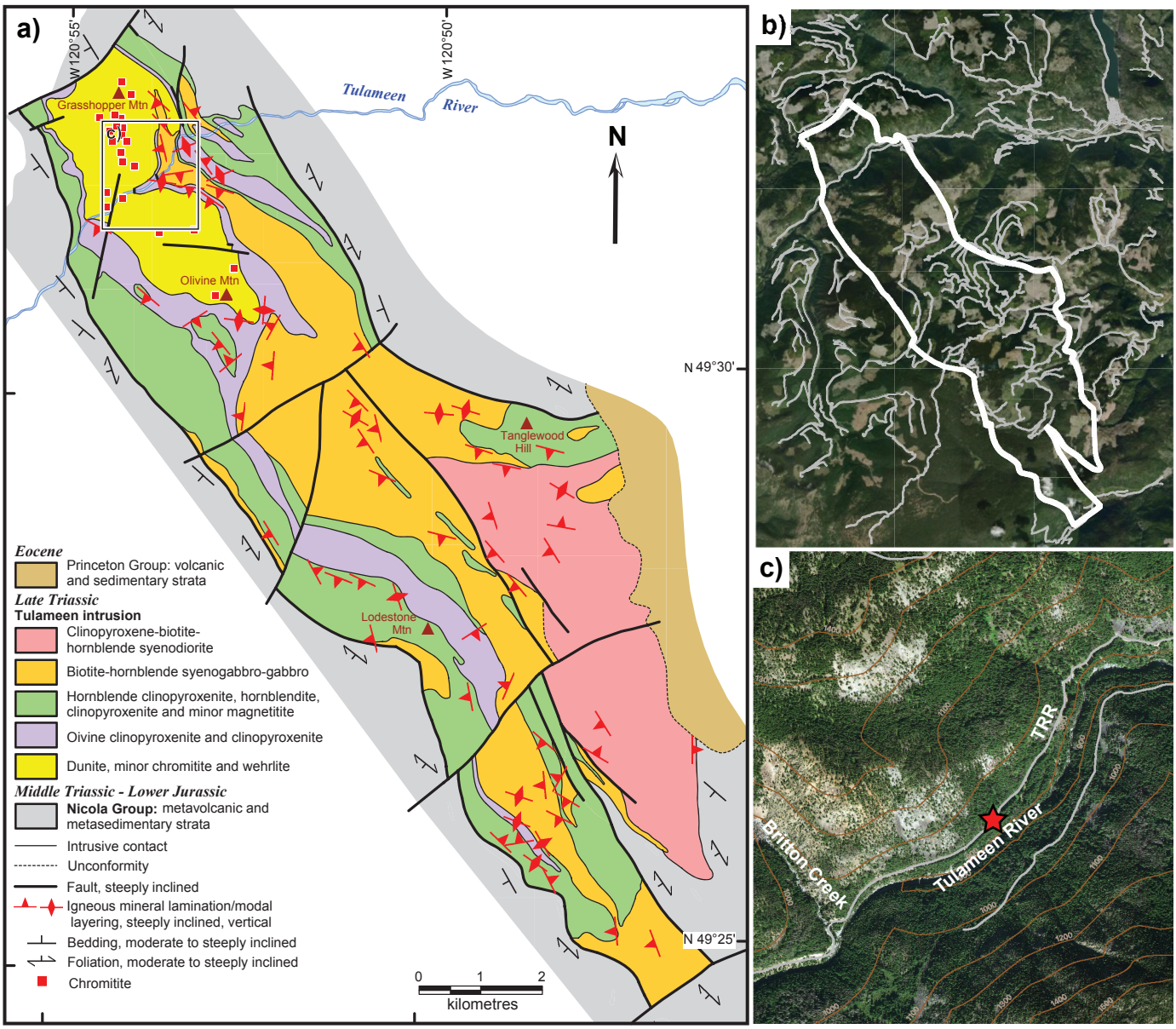

Fig. 3. Tulameen Alaskan-type intrusion. **a)** Generalized geology (Nixon et al., 1997; Nixon, 2018) illustrating lithostratigraphic units, contact relationships, and intrusive rock types. **b)** Tiled ESRI satellite image (October 15, 2018; downloaded November 7, 2021) with the outline of the Tulameen intrusion (white) and forest service roads (grey). **c)** Microsoft Bing satellite image (downloaded November 7, 2021) of the Tulameen River. Red star indicates location of parking pull-out and trail access. The Tulameen River Road (TRR) is in grey.

establishing a geochronological framework through U-Pb zircon geochronology and evaluating the extent and mineralogy of the mineralized Champion zone (e.g., Nixon et al., 2020).

3. Geological setting

The Tulameen Alaskan-type intrusion is in the Intermontane Belt of south-central British Columbia, in the southern part of the Quesnel terrane (Fig. 1). The 60 km^2 intrusion has a dike- or sill-like form (18 km long by 6 km maximum width) that is broadly concordant with the regional structural grain. Bedding attitudes in mafic to felsic metavolcanic and metasedimentary host rocks of the Nicola Group (Upper Triassic) strike northwesterly and dip moderately to steeply to the west (Fig. 3; Nixon, 2018). Contacts with rocks of the Nicola Group are defined by shear zones (Nixon and Rublee, 1988; Rublee, 1989). The Tulameen intrusion and its Nicola Group host rocks are unconformably overlain by terrigenous siliciclastic and volcanic rocks of the Princeton Group (Eocene) to the east (Nixon, 2018). Both the Nicola Group and the Tulameen intrusion are overprinted by post-Triassic deformation and upper greenschist- to lower amphibolite-facies metamorphism. The age of the deformation and metamorphism is considered to be broadly synchronous with the intrusion of the Late Jurassic Eagle granodiorite-tonalite pluton (ca. 157-148 Ma, U-Pb

zircon; Greig et al., 1992), 1 km to the west.

Preliminary U-Pb zircon geochronology indicates emplacement and crystallization of the Tulameen intrusion during a relatively restricted time interval (204-206 Ma) in the Late Triassic (Nixon et al., 2020). This interval coincides with a 6 million-year magmatic flare-up centred on 205 Ma in the Stikine and Quesnel arcs that produced more than 90% of the known copper endowment of these two terranes (Logan and Mihalynuk, 2014). Enhanced magmatic activity at this time has been attributed to stalled subduction and arc-parallel tearing of the subducting slab that led to early (ca. 210 Ma) production of picritic magmas followed by lower degree partial melts parental to the alkalic porphyry Cu-Au deposits (Logan and Mihalynuk, 2014). The age of the Tulameen intrusion suggests a possible petrogenetic relationship between Alaskan-type ultramafic-mafic intrusions, the cumulate products of hydrous, near-primary (e.g., up to Fo_{92} olivine, Nixon et al., 1990; Rublee, 1994; Scheel, 2007; Spence, 2020), mantle-derived arc magmas, and the tectonomagmatic mechanisms that produced the Late Triassic-Early Jurassic porphyry Cu-Au deposits in the Stikine-Quesnel arc systems.

4. Remotely piloted aircraft system photogrammetry methods

4.1. Remotely piloted aircraft systems

A remotely piloted aircraft system (RPAS) assisted with mapping and spatially recording sample sites by acquiring aerial photographs. Commonly referred to as unmanned aerial vehicles (UAV), unmanned aircraft systems (UAS), or informally, drones, RPAS are defined as "a navigable aircraft, other than a balloon, rocket or kite, that is operated by a pilot who is not on board" (Transport Canada, 2021). The utility of RPAS in geological field investigations has been demonstrated in the past decade (e.g., Carrivick et al., 2013; Hansman and Ring, 2019; Elia and Ferbey, 2020). For this study, we used a DJI Mini 2 quadcopter to acquire aerial photographs obliquely and at nadir (Fig. 4). This RPAS is controlled remotely using a mobile device, running the DJI Fly app, that is plugged into a handheld controller. The 12-megapixel camera has a 1/2.3-inch CMOS sensor and a fixed 24 mm focal length lens with fixed aperture (f/2.8); camera orientation is manipulated using a 3-axis motorized gimbal. This RPAS is small and can easily fit into a backpack for field use and, because it is <250 g, registration with Transport Canada is not required, nor does the pilot require a Transport Canada issued RPAS licence. Because the DJI Mini 2 quadcopter does not have autopilot capabilities, the RPAS was flown manually, and photographs were captured with two-thirds overlap between adjacent photos to improve image alignment. Imagery was observed live using the DJI Fly app with a 'rule of thirds' grid, and the shutter was triggered using the handheld controller at optimal overlap.

4.2. Photogrammetric DEMs and orthomosaics

High-resolution RPAS-borne digital imagery can be processed into products that support geological mapping. Structure from motion (SfM) is the photogrammetric imaging method used to generate 3D representations of scenes and objects as digital point clouds from these data. This method simultaneously resolves camera orientation and geometry by matching similar points between images of different perspectives. The 'structure' of a scene is derived from changes in perspective, or 'motion', of the camera (Shervais, 2016). The process identifies matching features, called keypoint descriptors, from overlapping photographs to generate a low-density point cloud, which is then used to establish a high-density point cloud (Carrivick et al., 2013; Shervais, 2016).

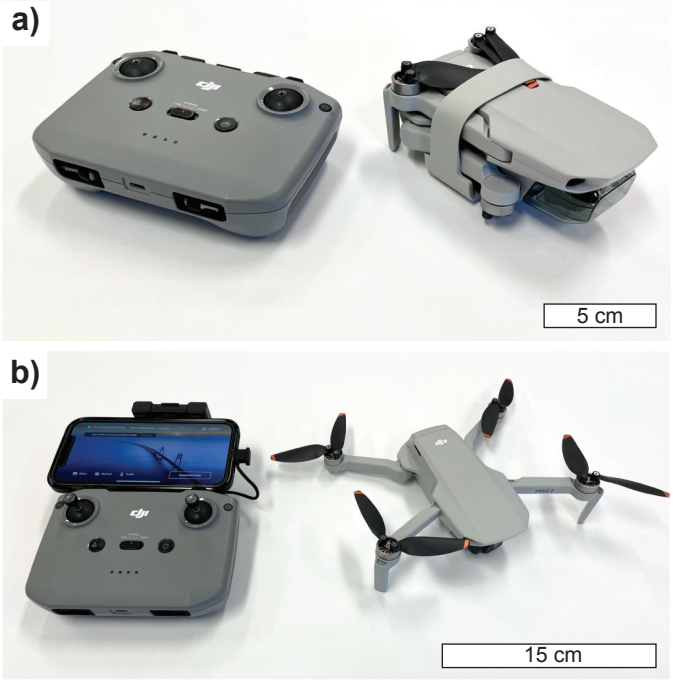

Fig. 4. Remotely piloted aircraft system (RPAS) equipment used in this study. **a)** RPAS controller and aircraft (DJI Mini 2) folded for easy transport. **b)** RPAS controller, monitor (mobile device), and unfolded aircraft ready for flight.

The raw SfM data are fixed in a local-coordinate plane, but when spatial controls are added to the model, these products become proportionally scaled and referenced in geographic space. Ground sampling distance (GSD), or spatial resolution, of output models is scalable because it is a product of sensor height and pixel quality (e.g., Westoby et al., 2012; Balaguer-Puig et al., 2017). This process commonly uses high-precision global positioning system (GPS) tools that use base stations like differential-GNSS, real-time kinematic (RTK) positioning, or precise point positioning to provide stable locations, known as ground control points (GCPs), in the studied area (Hansman and Ring, 2019). The RPA may have onboard RTK capability, which would reduce the need for GCPs (Elia and Ferbey, 2020).

A suite of products can be derived from generated point clouds such as 3D meshes, digital elevation models (DEMs), and orthomosaics. These digital representations, or models, have the potential to be highly accurate estimations of real-

world topography if proper data acquisition and processing steps are taken (Mosbrucker et al., 2017; James et al., 2019). This ability to quantify, manipulate, and archive features in the field, using relatively low-cost equipment, makes SfM an accessible method of 3D reconstruction (e.g., James and Robsin, 2012; Westoby et al., 2012; Eltner et al., 2016; Smith et al., 2016; Mosbrucker et al., 2017; Hansman and Ring, 2019; James et al., 2019; Elia and Ferbey, 2020).

4.3. Data acquisition and processing

Image collection and photogrammetry processing methods for acquiring semi-quantitative data can be split into four main components (Fig. 5): 1) data acquisition; 2) processing to make digital point clouds; 3) orthographic modelling to produce DEMs and orthomosaics; and 4) 3D model generation. To obtain cm-scale GSD, the drone was flown at ca.10 m above ground level (AGL). Photographs were captured at a stationary hover. GCPs were not used in this study because of trade-offs between spatial accuracy, ground resolution, and field-time, and the latter two were prioritized. Obtaining enough photographs for each GCP at low flying elevations requires greater than two-thirds overlap due to the small image footprint, making it a time- and computationally-intensive process. Furthermore, because RPAS in this study was used to record detailed lithological relationships and portray them in 3D rather than for quantitative analysis, the precision of the on-board GPS system was considered sufficient for location and scaling.

Five flights were conducted during this study, which were processed as two model groups. Flights 1, 2, and 3 prioritized a well-exposed section of bedrock mapped as olivine clinopyroxenite (Fig. 6) that was considered a 'syn-magmatic avalanche deposit' by Nixon et al. (2020). Flights 4 and 5 obtained imagery for the mapped contact between olivine clinopyroxenite and dunite (Fig. 6). Images were taken using consistent ISO (100 or 200) and shutter speed (1/800 or 1/1000) for each flight. Image alignment and generation of the dense point cloud were locally processed in the field using Agisoft Metashape software (version 1.7.3) on a laptop with a 2.3 GHz 8-Core Intel processor, 16 GB RAM, and an AMD Radeon Pro 5500M graphics card. Photographs were aligned using their full quality to resolve the most accurate tie points between images, whereas building of the dense point cloud was completed in 'low' quality because this process is computationally intensive (Table 1).

5. Photogrammetric analysis

Flights 1, 2, and 3 have an average image overlap of seven photographs per point and yielded a dense cloud of 1.38 x 10^7 points. A greater photo overlap for a given location typically results in a more resolved spatial model (Fig. 7a; Elia and Ferbey, 2020). The DEM produced from these flights shows relative topography at a detailed resolution of 2.79 cm/pixel (Fig. 7b). In this part of the Tulameen River, the total elevation range is approximately 14 m rising from east to west. The

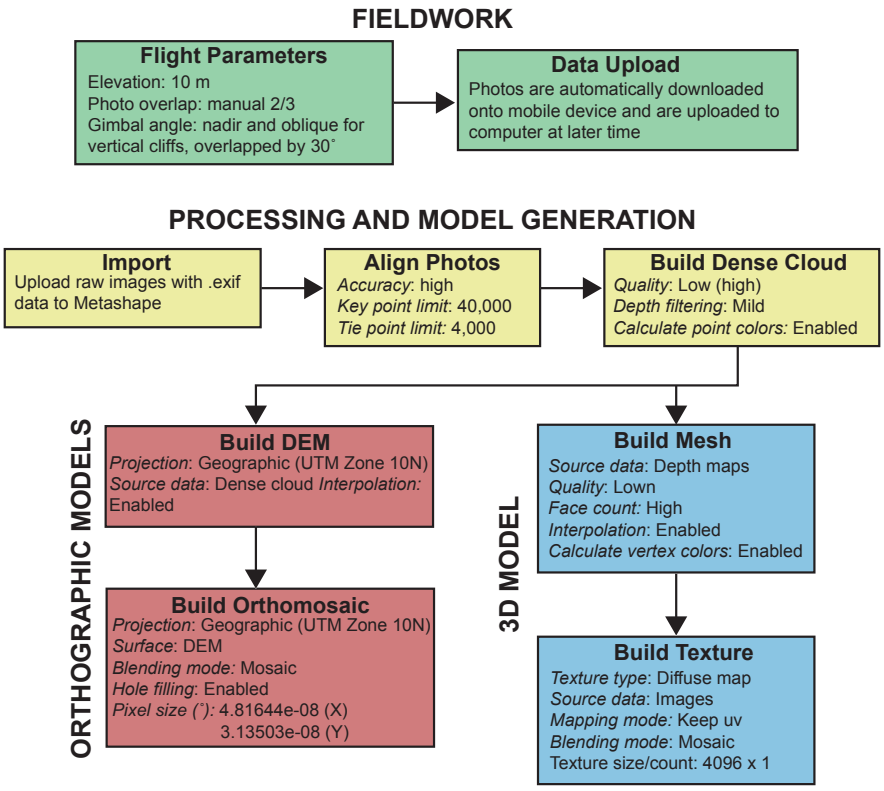

Fig. 5. Flow chart illustrating the methods and parameters used to create photogrammetric data products from RPAS-acquired imagery. Italicized words represent software settings used during data processing and model generation. Data were processed using Agisoft Metashape software (version 1.7.3).

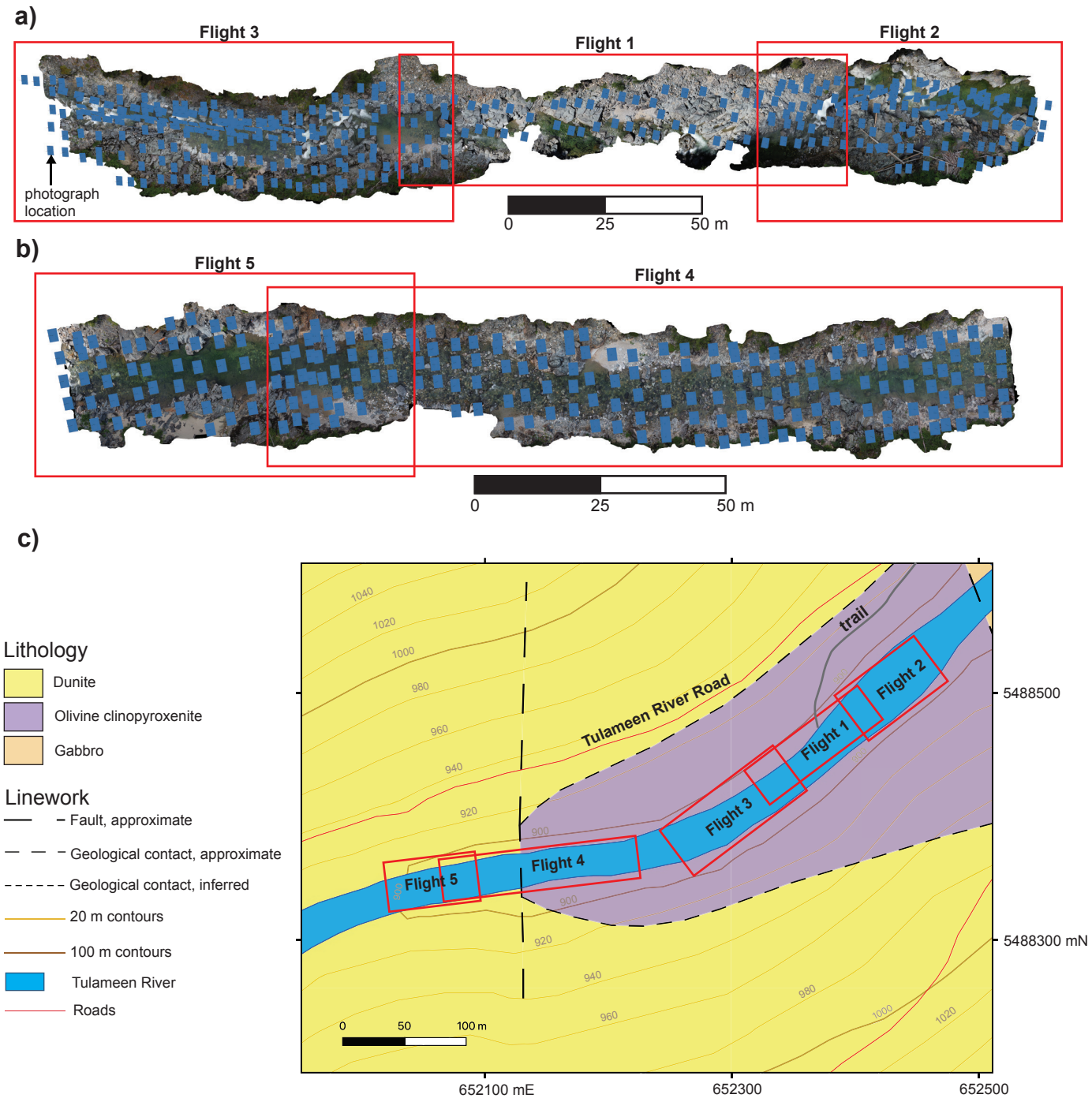

Fig. 6. RPAS survey flight and image locations. **a)** Photograph locations (blue squares) for flights 1, 2, 3. **b)** Photograph locations (blue squares) for flights 4 and 5. **c)** Locations of each flight (outlined by red boxes) on a simplified geological map centred on the Tulameen River (UTM Zone 10N, NAD83). Geology modified from (Nixon, 2018).

Table 1. Data acquisition and processing times for flights 1, 2, and 3, and 4 and 5.

Combined area	Photos	Combined flight time (min)	Sparse point cloud generation (min)	Dense point cloud generation (min)	Model generation (min)	DEM generation (min)	Orthomosaic Generation (min)	Total time (hrs)	File Size (GB)
Flights 1, 2, and 3	430	75	14.35	49.02	12.67	0.35	10.72	2.7	6.17
Flights 4 and 5	223	50	6.95	18.07	9.3	0.17	6.3	1.5	3.55

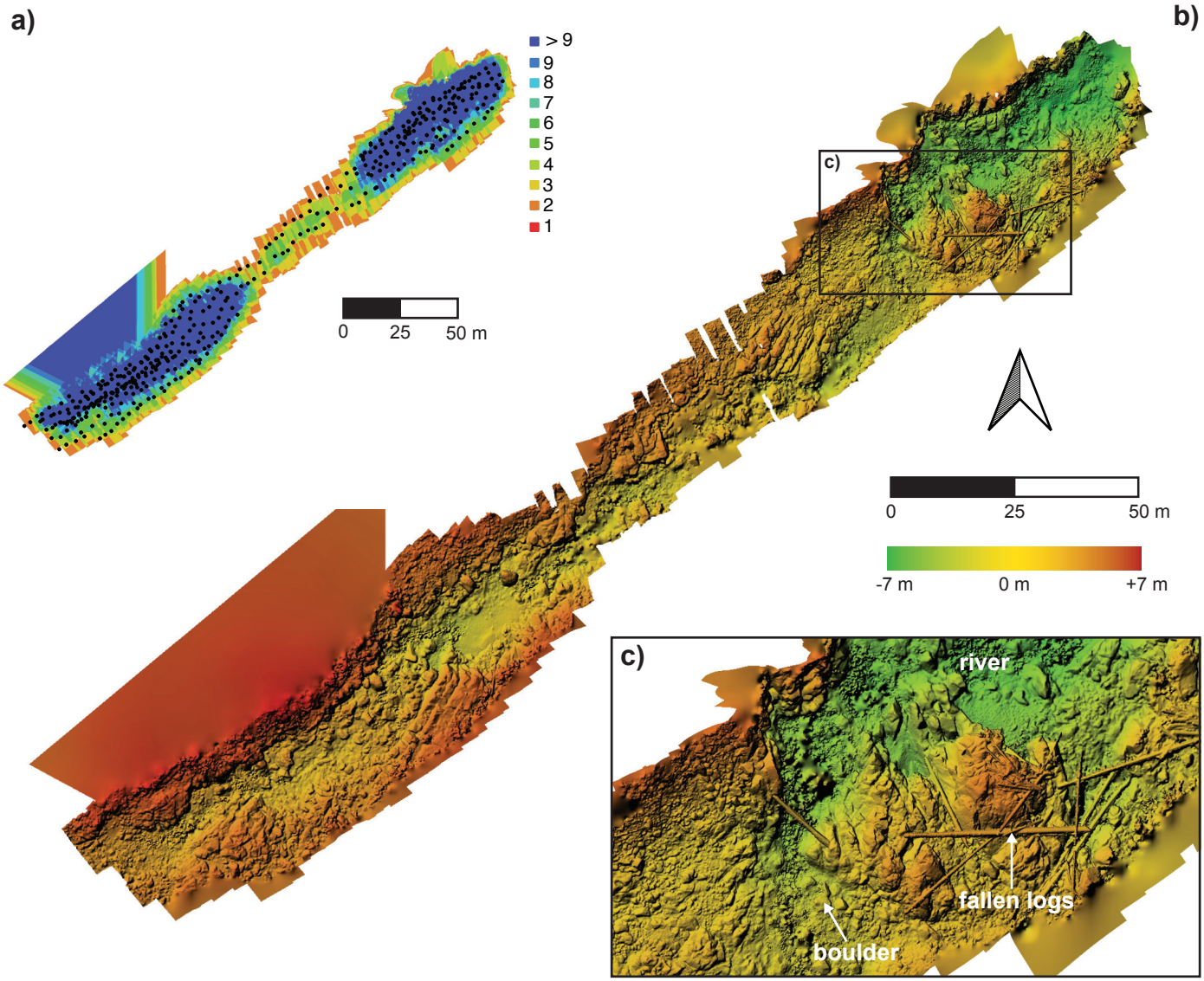

Fig. 7. Photograph density and digital elevation models along the Tulameen River section. **a)** Photograph density model of flights 1, 2, and 3. Black points indicate photograph-centres with each colour representing the number of overlapping photographs used in producing the DEM. **b)** Colourized photogrammetric DEM (resolution: 2.79 cm/pixel) of the river section covered by flights 1, 2, and 3. **c)** Detailed view of DEM showing bedrock topography, individual boulders, and fallen logs.

detail provided by the low-flying survey helps identify features in three-dimensions that would be unresolvable with existing elevation data. Features including individual boulders, fallen logs, and the river extent can be visualized in the DEM (Fig. 7c). Flight 2 traversed a cliff wall above the Tulameen River that is inaccessible by foot. To produce the digital model for this cliff, the RPAS was used to take overlapping photos at increasingly oblique angles to the vertical wall. The camera angle was flown at nadir and then decreased in 30-degree intervals accompanied by an approximately 3 m drop in elevation with each pass along the wall. This method enabled image alignment with the rest of the study area, and a greater level of detail to be recorded along the cliff.

Stitched imagery was overlain on the DEM to produce a georeferenced and coloured orthomosaic (Fig. 8a). The orthomosaic sits in the olivine clinopyroxenite map unit of Nixon (2018) and spatially aligns with the satellite imagery, within a few m. Because of high colour contrast, the orthomosaic captures the detailed heterogeneity of rock types and their interrelationships in this generalized map unit. For example, a dunite body in clinopyroxenite (Fig. 8b), and olivine wehrlite and dunite in olivine clinopyroxenite are cut by layered and brecciated gabbro-diorite (Fig. 8c; see section 6). For the cliff surveyed in flight 2, close-up views of the model illustrate dunite dikes cutting olivine clinopyroxenite, both of which are cut by mafic dikes (Fig. 9).

6. Geology of the Tulameen River section

Low water levels of the Tulameen River in the summer of 2021 allowed us to examine a >4 km-long transect of

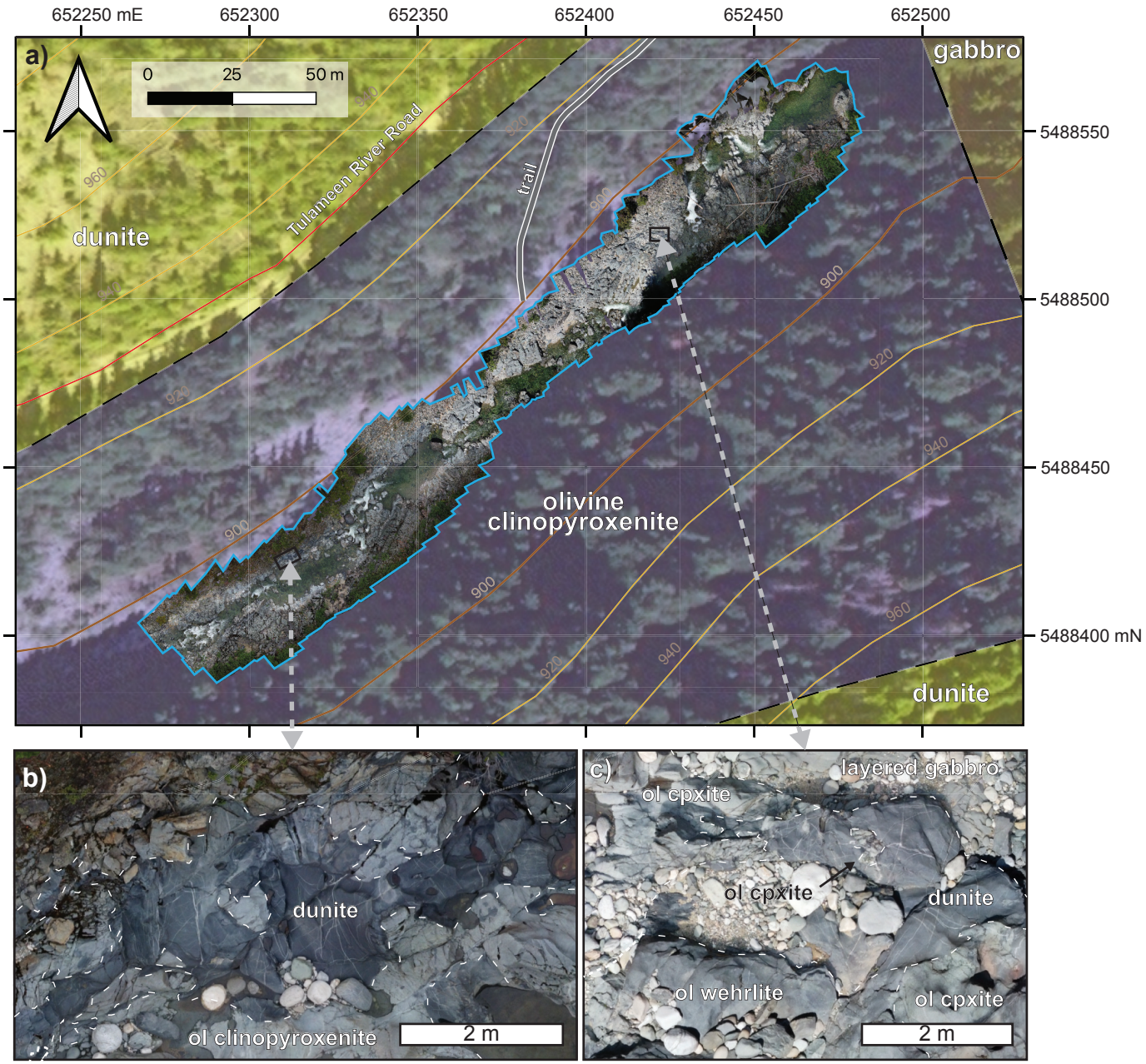

Fig. 8. Orthomosaic of the Tulameen River section covered by flights 1, 2, and 3. **a)** Complete stitched orthomosaic (outlined in blue) of flights 1, 2, and 3 overlain on Microsoft Bing composite satellite imagery (downloaded November 7, 2021) and a simplified geological map (modified from Nixon, 2018); see Fig. 6 for complete legend. **b)** and **c)** show detailed extracts from the orthomosaic. Abbreviations: ol = olivine; cpxite = clinopyroxenite.

continuous outcrop spanning the entire width of the northern portion of the Tulameen intrusion, from its western and eastern contacts with the Nicola Group. Contacts between the intrusion and Nicola Group country rocks are generally shear zones, although enclaves of Nicola Group enclosed by intrusive rocks were described by Nixon et al. (1997). From this transect, a detailed photogrammetric orthophoto (~270 m long) of outcrops along the Tulameen River (flights 1, 2, and 3) was annotated with features defined from both RPAS imagery and mapping on the ground (Fig. 10). The main rock type is clinopyroxenite. Dunite enclaves are present throughout the area but tend to be more concentrated near larger bodies of dunite and wehrlite. Commonly, dunite enclaves are in clusters that are distributed along a westward trend. Some zones have rare dunite enclaves but have higher concentrations of dunite dikes. Layered gabbro-diorite dikes with cores of gabbro-diorite enclaves crosscut olivine clinopyroxenite and dunitic units. Fine-grained mafic to intermediate dikes occur in both the ultramafic rocks and the gabbroic intrusions. Carbonate alteration veins are spatially related to a prominent steeply dipping, north-striking shear zone.

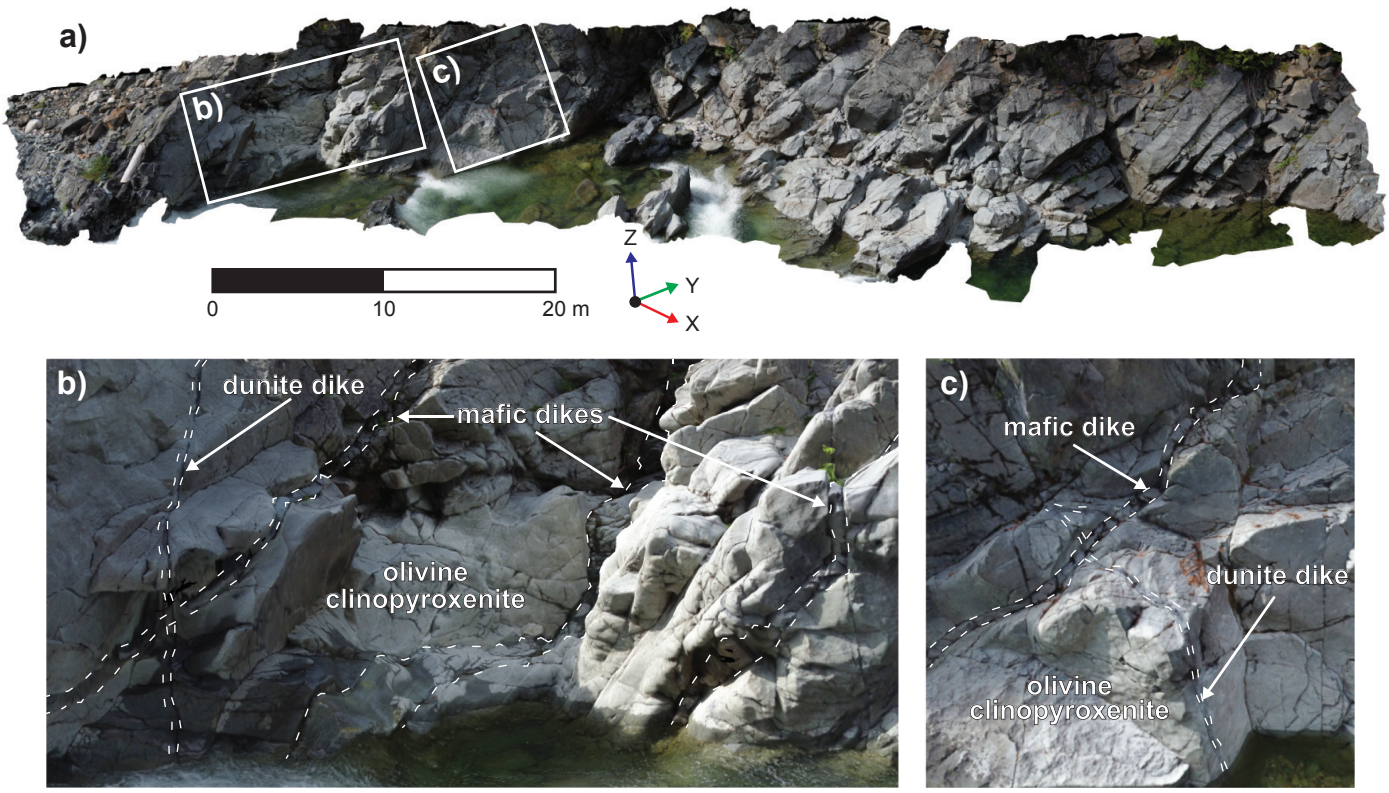

Fig. 9. Oblique 3D photogrammetric model along the Tulameen River created from RPAS-acquired photographs. **a)** Oblique 3D photogrammetric model of a cliff-face (flight 2). **b)** and **c)** are detailed extracts from the 3D model.

6.1. Lithological units

The Tulameen River section exposes many of the rock types in the Tulameen intrusion regionally, including dunite, olivine clinopyroxenite and clinopyroxenite, hornblende clinopyroxenite, gabbro and layered gabbro, and mafic to intermediate dikes (Fig. 11). Narrow (<10 m) north-trending shear zones commonly obscure primary intrusive contacts, and strain partitioning is common, with relatively incompetent rock types being more highly deformed. Primary intrusive relationships are locally preserved (Fig. 12).

6.1.1. Dunite

Regionally, dunite forms the core of the Tulameen intrusion in its northwestern part (Fig. 3). Dunite weathers orange-brown and has smooth to hackly-jointed surfaces caused by serpentinization fabrics. On fresh surfaces, dunite is generally dark grey (Fig. 11a) and, rarely, light green. This colouration is controlled by the degree of alteration. Dunite consists of >90 vol.%, fine-grained (<2 mm across) olivine (Fig. 2) and generally minor (<5 vol.%) interstitial accessory minerals. Although rare, dunite can also contain coarse-grained (>2 mm across) olivine in a matrix of smaller olivine grains. Accessory minerals include interstitial clinopyroxene and fine-grained, subhedral to euhedral chromite. Trace biotite may also be present. The dunite locally contains discontinuous segregations of chromite (Fig. 11a, inset) and massive chromitite layers and schlieren. The size and morphology of chromitite in the dunite core ranges from small mm-scale nodules to m-long layers. Chromitite layers and segregations are deformed and discontinuous, providing evidence for remobilization of cumulates. Chromitites in the Tulameen intrusion may enclose grains of platinum group minerals (Cabri et al., 1973; St. Louis et al., 1986; Nixon et al., 1997) such as Pt-Fe alloys, tulameenite (Pt_2CuFe), and sperrylite ($PtAs_2$).

Dunite forms a discrete unit and also forms cm- to m-scale enclaves and discrete bodies in olivine clinopyroxenite (Figs. 8b, 13, 14). The olivine clinopyroxenite unit east of the dunite core (Fig. 10) preserves dunite enclaves of different sizes and shapes (Fig. 13). The enclaves commonly have sharp and cuspate-lobate contacts with their olivine clinopyroxenite host and are typically amoeboid in shape. Where isolated, enclaves may be rounded (Fig. 13b), but they commonly terminate with sharp tips (Fig. 13d). The dunite is homogeneous, except for coarse to pegmatitic clinopyroxene and segregations containing clots (>5 mm diameter) of clinopyroxene (Figs. 14a-c). Clusters of small dunite enclaves are also near larger, 10-20 m-wide bodies of dunite and wehrlite. These clusters commonly form elongate zones that have an approximate easterly trend (Fig. 13a) and may have an interconnected system of dunite stringers (Fig. 13c). Dunite and olivine wehrlite locally have diffuse contacts with wehrlite, which, in turn, has diffuse contacts with olivine clinopyroxenite (Figs. 8c, 13d). The shapes of enclaves and diffuse contacts suggest mechanical disaggregation of poorly consolidated and ductile cumulates before final crystallization.

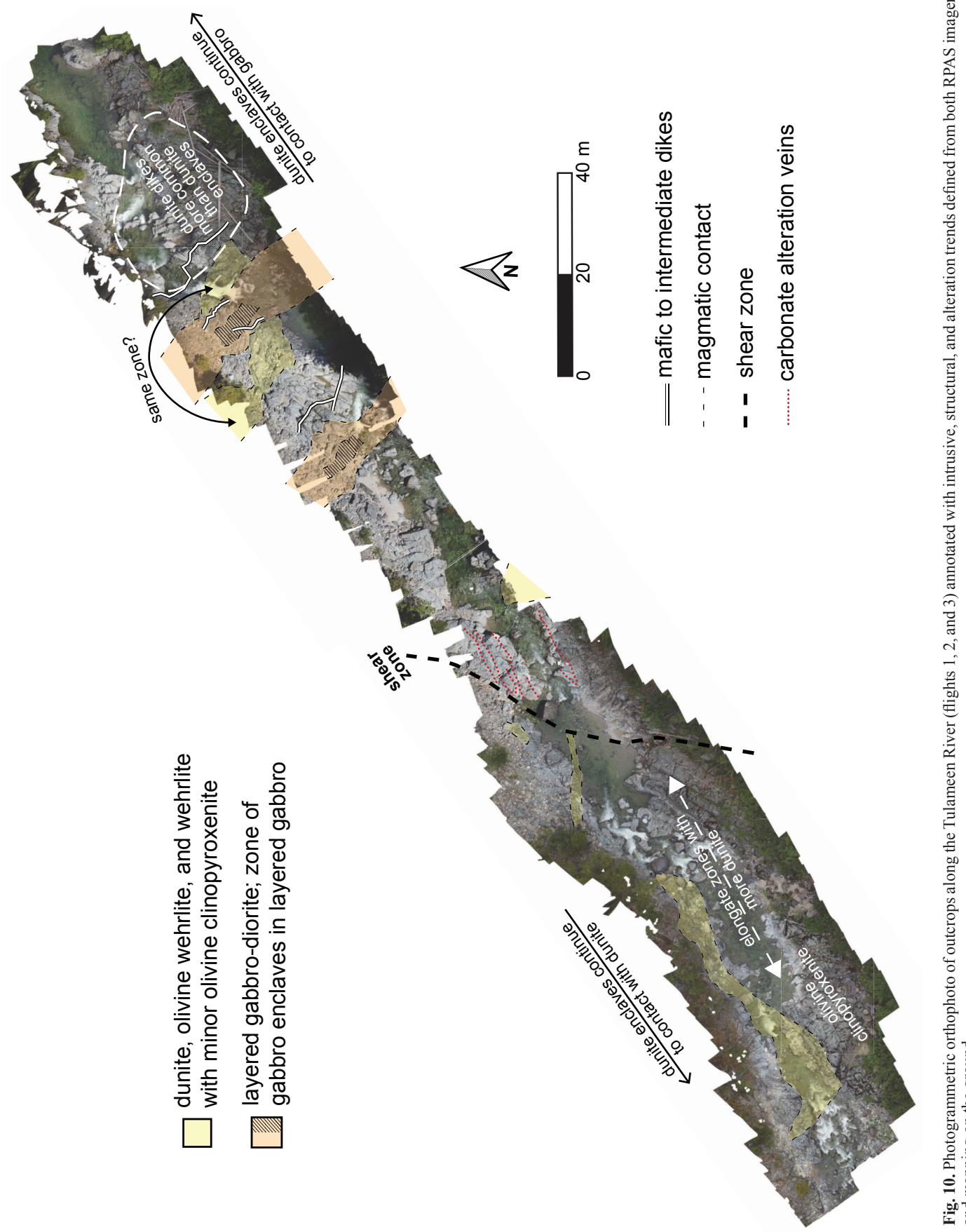

Fig. 10. Photogrammetric orthophoto of outcrops along the Tulameen River (flights 1, 2, and 3) annotated with intrusive, structural, and alteration trends defined from both RPAS imagery and mapping on the ground.

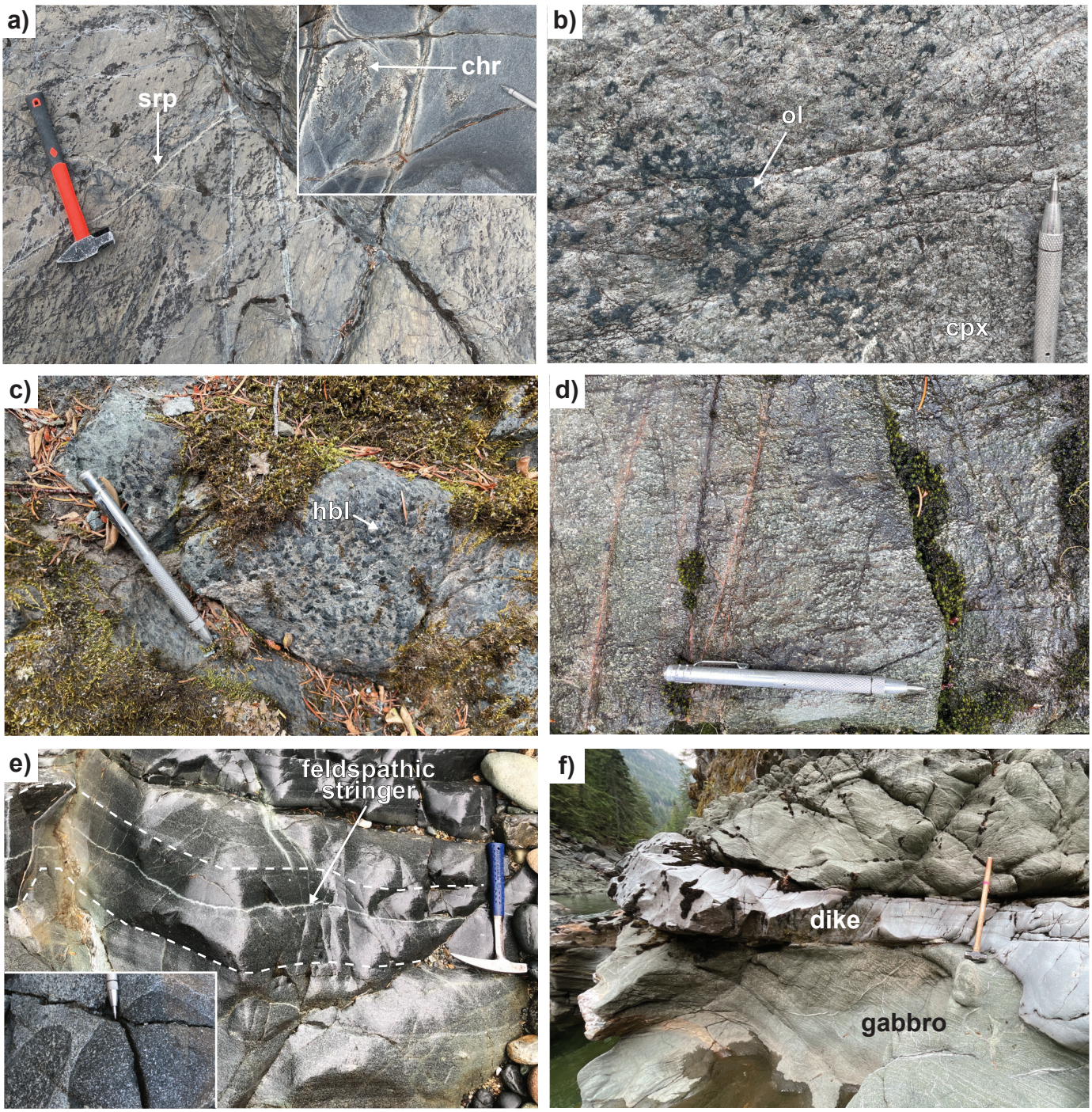

Fig. 11. Representative intrusive rock types in the Tulameen River transect. **a)** Dun-brown dunite with serpentine veins and chromite schlieren (inset). **b)** Close-up of olivine clinopyroxenite showing heterogeneously distributed dark olivine grains in a matrix of grey clinopyroxene. **c)** Hornblende clinopyroxenite with spotty, black hornblende crystals in a grey-green matrix of clinopyroxene. **d)** Gabbro with typical grey-and-white speckled appearance; the green tint is due to saussuritization of plagioclase. **e)** Layering in ca. 10 m-wide tabular gabbro bodies. Inset illustrates rounded gabbroic enclaves in the central portions of these tabular bodies. **f)** Fine-grained mafic to intermediate dike, cutting gabbro. Abbreviations: srp = serpentine; chr = chromite; ol = olivine; cpx = clinopyroxene; hbl = hornblende.

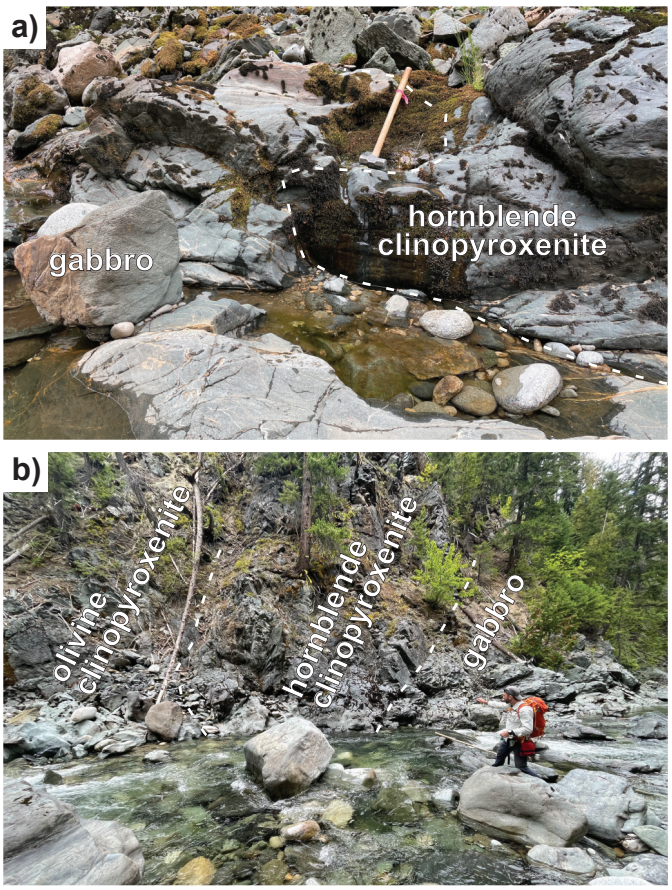

Fig. 12. Representative examples of intrusive contacts in the Tulameen intrusion. **a)** Sharp intrusive contact of gabbro cutting hornblende clinopyroxenite. **b)** Intrusive contacts between gabbro, hornblende clinopyroxenite, and olivine clinopyroxenite.

Dunite dikes are common in zones of intermingled cumulates in olivine clinopyroxenite (Figs. 9b, c, 15). The dikes are <10 cm wide, have sharp contacts, and display pinch and swell, pinch-out, bend, and bifurcation geometries rather than simple tabular bodies. Dunite dikes commonly crosscut deformed and disaggregated dunite and wehrlite enclaves (Figs. 15b-c). Small dike-like dunite projections extend from some dunite enclaves (Fig. 15d).

6.1.2. Olivine clinopyroxenite and clinopyroxenite

Regionally, olivine clinopyroxenite (Fig. 11b) and clinopyroxenite are on the margins of the dunite core and form discrete northwest-trending bodies (Fig. 3). Olivine clinopyroxenite and clinopyroxenite weather light grey-green and, where polished by the Tulameen River, have a mottled black appearance due to serpentinized olivine. Olivine clinopyroxenite contains 10-40 vol.% olivine and 60-90 vol.% clinopyroxene, whereas clinopyroxenite has >90 vol.% clinopyroxene and <10 vol.% olivine (Fig. 2). Clinopyroxene grains are typically 2-5 mm in diameter, but locally may be as large as 8 cm. Clinopyroxenite locally contains discontinuous layers of magnetite and may include trace biotite. Defining units of olivine clinopyroxenite by modal abundance is challenging in the Tulameen intrusion because olivine is commonly present in clumps or segregations (Fig. 11b) rather than dispersed homogeneously throughout the rock.

Clinopyroxenite rarely forms distinct units within the dunite core, occurring as discontinuous segregations of homogeneous clinopyroxenite up to 1 m-wide (Fig. 16a) and as thin (<10 cm) dikes (Figs. 16b, c). Clinopyroxenite dikes are continuous over 100s of m; they are undulatory and may pinch-out (Fig. 16b) or be broken into discrete segments (Fig. 16c). These characteristics are inferred to indicate that interstitial liquids from an olivine-rich cumulate were expelled to form semi-tabular bodies. The break-up of tabular clinopyroxenite dikes fails to preserve crosscutting relationships within the dunite, suggesting that the clinopyroxenite formed in a hot, variably mobile body of dunite that experienced post-intrusion deformation before final solidification.

Rarely, clinopyroxenite and magnetitite define igneous layering in the olivine clinopyroxenite unit (Fig. 17a). Centimetre- to dm-scale tabular units of dunite, wehrlite, and olivine clinopyroxenite with diffuse boundaries also define igneous layering (Fig. 17b). Locally, zones of magnetite-bearing olivine clinopyroxenite form lenses in clinopyroxenite. These lenses contain an internal fabric defined by alignment of olivine-rich zones in a matrix of apparently undeformed clinopyroxene crystals (Fig. 18), features that are consistent with syn-magmatic strain.

6.1.3. Hornblende clinopyroxenite

Regionally, hornblende clinopyroxenite (Fig. 11c) is mainly on the margins of the Tulameen intrusion, extending along its length (Fig. 3). It is volumetrically minor in the Tulameen River section relative to dunite, olivine clinopyroxenite, and gabbro. Black crystals of hornblende in grey-green weathering clinopyroxenite give the hornblende clinopyroxenite a distinctive spotted appearance. Although the hornblende grain size averages 2-10 mm, it is locally pegmatitic. Where grain size is large, coarse biotite is common. Rarely, hornblende clinopyroxenite contains segregations with an increased modal abundance of interstitial plagioclase, locally grading into gabbro.

The contacts between hornblende clinopyroxenite and crosscutting gabbro may be sharp (Fig. 12a), gradational (Fig. 12b), or brecciated with fragments of hornblende clinopyroxenite in a gabbro matrix and hornblende clinopyroxenite containing stringers of gabbro.

6.1.4. Gabbro and layered gabbro

Gabbro to syenogabbro extends along the eastern portion of the Tulameen intrusion, thinning toward the northwest (Fig. 3). In the Tulameen River section, gabbro is green-grey and white speckled due to plagioclase feldspar (Fig. 11d); the proportion of mafic minerals relative to plagioclase varies and is locally foliated. The main constituents (plagioclase, clinopyroxene, hornblende) have a limited grain size variation (2-4 mm

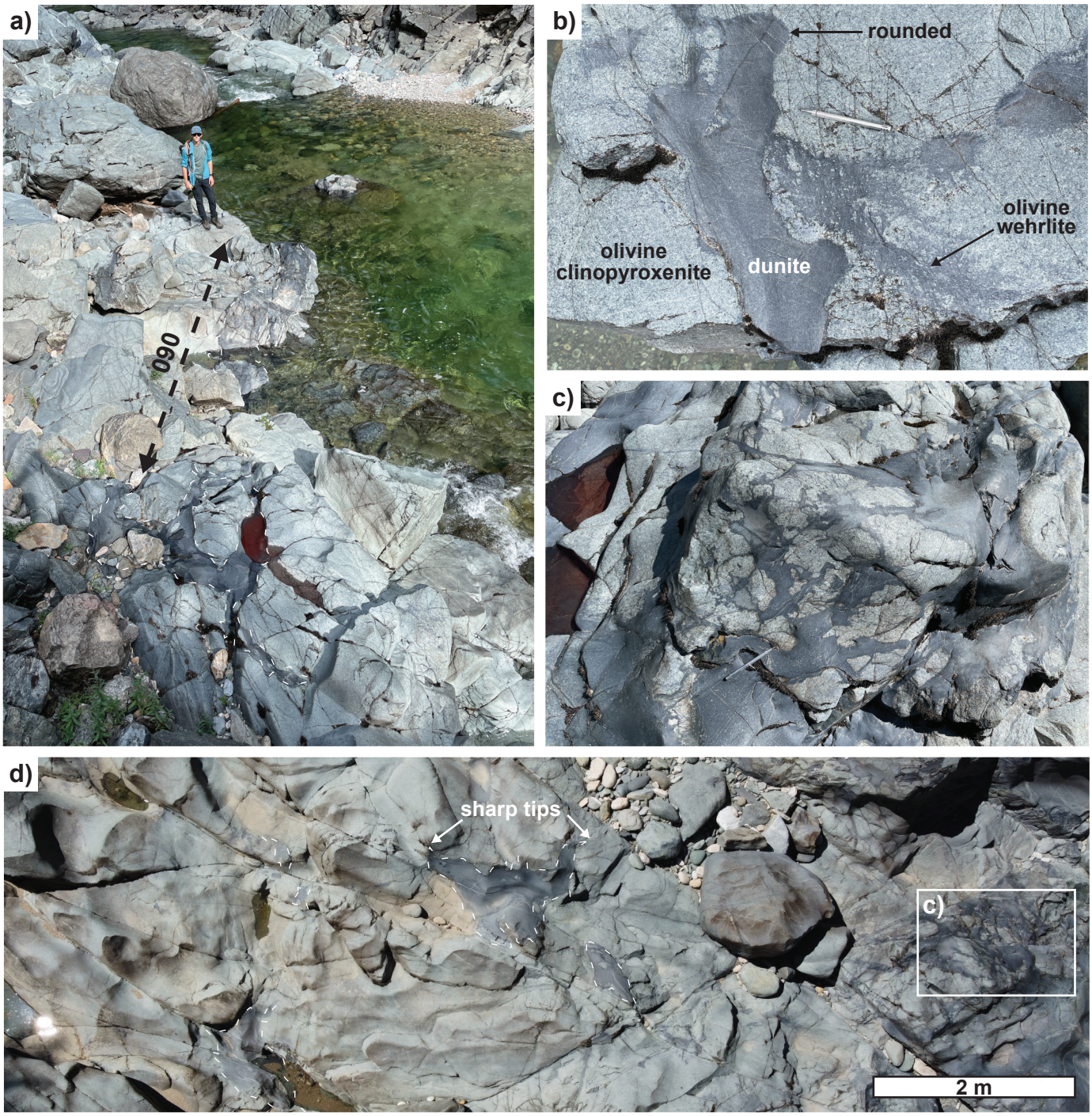

Fig. 13. Representative examples of dunite enclaves and clusters (dark rock) in olivine clinopyroxenite (light rock). **a)** Stringy, elongate dunite enclaves, many of which trend east. **b)** Ameboid blob of dunite in olivine clinopyroxenite, disaggregated dunite, and olivine wehrlite. **c)** Dunite (dark) forming an interconnected network in olivine clinopyroxenite with minimal crystal-scale disaggregation. See box in d) for location. **d)** Photograph from RPAS illustrating isolated dark dunite enclaves in olivine clinopyroxenite. Dunite enclaves commonly have sharp, undulatory contacts with olivine clinopyroxenite and sharp tips.

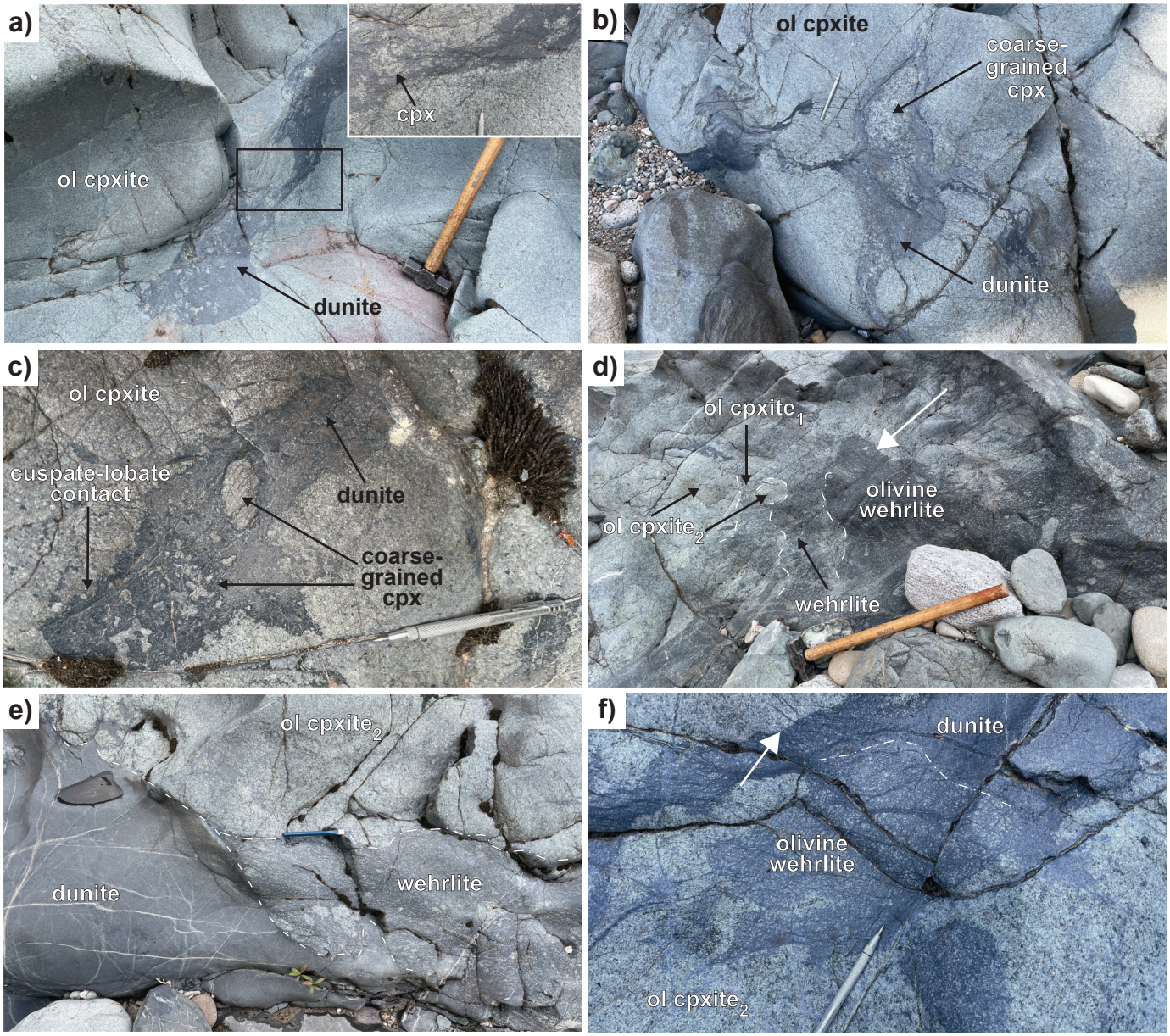

Fig. 14. Dunite enclaves with diverse morphological and textural relationships. a-c) Morphologies of dunite enclaves with coarse-grained to pegmatitic clinopyroxenite. **a)** Dunite enclave with ca. 4 cm-wide clinopyroxene crystals (inset) in medium-grained olivine clinopyroxenite. **b)** Dunite enclave with coarse segregation of olivine clinopyroxenite. **c)** Dunite enclave with cuspate-lobate, locally flame-like contact against olivine clinopyroxenite; elliptical and ameboid bodies of coarse-grained clinopyroxene inside the dunite enclave. d-f) Examples of diffuse contacts (dot-dash white lines) between olivine wehrlite or dunite and olivine clinopyroxenite. **d)** Gradational contact between olivine wehrlite and olivine clinopyroxenite, between wehrlite and olivine clinopyroxenite with >20 vol.% olivine ("ol cpxite$_1$"), and between olivine clinopyroxenite with >20 vol.% olivine and olivine clinopyroxenite with <20 vol.% olivine ("ol cpxite$_2$"). Olivine wehrlite also shows a sharp contact (dashed white line) with a rounded enclave of ol cpxite$_2$ and diffuse contact with ol cpxite$_2$ (white arrow). **e)** Diffuse contact between wehrlite and olivine clinopyroxenite, and sharp contact with (cross-cutting?) dunite. **f)** Dunite enclave with a diffuse contact against olivine wehrlite; olivine wehrlite with a diffuse contact against olivine clinopyroxenite. The top of the dunite enclave has a sharp contact with olivine clinopyroxenite (white arrow). Abbreviations: cpx = clinopyroxene; cpxite = clinopyroxenite; ol = olivine.

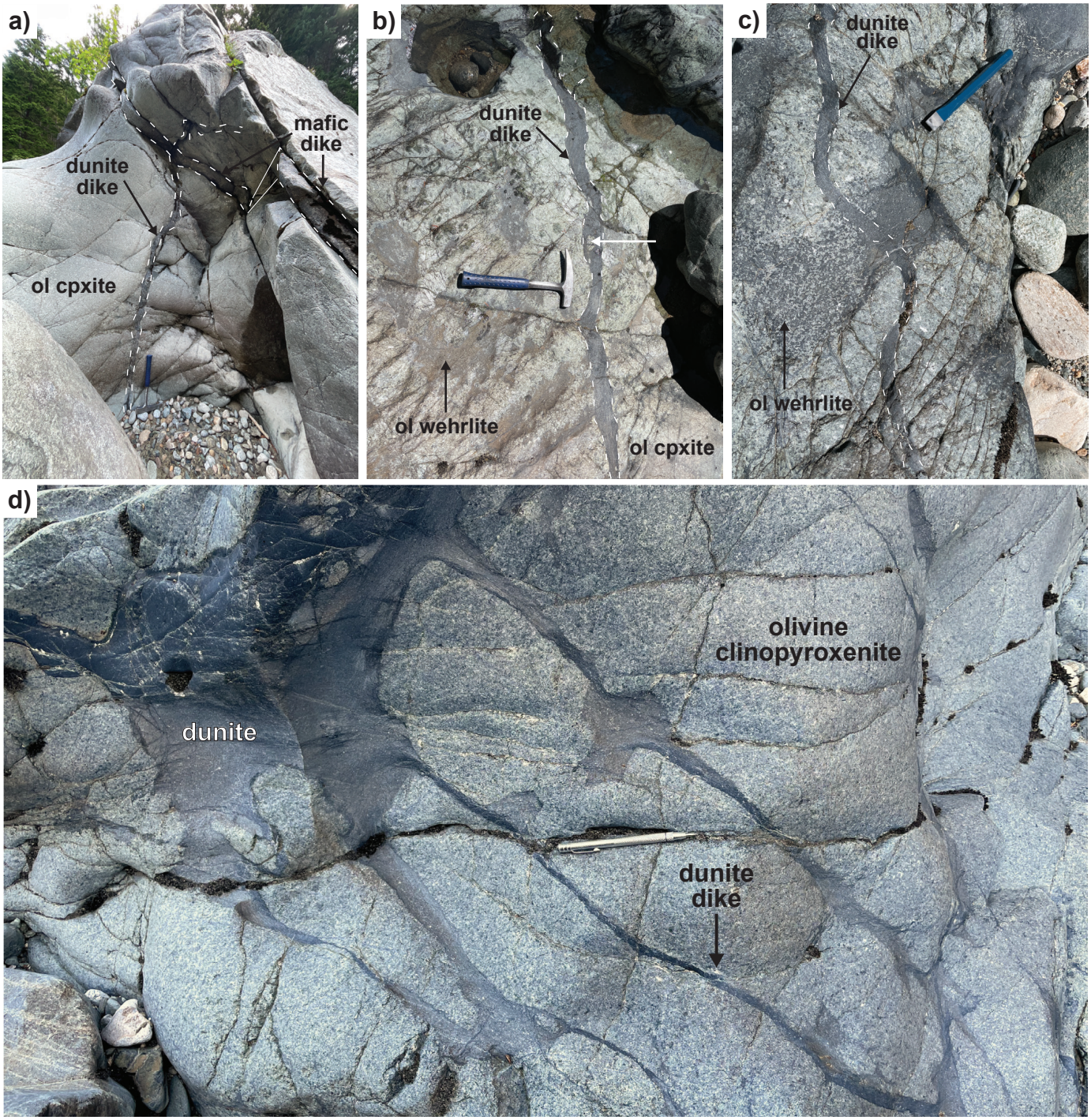

Fig. 15. Dunite dikes in olivine clinopyroxenite. **a)** Discontinuous and undulatory ca. 5 cm-wide dunite dike; the dike is subvertical and trends east-west. The dunite dike is crosscut by a ca. 10 cm-wide mafic dike that has either been offset or pinches out. **b)** A 5-7 cm-wide, undulatory dunite dike with small enclaves of olivine clinopyroxenite (white arrow). This dike crosscuts olivine clinopyroxenite with olivine wehrlite enclaves. The dunite dike has a general strike and dip of 045/45°SE. **c)** A ca. 2 cm-wide dunite dike crosscutting olivine clinopyroxenite with disaggregated dunite. The dike is undulatory, subvertical, and strikes east-west. **d)** Dunite dikes emanating from a dunite enclave. Abbreviations: cpxite = clinopyroxenite; ol = olivine.

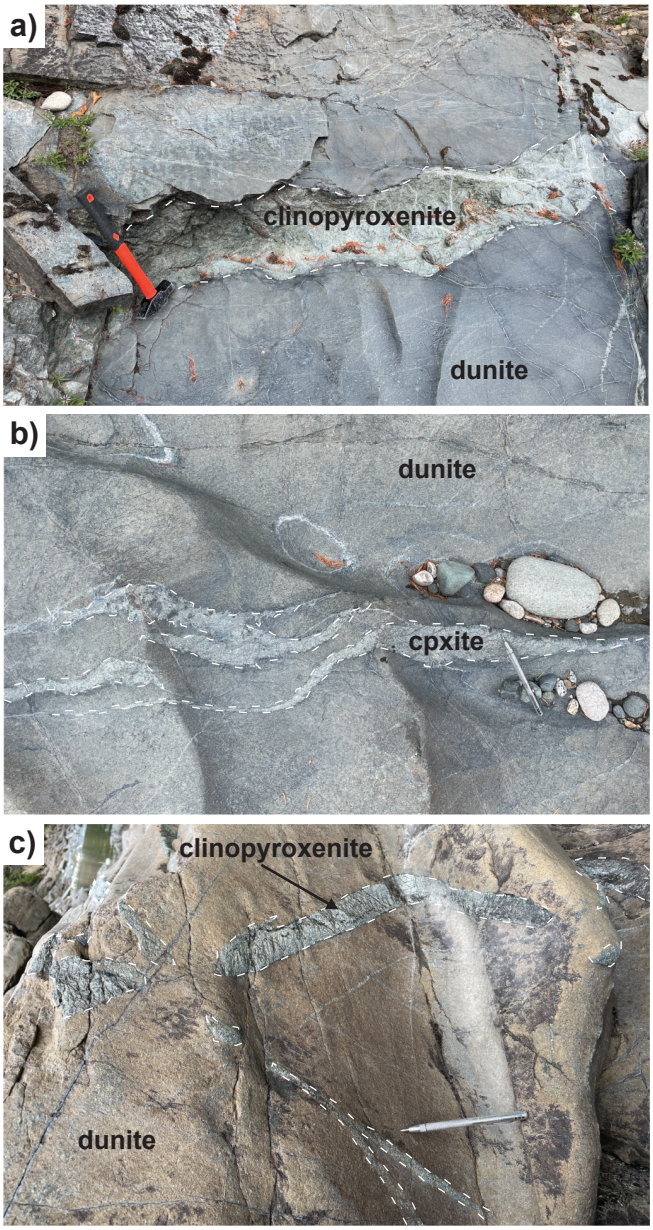

Fig. 16. Clinopyroxenite cutting dunite. **a)** Body of clinopyroxenite in dunite with sharp, undulatory contacts. **b)** Thin (1 to >5 cm-wide) clinopyroxenite dikes with sharp contacts and cuspate-lobate margins in dunite. **c)** Tabular, discontinuous clinopyroxenite dikes with sharp contacts in dunite. Abbreviations: cpxite = clinopyroxenite.

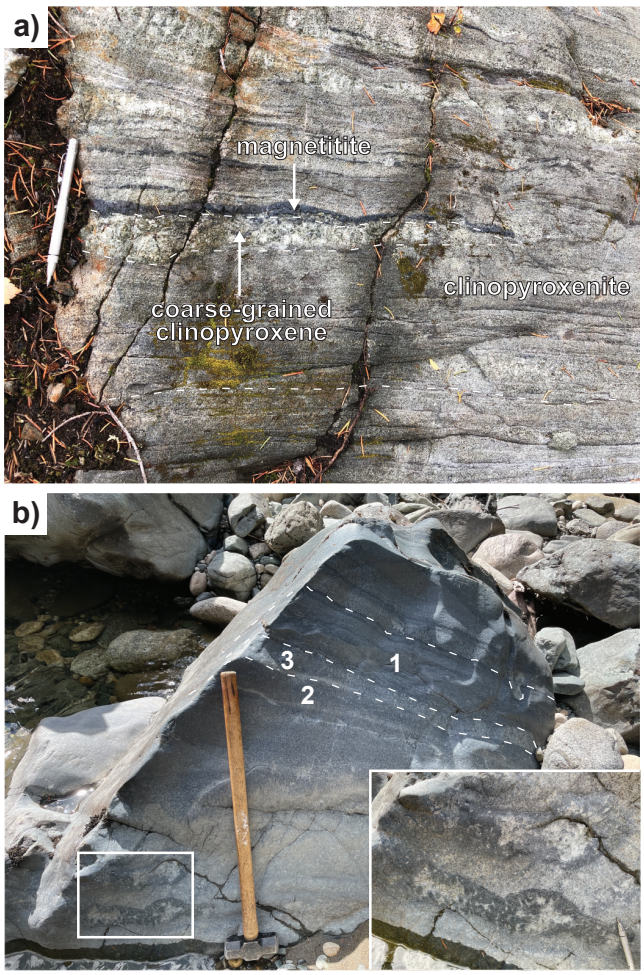

Fig. 17. Magmatic layering in ultramafic rocks. **a)** Interlayered clinopyroxenite and magnetite; layering also defined by grain size variation in clinopyroxenite. **b)** Boulder illustrating tabular units with diffuse boundaries of dunite (1), wehrlite (2), and olivine clinopyroxenite (3) considered to represent magmatic layering. Inset shows an irregular pegmatitic segregation with a dunite rim and coarse clinopyroxene core.

Fig. 18. Magnetite-bearing olivine clinopyroxenite lens and clinopyroxenite (white dashed lines). Olivine-rich zones are aligned to define a fabric, likely recording syn-magmatic strain.

diameter). The green colouration of gabbro results from intense saussuritization of plagioclase.

Late intrusions exposed in the Tulameen River include layered gabbro-diorite tabular bodies (Figs. 10, 11e) and fine-grained mafic to intermediate dikes (Figs. 10, 11f). The layered gabbro-diorite forms two tabular bodies that dip steeply southwest and cut olivine clinopyroxenite. These bodies are approximately 10 m-wide and contain upper and lower zones bounding an interior zone containing gabbro-diorite enclaves. Layering is defined by variations in relative proportions of hornblende and plagioclase. The layers are locally graded, with the amount

of hornblende decreasing toward what was presumably the paleosurface, and basal erosional scours are common. The interior zones of these tabular bodies contain rounded to subangular blocks (<1 m) of leucocratic to melanocratic gabbro-diorite (Fig. 11e, inset). These blocks are in a matrix of gabbro-diorite with a different modal abundance of the same constituent minerals. Feldspathic stringers are both concordant and discordant with layering (Fig. 11e). Contacts with olivine clinopyroxenite are sharp and have chilled margins, suggesting that olivine clinopyroxenite had cooled before intrusion of the layered units.

6.1.5. Mafic to intermediate dikes

Fine-grained mafic to intermediate dikes, <3 m wide, are common in the Tulameen River section, and crosscut every rock type, except dunite (Figs. 10, 11f). These dikes are dark grey-green to pinkish grey and aphanitic to fine grained. Dikes are commonly tabular, with sharp contacts that may undulate in a general northwest trend. Bifurcations and abrupt jogs in the trend of the dikes are common. The widest dikes display dike-parallel layering and dike centers may have phenocrysts of pyroxene up to 2 mm in diameter. The mafic to intermediate dikes are commonly observed within shear zones and are also sub-parallel to igneous layering in the gabbro-diorite tabular bodies, suggesting that they were injected along pre-existing anisotropies. Locally, the dikes cut this layering. Nixon et al. (1997) considered these dikes as feeders for lavas in the Princeton Group (Eocene).

7. Discussion

7.1. Geologic fieldwork assisted by remotely piloted aircraft systems

Unlike traditional two-dimensional field photographs, the orientation of contacts and relationships between rock types can be documented in their entirety using an RPAS (e.g., Fig. 10). The models provide the ability to dynamically pan, zoom, and reorient observations at any scale and enable detailed 3D examination of inaccessible outcrops such as cliff faces by foot. The resultant digital models can also be used to digitally archive the physical conditions of a field site at point in time, such as the exceptional outcrop exposed due to low water levels along the Tulameen River in the summer of 2021. Generally, using RPAS can reduce time spent documenting outcrop-scale geological relationships, which are recorded in 3D and scaled by the photogrammetric model. Additionally, RPAS-assisted geological mapping provides real-time aerial perspectives for outcrop-scale mapping that are unattainable while on the ground, which may provide context for geological relationships. In this study, the use of RPAS and subsequent photogrammetric models decreased the duration of field work at the Tulameen River section, which allowed for detailed investigation elsewhere in the Tulameen intrusion.

7.2. Implications for Tulameen magmatic processes

In mafic plutonic systems, numerical modelling predicts fluidization and mixing of resident crystal mush near sites of new magma injection (Bergantz et al., 2015; Schleicher et al., 2016). Preliminary observations from the present study, including remobilized and deformed chromitite layers and zones of intermingled and disaggregated olivine clinopyroxenite and dunite cumulates, are consistent with recharge and remobilization of crystal-rich magma mushes over a range of physical and rheological conditions in the ultramafic portions of the Tulameen intrusion. Similar observations and interpretations have been made from recent studies of the Polaris Alaskan-type intrusion (e.g., Nixon et al., 2020; Nott et al., 2020a, 2020b).

8. Conclusions

This study of the Tulameen Alaskan-type ultramafic-mafic intrusion of south-central British Columbia is an example of how RPAS-acquired photogrammetric models can aid geological mapping in areas of exceptional outcrop. RPAS photogrammetric surveys enable efficient archiving of 3D visual data, and allow observations of inaccessible geological features. The rock types exposed in the Tulameen River include dunite, olivine clinopyroxenite, hornblende clinopyroxenite, gabbro, layered gabbro-diorite, and mafic to intermediate dikes. Magma mingling relationships between dunite, wehrlite, and olivine clinopyroxenite are common and the textural diversity indicates a dynamic crystallization environment. Ongoing work will test geochemical predictions for the emplacement and mixing of crystal-rich magma mushes by characterizing major, minor, and trace element chemistry of the constituent minerals through both electron-probe microanalysis (EPMA) and laser ablation-inductively coupled plasma-mass spectrometry (LA-ICP-MS).

Acknowledgments

We thank Andrea Sanlorenzo for exceptional assistance and discussion while in the field and Travis Ferbey and Easton Elia for discussions regarding RPAS equipment and photogrammetric analysis. Thanks to Ken Hickey for general advice pertaining to field mapping. The senior author is grateful for salary assistance from an NSERC CGS-M scholarship. Funding for this project is provided by a NSERC Discovery Grant to James Scoates. This is a Natural Resources Canada Contribution #20210517. Constructive reviews of the manuscript by Alex Zagorevski, Travis Ferbey, and Lawrence Aspler are greatly appreciated.

References cited

Annen, C., Blundy, J.D., Leuthold, J., and Sparks, R.S.J., 2015. Construction and evolution of igneous bodies: Towards an integrated perspective of crustal magmatism. Lithos, 230, 206-221.

Balaguer-Puig, M., Marqués-Mateu, Á., Lerma, J.L., and Ibáñez-Asensio, S., 2017. Estimation of small-scale soil erosion in laboratory experiments with Structure from Motion photogrammetry. Geomorphology, 295, 285-296.

Bergantz, G.W., Schleicher, J.M., and Burgisser, A., 2015. Open-system dynamics and mixing in magma mushes. Nature Geoscience, 8, 793-796.

Cabri, L.J., Owens, D.R., and Laflamme, J.H.G., 1973. Tulameenite, a new platinum-iron-copper mineral from placers in the Tulameen River Area, British Columbia. Canadian Mineralogist, 12, 21-25.

Camsell, C., 1913. Geology and mineral deposits of the Tulameen District, British Columbia. Geological Survey of Canada, Memoir 26, 188 p.

Carrivick, J.L., Smith, M.W., Quincey, D.J., and Carver, S.J., 2013. Developments in budget remote sensing for the geosciences. Geology Today, 29, 138-143.

Colpron, M., and Nelson, J.L., 2011. A digital atlas of terranes for the Northern Cordillera. British Columbia Ministry of Energy and Mines, British Columbia Geological Survey Geofile, 2011-11.

Elia, E., and Ferbey, T., 2020. Generating photogrammetric DEMs in the field from remotely piloted aircraft systems. In: Geological Fieldwork 2019, British Columbia Ministry of Energy, Mines and Petroleum Resources, British Columbia Geological Survey Paper 2020-1, pp. 189-200.

Eltner, A., Kaiser, A., Castillo, C., Rock, G., Neugirg, F., and Abellán, A., 2016. Image-based surface reconstruction in geomorphometry-merits, limits and developments. Earth Surface Dynamics, 4, 359-389. <https://doi.org/10.5194/esurf-4-359-2016>

Findlay, D.C., 1963. Petrology of the Tulameen ultramafic complex, Yale District, British Columbia. Unpublished Ph.D. thesis, Queen's University, Kingston, Ontario, 415 p.

Findlay, D.C., 1969. Origin of the Tulameen ultramafic-gabbro complex, southern British Columbia. Canadian Journal of Earth Sciences, 6, 399-425.

Greig, C.J., Armstrong, R.L., Harakal, J.E., Runkle, D., and van der Heyden, P., 1992. Geochronometry of the Eagle Plutonic Complex and the Coquihalla area, southwestern British Columbia. Canadian Journal of Earth Sciences, 29, 812-829.

Hansman, R.J., and Ring, U., 2019. Workflow: From photo-based 3-D reconstruction of remotely piloted aircraft images to a 3-D geological model. Geosphere, 15, 1393-1408. <https://doi.org/10.1130/GES02031.1>

Himmelberg, G.R., and Loney, R.A., 1995. Characteristics and petrogenesis of Alaskan-type ultramafic-mafic intrusions, southeastern Alaska. U.S. Geological Survey Professional Paper, 1564, 47 p.

Irvine, T.N., 1974. Petrology of the Duke Island ultramafic complex, southeastern Alaska. Geological Society of America, Memoir 138, 240 p.

Jackson-Brown, S., 2017. Origin of the Cu-PGE-rich sulphide mineralization in the DJ/DB zone of the Turnagain Alaskan-type intrusion, British Columbia. Unpublished M.Sc. thesis, University of British Columbia, Vancouver, British Columbia, 290 p.

James, M.R., and Robson, S., 2012. Straightforward reconstruction of 3D surfaces and topography with a camera: Accuracy and geoscience application. Journal of Geophysical Research: Earth Surface, 117, 17 p. < https://doi.org/10.1029/2011JF002289>

James, M.R., Chandler, J.H., Eltner, A., Fraser, C., Miller, P.E., Mills, J.P., Noble, T., Robson, S., and Lane, S.N., 2019. Guidelines on the use of structure-from-motion photogrammetry in geomorphic research: Earth Surface Processes and Landforms, 44, 2081-2084.

Kemp, J.F., 1902. The geological relations and distribution of platinum and associated metals. In: Bulletin of the United States Geological Survey, Department of the Interior, No. 193, 94 p.

Le Maitre, R.W., 1989. A classification of igneous rocks and glossary of terms. Oxford, Blackwell Scientific Publications, 193 p.

Logan, J.M., and Mihalynuk, M.G., 2014. Tectonic controls on early Mesozoic paired alkaline porphyry deposit belts (Cu-Au ±Ag-Pt-Pd-Mo) within the Canadian Cordillera. Economic Geology, 109, 827-858.

Manor, M.J., Wall, C.J., Nixon, G.T., Scoates, J.S., Pinsent, R.H., and Ames, D.E., 2014. Preliminary geology and geochemistry of the Giant Mascot ultramafic-mafic intrusion, Hope, southwestern British Columbia. British Columbia Ministry of Energy and Mines, British Columbia Geological Survey Open File 2014-3, 1:10,000 scale.

Manor, M.J., Scoates, J.S., Nixon, G.T., and Ames, D.E., 2016. The Giant Mascot Ni-Cu-PGE deposit, British Columbia: mineralized conduits in a convergent margin tectonic setting. Economic Geology, 111, 57-87.

Manor, M.J., Scoates, J.S., Wall, C.J., Nixon, G.T., Friedman, R.M., Amini, M., and Ames, D.E., 2017. Age of the Late Cretaceous ultramafic-hosted Giant Mascot Ni-Cu-PGE deposit, southern Canadian Cordillera: integrating CA-ID-TIMS and LA-ICP- MS U-Pb geochronology and trace element geochemistry of zircon. Economic Geology, 112, 1395-1418.

Matzel, J.E., Bowring, S.A., and Miller, R.B., 2006. Time scales of pluton construction at differing crustal levels: Examples from the Mount Stuart and Tenpeak intrusions, North Cascades, Washington. Geological Society of America Bulletin, 118, 1412-1430.

Mosbrucker, A.R., Major, J.J., Spicer, K.R., and Pitlick, J., 2017. Camera system considerations for geomorphic applications of SfM photogrammetry: camera system configuration to optimize SfM imagery. Earth Surface Processes and Landforms, 42, 969-986.

Mungall, J.E., Kamo, S.L., and McQuade, S., 2016. U-Pb geochronology documents out-of-sequence emplacement of ultramafic layers in the Bushveld Igneous Complex of South Africa. Nature Communications, 7, 13385. <https://doi.org/10.1038/ncomms13385>

Nixon, G.T., and Rublee, V.J., 1988. Alaskan-type ultramafic rocks in British Columbia: New concepts of the structure of the Tulameen Complex. In: Geological Fieldwork 1987, British Columbia Ministry of Energy, Mines and Petroleum Resources, Paper 1988-1, pp. 281-294.

Nixon, G.T., Cabri, L.J., and Laflamme, J.H.G., 1990. Platinum-group-element mineralization in lode and placer deposits associated with the Tulameen Alaskan-type complex, British Columbia. The Canadian Mineralogist, 28, 503-535.

Nixon, G.T., Hammack, J.L., Ash, C.H., Cabri, L.J., Case, G., Connelly, J.N., Heaman, L.M., Laflamme, J.H.G., Nuttall, C., Paterson, W.P.E., and Wong, R.H., 1997. Geology and platinum group element mineralization of Alaskan-type ultramafic-mafic complexes in British Columbia. British Columbia Ministry of Employment and Investment, British Columbia Geological Survey, Bulletin 93, 142 p.

Nixon, G.T., Manor, M.J., Jackson-Brown, S., Scoates, J.S., and Ames, D.E., 2015. Magmatic Ni-Cu-PGE sulphide deposits at convergent margins. In: Ames, D.E., and M.G. Houlé, M.G., (Eds.), Targeted Geoscience Initiative 4: Canadian Nickel-Copper-Platinum Group Elements-Chromium Ore Systems-Fertility, Pathfinders, New and Revised Models, Geological Survey of Canada, Open File 7856, pp. 17-34.

Nixon, G.T., Scheel, J.E., Friedman, R.M., Wall, C.J., Gabites, J., Miller, D., and Scoates, J.S., 2017. Geology and geochronology of the Turnagain ultramafic-mafic intrusion, British Columbia. British Columbia Ministry of Energy, Mines and Petroleum Resources, British Columbia Geological Survey Geoscience Map 2017-1, 1:10,000 scale.

Nixon, G.T., 2018. Geology of the Tulameen Alaskan-type ultramafic-mafic intrusion, British Columbia. British Columbia Ministry of Energy, Mines and Petroleum Resources, British Columbia Geological Survey Open File 2018-2, 1:20,000 scale.

Nixon, G.T., Scoates, J.S., Milidragovic, D., Nott, J., Moerhuis, N., Ver Hoeve, T.J., Manor, M.J., and Kjarsgaard, I.M., 2020. Convergent margin Ni-Cu-PGE-Cr ore systems. In: Targeted Geoscience Initiative 5: Advances in the Understanding of Canadian Ni-Cu-PGE and Cr Ore Systems, Geological Survey of Canada Open File 8722, pp. 197-218.

Nott, J., Milidragovic, D., Nixon, G.T., and Scoates, J.S., 2020a. New geological investigations of the Early Jurassic Polaris ultramafic-

mafic Alaskan-type intrusion, north-central British Columbia. In: Geological Fieldwork 2019. British Columbia Ministry of Energy, Mines and Petroleum Resources, British Columbia Geological Survey, Paper 2020-1, pp. 59-76.

Nott, J.A., Milidragovic, D., Nixon, G.T., and Scoates, J.S., 2020b. Geology of the Polaris Alaskan-type ultramafic-mafic intrusion, north-central British Columbia. British Columbia Ministry of Energy, Mines and Low Carbon Innovation, British Columbia Geological Survey Open File 2020-4, 1:15,000 scale.

Paterson, S.R., 2009. Magmatic tubes, pipes, troughs, diapirs, and plumes: Late-stage convective instabilities resulting in compositional diversity and permeable networks in crystal-rich magmas of the Tuolumne batholith, Sierra Nevada, California. Geosphere, 5, 496-527. <https://doi.org/10.1130/GES00214.1>

Rice, H.M.A., 1947. Geology and mineral deposits of Princeton map area, British Columbia. Geological Survey of Canada, Memoir 243, 136 p.

Rublee, V.J., 1989. The structural control of the Tulameen complex and outlying ultramafic bodies, 92H/7, 10. In: Exploration in British Columbia 1988. British Columbia Ministry of Energy, Mines and Petroleum Resources, British Columbia Geological Survey, pp. B71-B81.

Rublee, V.J., 1994. Chemical petrology, mineralogy and structure of the Tulameen complex, Princeton area, British Columbia. Unpublished M.Sc. thesis, University of Ottawa, Ottawa, Ontario, 183 p.

Scheel, J.E., 2007. Age and origin of the Turnagain Alaskan-type intrusion and associated Ni-sulphide mineralization, north-central British Columbia, Canada. Unpublished M.Sc. thesis, University of British Columbia, Vancouver, British Columbia, 210 p.

Scheel, J.E., Scoates, J.S., and Nixon, G.T., 2009. Chromian spinel in the Turnagain Alaskan-type ultramafic intrusion, northern British Columbia, Canada. The Canadian Mineralogist, 47, 63-80.

Schleicher, J.M., Bergantz, G.W., Breidenthal, R.E., and Burgisser, A., 2016. Time scales of crystal mixing in magma mushes. Geophysical Research Letters, 43, 1543-1550.

Schoene, B., Schaltegger, U., Brack, P., Latkoczy, C., Stracke, A., and Guenther, D., 2012. Rates of magma differentiation and emplacement in a ballooning pluton recorded by U-Pb TIMS-TEA, Adamello Batholith, Italy. Earth and Planetary Science Letters, 355-356, 162-173.

Scoates, J.S., Wall, C.J., Friedman, R.M., Weis, D., Mathez, E.A., and VanTongeren, J.A., 2021. Dating the Bushveld Complex: Timing of crystallization, duration of magmatism, and cooling of the world's largest layered intrusion and related rocks. Journal of Petrology, 62, 1-39.

Shervais, K., 2016. Structure from Motion (SfM) Photogrammetry Field Methods Manual for Students. Unpublished Manual, University NAVSTAR Consortium (UNAVCO), National Science Foundation and NASA, 10 p.

Smith, M.W., Carrivick, J.L., and Quincey, D.J., 2016. Structure from motion photogrammetry in physical geography. Progress in Physical Geography: Earth and Environment, 40, 247-275.

Spence, D.W., 2020. Olivine in the Polaris Alaskan-type intrusion of north-central British Columbia: Implications for the magmatic evolution of primitive arc magmas and for convergent margin Ni-Cu-PGE ore-forming systems. Unpublished B.Sc. thesis, University of British Columbia, Vancouver, British Columbia, 144 p.

St. Louis, R.M., Nesbitt, B.E., and Morton, R.D., 1986. Geochemistry of platinum group elements in the Tulameen ultramafic complex, southern British Columbia. Economic Geology, 81, 961-973.

Transport Canada, 2021. Canadian Aviation Regulations (SOR/96-433), 1001 p.

Wall, C.J., Scoates, J.S., Weis, D., Friedman, R.M., Amini, M., and Meurer, W.P., 2018. The Stillwater Complex: integrating zircon geochronological and geochemical constraints on the age, emplacement history and crystallization of a large, open-system layered intrusion. Journal of Petrology, 59, 153-190.

Weinberg, R.F., Vernon, R.H., and Schmeling, H., 2021. Processes in mushes and their role in the differentiation of granitic rocks. Earth-Science Reviews, 220, 1-30.

Westoby, M.J., Brasington, J., Glasser, N.F., Hambrey, M.J., and Reynolds, J.M., 2012. 'Structure-from-Motion' photogrammetry: A low-cost, effective tool for geoscience applications. Geomorphology, 179, 300-314.

Yao, Z., Mungall, J.E., and Jenkins, M.C., 2021. The Rustenburg Layered Suite formed as a stack of mush with transient magma chambers. Nature Communications, 12, 505. <https://10.1038/s41467-020-20778-w>

Gaseous elemental mercury (GEM) response from sediment-covered, volcanogenic massive sulphide mineralization on southern Vancouver Island

Alexei S. Rukhlov[1, a], Nikolay R. Mashyanov[2], Pavel V. Pitirimov[3], Adrian S. Hickin[1], Maksym Golovetskyy[1], and Ben Coats[1]

[1] British Columbia Geological Survey, Ministry of Energy, Mines and Low Carbon Innovation, Victoria, BC, V8W 9N3
[2] Lumex-marketing LLC, 1 lit. B, Obruchevykh Street, St. Petersburg, 195220, Russia
[3] Lumex Instruments, Mission, BC, V4S 0A3
[a] corresponding author: Alexei.Rukhlov@gov.bc.ca

Recommended citation: Rukhlov, A.S., Mashyanov, N.R., Pitirimov, P.V., Hickin, A.S., Golovetskyy, M., and Coats, B., 2022. Gaseous elemental mercury (GEM) response from sediment-covered, volcanogenic massive sulphide mineralization on southern Vancouver Island. British Columbia Ministry of Energy, Mines and Low Carbon Innovation, British Columbia Geological Survey Paper 2022-01, pp. 123-135.

Abstract

New data from the Lara-Coronation polymetallic occurrence, southern Vancouver Island confirm that direct and continuous analysis of gaseous elemental mercury (GEM) concentrations in near-surface air using a portable RA-915M Zeeman Hg analyzer can map sediment-covered mineralization in real time. Detailed surveys across steeply dipping, massive sulphide zones in volcanic rocks of the McLaughlin Ridge Formation (Sicker Group; Middle to Late Devonian) confirm GEM haloes in near-surface air above the mineralization. Measured GEM concentrations range from 0.61 to 251 $ng \cdot m^{-3}$ in this study, with the strongest halo (206x background Hg) above exposed mineralization. Weak haloes (1.7x background Hg) mark sediment-covered mineralized zones. Simultaneously measured meteorological and in situ soil parameters appear to have no effect on measured GEM concentrations. Before sampling GEM above overburden, we disturbed surface sediment mechanically with a hoe. To model this method, we conducted experiments that measured GEM concentrations in the air of jars containing non-Hg ore minerals. These experiments suggest that elevated concentrations in Hg haloes reflect mechanically induced release of Hg^0 adsorbed in soils and vegetation. Real-time grid sampling of near-surface air reveals a pattern of northwest-trending GEM haloes reflecting bedrock structure, including a 224 by 30 m halo above the polymetallic VMS Coronation zone, covered by up to 22 m of overburden. This study confirms that the real-time GEM sampling of near-surface air can instantly delineate mineralized zones that are buried beneath overburden 10s of m thick. Real-time GEM sampling is a simple and effective technique for mineral exploration in overburden-covered areas.

Keywords: Gaseous elemental mercury (GEM), near-surface air, real-time survey, portable Lumex RA-915M Hg analyzer, ore minerals, bornite, galena, molybdenite, native copper, native silver, sphalerite, volcanic rocks, Sicker Group, Devonian, sediment-covered Lara-Coronation polymetallic occurrence, volcanogenic massive sulphide (VMS) mineralization, overburden, glacial deposits, mineral exploration under cover, southern Vancouver Island

1. Introduction

Mineral exploration in overburden-covered areas requires effective techniques such as atmochemical methods that sample highly mobile volatiles (e.g., CO_2, SO_2, He, Rn, and Hg), which form haloes in soil gas and near-surface atmosphere directly above mineral deposits (see Rukhlov et al., 2021b for an overview). Among atmochemical exploration methods, Hg vapour or gaseous elemental mercury (GEM) surveys are particularly informative (e.g., Fursov, 2006). This is because Hg is: 1) highly mobile (exists mostly as GEM); 2) common in many ore deposits (Babkin et al., 1976); and 3) a trace metal, with the very low background abundance in the Earth's crust of 45 ppb (Saukov et al., 1972; Rudnick and Gao, 2005) and ultra-low background concentrations in the atmosphere (<1.5 $ng \cdot m^{-3}$; Sprovieri et al., 2016).

Modern GEM surveys use passive air sampling (e.g., McLagan et al., 2016; Jeon et al., 2020) or direct analysis of GEM concentrations in soil gas or air (e.g., Sun et al., 2017; Rukhlov et al., 2021b; Cabassi et al., 2022). Rukhlov et al. (2021b) reported GEM haloes in near-surface air at the sediment-covered, polymetallic Lara-Coronation occurrence, southern Vancouver Island (Fig. 1 inset). In the present study, we follow up this reconnaissance with detailed surveys across the mineralized zone at Lara-Coronation. We measured GEM concentrations in air 1 cm above ground in real time using a portable RA-915M Zeeman Hg analyzer, and simultaneously measured meteorological and in situ soil parameters. To minimize GEM removal and dilution due to wind and turbulent air movement, we sampled near-surface air under a bucket (cf. Rukhlov et al., 2021b). We performed experiments measuring GEM concentrations in the air of sealed glass jars containing samples of selected ore minerals to model the instant release of GEM adsorbed in overburden at superimposed Hg haloes in response to mechanical disturbance. Our study

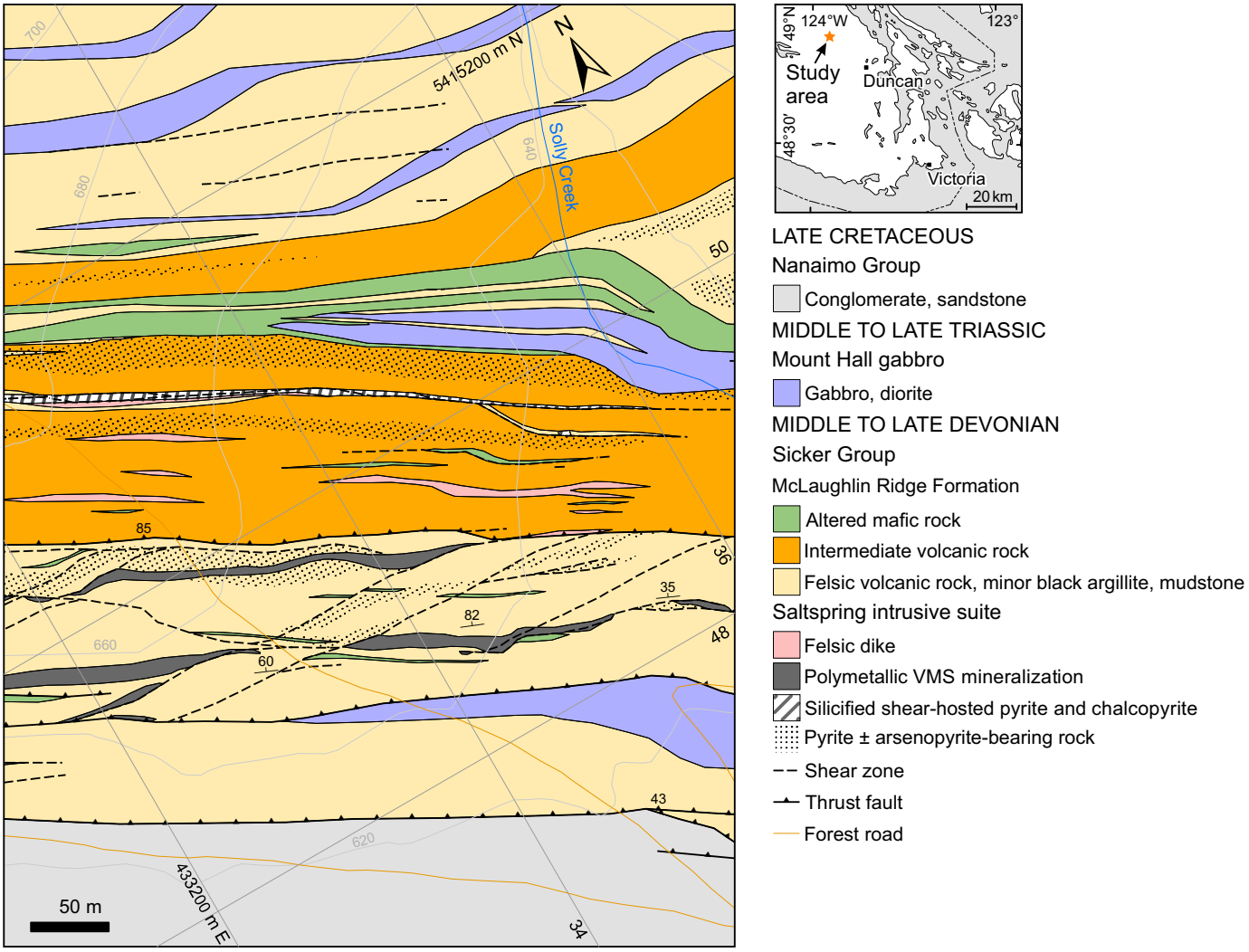

Fig. 1. Location (inset) and geology of the Lara-Coronation occurrence; NAD 83, UTM zone 10. Geology after Muller (1977), Kapusta et al. (1988), Massey et al. (1991), Massey (1995), Wetherup (2010), Ruks (2015), and Bodnar (2017).

confirms that simple, real-time GEM sampling of near-surface air can instantly map mineralized zones covered by overburden 10s of m thick.

2. Geological setting, Lara-Coronation polymetallic volcanogenic massive sulphide occurrence

The Lara-Coronation volcanogenic massive sulphide (VMS) Zn-Cu-Pb-Ag-Au occurrence (MINFILE 092B 129) is about 15 km northwest of Duncan, in the traditional lands of the Hul'qumi'num and Snuneymuxw First Nations, southern Vancouver Island (Fig. 1). The area is mostly covered by up to 30 m of glacial sediments (Kapusta et al., 1988; Bodnar, 2017). The polymetallic mineralization (Coronation zone) comprises lenses (up to 16 m thick) of banded and massive sphalerite, pyrite, chalcopyrite, and galena with minor tetrahedrite, tennantite, bornite, electrum, pearceite, and arsenopyrite. Associated mineralization includes chalcopyrite-pyrite stringers in silicified shear zones and pyrite-rich horizons (Northcote and Muller, 1972; Kapusta et al., 1988; Kelso and Wetherup, 2008; Wetherup, 2010; Ruks, 2015; Bodnar, 2017). Host rocks are greenschist-facies, sheared and silicified, felsic and intermediate volcanic rocks of the McLaughlin Ridge Formation (Sicker Group; Middle to Late Devonian), which dip steeply northeast. Coeval felsic intrusions of the Saltspring plutonic suite and mafic to intermediate intrusions of the Mount Hall gabbro (Middle to Late Triassic) cut the volcanic rocks. Folded and imbricated by thrust faults, the older rocks are juxtaposed against siliciclastic rocks of the Nanaimo Group (Late Cretaceous) along a northwest-trending fault (Muller, 1977; Kapusta et al., 1988; Masey et al., 1991; Massey, 1995; Wetherup, 2010; Ruks, 2015; Bodnar, 2017).

3. Methods

Real-time GEM mass concentrations (in $ng \cdot m^{-3}$) in near-surface air were directly and continuously measured using a portable Lumex RA-915M Zeeman Hg analyzer during foot

traversing at the Lara-Coronation occurrence. The instrument has a concentration detection range of 0.5 to 20,000 ng·m^{-3} and a response time of one second. Baseline (zero Hg signal) was automatically measured for 60 seconds every 2 to 3 minutes using a built-in, high-efficiency (>98%) sorption filter. The relative intrinsic error of the measurement is less than ±20%. GEM concentrations were automatically corrected for drift and normalized to standard temperature (20°C) and pressure (101.3 kPa). We used the average of 60 or 120 readings (1 second each) per station, which were automatically processed by a Lumex RAPID software running on a pocket PC connected to the instrument in the field. Stations were spaced 4 to 36 m along traverses (260 to 500 m long; Table 1). We sampled air at 1 cm above ground via a probe attached to the instrument's air intake inlet with a built-in dust filter (Fig. 2). The probe consists of: 1) a 1.3 m hose (2 cm diameter); 2) a dust filter (6.4 cm diameter housing; 5.1 cm diameter insert) with barb connectors and an intake tube (23 cm long; 8 mm diameter); 3) a 4.2 L bucket (21 cm diameter) with a fitting through bottom for the intake tube; and 4) a stick holding the bucket and about one third of the hose secured with tape (Fig. 3). The distance between the end of the tube inside the bucket and ground (the air sampling height) was set to approximately 1 cm. In contrast to Rukhlov et al. (2021b), we sampled the air under the bucket to minimize wind influence on GEM concentration (Yasutake et al., 2011).

Fig. 2. Measuring real-time gaseous elemental mercury (GEM) in air 1 cm above ground.

Fig. 3. Air probe.

A chopstick attached to the edge of the bucket creates a small gap when the probe is placed against the ground, which is necessary to maintain the analyzed air flow of 10 L·min^{-1}.

We performed five orientation surveys along two southwest-northeast profiles (A′-A and B′-B; Figs. 4, 5) across the known mineralized zones to determine optimal parameters. GEM concentrations in near-surface air were measured: 1) without mechanical disturbance of the surface before sampling; and 2) immediately after punching several times or partly removing the top 5-15 cm layer across an area ca. 20 cm in diameter with the pointed edge of an Estwing GP100 hoe pick (Fig. 6). The shorter measurements (1 min per station), coupled with mechanically agitated surface immediately before sampling, yielded the strongest GEM haloes above the known mineralization (Table 1). We adopted these parameters for an areal survey, following a grid of 5 lines (450 m long each; 50 m spacing), with stations every 13 to 36 m along the lines.

To model mechanically induced release of volatile Hg^0 adsorbed in overburden, we measured GEM concentrations in the air of sealed glass jars (1 L) containing samples of sphalerite, galena, molybdenite, bornite, and native metals (Table 2). Air was sampled via a hose with a dust filter 1 cm above samples: 1) after several days of undisturbed storage in closed jars, and 2) two to five minutes after gently shaking the samples in re-closed jars. The GEM concentrations in air were continuously measured until a plateau concentration in terms of time (s) vs. GEM (ng·m^{-3}), with 55 to 108 readings (1 second each) acquired per run. We also measured air 1 m above ground in Victoria, B.C. (total 3 runs; 80 seconds each) to check the background GEM concentrations between 3 to 6 runs of air above the samples of ore minerals.

Air temperature, relative humidity, barometric pressure, wind speed, and wind direction (azimuth) were simultaneously measured every 5 seconds using a Kestrel 5500 meter mounted on a tripod under umbrella at a fixed location in the study area (Fig. 7). We used a Garmin Glo 2 GPS-GLONASS to acquire coordinates every 2 seconds. In-situ soil parameters (temperature, moisture content, electrical conductivity, and pH) were measured at stations along profile 1 (A′-A) simultaneously with the first GEM orientation on July 15, 2021 (Table 1). We used an Extech 39240 thermometer with a 7 cm long stainless-steel probe; an Extech MO750 soil moisture meter with a

Table 1. Summary of GEM surveys in air 1 cm above ground at the Lara-Coronation polymetallic occurrence.

Survey		Sampling site		GEM data[1]		Meteorological parameters[2]						GEM halo	
Date	**Time**	**Spacing**	**Surface[3]**	**Readings**	**Baseline**	**T (°C)**	**RH (%)**	**P_0 (mb)**	**Wind (m·s^{-1})**	**Azimuth**	**Weather**	**Contrast[4]**	**Extent (m)[5]**
Profile 1 (A'-A; 260 m) across mineralization exposed in an old exploration trench (2020 GEM anomaly); overburden thickness varies from 0 to 18 m.													
15.07.2021	12:01 to 14:48	4 to 25 m	Undisturbed	120	60 s, every 3 min	19.2 to 26.3	39.4 to 52.2	1019.7 to 1020.4	0 to 5.6	160 to 190	Sunny	3.5	20
	15:09 to 15:52	4 to 25 m	Undisturbed	60	60 s, every 2 min	20.0 to 25.6	37.9 to 47.2	1019.7 to 1020.0	0 to 4.9	150 to 180	Few clouds	6.0	20
20.07.2021	11:55 to 12:38	4 to 25 m	Agitated	60	60 s, every 2 min	18.8 to 23.4	31.6 to 41.3	1024.5 to 1024.6	0 to 4.3	290 to 300	Few clouds	206	29
Profile 2 (B'-B; 500 m) across sediment-covered mineralization (2020 GEM anomaly); overburden thickness varies from 5 to 17 m.													
20.07.2021	13:20 to 14:27	6 to 25 m	Undisturbed	60	60 s, every 2 min	19.4 to 24.6	29.2 to 39.1	1024.1 to 1024.5	0 to 5.4	280 to 340	Few clouds	1.4	22
	15:10 to 16:17	4 to 33 m	Agitated	60	60 s, every 2 min	20.0 to 24.1	29.8 to 39.5	1023.5 to 1024.0	0 to 4.4	280 to 340	Few clouds	1.7	25
Grid of 5 x 450 m lines (50 m spacing); overburden thickness varies from <1 to 22 m.													
21.07.2021	11:01 to 14:55	13 to 36 m	Agitated	60	60 s, every 2 min	14.5 to 22.0	37.8 to 49.1	1023.4 to 1024.3	0 to 6.5	280 to 70	Few clouds	1.7	224 x 30[6]

[1] Real-time, gaseous elemental mercury (GEM) mass concentrations (one reading per second; 60 or 120 readings per site); baseline (zero Hg signal) measured for 60 seconds every 2 to 3 minutes.
[2] Meteorological parameters every 5 seconds: **T**- air temperature (°C); **RH** - relative humidity (%); **P_0** - barometric pressure (mb); **Wind** - wind speed (m·s^{-1}); **Azimuth** – predominant wind direction.
[3] **Undisturbed** – no intentional agitation of surface immediately before measuring GEM; **Agitated** - top 5 to 15 cm surface layer disturbed with a hoe pick immediately before measuring GEM.
[4] Ratio of the mean GEM concentration (based on 60 or 120 measurements per site) in near-surface air above a known mineralized zone to the median GEM concentration of the survey.
[5] Width of a GEM (ng·m^{-3}) peak above a known mineralized zone on profile (see Fig. 5).
[6] Footprint of a GEM halo in near-surface air above the polymetallic Coronation zone (volcanogenic massive sulphide; see Fig. 4).

20 cm long, heavy-duty probe; a Hanna HI98331 direct soil EC tester with an 11.4 cm long, stainless-steel probe; and a Hanna HI99121 direct soil pH meter with a glass electrode. The single-junction pH electrode was calibrated using pH 4.01 and 7.00 buffers on the same day. We used a conical plastic auger to perforate dry soil 3 to 4 cm deep and a few mL of deionized water added to the borehole before inserting the pH sensor. The equipment was carefully rinsed with deionized water after each measurement.

4. Results

The complete dataset upon which the following is summarized is presented in Rukhlov et al. (2021a). The GEM surveys at the Lara-Coronation VMS Zn-Cu-Pb-Ag-Au occurrence (MINFILE 092B 129) include orientation profiles performed on July 15, 2021 and July 20, 2021 and a grid survey performed on July 21, 2021 (Fig. 4). Table 1 provides a summary of the surveys, GEM haloes, and simultaneously measured meteorological parameters. Table 2 provides a statistical summary of the real-time GEM data for air sampled at 1 cm above ground at the Lara-Coronation occurrence; air 1 m above ground in Victoria, B.C.; and air of sealed glass jars containing selected ore minerals.

4.1. GEM in near-surface air

We carried out surveys along the southwest-northeast traverses (030° azimuth; 260 to 500 m long) on a clearcut across polymetallic mineralization at the Coronation zone, covered by up to 22 m of glacial sediments (Fig. 4; Kapusta et al., 1988; Bodnar, 2017). Profile 1 (A′-A; 260 m) is across the main mineralized zone exposed in an overgrown, partly flooded exploration pit trenched in approximately 1986. Profile 2 (B′-B; 500 m) is across the same zone, 230 m along strike to the northwest, where mineralization is covered by at least 17 m of glacial sediments (Fig. 4). Weather conditions (sunny to a mix of sun and clouds) were generally consistent for all surveys. Air temperature varied between 14.5 and 26.3°C, relative humidity between 29.2 and 52.2%, and barometric pressure between 1019.7 and 1024.6 mb. Predominantly southerly winds (150 to 190° azimuth) with gusts up to 5.6 $m \cdot s^{-1}$ on July 15, 2021 became predominantly west and east (280 to 070° azimuth), with gusts up to 6.5 $m \cdot s^{-1}$ on July 20 and 21 (Table 1).

Measured GEM concentrations (the average of 60 or 120 values per point) in air 1 cm above ground at the Lara-Coronation occurrence range from 0.61 to 251 $ng \cdot m^{-3}$, averaging 2.37 ±16.4 $ng \cdot m^{-3}$ (n=231; Table 2). The strongest GEM halo marks exposed massive sulphide mineralization containing up to 90 ppm Hg in the trench (Kelso and Wetherup, 2008; Bodnar, 2017). The median value of 1.13 $ng \cdot m^{-3}$ is consistent with the average GEM concentration (background) in air 1 m above ground in Victoria, B.C. (1.03 ±0.32 $ng \cdot m^{-3}$; n=240; based on 3 runs, 80 s each), and with the median GEM concentration in near-surface air for southern Vancouver Island (1.40 $ng \cdot m^{-3}$; n=9660; based on the average of 10 values per point; Rukhlov et al., 2021b).

Orientation surveys in this study confirm the anomalous GEM haloes in near-surface air at Lara-Coronation (Fig. 5; Rukhlov et al. 2021b). GEM concentrations, measured without mechanical disturbance of surface materials immediately before sampling, range from 0.79 to 5.86 $ng \cdot m^{-3}$, with the median (background) value of 1.05 $ng \cdot m^{-3}$ (n=75; Table 2). The shorter measurements (1 min per site) yielded a slightly stronger GEM halo (6.0x background Hg) than the longer measurements (2 min per site; 3.5x background Hg; Table 1; Fig. 5a). In contrast, GEM concentrations in near-surface air, measured immediately after mechanically agitating the top 5 to 15 cm surface layer, range from 0.61 to 251 $ng \cdot m^{-3}$, with the median (background) value of 1.21 $ng \cdot m^{-3}$ (n=156; Table 2). Therefore, the effect of mechanically disturbing a site before sampling yields a GEM response that is two orders of magnitude stronger (206x background Hg) relative to the undisturbed surface at the same location (Table 1; Fig. 5). Regardless of bedrock, GEM concentrations in near-surface air away from the mineralized zone along profile 1 are generally <2 $ng \cdot m^{-3}$ (i.e. background-level), consistent with the low Clarke value for the Earth's crust (45 ppb Hg; Saukov et al., 1972; Rudnick and Gao, 2005) and with generally uniform Hg abundances in different rock types away from Hg anomalies (Fursov, 2006). An anomalous GEM halo (3.16 $ng \cdot m^{-3}$) also marks a steep fault covered by 8 m of overburden at about 125 m along section A′-A (Rukhlov et al., 2021b; Fig. 5a).

Orientation surveys along profile 2 (B′-B; Fig. 4) revealed background-level GEM variations (up to 1.7x background Hg) above the mineralization covered by at least 17 m of clay-bearing glacial sediments (Fig. 5b). GEM concentrations in near-surface air, measured above mechanically disturbed materials (0.89 to 2.23 $ng \cdot m^{-3}$, averaging 1.37 ±0.34 $ng \cdot m^{-3}$; n=34), are slightly higher than those above undisturbed surfaces (0.83 to 1.44 $ng \cdot m^{-3}$, averaging 1.08 ±0.14 $ng \cdot m^{-3}$; n=33). A GEM spike at about 300 m along the profile marks a silicified shear zone with pyrite-chalcopyrite stringers (Rukhlov et al., 2021b), but spikes at about 50 m, 250 m, and between 350 and 450 m along the profile do not correspond to known mineralization (Fig. 5b). An extensive GEM halo (100 m wide) near the northeastern end of the profile is above felsic volcanic rocks of the McLaughlin Ridge Formation (Sicker Group), which host the Coronation zone, 200 m to the southwest, and several other polymetallic zones in the area (Kapusta et al., 1988; Kelso and Wetherup, 2008; Ruks, 2015; Bodnar, 2017). Previous multi-media geochemical surveys at Lara revealed a Hg aureole at Lara-Coronation, with up to 460 ppb Hg in soils and up to 133 ppb Hg in vegetation, reflecting the massive sulphide mineralization (Kapusta et al., 1988; Kelso and Wetherup, 2008; Bodnar, 2017; Heberlein et al., 2017). Elevated Hg contents in soils and vegetation correlate with the GEM halo near the northeastern end of B′-B, which may indicate an unknown mineralized zone (Fig. 5b).

Based on the orientation surveys, we consider that the optimal survey parameters include mechanically disturbing surface materials immediately before measurements are taken

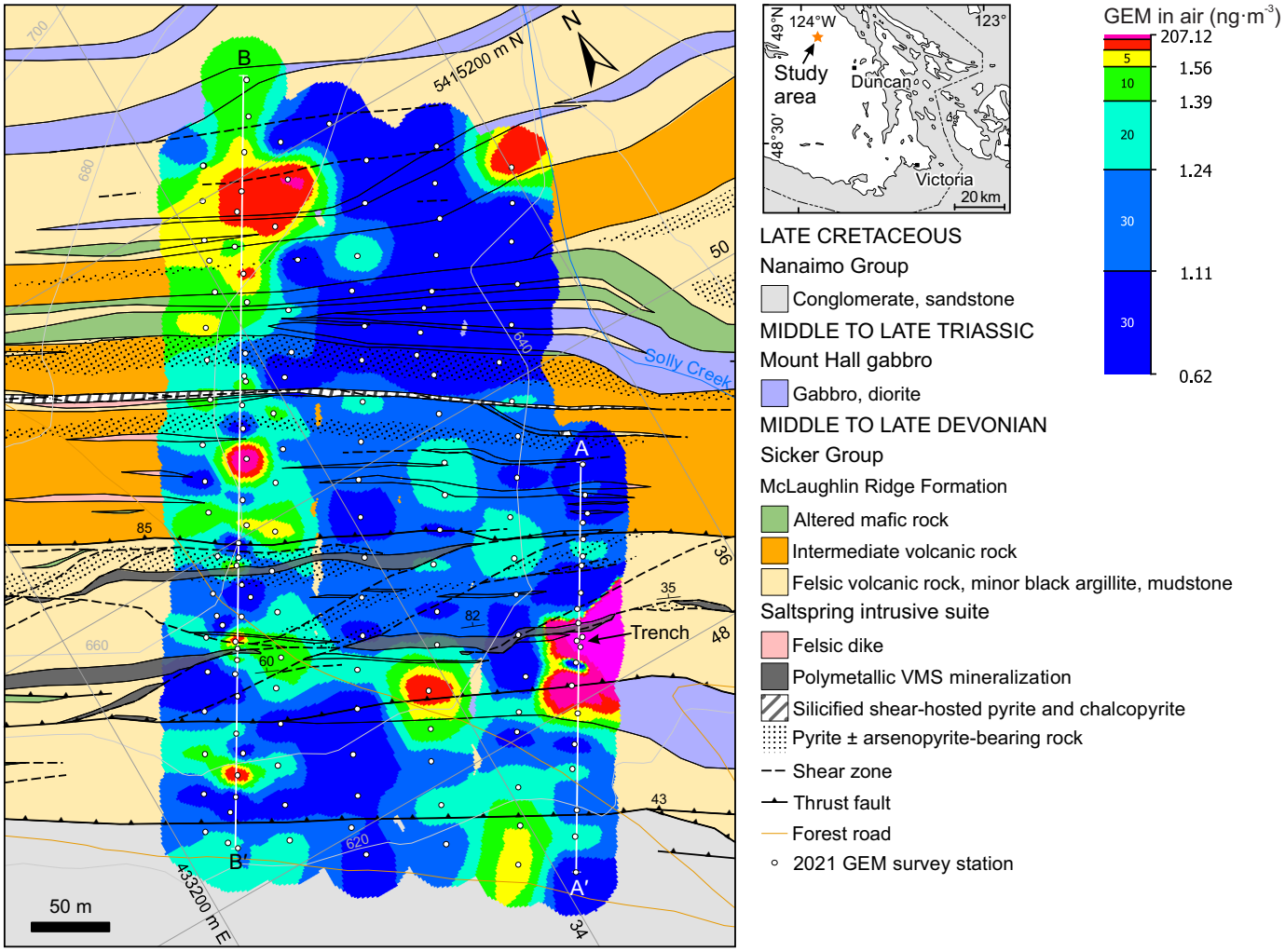

Fig. 4. Percentile-gridded, real-time GEM concentrations (ng·m^{-3}) in air 1 cm above ground and position of section lines A′-A and B′-B. Gridding interpolation based on modified inverse distance weighting method.

and briefer measurement times (1 minute per site). We adopted these parameters for a grid survey at Lara-Coronation on July 21, 2021. GEM concentrations measured every 13 to 36 m along 5 southwest-northeast traverses (030° azimuth; 450 m long each; 50 m spacing) range from 0.61 to 1.98 ng·m^{-3}, averaging 1.21 ±0.24 ng·m^{-3} (n=101). GEM response from the sediment-covered polymetallic mineralization is 1.7x background Hg, consistent with the orientation results discussed above (Table 1). Combined with the orientation data for mechanically disturbed sites, the percentile-gridded, real-time GEM values reveal a 224 by 30 m halo above the Coronation zone (Fig. 4). Weak haloes also trace the silicified shear zone with sulphide stringers at 300 m along B′-B for at least 220 m along strike. The prominent halo in the northern corner of the grid discussed above extends both to the southeast and northwest (open), with a footprint of at least 100 by 60 m. Except for a lone anomaly above felsic volcanic rocks in the eastern corner of the grid, background GEM concentrations characterize much of the area immediately west of Solly Creek (Fig. 4). On the other hand, GEM anomalies are more common to the west, within a band along B′-B at least 50 m wide. Notably, a pattern of northwest-trending GEM haloes emerges that reflects the bedrock structure (Fig. 4).

4.2. Experiment to investigate mechanically induced release of GEM

Surveys using mechanical agitation of surface materials immediately before sampling yielded up to two orders of magnitude stronger GEM anomalies (see above). The effect of mechanically induced emission of adsorbed Hg^0 is well known from soil-gas surveys (e.g., Zherebtsov et al., 1992) and is the basis for GEM-monitoring of Neotectonic activity and other geohazards such as landslides (e.g., Stepanov, 1997; Sun et al., 2017).

To investigate the release of GEM from mechanically disturbed overburden, we performed experiments measuring GEM concentrations in the air of glass jars (1 L) containing samples of ore minerals such as sphalerite, galena, molybdenite,

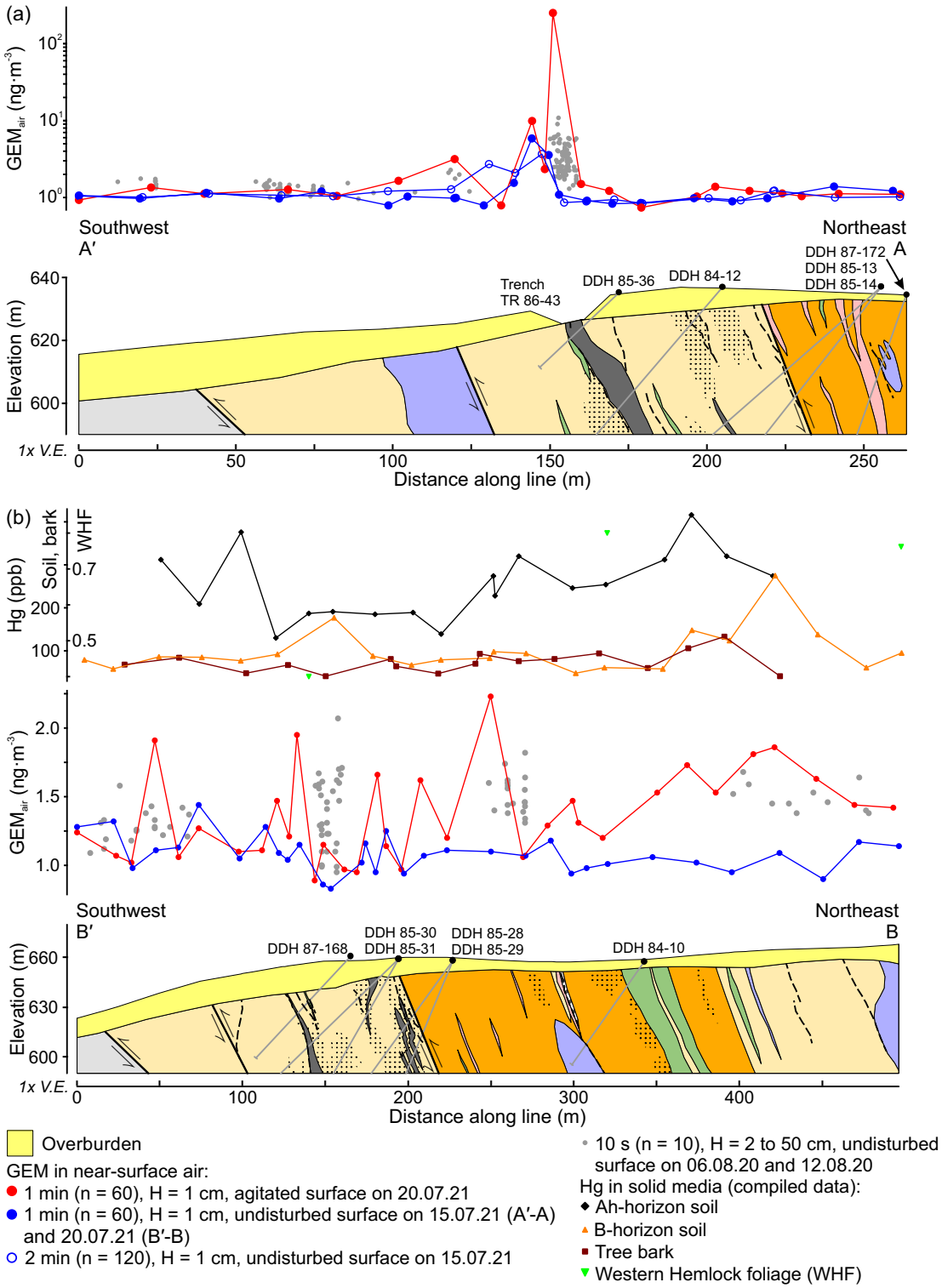

Fig. 5. Mercury concentrations with respect to distance along line (m) and cross-sections at the Lara-Coronation occurrence (see Fig. 4). Overburden thickness from Kapusta et al. (1988) and Bodnar (2017); diamond drill hole (DDH) collar locations and paths from Kapusta et al. (1988); geology legend as in Figure 4. H-sampling height above ground; n-number of GEM measurements (one per second) per site; grey symbols-mean GEM concentrations in air 2 to 50 cm above ground on August 6, 2020 and August 12, 2020 (from Rukhlov et al., 2021b). **a)** Profile 1 showing mean GEM (ng·m^{-3}; note the logarithmic scale) in air 1 cm above ground on July 15, 2021 (undisturbed surface; blue symbols) and on July 20, 2021 (agitated surface; red symbols) and southwest-northeast cross-section A′-A (1x vertical exaggeration). **b**) Profile 2 showing Hg (ppm) in soil and vegetation and mean GEM (ng·m^{-3}) in air 1 cm above ground on July 20, 2021 (symbols as in a), and southwest-northeast cross-section B′-B (1x vertical exaggeration). Soil and vegetation geochemical data compiled from Bodnar (2017) and Heberlein et al. (2017).

Fig. 6. Sediment surface mechanically disturbed using an Estwing GP100 hoe pick immediately before measuring GEM concentration.

Fig. 7. Measuring air temperature, barometric pressure, relative humidity, wind speed, and wind direction (azimuth) simultaneously with the GEM concentrations.

bornite, native copper, and native silver (Table 2). Even though these are non-Hg minerals, they contain trace amounts of Hg (0.15 to 92.2 ppm), directly measured by thermal decomposition of small splits of the samples (34 to 103 mg) using a Lumex RA-915 Lab analyzer in this study. Having stored the samples undisturbed in closed jars with screw lids for several days, the jars were opened immediately before sampling air 1 cm above the samples for 70 to 93 seconds, until the real-time GEM concentration reached a plateau in terms of time (s) vs. GEM ($ng \cdot m^{-3}$; Fig. 8). The jars were re-closed and gently shaken, and the air was reanalyzed 2 to 5 minutes after shaking. We measured GEM concentrations in air 1 m above ground in Victoria to check the background GEM concentrations after every 3 to 6 runs. The consistent background GEM concentrations rule out any Hg settling on the instrument's communications during the analysis (Table 2).

Running one-second GEM values in undisturbed jars ranged from <0.5 (the instrument's detection limit) to 274 $ng \cdot m^{-3}$ (n=549; Table 2). Time (s) vs. GEM ($ng \cdot m^{-3}$) profiles for all but one sample had a peak at about 10 seconds, with native silver (89 g) and galena (246 g) showing the maximum GEM concentrations (Fig. 8). Jars with molybdenite, sphalerite, native copper, and coarse-grained galena (54 g) had lower, but still anomalous GEM concentrations. Bornite (75 g), on the other hand, showed no peak, with background-level GEM concentrations up to 2.4 $ng \cdot m^{-3}$ (Fig. 8f; Table 2). The plateau-level GEM concentrations at the end of the first run (undisturbed samples) for all samples ranged from 1.53 to 11.4 $ng \cdot m^{-3}$, based on the median values (Table 2). The running one-second GEM values in the air of the shaken jars ranged from <0.5 to 124 $ng \cdot m^{-3}$ (n=502; Table 2). Time (s) vs. GEM ($ng \cdot m^{-3}$) profiles of the shaken samples are generally like those of undisturbed samples, having peak concentrations at 10 seconds, but show different sample vs. maximum GEM ($ng \cdot m^{-3}$) relationships. In contrast to GEM released from samples undisturbed for several days, native copper yielded almost 4x higher GEM concentration (124 $ng \cdot m^{-3}$) five minutes after shaking (Fig. 8c). Sphalerite and coarse-grained galena show similar levels of GEM before and after shaking, but a fragment of a large galena crystal (246 g), native silver, and molybdenite yielded 2 to 16x lower GEM levels after shaking relative to those released from the samples after undisturbed storage for several days (Table 2; Fig. 8). GEM concentrations (up to 1.6 $ng \cdot m^{-3}$) in a jar with bornite after shaking were indistinguishable from background GEM in air (Fig. 8f).

In summary, our experiments confirm release of adsorbed Hg at superimposed haloes when measurements were taken after surface materials at sample sites were mechanically disturbed. That the non-Hg ore minerals "exhale" Hg underlines the usefulness of GEM surveys in exploring for diverse deposits (Fursov, 2006).

4.3. Meteorological measurements

Seasonal and diurnal changes in meteorological conditions can influence GEM emission (see discussion in Rukhlov et al., 2021b). In contrast to Rukhlov et al. (2021b), measured GEM concentrations in this study do not show any effects of meteorological parameters, which were simultaneously measured (Fig. 9).

Table 2. Statistical summary of GEM concentrations in air 1 cm above ground and air of jars containing selected ore minerals.

Analysis	Run[1]	N	n	GEM concentrations in air (ng·m^{-3})									
				Mean	σ	Minimum	Percentiles						Maximum
							25	50	80	90	95	98	99	
Air 1 cm above ground at the Lara-Coronation polymetallic occurrence														
Undisturbed surface	na	75	na	1.23	0.73	0.79	0.97	1.05	1.22	1.41	2.89	4.73	5.86	5.86
Agitated surface	na	156	na	2.91	20.0	0.61	1.06	1.21	1.49	1.65	1.92	3.05	114	251
All data	na	231	na	2.37	16.4	0.61	1.02	1.13	1.41	1.64	1.96	3.61	8.60	251
Air 1 m above ground in Victoria, B.C.														
Background		na	240	1.03	0.32	0.05	0.83	1.02	1.29	1.48	1.60	1.66	1.77	1.82
Air 1 cm above samples of selected ore minerals in sealed glass jars														
Sphalerite (ZnS), coarse-grained aggregate; 47 g	1	na	70	12.1	13.9	0.58	4.90	7.71	14.8	31.8	52.6	64.8	66.6	66.6
	2	na	65	8.44	12.7	0.52	2.59	3.28	8.68	29.7	47.3	53.4	54.9	54.9
Galena (PbS), fragment of a large crystal; 246 g	1	na	72	26.1	48.6	0.76	3.32	3.94	39.0	92.4	161	212	225	225
	2	na	61	2.85	2.88	0.60	1.39	1.90	3.36	6.48	10.8	13.9	14.0	14.0
Native copper (Cu), dendritic aggregate; 24 g	1	na	93	5.63	3.89	0.36	4.26	4.88	5.99	7.16	12.8	23.5	26.7	26.7
	2	na	108	15.3	16.9	0.81	9.00	10.4	14.0	27.3	55.7	90.8	102	103
Native silver (Ag), dendritic aggregate; 89 g	1	na	93	27.5	51.9	0.74	9.71	11.4	13.5	68.2	180	258	274	274
	2	na	77	15.2	22.0	1.02	7.36	9.68	14.3	22.3	76.6	121	124	124
Molybdenite (MoS_2), single crystal; 18 g	1	na	71	9.12	19.8	0.69	1.38	1.86	5.76	28.1	64.6	94.2	94.7	94.7
	2	na	69	2.10	2.12	0.47	1.11	1.43	2.08	5.20	7.95	10.4	10.5	10.5
Bornite (Cu_5FeS_4), massive aggregate; 75 g	1	na	72	1.52	0.39	0.13	1.26	1.53	1.91	2.02	2.11	2.27	2.36	2.36
	2	na	55	0.94	0.34	0.18	0.68	0.96	1.26	1.37	1.48	1.62	1.63	1.63
Galena (PbS), coarse-grained aggregate; 54 g	1	na	78	2.73	0.91	0.50	2.25	2.69	3.43	3.88	4.56	4.93	4.99	4.99
	2	na	67	3.51	1.15	0.52	3.14	3.60	4.11	4.33	5.97	6.81	6.91	6.91

[1] Air of jars containing ore minerals: **1** - after several days of undisturbed storage; **2** - two to five minutes after gently shaking the sample. **N** - number of mean values used to calculate the statistical parameters; **n** – number of one-second measurements used to calculate the statistical parameters for air in Victoria, B.C. and air of jars containing samples of ore minerals; **σ** - standard deviation.

4.4. In-situ soil parameters

Rukhlov et al. (2021b) attributed the variable intensity of GEM haloes at Lara-Coronation to changes in overburden moisture. To investigate the influence of soil conditions in the present study, we measured in situ soil (2 to 5 cm deep) temperature, moisture, electrical conductivity, and pH at 19 stations along profile A'-A, simultaneously with the GEM survey on July 15, 2021 (from 12:01 to 14:48; Table 1). Soil temperature ranged from 16.9 to 44.1°C (averaging 27.93 ±7.82°C), moisture content (humidity) from 0 to 16.4%, (averaging 1.70 ±4.35%), electrical conductivity (EC; in microsiemens per cm) from 0 to 178 µS·cm^{-1} (averaging 20.5 ±42.2 µS·cm^{-1}), and pH from 4.3 to 6.4 (averaging 5.38 ±0.65). Variations in soil temperature mainly reflect direct exposure to the sun. Because of persistent dry weather, detectable moisture in soil was measured only at: 119 m (7.9%), 131 m (8.0%), and 147 m (16.4%) along profile A′-A (Fig. 5a). The maximum moisture content coincides with the maximum EC and pH values, and the minimum temperature was measured in rusty mud near the bottom of the partly flooded trench with exposed mineralization.

In summary, in-situ soil moisture and electrical conductivity display a weak correlation with simultaneously measured GEM concentrations, but in-situ soil temperature and pH generally do not (Fig. 10). Because all surveys in this study were performed in consistently dry weather conditions, we could not evaluate the moisture effect.

5. Discussion: GEM haloes above mineralization

Detailed, real-time sampling of GEM in air 1 cm above ground in this study confirmed GEM haloes in near-surface atmosphere above sediment-covered, polymetallic mineralization at Lara-Coronation (Figs. 4, 5; Rukhlov et al., 2021b). Background-level GEM haloes mark mineralized zones covered by glacial sediments (up to 22 m thick; Fig. 5b). Figure 11 schematically illustrates Hg dispersal from a drift-covered ore deposit and the processes that form GEM haloes in soil gas and near-surface atmosphere. The ore and its primary and secondary haloes release highly mobile and chemically stable Hg^0 (i.e., GEM) via sublimation, reduction, electrochemical reactions, and biogenic oxidation in the supergene zone. Concentration, temperature, and pressure gradients drive the upward GEM flux by diffusion and filtration along permeable zones, thereby forming constantly renewed superimposed Hg haloes directly above the ore.

Rather than forming dispersal plumes, GEM haloes in near-surface atmosphere occur directly above deposits because

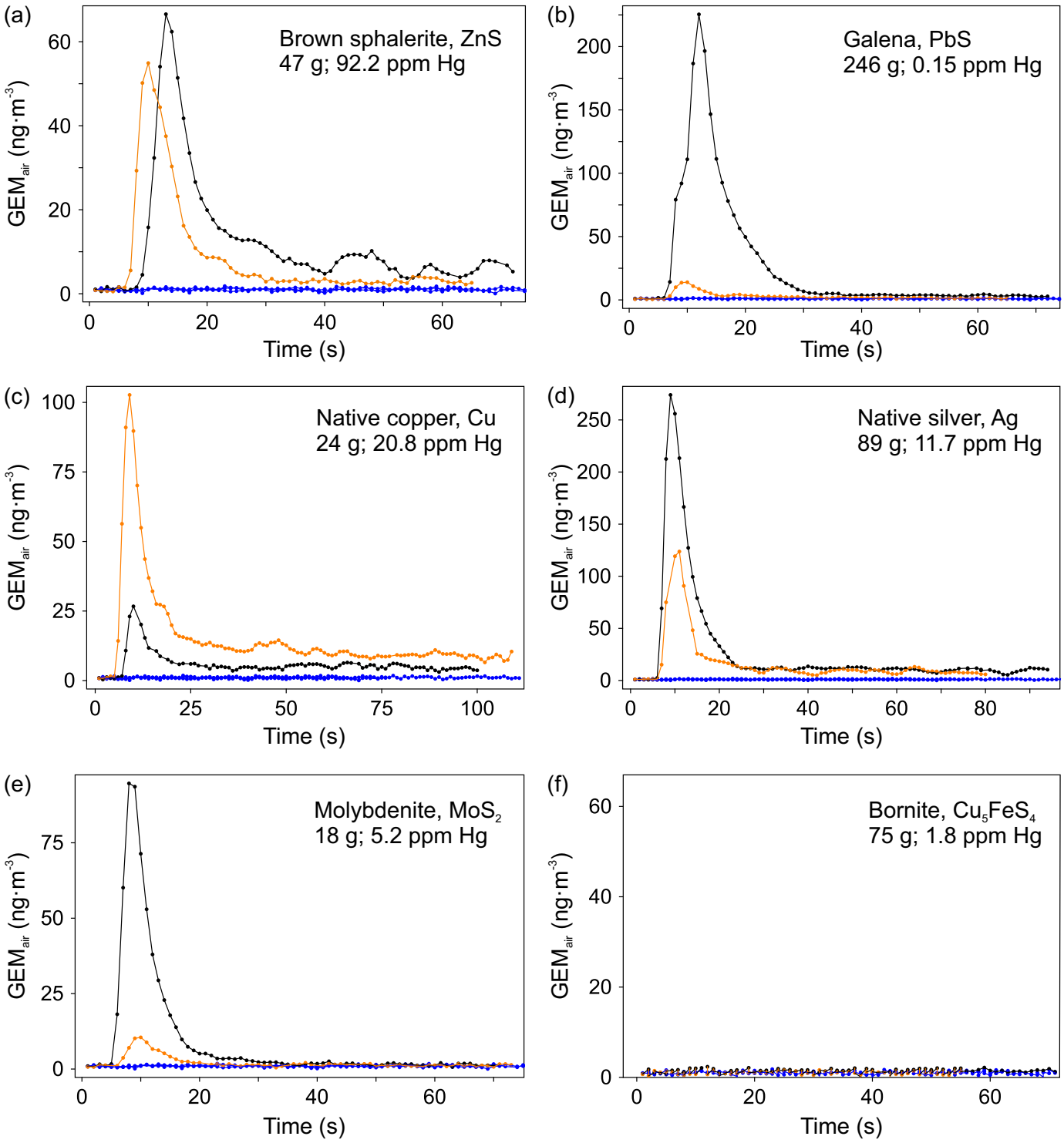

Fig. 8. Time (s) vs. GEM (ng·m^{-3}) in air 1 cm above samples of selected ore minerals in glass jars (1 L) after several days of undisturbed storage in closed jars (black symbols) and 2 to 5 min after the jars were re-sealed and gently shaken (orange symbols), and 1 m above ground in Victoria, B.C. (background GEM concentrations; blue symbols). **a)** Brown sphalerite, ZnS. **b)** Galena, PbS. **c)** Native copper, Cu. **d)** Native silver, Ag. **e)** Molybdenite, MoS_2. **f)** Bornite, Cu_5FeS_4. Total Hg concentrations in the samples (34 to 103 mg splits) of ore minerals directly measured by thermal decomposition using a Lumex RA-915Lab analyzer.

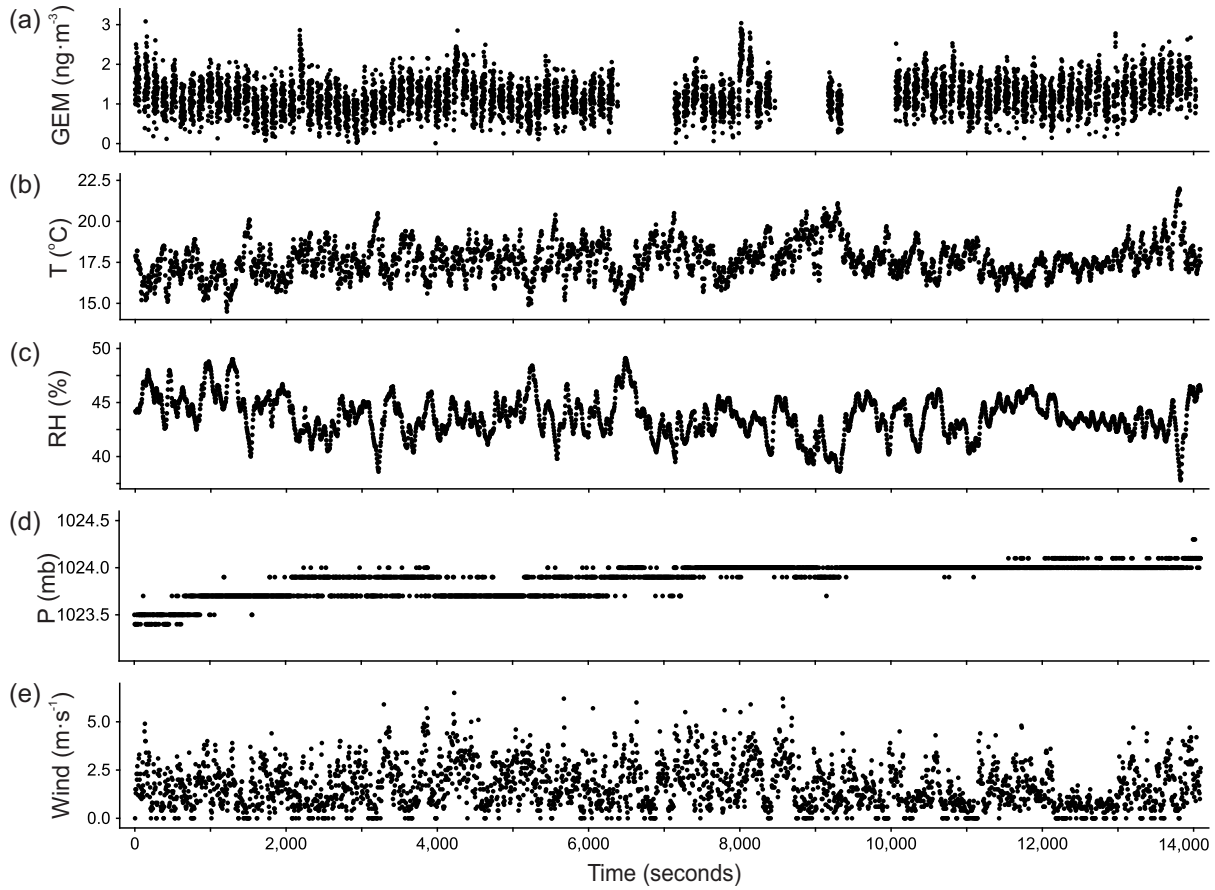

Fig. 9. Scatter plots of time (in seconds) vs. simultaneously measured, real-time GEM concentrations in near-surface air (GEM, in nanograms per cubic metre), air temperature (T, in degrees Celsius), relative humidity (RH, in %), barometric pressure at sea level (P, in millibars), and wind speed (Wind, in m per second) on July 21, 2021. **a)** Time (s) vs. GEM (ng·m^{-3}). **b)** Time (s) vs. T (°C). **c)** Time (s) vs. RH (%). **d)** Time (s) vs. P (mb). **e)** Time (s) vs. wind (m·s^{-1}).

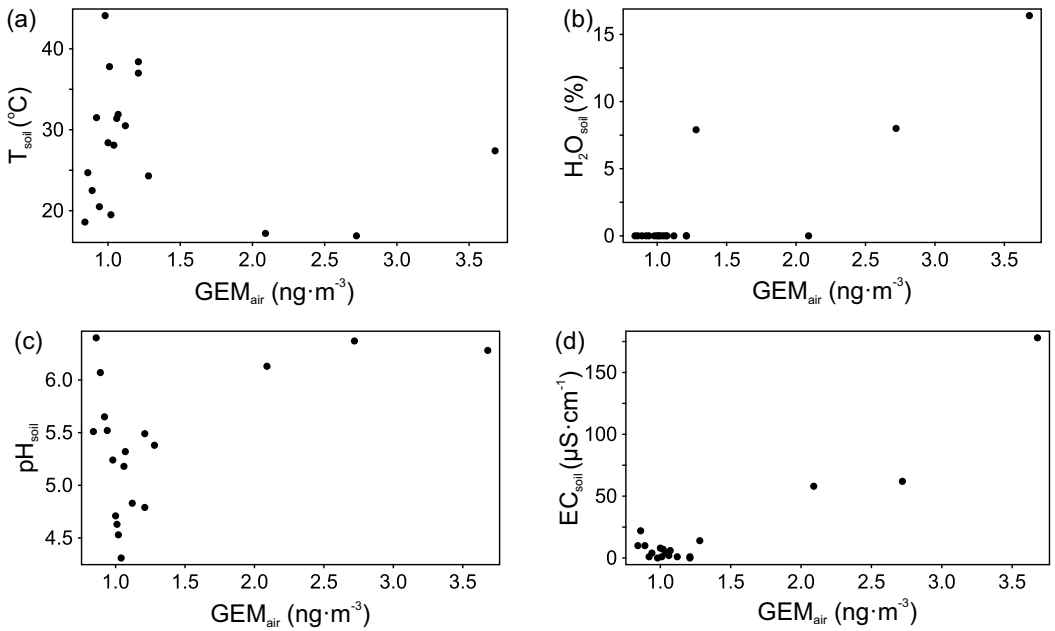

Fig. 10. Scatter plots of GEM concentrations in near-surface air (GEM_{air}, in nanograms per cubic metre) vs. in situ soil temperature (T_{soil}, in degrees Celsius); moisture content (H_2O_{soil}, %); hydrogen ion activity, defined as $-\log_{10}a(H^+)$, where $a(H^+)$ is the activity of the hydrogen ion (pH_{soil}); and electrical conductivity (EC_{soil}, in microsiemens per cm) for line A′-A) on July 15, 2021. **a)** GEM_{air} (ng·m^{-3}) vs. T_{soil} (°C). **b)** GEM_{air} (ng·m^{-3}) vs. H_2O_{soil} (%). **c)** GEM_{air} (ng·m^{-3}) vs. pH_{soil}. **d)** GEM_{air} (ng·m^{-3}) vs. EC_{soil} (µS·cm^{-1}).

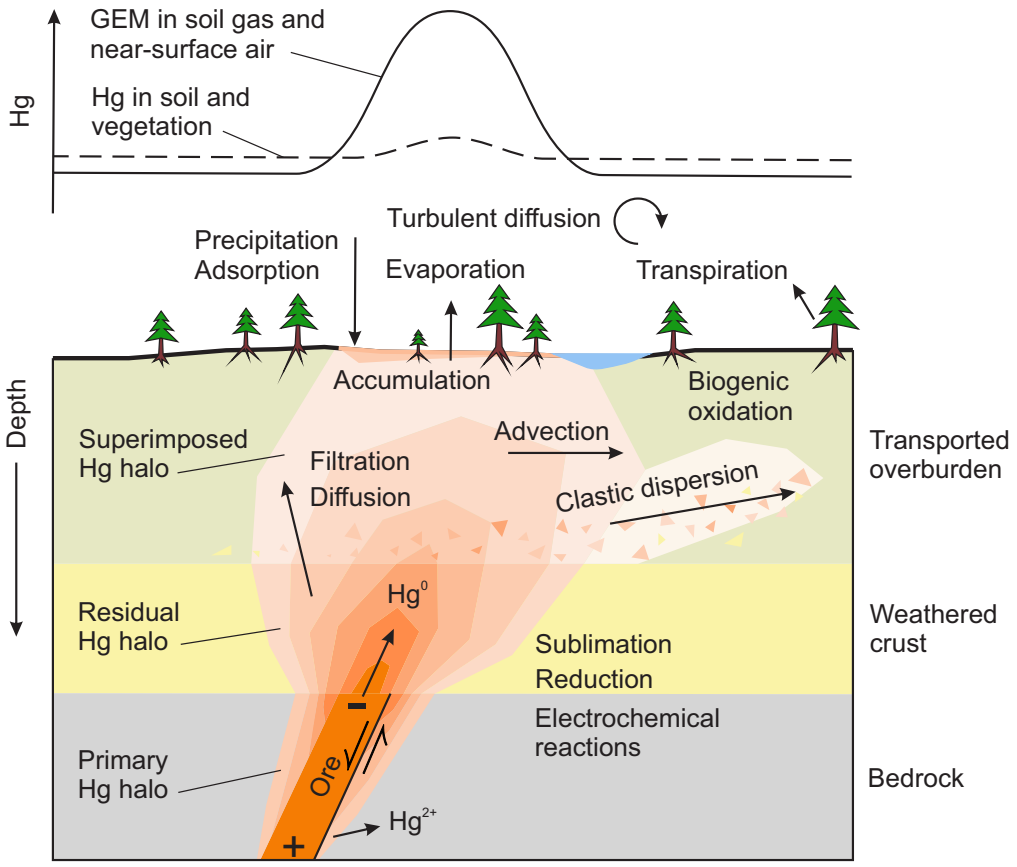

Fig. 11. Model illustrating Hg dispersal from a drift-covered ore deposit and the processes forming gaseous elemental mercury haloes in soil gas, near-surface air and mercury in soil and vegetation. Schematic cross-section showing primary Hg halo of a partly eroded polymetallic ore, residual Hg halo in weathered crust, superimposed Hg halo in a transported overburden, and processes of GEM dispersion and concentration in the surface environment. After Solovov (1985) and Fursov (2006).

Hg emitted into atmosphere is diluted by turbulent diffusion and transferred with air mass movement. Precipitation of atmospheric Hg adsorbed on aerosols and dust leads to Hg accumulation in soil and the hydrosphere. However, if overburden is transported, clastic, hydrochemical, and biochemical dispersion aureoles can be displaced or obscured (Fig. 11).

6. Conclusions

This study follows up on Rukhlov et al. (2021b) with detailed surveys measuring real-time gaseous elemental mercury (GEM) concentrations in air 1 cm above ground across sediment-covered, polymetallic VMS mineralization at the Lara-Coronation occurrence, southern Vancouver Island. New data confirm that direct and continuous analysis using a portable RA-915M Zeeman Hg analyzer can delineate buried mineralization in real-time. Improving on our previous technique, we sampled near-surface air under a bucket to minimize GEM removal and dilution due to wind and turbulent air movement, immediately after disturbing surface materials with a hoe pick. Coupled with more robust signal statistics, the improved technique yielded anomalies up to two orders of magnitude stronger than those reported in Rukhlov et al. (2021b).

To model the release of Hg from mechanically disrupted surface materials, we conducted experiments that measured GEM concentrations in the air of sealed jars containing samples of non-Hg ore minerals before and shortly after shaking. Because GEM levels in shaken jars were up to 122x background Hg, these experiments confirmed the release of weakly adsorbed Hg from overburden sediment and vegetation that were physically disturbed immediately before being sampled.

Our real-time grid survey revealed a pattern of northwest-trending GEM haloes reflecting bedrock structure, including a 224 by 30 m halo above the polymetallic VMS Coronation zone, covered by up to 22 m of overburden. Unrelated to any known mineralization, a prominent GEM halo in the northeast (Fig. 4), that coincides with Hg aureole in soils and vegetation (Fig. 5b), warrants follow-up exploration.

Measuring gaseous mercury using a portable device is simple, effective, and more efficient than standard geochemical surveys that collect sediment, soils, and vegetation. The method will become increasingly useful to the mineral industry as exploration shifts into areas covered by overburden. Future studies should consider porphyry Cu-Mo-Au and epithermal Au-Ag-Cu belts in the province, particularly in the commonly drift-covered Interior Plateau.

Acknowledgments

Lumex Instruments Canada kindly rented out a portable RA-915M Hg analyzer for this study and Mosaic Forest Management kindly granted a permit to access private lands on southern Vancouver Island. We very much appreciate thorough reviews and comments of Professor Elena G. Panova (Institute of Earth Science, Saint-Petersburg State University), and Lawrence B. Aspler (British Columbia Geological Survey).

References cited

Babkin, P.V., Baranov, Yu.E., Vasiliev, V.I., Demidov, N.G., Kirikilitsa, S.I., Kuznetsov, V.A., Nikiforov, N.A., Obolenskiy, A.A., Ozerova, N.A., Smirnov, V.I., Terekhova, G.A., and Fedorchuk, V.P., 1976. Metallogeny of mercury. Nedra, Moscow, 255 p. (in Russian).

Bodnar, M.M., 2017. Modelling geochemical dispersion above a buried polymetallic volcanogenic massive sulphide deposit in a recently glaciated terrain. Unpublished M.Sc. thesis, University of British Columbia, Canada, 212 p.

Cabassi, J., Lazzaroni, M., Giannini, L., Mariottini, D., Nisi, B., Rappuoli, D., and Vaselli, O., 2022. Continuous and near real-time measurements of gaseous elemental mercury (GEM) from an Unmanned Aerial Vehicle: A new approach to investigate the 3D distribution of GEM in the lower atmosphere. Chemosphere 288, 132547. <https://doi.org/10.1016/j.chemosphere.2021.132547>

Fursov, V.Z., 2006. Mercurometric Methods for Geologic Mapping and Ecological Investigations (Methodological Guide). Rosnedra, Geokart, Geos, Moscow, 315 p. (in Russian).

Heberlein, D.R., Dunn, C.E., and Rice, S., 2017. Halogens and other volatile compounds in surface sample media as indicators of mineralization. Part 1: Lara VMS deposit, Vancouver Island, BC (NTS 092B/13). Geoscience BC Report 2017-11, 43 p.

Jeon, B., Cizdziel, J.V., Brewer, J.S., Luke, W.T., Cohen, M.D., Ren, X., and Kelley, P., 2020. Gaseous elemental mercury concentrations along the northern Gulf of Mexico using passive air sampling, with a comparison to active sampling. Atmosphere 11, 1034. <https://doi.org/10.3390/atmos11101034>

Kapusta, J.D., Blackadar, D.W., and McLaughlin, A.D., 1988. 1987 report for drilling conducted on the Lara group I and Lara group II. British Columbia Ministry of Energy, Mines and Petroleum Resources, British Columbia Geological Survey, Assessment Report 17857, 71 p., 7 appendices, scale 1:500 to 1:10,000.

Kelso, I., and Wetherup, S., 2008. Independent technical report and mineral resource estimation: Lara polymetallic property, British Columbia, Canada. NI 43-101 Technical Report, 121 p.

Massey, N.W.D., 1995. Geology and mineral resources of the Duncan sheet, Vancouver Island, 92B/13. British Columbia Ministry of Energy, Mines and Petroleum Resources, British Columbia Geological Survey Paper 1992-4, 124 p.

Massey, N.W.D., Friday, S.J., Tercier, P.E., and Potter, T.E., 1991. Geology of the Duncan area (92B/13). British Columbia Ministry of Energy, Mines and Petroleum Resources, British Columbia Geological Survey Geoscience Map 1991-03, scale 1:50,000.

McLagan, D.S., Mitchell, C.P.J., Huang, H., Lei, Y.D., Cole, A.S., Steffen, A., Hung, H., and Wania, F., 2016. A high-precision passive air sampler for gaseous mercury. Environmental Science & Technology Letters 3, 24-29.

Muller, J.E., 1977. Geology of Vancouver Island. Geological Association of Canada, Mineralogical Association of Canada, Joint Annual Meeting 1977, Field Trip 7, April 21-24, Guidebook, 54 p.

Northcote, K.E., and Muller, J.E., 1972. Volcanism, plutonism, and mineralization: Vancouver Island. Canadian Institute of Mining, Metallurgy and Petroleum, Bulletin 65, 49-57.

Rudnick, R.L., and Gao, S., 2005. Composition of the continental crust. In: Heinrich, D.H., Rudnick, R.L., and Turekian, K.K., (Eds.), The Crust, Treatise on Geochemistry, Volume 3, Elsievier, Amsterdam, pp. 1-64.

Rukhlov, A.S., Mashyanov, N.R., Pitirimov, P.V., Hickin, A.S., Golovetskyy, M., and Coats, B., 2021a. Supplementary data for gaseous elemental mercury (GEM) response from sediment-covered, volcanogenic massive sulphide mineralization on southern Vancouver Island. British Columbia Ministry of Energy, Mines and Low Carbon Innovation, British Columbia Geological Survey GeoFile 2021-15, 1 p.

Rukhlov, A.S., Ootes, L., Hickin, A.S., and Mashyanov, N.R., 2021b. Near-surface mercury vapour haloes in air above ore deposits and faults on Vancouver Island: Insights into buried materials in real-time? In: Geological Fieldwork 2020, British Columbia Ministry of Energy, Mines and Low Carbon Innovation, British Columbia Geological Survey Paper 2021-01, pp. 113-143.

Ruks, T.W., 2015. Stratigraphic and paleotectonic studies of Paleozoic Wrangellia and its contained volcanogenic massive sulfide (VMS) occurrences, Vancouver Island, British Columbia, Canada. Unpublished Ph.D. thesis, University of British Columbia, Canada, 185 p.

Saukov, A.A., Aidinyan, N.K., and Ozerova, N.A., 1972. Studies of Mercury Geochemistry. Nauka, Moscow, 336 p. (in Russian).

Solovov, A.P., 1985. Methods of Geochemical Exploration for Ore Deposits: Textbook. Nedra, Moscow, 294 p. (in Russian).

Sprovieri, F., Pirrone, N., Bencardino, M., D'Amore, F., Carbone, F., Cinnirella, S., Mannarino, V., Landis, M., Ebinghaus, R., Weigelt, A., Brunke, E.-G., Labuschagne, C., Martin, L., Munthe, J., Wängberg, I., Artaxo, P., Morais, F., de Melo Jorge Barbosa, H., Brito, J., Cairns, W., Barbante, C., del Carmen Diéguez, M., Garcia, P. E., Dommergue, A., Angot, H., Magand, O., Skov, H., Horvat, M., Kotnik, J., Read, K.A., Neves, L. M., Gawlik, B. M., Sena, F., Mashyanov, N., Obolkin, V., Wip, D., Feng, X.B., Zhang, H., Fu, X., and Ramachan, R., 2016. Atmospheric mercury concentrations observed at ground-based monitoring sites globally distributed in the framework of the GMOS network. Atmospheric Chemistry and Physics 16, 11915-11935.

Stepanov, I.I., 1997. Mercury-indicator of "hot" hydrothermal zones and dynamic processes accompanied by deformation of rocks. Unpublished D.Sc. thesis, Institute of Mineralogy, Geochemistry and Crystal Chemistry of Rare Elements (IMGRE), Moscow, 165 p. (in Russian).

Sun, X., Si, X., Xiang, Y., and Liu, D., 2017. Soil mercury spatial variations in the fault zone and corresponding influence factors. Terrestrial, Atmospheric and Oceanic Sciences 28, 283-294.

Wetherup, S., 2010. Structural mapping and whole rock geochemical sampling: Lara polymetallic property. British Columbia Ministry of Energy, Mines and Petroleum Resources, British Columbia Geological Survey, Assessment Report 31578, 42 p., 4 appendices, scale 1:20,000.

Yasutake, A., Cheng, J.P., Kiyono, M., Uraguchi, S., Liu, X., Miura, K., Yasuda, Y., and Mashyanov, N.R., 2011. Rapid monitoring of mercury in air from an organic chemical factory in China using a portable mercury analyzer. The Scientific World Journal 11, 1630-1640.

Zherebtsov, Yu.D., Politikov, M.I., and Sikorskiy, V.Yu., 1992. Technology of Mercurometric Prospecting of Ore Deposits. Nedra, Moscow, 176 p. (in Russian).

British Columbia Geological Survey Publications 2021
including peer-reviewed external papers co-authored by BCGS staff

All BCGS publications are available for download, free of charge, from www.BCGeologicalSurvey.ca

To receive notification of our latest releases email Geological.Survey@gov.bc.ca

Papers

Paper 2021-01
Geological fieldwork 2020, a summary of field activities and current research, 172 p.

Wildgust, N., Jones, L.D., Clarke, G., and Hickin, A.S., 2021. British Columbia Geological Survey annual program review 2020-2021. In: Geological Fieldwork 2020, Ministry of Energy, Mines and Low Carbon Innovation, British Columbia Geological Survey Paper 2021-01, pp. 1-14.

Schiarizza, P., and Friedman, R.M., 2021. U-Pb zircon date for Eocene volcanic rocks on Mount Timothy, south-central British Columbia. In: Geological Fieldwork 2020, British Columbia Ministry of Energy, Mines and Low Carbon Innovation, British Columbia Geological Survey Paper 2021-01, pp. 15-21.

Schiarizza, P., and Friedman, R.M., 2021. U-Pb zircon dates for the Granite Mountain batholith, Burgess Creek stock, and Sheridan Creek stock, Gibraltar Mine area, south-central British Columbia. In: Geological Fieldwork 2020, British Columbia Ministry of Energy, Mines and Low Carbon Innovation, British Columbia Geological Survey Paper 2021-01, pp. 23-35.

Jones, G., Ootes, L., Milidragovic, D., Friedman, R., Camacho, A., Luo, Y., Vezinet, A., Pearson, D.G., and Schiarizza, P., 2021. Geochronology of northern Hogem batholith, Quesnel terrane, north-central British Columbia. In: Geological Fieldwork 2020, British Columbia Ministry of Energy, Mines and Low Carbon Innovation, British Columbia Geological Survey Paper 2021-01, pp. 37-56.

Ferbey, T., and Elia, E.A., 2021. Preliminary surficial geology of the northern Hogem batholith area, north-central British Columbia. In: Geological Fieldwork 2020, British Columbia Ministry of Energy, Mines and Low Carbon Innovation, British Columbia Geological Survey Paper 2021-01, pp. 57-64.

Van Wagoner, N., Ootes, L., and Thomson-Gladish, J., 2021. Volcanism and geochemistry of the Kamloops Group, south-central British Columbia. In: Geological Fieldwork 2020, British Columbia Ministry of Energy, Mines and Low Carbon Innovation, British Columbia Geological Survey Paper 2021-01, pp. 65-88.

Greig, C.J., Dudek, N.P., ver Hoeve, T.J., Quinn, T.D.M., Newton, G., Makin, S.A., and Greig, R.E., 2021. Geology of the Tatogga property: Geologic framework for the Saddle North porphyry Cu-Au deposit and the Saddle South epithermal Au-Ag vein system, Iskut district, northwestern British Columbia. In: Geological Fieldwork 2020, British Columbia Ministry of Energy, Mines and Low Carbon Innovation, British Columbia Geological Survey Paper 2021-01, pp. 89-111.

Rukhlov, A.S., Ootes, L., Hickin, A.S., and Mashyanov, N.R., 2021. Near-surface mercury vapour haloes in air above ore deposits and faults on Vancouver Island: Insights into buried materials in real-time? In: Geological Fieldwork 2020, British Columbia Ministry of Energy, Mines and Low Carbon Innovation, British Columbia Geological Survey Paper 2021-01, pp. 113-143.

Lett, R.E., and Paulen, R.C., 2021. Soil and till geochemical surveys at the Ace mineral property, central British Columbia. In: Geological Fieldwork 2020, British Columbia Ministry of Energy, Mines and Low Carbon Innovation, British Columbia Geological Survey Paper 2021-01, pp. 145-165.

Appendix: British Columbia Geological Survey publications and peer-reviewed journal papers authored by BCGS staff and released in 2020, pp. 167-172.

Ferri, F., McMechan, M., Richards, M.B., and Friedman, R., 2021. Organic-rich Upper Devonian shales of the Patry and Exshaw formations (Besa River Group) in the subsurface of Liard basin. British Columbia Ministry of Energy, Mines and Low Carbon Innovation, British Columbia Geological Survey Paper 2021-02, 42 p.

Cui, Y., 2021. A geospatial frame data model to simplify digital map compilation and integration. British Columbia Ministry of Energy, Mines and Low Carbon Innovation, British Columbia Geological Survey Paper 2021-03, 20 p.

Open Files

OF 2021-01

Clarke, G., Northcote, B., Katay, F., and Tombe, S., 2021. Mines, mine development, selected proposed mines, and selected exploration projects in British Columbia, 2020. British Columbia Ministry of Energy, Mines and Low Carbon Innovation, British Columbia Geological Survey Open File 2021-01.

GeoFiles

GF 2021-01

Clarke, G., Northcote, B., Katay, F., and Tombe, S.P., 2021. Exploration and mining in British Columbia, 2020. British Columbia Ministry of Energy, Mines and Low Carbon Innovation, British Columbia Geological Survey GeoFile 2021-01 (poster).

GF 2021-02

Tombe, S.P., 2021. Exploration and mining highlights, Northwest Region, 2020. British Columbia Ministry of Energy, Mines and Low Carbon Innovation, British Columbia Geological Survey GeoFile 2021-02 (poster).

GF 2021-03

Clarke, G., 2021. Exploration and mining highlights, North Central and Northeast regions, 2020. British Columbia Ministry of Energy, Mines and Low Carbon Innovation, British Columbia Geological Survey GeoFile 2021-03 (poster).

GF 2021-04

Northcote, B., 2021. Exploration and mining highlights, Southwest and South Central regions, 2020. British Columbia Ministry of Energy, Mines and Low Carbon Innovation, British Columbia Geological Survey GeoFile 2021-04 (poster).

GF 2021-05

Katay, F., 2021. Exploration and mining highlights, Southeast Region, 2020. British Columbia Ministry of Energy, Mines and Low Carbon Innovation, British Columbia Geological Survey GeoFile 2021-05 (poster).

GF 2021-06

Norris, J., and Wallace, B., 2021. Assessment report summary: Expenditures and activities 2019. British Columbia Ministry of Energy, Mines and Low Carbon Innovation, British Columbia Geological Survey GeoFile 2021-06 (poster).

GF 2021-07

Nixon, G.T., Scoates, J.S., Milidragovic, D., Nott, J.A.M., Manor, M.J., Spence, D.W., and Kjarsgaard, I.M., 2021. Cu-PGE vs. Cr-PGE mineralization in Alaskan-type mafic-ultramafic intrusions. British Columbia Ministry of Energy, Mines and Low Carbon Innovation, British Columbia Geological Survey GeoFile 2021-07 (poster).

GF 2021-08
Rukhlov, A.S., Spence, J., LaForge, N., Czech, E., Kabel, J., and Kaplenkov, G.N., 2021. Yttrium-rich garnet: a source of HREE? British Columbia Ministry of Energy, Mines and Low Carbon Innovation, British Columbia Geological Survey GeoFile 2021-08 (poster).

GF 2021-09
Cui, Y., Miller, D., Fortin, G., Zhao, S., Elia, E., and Orovan, E., 2021. Digital transformation of geoscience to enable analytics in mineral exploration. British Columbia Ministry of Energy, Mines and Low Carbon Innovation, British Columbia Geological Survey GeoFile 2021-09 (poster).

GF 2021-10
Nelson, J.L., Friedman, R., and van Straaten, B., 2021. LA-ICP-MS and TIMS U-Pb data files from the Iskut project (Dease Lake to Kitsault). British Columbia Ministry of Energy, Mines and Low Carbon Innovation, British Columbia Geological Survey GeoFile 2021-10, 13 p.

GF 2021-11
Lett, R.E., and Paulen, R.C., 2021. A compilation of soil and till geochemical data from surveys at the Ace and Getty South mineral properties, British Columbia. British Columbia Ministry of Energy, Mines and Low Carbon Innovation, British Columbia Geological Survey GeoFile 2021-11, 9 p.

GF 2021-12
Riddell, J., Soriano, J., and Lane, G., 2021. Mineral content of some Gething Formation coals. British Columbia Ministry of Energy, Mines and Low Carbon Innovation, British Columbia Geological Survey GeoFile 2021-12, 10 p.

GF 2021-13
Arnold, H., 2021. Depth to bedrock dataset for the Interior Plateau. British Columbia Ministry of Energy, Mines and Low Carbon Innovation, British Columbia Geological Survey GeoFile 2021-13, 6 p.

GF 2021-14
British Columbia Geological Survey, 2021. Critical minerals: From discovery to supply chain, program with abstracts. British Columbia Ministry of Energy, Mines and Low Carbon Innovation, British Columbia Geological Survey GeoFile 2021-14, 74 p.

GF 2021-15
Rukhlov, A.S., Mashyanov, N.R., Pitirimov, P.V., Hickin, A.S., Golovetskyy, M., and Coats, B., 2021. Supplementary data for gaseous elemental mercury (GEM) response from sediment-covered, volcanogenic massive sulphide mineralization on southern Vancouver Island. British Columbia Ministry of Energy, Mines and Low Carbon Innovation, British Columbia Geological Survey GeoFile 2021-15, 1 p.

GF 2021-16
Van Wagoner, N., Ootes, L., and Sutcliffe, B., 2021. Geochemical data from the Kamloops Group. British Columbia Ministry of Energy, Mines and Low Carbon Innovation, British Columbia Geological Survey GeoFile 2021-16, 2 p.

Information Circulars

IC 2021-01
Provincial Overview of Exploration and Mining in British Columbia, 2020. British Columbia Ministry of Energy, Mines and Low Carbon Innovation, British Columbia Geological Survey, Information Circular 2021-01, 134 p.

Clarke, G., Northcote, B., Katay, F., and Tombe, S.P., 2021. Exploration and Mining in British Columbia, 2020: A summary. In: Provincial Overview of Exploration and Mining in British Columbia, 2020. British Columbia Ministry of Energy, Mines and Low Carbon Innovation, British Columbia Geological Survey, Information Circular 2021-01, pp. 1-45.

Tombe, S.P., 2021. Exploration and mining in the Northwest Region, British Columbia. In: Provincial Overview of Exploration and Mining in British Columbia, 2020. British Columbia Ministry of Energy, Mines and and Low Carbon Innovation, British Columbia Geological Survey, Information Circular 2021-01, pp. 47-64.

Clarke, G., 2021. Exploration and mining in the North Central and Northeast regions, British Columbia. In: Provincial Overview of Exploration and Mining in British Columbia, 2020. British Columbia Ministry of Energy, Mines and and Low Carbon Innovation, British Columbia Geological Survey, Information Circular 2021-01, pp. 65-79.

Northcote, B., 2021. Exploration and mining in the South Central Region, British Columbia. In: Provincial Overview of Exploration and Mining in British Columbia, 2020. British Columbia Ministry of Energy, Mines and and Low Carbon Innovation, British Columbia Geological Survey, Information Circular 2021-01, pp. 81-100.

Katay, F., 2021. Exploration and mining in the Southeast Region, British Columbia. In: Provincial Overview of Exploration and Mining in British Columbia, 2020. British Columbia Ministry of Energy, Mines and and Low Carbon Innovation, British Columbia Geological Survey, Information Circular 2021-01, pp. 101-119.

Northcote, B., 2021. Exploration and mining in the Southwest Region, British Columbia. In: Provincial Overview of Exploration and Mining in British Columbia, 2020. British Columbia Ministry of Energy, Mines and Low Carbon Innovation, British Columbia Geological Survey, Information Circular 2021-01, pp. 121-134.

IC 2021-02
British Columbia Geological Survey, 2021. British Columbia coal industry overview 2020. British Columbia Ministry of Energy, Mines and Low Carbon Innovation, British Columbia Geological Survey Information Circular 2021-02, 13 p.

IC 2021-03
British Columbia Geological Survey, 2021. British Columbia Geological Survey. British Columbia Ministry of Energy, Mines and Low Carbon Innovation, British Columbia Geological Survey Information Circular 2021-03, 14 p. (brochure)

IC 2021-04
British Columbia Geological Survey, 2021. Mineral Development Office. British Columbia Ministry of Energy, Mines and Low Carbon Innovation, British Columbia Geological Survey Information Circular 2021-04, 4 p.

IC 2021-05
British Columbia Geological Survey, 2021. Online databases at the British Columbia Geological Survey. British Columbia Ministry of Energy, Mines and Low Carbon Innovation, British Columbia Geological Survey Information Circular 2021-05, 14 p.

IC 2021-06
The Golden Triangle of northwestern British Columbia. British Columbia. Ministry of Energy, Mines and Low Carbon Innovation, British Columbia Geological Survey Information Circular 2021-06, 6 p.

Contributions to partner publications

Bouzari, F., Lee, R.G., Hart, C.J.R., and van Straaten, B.I., 2021. Mineralogical and geochemical vectors within advanced argillic-altered rocks of north-central British Columbia (NTS 094E/02, 15, 104I/05). In: Geoscience BC Summary of Activities 2020: Minerals, Geoscience BC, Report 2021-01, pp. 91-104.

Jones, G.O., Pearson, D.G., Vezinet, A., Luo, Y., Stern, R.A., Milidragovic, D., and Ootes, L., 2021. Preliminary zircon geochemistry of northern Hogem batholith, Quesnel terrane, north-central British Columbia (parts of NTS 093M/16, 093N/13, 14, 094C/03-06, 094D/01, 08). In: Geoscience BC Summary of Activities 2020: Minerals and Mining, Geoscience BC, Report 2021-01, pp. 105-120.

Zagorevski, A., van Staal, C.R., Bédard, J.H., Bogatu, A., Canil, D., Coleman, M., Golding, M., Joyce, N.L., Lawley, C., McGoldrick, S., Mihalynuk, M.G., Milidragovic, D., Parsons, A., and Schiarizza, P., 2021. Overview of Cordilleran oceanic terranes and their significance for the tectonic evolution of the northern Cordillera. In: Ryan, J.J., and Zagorevski, A., (Eds.), Northern Cordillera geology: a synthesis of research from the Geo-mapping for Energy and Minerals program, British Columbia and Yukon; Geological Survey of Canada, Bulletin 610, 2021 pp. 21-65. <https://doi.org/10.4095/326053>

External peer-reviewed journal and volume publications (access may be limited by publisher)

Alberts, D., Gehrels, G., and Nelson, J.L., 2021. U-Pb and Hf analyses of detrital zircons from Paleozoic and Cretaceous strata on Vancouver Island, British Columbia: Constraints on the Paleozoic tectonic evolution of southern Wrangellia. Lithosphere, <https://doi.org/10.2113/2021/7866944>

Colpron, M., and Nelson, J.L., 2021. Northern Cordillera: Canada and Alaska. In: Elias, S., and Alderton, D., (Eds.), Encyclopedia of Geology, Second Edition. Academic Press, pp. 93-106.

George, S.W.M., Nelson, J.L., Alberts, D., Greig, C.J., and Gehrels, G.E., 2021. Triassic-Jurassic accretionary history and tectonic origin of Stikinia from U-Pb geochronology and Lu-Hf isotope analysis, British Columbia. Tectonics, 40. <https://doi.org/10.1029/2020TC006505>

Haugaard, R., Waterton, P., Ootes, L., Pearson, D.G., Yan Luo, Y., and Konhauser, K., 2021. Detrital chromites reveal Slave craton's missing komatiite. Geology, 49, <https://doi.org/10.1130/G48840.1>

Hickin, A.S., Lian, O.B., Telka, A., Levson, V.M., and Geertsema, M., 2021. Geomorphic and ecological age constraints for paraglacial to non-glacial transition in northeastern British Columbia, Canada. Quaternary Science Reviews 268, 107002. <https://doi.org/10.1016/j.quascirev.2021.107002>

Hunter, R.C., Lafrance, B., Heaman, L.M., and Thomas, D., 2021. Long-lived deformation history recorded along the Precambrian Thelon and Judge Sissons faults, northeastern Thelon Basin, Nunavut. Canadian Journal of Earth Sciences 58, 433-457. <https://doi.org/10.1139/cjes-2020-0108>

Lee, R.G., Plouffe, A., Ferbey, T., Hart, C.J.R., Hollings, P., and Gleeson, S.A., 2021. Recognizing porphyry copper potential from till zircon composition: A case study from the Highland Valley porphyry district, south-central British Columbia. Economic Geology, 116, 1035-1045. <https://doi:10.5382/econgeo.4808>

Milidragovic, D., Nixon, G.T., Scoates, J.S., Nott, J.A., and Spence, D.W., 2021. Redox-controlled chalcophile element geochemistry of the Polaris Alaskan-type ultramafic complex, British Columbia, Canada. The Canadian Mineralogist, 59, 1627-1660. <https://doi.org/10.3749/canmin.2100006>

Mohammadzaheri, A., Sigloch, K., Hosseini, K., and Mihalynuk, M.G., 2021. Subducted lithosphere under South America from multifrequency P wave tomography. Journal of Geophysical Research: Solid Earth, American Geophysical Union, 126. <https://doi.org/10.1002/essoar.10503967.2>

Poblete, F., Dupont-Nivet, G., Licht, A., Van Hinsbergen, D.J., Roperch, P., Mihalynuk, M.G., Johnston, S.T., Guillocheau, F., Baby, G., Fluteau, F., and Robin, C., 2021. Towards interactive global paleogeographic maps, new reconstructions at 60, 40 and 20 Ma. Earth-Science Reviews, 214, p.103508. <https://doi.org/10.1016/j.earscirev.2021.103508>

Simandl, G.J., Paradis, S., Savard, J., Miller, D., D'Souza, R., Araoka, D., Carlee Akam, C., Hoshino, M., and Kon, Y., 2021. Mineral control on the geochemistry of the Rock Canyon Creek REE-F-Ba deposit, British Columbia, Canada. Geochemistry: Exploration, Environment, Analysis. <https://doi.org/10.1144/geochem2020-010>

Simandl, L., Simandl, G.J., and Paradis, S., 2021. Specialty, critical, battery, magnet and photovoltaic materials: Market facts, projections and implications for exploration and development. Geoscience Canada, 48, 73-91. <https://doi.org/10.12789/geocanj.2021.48.174>

Each year, the British Columbia Geological Survey publishes Geological Fieldwork, a Summary of Fieldwork and Current Research (this volume), and the Provincial Overview of Mining and Exploration in British Columbia. All British Columbia Geological Survey publications can be downloaded, at no cost, from www.BCGeologicalSurvey.ca

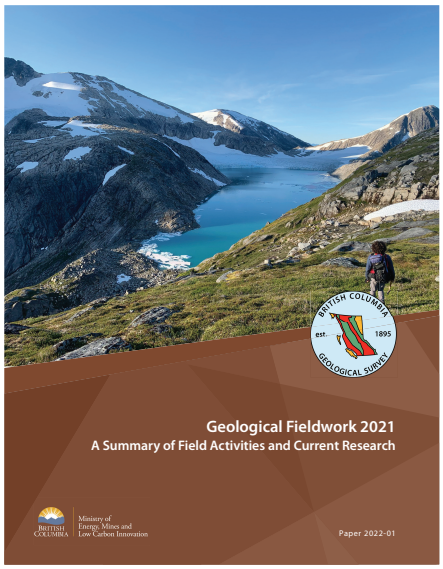

Geological Fieldwork volume, British Columbia Geological Survey Paper 2022-01

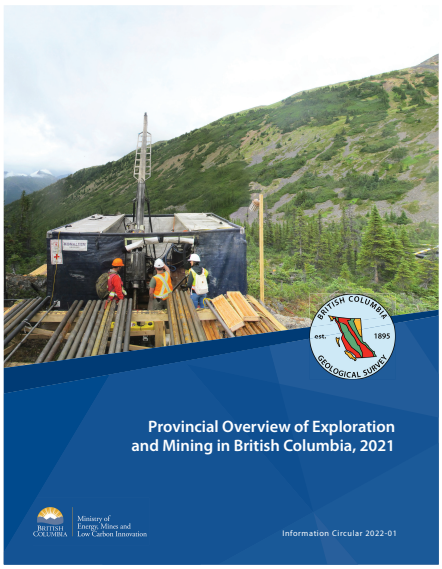

Provincial Overview of Mining and Exploration in British Columbia volume, Information Circular 2022-01

BRITISH COLUMBIA

Ministry of
Energy, Mines and
Low Carbon Innovation

BRITISH COLUMBIA
est. 1895
GEOLOGICAL SURVEY